Конденсированные среды и межфазные границы

РЕЦЕНЗИРУЕМЫЙ НАУЧНЫЙ ЖУРНАЛ

Condensed Matter and Interphases

PEER-REVIEWED SCIENTIFIC JOURNAL

Том/Vol. 25, №/No. 1

2023

Co 27 58.933 Cobalt
Ni 28 58.693 Nickel
Cu 29 63.546 Copper
Rh 45 102.91 Rhodium
Pd 46 106.42 Palladium
Ag 47 107.87 Silver
Ir 77 192.22 Iridium
Pt 78 195.08 Platinum
Au 79 196.97 Gold

Condensed Matter and Interphases
Kondensirovannye sredy i mezhfaznye granitsy

Condensed Matter and Interphases (Kondensirovannye Sredy i Mezhfaznye Granitsy) publishes articles in Russian and English dedicated to key issues of condensed matter and physicochemical processes at interfaces and in volumes.
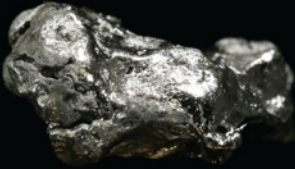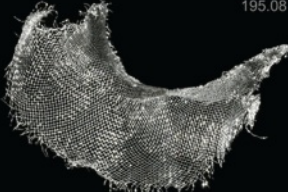
The mission of the journal is to provide open access to the results of original research (theoretical and experimental) at the intersection of contemporary condensed matter physics and chemistry, material science and nanoindustry, solid state chemistry, inorganic chemistry, and physical chemistry, and to share scientific data in the **following sections**: atomic, electron, and cluster structure of solids, liquids, and interphase boundaries; phase equilibria and defect formation processes; structure and physical and chemical properties of interphases; laser thermochemistry and photostimulated processes on solid surfaces; physics and chemistry of surface, thin films and heterostructures; kinetics and mechanism of formation of film structures; electrophysical processes in interphase boundaries; chemistry of surface phenomena in sorbents; devices and new research methods.

The journal accepts for publication: reviews, original articles, short communications by leading Russian scientists, foreign researchers, lecturers, postgraduate and undergraduate students.

CONTENTS

Condensed Matter and Interphases

Original articles

Atomic composition, microstructure, and electromagnetic properties of schungite micropowder

V. Yu. Buz'ko, S. N. Ivanin ✉, I. Yu. Shutkin, A. I. Goryachko, S. A. Udodov, A. V. Ozolin

*Kuban State Technological University,
2 Moskovskaya str., Krasnodar 350072, Russian Federation*

Abstract

The goal of the work was to study the microstructural, elemental, and electromagnetic properties of the samples of micropowder made from a natural mineral schungite. It was found that according to an X-ray spectral microanalysis, the carbon content in the studied samples of the mineral schungite was from 44 to 54 wt% while the iron content did not exceed 3.9 wt%. The iron content increased up to 6.1 wt% in the produced schungite micropowder.

It can be presumed that in the schungite, micropowder iron exists in the form of ferrimagnetic nanoparticles of magnetite and pyrite, which is formed when grinding schungite particles in ball mills with a steel body and a milling bowl. The produced schungite micropowder also showed the presence of weak ferrimagnetic properties according to the measurements of magnetic permeability performed by vector analysis of the impedance of electrical circuits.

In accordance with its electromagnetic characteristics, schungite micropowder made from shungite mineral is an effective radio-absorbing filler for building materials for cellular communication frequency bands.

Keywords: Schungite, Elemental composition, Microstructure, Electromagnetic characteristics, Building materials

For citation: Buz'ko V. Yu., Ivanin S. N., Shutkin I, Yu., Goryachko A. I., Udodov S. A., Ozolin A. V. Atomic composition, microstructure, and electromagnetic properties of schungite micropowder. *Condensed Matter and Interphases*. 2023;25(1): 3–13. https://doi.org/10.17308/kcmf.2023.25/10970

Для цитирования: Бузько В. Ю., Иванин С. Н., Шуткин И. Ю., Горячко А. И., Удодов С. А., Озолин А. В. Атомный состав, микроструктура и электромагнитные свойства микропорошка шунгита. *Конденсированные среды и межфазные границы*. 2023;25(1): 3–13. https://doi.org/10.17308/kcmf.2023.25/10970

✉ Sergey N. Ivanin, e-mail: Ivanin18071993@mail.ru

Condensed Matter and Interphases / Конденсированные среды и межфазные границы   2023;25(1): 3–13

V. Yu. Buz'ko et al. Atomic composition, microstructure, and electromagnetic properties of schungite micropowder

1. Introduction

Schungite is a unique natural carbon-containing mineral with a hybrid microstructure the proven reserves of 38-40 million tons of which are located in Karelia [1–3]. The total reserves of schungite rocks in Karelia is estimated to be several billion tons [4, 5]. It is known that the mineral content of schungite-containing rocks is formed by nanostructured schungite carbon, quartz, silicates (sericite, chlorite, feldspars), carbonates (siderite and dolomite), and sulphides (pyrite, pyritine, sphalerite, and chalcopyrite) [1-7]. The main chemical components of schungite rocks are schungite carbon with the content from 15 to 50 % [1, 3, 7], silica in the form of quarts of various modifications with the content from 25 to 75 % [1, 2], and pyrite with the content from 2 to 5.8 % [8–11].

Schungite rocks are natural microheterogeneous composite materials with various nanostructured forms of carbon. Being nanosized structures of different nature, schungite is considered to closely cover the surface of mineral particles of jointly present minerals with a film in the form of flakes [4–7, 12]. Due to the high content of the electrically conductive carbon phase [4–7, 12], schungite materials in the form of small particles or micropowders can be used as a dielectric filer for the production of radio-absorbing and radio-shielding composite materials [4–7, 12]. For example, schungite in the form of ground particles and micropowders is used as a dielectric filer in radio-absorbing construction materials [13–20] and radio-shielding concrete compositions [21–23].

Scanning electron microscopy (SEM) is widely used in practical material science to study a wide range of heterogeneous materials, such as metal, composite, building, and geological materials. This is due to the fact that the obtained images of the microstructure are of high quality and the process of preparation of the objects for microscopic studies is relatively simple and does not require long sample preparation. In case of natural minerals and rocks, the combination of the SEM method and microprobe analysis provides great potential for studying the structural features of the microstructure and phase microheterogeneity of minerals and mineral raw materials [25].

As for electron microscopy of rocks and raw building materials, the signal of the so-called "secondary electrons", the electrons of atoms emitted from the sample as a result of inelastic scattering (*secondary electron image* – SEI) [25, 26], is most often used to obtain images of particles. Secondary electrons are electrons with low energy, which is less than 50 eV, as they are mostly formed only in the ultrathin surface layer of the material up to 10 nm [28]. Is is known that secondary electrons allow obtaining a higher resolution (< 10 nm) signal, than in the case of the analysis of backscattered electrons signals [26].

A special mode (*backscattered electron image* – BEI) of signal registration by backscattered electrons is used to obtain the information on the surface distribution of phases in the studied samples when using SEM [25, 26]. In this mode, which can be named BSE, COMPO, or BSD depending on the manufacturer of the electronic microscope, image contrast is formed by backscattered electrons based on the difference between average atomic masses of the sample's components in the studied regions or phases [25, 26]. The emission of backscattered electrons significantly depends on the atomic number and, correspondingly, the atomic mass of the chemical elements. The greater the value of the average atomic mass of the studied area of the sample is, the greater the number of electrons are backscattered from these atoms at a smaller depth in the sample when the sample is exposed to the probing beam. Correspondingly, the areas of the sample with smaller average atomic masses look darker on the photo of the microstructure. Recently, the electron microscopy in backscattered electrons has been widely used in material science for construction and raw materials [27, 28].

In a number of works [5, 6, 12, 16], schungite powders used as a radio-absorbing filler for building and construction materials were considered as purely dielectric radio-absorbing fillers with electrically conductive carbon particles. However, doubts occur as to whether this assumption is correct as iron is known to be present in schungite rocks in the form of particles of such minerals as pyrite, magnetite, and siderite and iron hydroxides [2, 3, 5, 9–11]. At least one of these forms of iron, natural magnetite, is a pronounced ferrimagnetic material [29, 30] while natural pyrite has a mixture

Condensed Matter and Interphases / Конденсированные среды и межфазные границы   2023;25(1): 3–13

V. Yu. Buz'ko et al. Atomic composition, microstructure, and electromagnetic properties of schungite micropowder

of both weak ferrimagnetic and paramagnetic properties [31, 32].

The goal of the work was to study the microstructural, elemental, and electromagnetic properties of the samples of the micropowder made of a natural mineral schungite. Such a powder can be used as a highly-permeable dielectric filler to create eco-friendly building radio-absorbing materials, therefore, a comprehensive study of its properties is relevant.

2. Experimental

2.1. The studied schungite samples

Samples of schungite mineral (produced in the Russian Federation) in the form of particles 2 to 12 mm in size from the schungite rock of the Zazhoginsky deposit were purchased commercially at different times in different batches (Table 1).

We produced a sample of schungite powder made from the particles of the mineral from sample No. 2 as it showed a smaller content of carbon, which is important for durability of concrete compositions based on it. The schungite micropowder was obtained through mechanic abrasion of schungite particles in in a ball mill MSHL-1 with a drum and milling balls made of non-magnetic stainless steel AISI SS304 in the course of 4 hours and through sifting of the obtained powder with a sieve with cell sizes of 100μm. Such a method of preparation of schungite micropowder allowed simulating the contamination of the powder with iron compounds which inevitably appear due to abrasion of schungite particles in a ball mill with the most common steel drum and steel/cast-iron milling bowl.

2.2. Scanning electron microscopy and elemental analysis

The microstructure of schungite samples was studied using a scanning electron microscope

Table 1. The studied schungite samples

Sample	Description	Particle size	Manufacturer
№ 1	mineral particles	5–12 mm	OOO "SHUGGE"
№ 2	mineral particles	2–5 mm	OOO NPK Karbon-Shungite
№ 3	micro-powder	<100 mkm	Self-made

EVO HD15 (ZEISS) with both modes of secondary electrons (SEI) and backscattered electrons (BSD). The BSD mode was chosen due to the fact that in this case the image reflects real phase composition of the sample and has a good phase contrast. The qualitative elemental analysis and mapping of the distribution of chemical elements were conducted using an INCA X-Max energy dispersive microanalysis attachment (Oxford Instruments) to the scanning electron microscope. The samples for measurements were placed on carbon tape with special duralumin holders. The elemental composition of each sample was measured three times in different areas, and the results were statistically averaged.

2.3. VNA measurements.

To determine the electromagnetic properties of the produced schungite micropowder, we measured the characteristics of losses upon reflection based on its composite with paraffin with mass fraction of the filler of 50 % in a 10-cm HP-11566A coaxial cell with the size of a toroid of 7.0×3.05 mm using a KC901V Deepace dual-port vector network analyser in the frequency range of 15 MHz to 7.0 GHz.

According to the theory of power lines, the damping constant of an electromagnetic wave in a material can be determined as follows [33]:

$$\gamma = j \cdot \frac{2\pi f}{c} \sqrt{\varepsilon \mu}, \tag{1}$$

where f is the frequency of the electromagnetic wave, c is the speed of light, ε and μ are the complex dielectric and magnetic permeability of the material.

Thus, the more the value ($\varepsilon \cdot \mu$) is, the more effective the electromagnetic wave is absorbed in this material with frequency f.

In the case of a perfect quarter wave electromagnetic absorber, the relationship between the frequency of maximum radio absorption f_m and its electromagnetic characteristics is determined by the following formula [34]:

$$f_m = \frac{c}{4d_m} \frac{1}{\sqrt{\varepsilon' \mu'}} \left(1 + \frac{1}{8} \tan^2 r_\mu \right), \tag{2}$$

where d_m is the thickness of the absorbing layer, c is the speed of light, ε' and μ' are the real parts

Condensed Matter and Interphases / Конденсированные среды и межфазные границы   2023;25(1): 3–13

V. Yu. Buz'ko et al.   Atomic composition, microstructure, and electromagnetic properties of schungite micropowder

of the dielectric and magnetic permeability of the material, tan r_μ is the magnetic loss angular tangent.

Taking into account the fact that schungite is not a pronounced magnetic material and that for its composite with paraffin a simplified formula can be obtained to describe the relationship between the peak frequency of maximum radio absorption f_m of the material and its electromagnetic characteristics [34]:

$$\sqrt{\varepsilon\mu} = \left(4 f_m d_m / nc\right), \qquad (3)$$

where $n = (1, 3, 5...)$ for the cases of resonant reflection of electromagnetic waves.

Magnetic permeability of the sample of a composite produced from the obtained schungite powder with paraffin was calculated by the experimental measurement of S-parameter S_{21} using a dual-port vector network analyser through the calculation of the corresponding impedance of electrical circuit Z [35–37], taking into account that with the used equipment $Z_0 = 50$ Ohm:

$$Z = Z_0 \frac{2\left(1 - S_{21}\right)}{S_{21}}. \qquad (4)$$

The approach of calculating the impedance of an electric circuit from the transmission parameter S_{21}, as compared to its calculation from the parameter S_{11}, is believed to provide more accurate values of the magnetic permeability of samples from the impedance of the circuit in a wide frequency range from 1 MHz to 6.5 GHz [36, 37].

Using the obtained frequency dependence of the impedance of circuit Z, we calculated the magnetic permeability of sample μ according to the following formula [36, 37]:

$$\mu = \mu' - j\mu'' = 1 + \frac{Z - Z_{air}}{jhf\mu_0 \ln\left(r_2 / r_1\right)}, \qquad (5)$$

where Z and Z_{air} are the values of the complex impedance of the circuit with the coaxial cell used in the presence and absence of the studied toroidal sample, h is the height of the toroidal sample, f is the frequency of electromagnetic radiation, μo is the magnetic permeability of free space, and r_2 and r_1 are the outer and inner radii of the toroidal sample.

3. Results and discussion

The microstructure of the surface of the studied schungite mineral is presented in Fig. 1. It was found that the studied samples of schungite mineral contained a nanostructured phase with an average size of nanoparticles of 85 ± 30 nm. According to the data of electron microscopy, such nanoparticles are grouped in submicrosized aggregates which fill the pores, fractures, and edge regions of microparticles of forming minerals. Thus, the images of the schungite surface obtained in secondary electrons provide information on the presence of pronounced microheterogeneities, large pores, and surface relief in the studied material.

To study the microheterogenous state of the schungite sample No. 1, we selected the BSD mode of backscattered electrons as in this case the image reflects the real phase composition of a sample and, as compared to the SEI mode of secondary
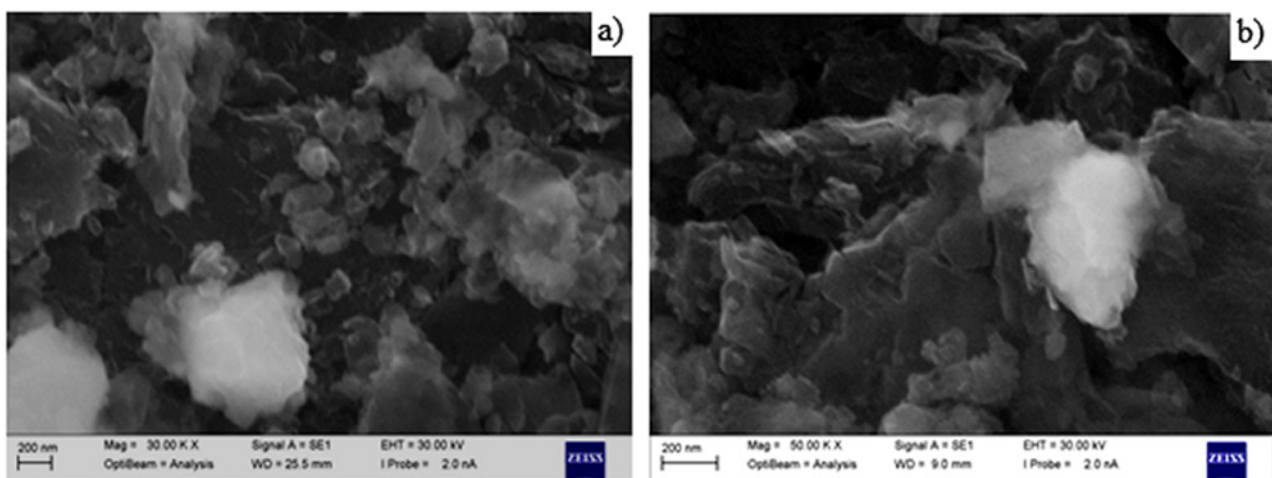
Fig. 1. Photos of the microstructure of the surface of the schungite mineral: a – sample No. 1; b – sample No. 2

Condensed Matter and Interphases / Конденсированные среды и межфазные границы   2023;25(1): 3–13

V. Yu. Buz'ko et al. Atomic composition, microstructure, and electromagnetic properties of schungite micropowder

electrons, it allows obtaining an image with a high phase contrast. The back reflected electrons were recorded by two semiconductor detectors located directly above the sample. In the BSD mode, the signals of two detectors were summed, which allowed minimising the influence of the relief irregularities on a raster image. Therefore, the total signal was mostly dependent on the change of the average atomic number, that is on the composition of the studied area of the sample.

Photos of the microstructure of the surface of the schungite mineral in the mode of backscattered electrons are presented in Fig. 2. According to the data in Fig. 2, in these photographs the phases based on elements with a small atomic mass (C, O, Al, Si) are dark areas while phases based on elements with a large atomic mass (Fe, S) correspond to light areas.

It can be seen that the ferric sulphide (in the form of a FeS_2 pyrite) in sample No. 1 was represented by the particles with the size of 200–300 nm while in sample No. 2 the ferric sulphide was represented by the particles of smaller sizes between 100 and 220 nm. Therefore, microscopic images of the schungite surface obtained in backscattered electrons provided information on the presence of a pronounced heterogeneous microstructure in the material.

Energy-dispersive X-ray spectroscopy microanalysis (EDS) allowed identifying relative concentrations of chemical elements in the schungite samples and reflect the distribution of chemical elements on the surface of the studied samples (Fig. 3).

According to the data of Fig. 3, there was a pronounced microheterogeneity of phases on the surface of the studied schungite mineral, and the association of iron and sulphur with the formation of pyrite microcrystals could also be observed. However, some atoms of sulphur did not have any direct relation with the location of iron atoms and it was most likely associated with the microphase of gypsum particles $CaSO_4 \cdot 2H_2O$.

The elemental composition of the studied schungite samples and its powder prepared according to the EDS data is presented in Table 2.

The obtained results on the elemental composition of schungite correlate well with the experimental data of other previous works [1, 2, 5–11]. It was discovered that the iron content in the studied schungite samples was relatively low and did not exceed 3.8 wt%. It is considered [1–3, 5–11] that iron is present in schungite rocks in the form of pyrite, magnetite, siderite, and iron hydroxides. Based on the obtained elemental ratios and the data from previous works [1–3, 5–11], we can conclude that in the studied samples of the schungite mineral, iron is partially found in the form of iron disulphide FeS_2 (pyrite), both as the main iron-containing mineral in schungites in accordance with [9-11] and in the form of iron oxides Fe_2O_3 (hematite) and Fe_3O_4 (magnetite).

According to the data of Table 2, milling schungite mineral sample No. 2 into sample No. 3 in a ball mill resulted in an increase of the share of elemental iron in it by 60 %. The
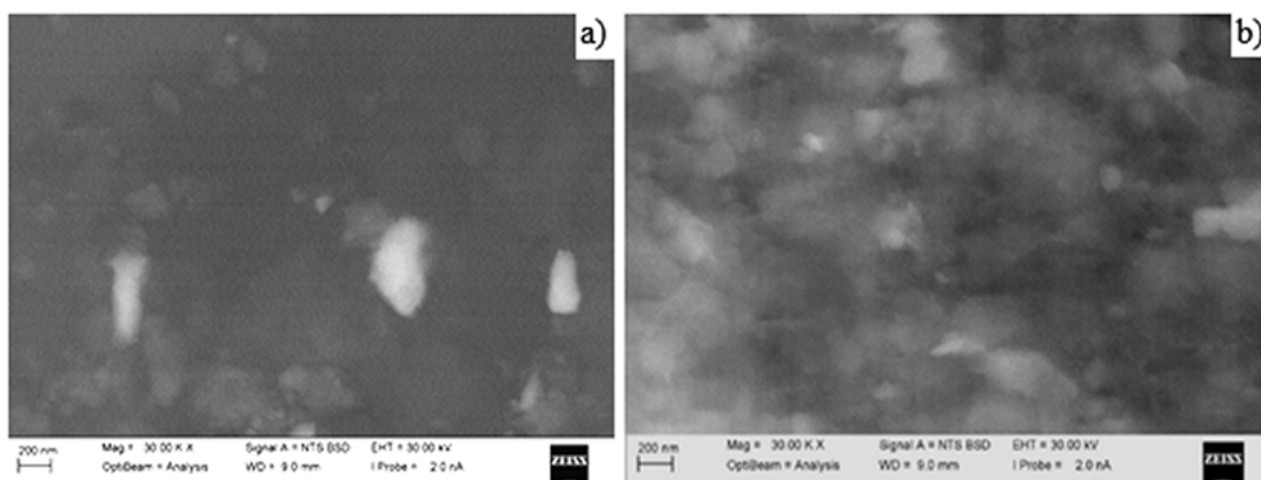
Fig. 2. Photos of the microstructure of the surface of the schungite mineral in the mode of backscattered electrons: a – sample No. 1; b – sample No. 2

Condensed Matter and Interphases / Конденсированные среды и межфазные границы 2023;25(1): 3–13

V. Yu. Buz'ko et al. Atomic composition, microstructure, and electromagnetic properties of schungite micropowder
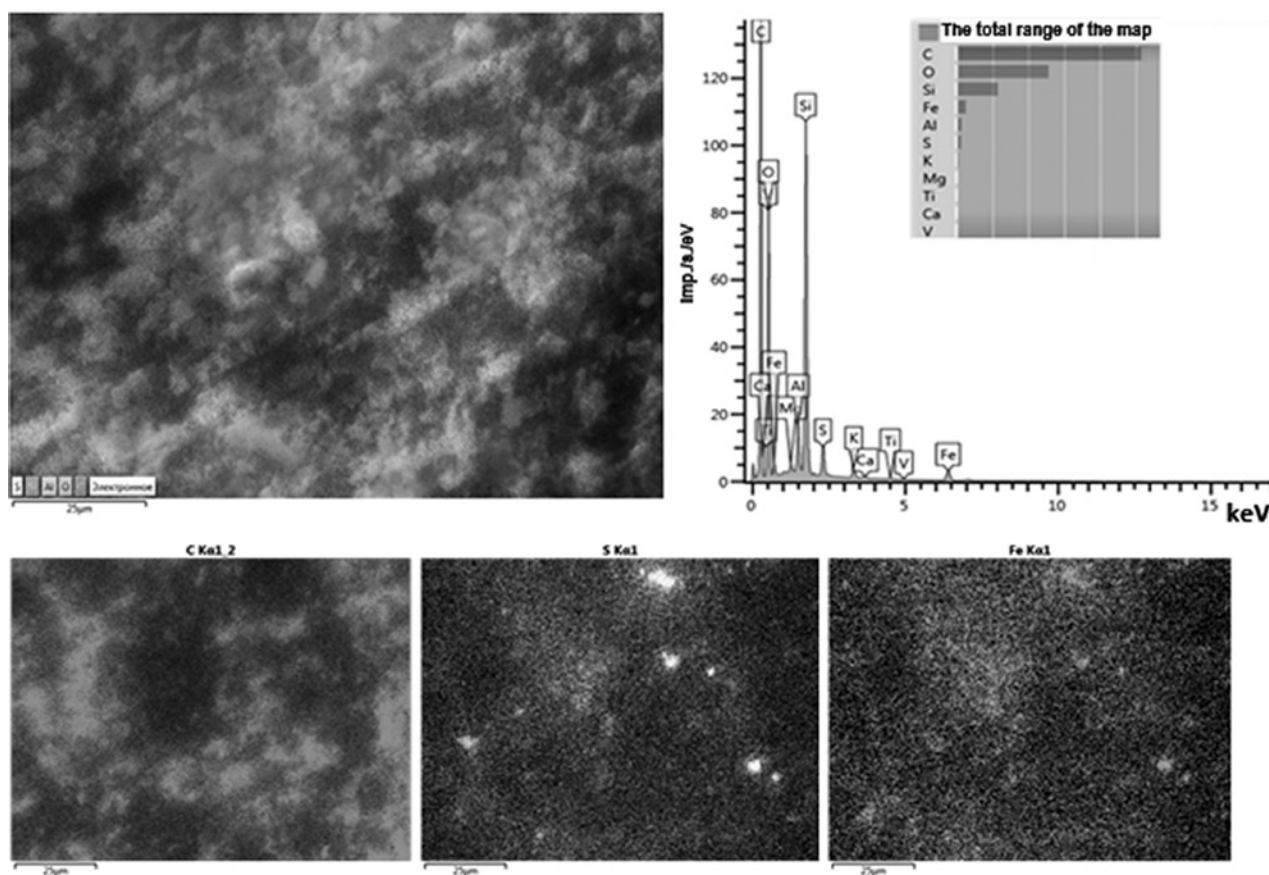
Fig. 3. The distribution of chemical elements on the surface of the schungite mineral No. 1 and the corresponding EDS spectrum

Table 2. Elemental composition of the studied schungite samples

Element	№1 (wt%)	№1 (at%)	№2 (wt%)	№2 (at%)	№3 (wt%)	№3 (at%)
C	50.91±0.19	63.77±0.24	44.11±1.22	57.01±1.58	32.34±3.78	43.80±5.12
O	27.72±0.12	26.07±0.11	31.79±0.88	30.85±0.85	43.24±2.91	43.97±2.96
Mg	0.36±0.03	0.22±0.02	0.20±0.09	0.13±0.06	0.14±0.10	0.09±0.06
Al	2.36±0.06	1.32±0.03	1.74±0.12	1.00±0.07	1.46±0.41	0.88±0.25
Si	11.59±0.12	6.21±0.06	16.57±0.45	9.16±0.25	14.89±1.09	8.62±0.63
S	1.77±0.07	0.83±0.03	0.98±0.12	0.47±0.06	1.05±0.22	0.53±0.11
K	1.07±0.05	0.41±0.02	0.82±0.14	0.33±0.06	0.80±0.15	0.33±0.06
Ca	0.25±0.03	0.09±0.01	–	–	–	–
Ti	0.22±0.03	0.07±0.01	–	–	–	–
V	0.04±0.02	0.01±0.01	–	–	–	–
Fe	3.68±0.11	0.99±0.01	3.80±0.22	1.06±0.18	6.08±1.53	1.77±0.45
Ni	0.04±0.02	0.01±0.01	–	–	–	–

increased elemental content of iron in the produced schungite powder was associated with the technological features of obtaining schungite micropowders through grinding pieces of schungite-containing rock in a ball mill with a steel milling bowl. Apparently, due to the process of mechanical oxidation of iron sulphide to sulphate ions and elemental iron to carbonate ions, the shares of carbon, aluminium, magnesium, silicon, and potassium systematically lowered. A considerable decrease in the proportion of carbon in sample No. 3 can also be associated with the formation of ultra-high dispersive carbon upon grinding which is

Condensed Matter and Interphases / Конденсированные среды и межфазные границы   2023;25(1): 3–13

V. Yu. Buz'ko et al. Atomic composition, microstructure, and electromagnetic properties of schungite micropowder

intensively lost in the course of sifting of the ground schungite micropowder.

To study the microheterogenous state of the produced schungite powder (Fig. 4), we selected the BSD mode of backscattered electrons as in this case the image reflected the real phase composition of a sample and, as compared to the SEI mode of secondary electrons, it allowed receiving an image with a high phase contrast.

The observation of the produced schungite micropowder in the BSD mode showed its pronounced microheterogeneity. It can be seen that the carbon and oxygen phases are distributed unevenly, and these areas are the darkest. The formation of multiple faults and edge cleavages of microparticles is also typical. In the course of schungite grinding, multiple point areas with lowered content of carbon appear (Fig. 4, BSD –

light areas). Therefore, according to the obtained experimental data of electron microscopy and EDS, significant microheterogeneity can be found in the distribution of chemical elements on the surface of the particles of the studied schungite powder sample. These results confirm that schungite mineral is a natural microheterogeneous composite material.

The frequency spectra of the radio absorption of the studied composite that are based on the produced schungite micropowder were processed and the results are presented in Fig. 5. It can be seen that there is a systemic shift of the resonance peak of radio absorption to the low frequency region upon an increase in the thickness of the sample.

It can also be observed that maximum losses upon reflection in the frequency range of 2 to 6.2
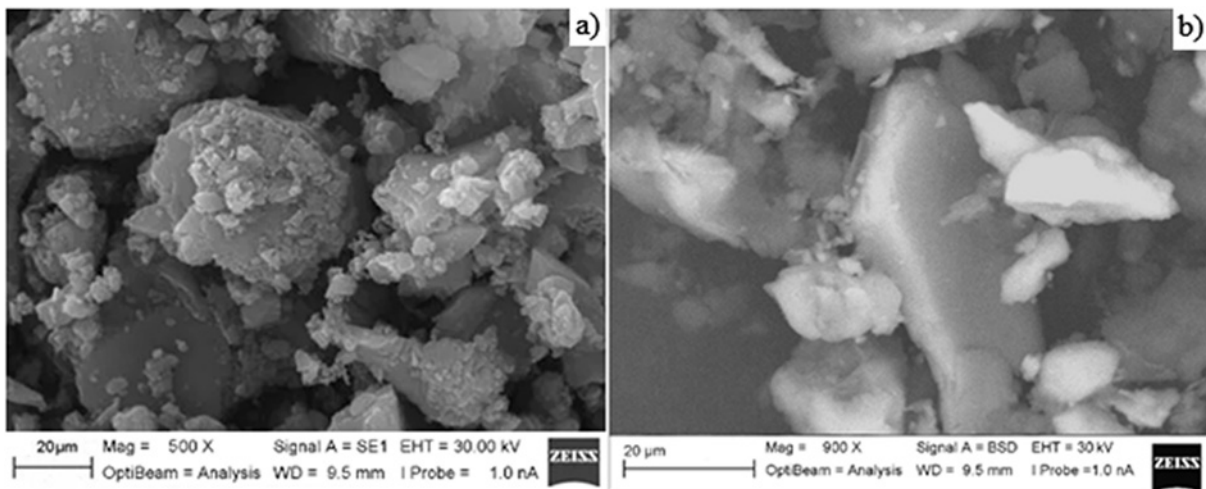
Fig. 4. Photos of the surface of particles of prepared schungite micropowder: a – in SEI mode; b – in BSD mode
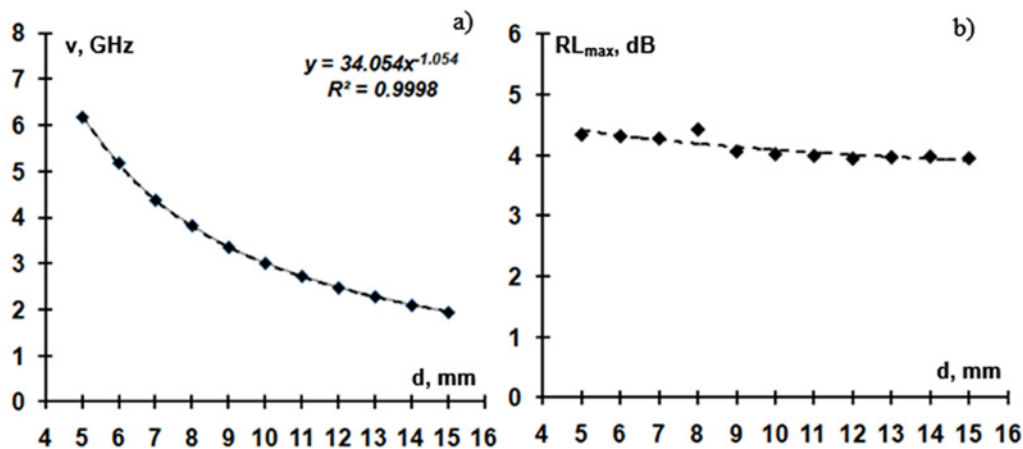
Fig. 5. Dependence of the resonance frequency (a) and the radio absorption peak (b) for the paraffin-schungite composite (50 wt%) on the sample thickness

Condensed Matter and Interphases / Конденсированные среды и межфазные границы   2023;25(1): 3–13

V. Yu. Buz'ko et al. Atomic composition, microstructure, and electromagnetic properties of schungite micropowder

GHz of the studied paraffin-schungite composite (50 wt%) are approximately 4–4.4 dB. These values correspond to the reflection coefficient of power R at the level of 0.4-0.36, which corresponds well with the results in [13-16].

The frequency dependence of the calculated value for the paraffin-schungite composite (50 wt%) according to equation (3) is presented in Fig. 6.

According to the obtained data in Fig. 6, schungite micropowder is a more appropriate dielectric filler for concrete building materials as compared to previously studied dielectric radio-absorbing fillers, such as rice husk ashes [38] or brass micropowder [39]. This is associated with the observed comparative property of the radio absorption ability of schungite (value $\varepsilon \cdot \mu$) as compared to rice husk ashes and brass micropowder and good compatibility of schungite
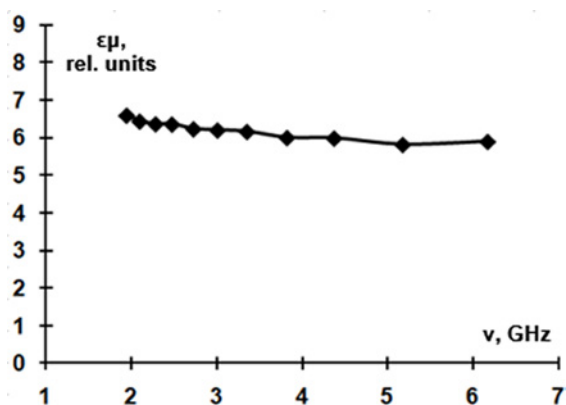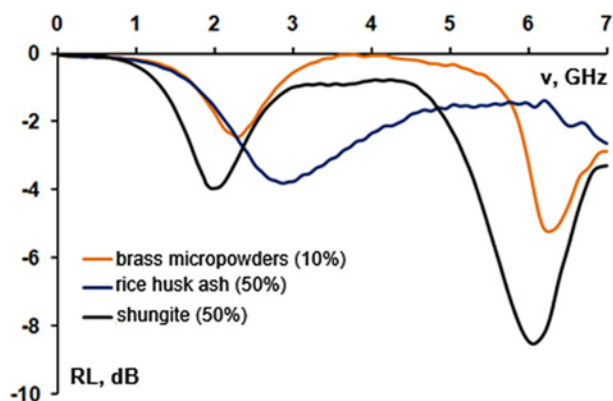
powder as a mineral metal-silicate material with concrete as compared to brass micropowder that shows a corrosion interaction with cement mixtures.

This conclusion is confirmed by the comparison of the effectiveness of radio absorption by paraffin-based composites with the corresponding optimum quantity additives of the discussed radio-absorbing fillers for concretes (Fig. 7): powder of rice husk ashes (50 wt%), brass micropowder (10 wt%), and schungite micropowder (50 wt%).

According to the data in Fig. 7, a comparison of the radio absorption efficiency of paraffin-based composites with the corresponding additives of the discussed radio-absorbing fillers for concrete demonstrated a pronounced radio-absorption efficiency of the shungite-based composite for 4G and 5G cellular communication range.

Nevertheless, it should be taken into account that the produced schungite micropowder also showed the presence of weak ferrimagnetic properties $\mu \gg 1$ (Fig. 8) in accordance with the conducted calculations of the magnetic permeability based on the experimental measurement of the S-parameter S_{21} using the dual-port vector network analyser.

It can be presumed that it is associated with the presence of a small quantity of ferrimagnetic nanoparticles of magnetite Fe_3O_4 in the produced schungite micropowder which are probably formed upon the atmospheric dry milling of schungite particles in a steel ball mill with a steel milling bowl. This can be assumed based on the chemical features of the oxidation of stainless

Fig. 6. Frequency dependence of the calculated value $\varepsilon \cdot \mu$ for the paraffin-schungite composite (50 wt%)

Fig. 7. Frequency dependence of reflection loss for composites based on paraffin and radio-absorbing fillers for concretes with a sample thickness of 15 mm
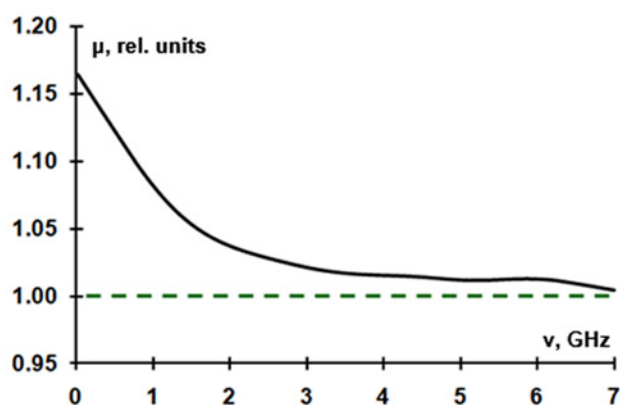
Fig. 8. Frequency dependence of the calculated value of magnetic permeability for the paraffin-schungite composite (50 wt%)

Condensed Matter and Interphases / Конденсированные среды и межфазные границы   2023;25(1): 3–13

V. Yu. Buz'ko et al. Atomic composition, microstructure, and electromagnetic properties of schungite micropowder

steel in the course of abrasion of abrasive metal powders in a ball mill with a drum and AISI SS304 non-magnetic stainless steel balls, as well as on the frequency behaviour of the high-frequency magnetic permeability calculated for the paraffin-schungite composite, which shows that Snoek's limit of the ferrimagnetic impurity is above 7 GHz. Therefore, the studied schungite micropowder cannot be considered as a purely dieletric radio-absorbing filler with electrically conductive carbon particles as is common in some works [5, 6, 12, 16, 40]. This conclusion corresponds well with the conclusion of [41], where it is stated that the frequency properties of the coefficients of reflection of electromagnetic radiation (EMR) from the surface of schungite-cement composites demonstrate a resonance effect at a frequency of 8.5 GHz, which can be explained by the content of metals in the structure of schungite and their impact on the reflection of EMR.

4. Conclusion

Thus, the conducted microscopic and energy spectral study of the schungite mineral and its produced micropowder showed that both the schungite itself and its micropowder contain significant concentrations of iron of 3.8 and 6.1 wt%, respectively. The schungite powder, apparently, contains iron in the form of ferrimagnetic nanoparticles of magnetite and pyrite, which also contributes to scattering and absorption of electromagnetic waves by schungite materials. The produced schungite micropowder also showed the presence of weak ferrimagnetic properties according to the measurements of magnetic permeability performed by vector analysis of the impedance of electrical circuits. This must be taken into account when discussing electromagnetic properties of industrially and independently produced schungite micropowders which are often used as radio-absorbing fillers for building materials.

Contribution of the authors

The authors contributed equally to this article.

Conflict of interests

The authors declare that they have no known competing financial interests or personal relationships that could have influenced the work reported in this paper.

References

1. Zavertkin A. S., Shchiptsov V. V. Technology for obtaining refractory and molding materials based on shungite rocks. *Scientific foundations of chemistry and technology for processing complex raw materials and synthesizing functional materials based on it*. 2008; 2. Available at: https://helion-ltd.ru/shungite-rocks-study/ (In Russ.)

2. Zavertkin A. S., Tyaganova V. I., Tupolev A. G. Application of chemicals and technological materials in pretreatment of shungite rock. In: *Problems in the rational use of natural and technogenic raw materials from the Barents region in the construction and technical material technology. Proceedings of Second International Conference 12–16 September,* 2005. p. 71–73. (In Russ., abstract in Eng.). Available at: http://resources.krc.karelia.ru/krc/doc/publ/problem_region_ispol/problem_region_ispol.pdf

3. Sadovnichy R. V., Rozhkova N. N., Gorbunova E. V., Chertov A. N. The Maksovskaya reserve (the Zazhoginskoye deposit) schungite rock photometric sorting possibilities study. *Obogashchenie Rud.* 2016;1: 10–15. (In Russ., abstract in Eng.). https://doi.org/10.17580/or.2016.01.02

4. Reznikov V. A., Polekhovskii Yu. S. Amorphous shungite carbon: A natural medium for the formation of fullerenes. *Technical Physics Letters*. 2000;26: 689–693. https://doi.org/10.1134/1.1307814

5. Golubev Y. A., Antonets I. V., Shcheglov V. I. Static and dynamic conductivity of nanostructured carbonaceous shungite geomaterials. *Materials Chemistry and Physics*. 2019;226: 195–203. https://doi.org/10.1016/j.matchemphys.2019.01.033

6. Antonets I. V., Golubev Y. A., Shcheglov V. I., Sun S. Electromagnetic shielding effectiveness of lightweight and flexible ultrathin shungite plates. *Current Applied Physics*. 2021;29: 97–106. https://doi.org/10.1016/j.cap.2021.06.008

7. Golubev E. V., Antonets I. V. Influence of mineralogical and petrographic features on microwave radiation reflection from shungite rocks in the range of 26–39 GHz. *Vestnik IG Komi SC UB RAS.* 2017;5: 43–48. (In Russ., abstract in Eng.). https://doi.org/10.19110/2221-1381-2017-5-43-48

8. Fujita T., Aoki T., Ponou, J., Dodbiba G., He C., Wang K., Ning S., Chen H., Wei Y. Removal of impurities from shungite via a combination of physical and chemical treatments. *Minerals*. 2021;11(3): 245. https://doi.org/10.3390/min11030245

9. Anufrieva S. I., Ozhogina E. G. Characteristics of the mineralogical and analytical study of natural types of shungite rocks. In: *The Significance of Technological Mineralogy Research in Solving the Problems of Integrated Development of Mineral Raw Materials*. Petrazavodsk: KarRC RAS. 2007. p. 135–145.

Condensed Matter and Interphases / Конденсированные среды и межфазные границы   2023;25(1): 3–13

V. Yu. Buz'ko et al. Atomic composition, microstructure, and electromagnetic properties of schungite micropowder

(In Russ.). Available at: http://resources.krc.karelia.ru/krc/doc/publ2008/mineralogia_135-145.pdf

10. Rafienko V. A. On the mechanism of leaching of sulfides from shungite rocks*. *Mining Informational and Analytical Bulletin (Scientific and Technical Journal)*. 2007;9: 38–48. (In Russ.). Available at: https://www.elibrary.ru/item.asp?id=9596187

11. Rafienko V. A., Yushin T. I. Development of technology for the processing of shungite rocks with the production of high quality dispersed shungite concentrates*. *Mining Informational and Analytical Bulletin (Scientific and Technical Journal)*. 2013;10: 102–110. (In Russ.). Available at: https://www.elibrary.ru/item.asp?id=20434286

12. Emelyanov S., Kuzmenko A., Rodionov V., Dobromyslov M. Mechanisms of microwave absorption in carbon compounds from shungite. *Journal of Nano- and Electronic Physics*. 2013;5(4): 40233. Режим доступа: https://www.elibrary.ru/item.asp?id=44952915

13. Lyn'kov L. M., Borbot'ko T. V., Krishtopova E. A. Radio-absorbing properties of nickel-containing schungite powder. *Technical Physics Letters*. 2009;35: 410–411. https://doi.org/10.1134/S1063785009050071

14. Pukhir G. A., Makhmud M. Sh., Nasonova N. V., Lynkov L. M. Protective properties of screens of electromagnetic radiation of a microwave range on the basis of the combined, dielectric and magnetic powder components. *Doklady BGUIR*. 2011;6(60): 94–97. (In Russ., abstract in Eng.). Available at: https://libeldoc.bsuir.by/bitstream/123456789/2005/1/Pukhir_Zashchitnyye.PDF

15. Lynkov L. M., Makhmud M. Sh., Krishtopova E. A. Screens of electromagnetic radiation based on powdered shungite. *Vestnik of Polotsk State University. Part C. Fundamental Sciences*. 2012;4: 103–108. (In Russ., abstract in Eng.). Available at: https://www.elibrary.ru/item.asp?id=23480159

16. Krishtopova E. A., Makhmud M. Sh., Lynkov L. M. Electromagnetic absorbers based on blends of powdered fillers. *Doklady BGUIR*. 2012;1(63): 17–21. (In Russ., abstract in Eng.). Available at: https://www.elibrary.ru/item.asp?id=29778573

17. Mukhametrahimov R. Kh., Shafigullin R. I., Kupriyanov V. N. Development of radioprotective shungite-containing gypsum-fiber facing sheets. *News of the KSUAE*. 2017;3(41): 224–231. (In Russ., abstract in Eng.). Available at: https://www.elibrary.ru/item.asp?id=30040186

18. Galautdinov A., Mukhametrakhimov R., Kupriyanov V. Gypsum-fiber radioprotective facing materials. *Lecture Notes in Civil Engineering*. 2021; 372–381. https://doi.org/10.1007/978-3-030-80103-8_40

19. Abdimuratov Zh. S., Manbetova Zh. D., Imankul M. N., Chezhimbayeva K. S., Davronbekov D. A.

Absorbers of electromagnetic radiation based on shungite species. *Series of Geology and Technical Sciences*. 2021;445(1): 6–12. https://doi.org/10.32014/2021.2518-170x.1

20. Mosin O. V, Ignatov I. Application of natural fullerene containing mineral shungite in construction industry and building technologies. *Nanobuild*. 2012; 6: 81–93. (In Russ., abstract in Eng.). Available at: https://www.elibrary.ru/item.asp?id=18268370

21. Podolsky V. P., Volkov V. V., Kukina O. B., Andreev A. V. Substantiation of the possibility of using shungite as an effective radio-absorbing material. *Russian Journal of Building Construction and Architecture*. 2022;1(65): 69–75. (In Russ., abstract in Eng.). https://doi.org/10.36622/VSTU.2022.65.1.006

22. Lukutsova N. P., Pykin A. A., Karpikov E. G. Peculiarities of structure formation of cement stone with carbon-silica nanodispersed additive*. *Stroitel'nye Materialy (Construction Materials)*. 2011;9: 66–67. (In Russ.). Available at: https://www.elibrary.ru/item.asp?id=17247606

23. Belousova E. S., Makhmud M. M., Lynkov L. M., Nasonova N. V. Radio shielding properties of concretes based on shungite nanomaterials. *Nanobuild*. 2013;5(2): 56–67. (In Russ., abstract in Eng.). Available at: http://www.nanobuild.ru/en_EN/journal/Nanobuild-2-2013/56-67.pdf

24. Egerton R. F. *Physical principles of electron microscopy*. Springer Science+Business Media, Inc.; 2005. 211 p.

25. Reed S. J. B. *Electron microprobe analysis and scanning electron microscopy in geology*. New York: Published in the United States of America by Cambridge University Press; 2005 216 p.

26. Vlasov A. I., Elsukov K. A., Kosolapov I. A. *Electron microscopy: textbook.** Moscow: Publishing House of MSTU im. N. E. Bauman; 2011. 168 p. (In Russ.)

27. Igarashi S., Kawamura M., Watanabe A. Analysis of cement pastes and mortars by a combination of backscatter-based SEM image analysis and calculations based on the Powers model. *Cement and Concrete Composites*. 2004;26(8): 977–985. https://doi.org/10.1016/j.cemconcomp.2004.02.031

28. Hu C., Ma H. Statistical analysis of backscattered electron image of hydrated cement paste. *Advances in Cement Research*. 2016;28(7): 469–474. https://doi.org/10.1680/jadcr.16.00002

29. Mashuri X., Lestari W., Triwikantoro X., Darminto X. Preparation and microwave absorbing properties in the X-band of natural ferrites from iron sands by high energy milling. *Materials Research Express*. 2018;5(1): 014003. https://doi.org/10.1088/2053-1591/aa68b4

30. Guan B., Ding D., Wang L., Wu J., Xiong R. The electromagnetic wave absorbing properties of cement-

Condensed Matter and Interphases / Конденсированные среды и межфазные границы   2023;25(1): 3–13

V. Yu. Buz'ko et al. Atomic composition, microstructure, and electromagnetic properties of schungite micropowder

based composites using natural magnetite powders as absorber. *Materials Research Express*. 2017;4(5): 056103. https://doi.org/10.1088/2053-1591/aa7025

31. Wu X., Xie X., Cao Y. Self-magnetization of pyrite and its application in flotation. *Transactions of Nonferrous Metals Society of China*. 2016;26(12): 3238–3244. https://doi.org/10.1016/s1003-6326(16)64456-4

32. Waters K. E., Rowson N. A., Greenwood R. W., Williams A. J. The effect of heat treatment on the magnetic properties of pyrite. *Minerals Engineering*. 2008;21(9): 679-682. https://doi.org/10.1016/j.mineng.2008.01.008

33. Yuping D., Hongtao G. *Microwave absorbing materials*. Singapore: Pan Stanford Publishing Pte. Ltd.; 2017. 387 p.

34. Liu L, Duan Y, Guo J. Influence of particle size on the electromagnetic and microwave absorption properties of FeSi/paraffin composites. *Physica B*. 2011;406(11): 2261–2265. https://doi.org/10.1016/j.physb.2011.03.045

35. Dosoudil R., Ušák E., Olah V. Computer controlled system for complex permeability measurement in the frequency range of 5 Hz – 1 GHz. *Journal of Electrical Engineering*. 2006;57(8/S): 105–109.

36. Dosoudil R., Ušák E., Olah V. Automated measurement of complex permeability and permittivity at high frequencies. *Journal of Electrical Engineering*. 2010;61(7/S): 111–114.

37. Dosoudil R. Determination of permeability from impedance measurement using vector network analyzer. *Journal of Electrical Engineering*. 2012;63(7s): 97–101.

38. Buz'ko V., Shamray I., Goryachko A., Udodov S., Abashin A. Electromagnetic characteristics of biosilica from rice husk. *E3S Web of Conferences*. 2021;263: 01013. https://doi.org/10.1051/e3sconf/202126301013

39. Buzko V. Yu., Udodov S. A., Litvinov A. E., Ivanin S. N., Goryachko A. I., Charikov G. Yu. Properties of radio-absorbing composites concrete-micropowders of the brass. *Scientific works of the Kuban State Technological University*. 2021;5: 25–33. (In Russ., abstract in Eng.). Available at: https://elibrary.ru/item.asp?id=47874005

40. Lisovskiy D. N., Mahmud M. S., Vlasova G. A., Pulko T. A. Absorbents of electromagnetic radiation based on the fire-proof paints with powder-like filler. *Doklady BGUIR*. 2012;4: 89–93. (In Russ., abstract in Eng.). Available at: https://elibrary.ru/item.asp?id=29425911

41. Belousova E. S., Lynkou L. M., Senyut V. T., Krishtopova E. A. Influence of heat treatment in vacuum on shungite shielding properties. *Doklady BGUIR*. 2014;8: 31–35. (In Russ., abstract in Eng.). Available at: https://elibrary.ru/item.asp?id=29674388

* *Translated by author of the article*

Информация об авторах

Vladimir Y. Buz'ko, Cand. Sci. (Chem.), Director of the REC "Center for Advanced Technologies and Nanomaterials", Kuban State Technological University (Krasnodar, Russian Federation).
https://orcid.org/0000-0002-6335-0230
buzkonmr@mail.ru

Sergey N. Ivanin, Cand. Sci (Chem), Research Fellow, "Center for Advanced Technologies and Nanomaterials", Kuban State Technological University (Krasnodar, Russian Federation).
https://orcid.org/0000-0001-9352-5970
ivanin18071993@mail.ru

Ivan Y. Shutkin, post-graduate student of the Department of Land Transport and Mechanics, Kuban State Technological University (Krasnodar, Russian Federation).
https://orcid.org/0000-0001-9705-7801
5206606@mail.ru

Alexander I. Goryachko, Research Fellow, "Center for Advanced Technologies and Nanomaterials", Kuban State Technological University (Krasnodar, Russian Federation).
https://orcid.org/0000-0001-6480-353X
alexandr_g_i@mail.ru

Sergey A. Udodov, Cand. Sci. (Tech.), Head of the Department of Production of Building Structures and Structural Mechanics Kuban State Technological University (Krasnodar, Russian Federation).
https://orcid.org/0000-0003-4023-9588
udodov-tec@mail.ru

Alexander V. Ozolin, Research Fellow, "Center for Advanced Technologies and Nanomaterials" Kuban State Technological University (Krasnodar, Russian Federation).
https://orcid.org/0000-0002-0173-1716
ozolinml@yandex.ru

Original articles

Solubility of calcium and strontium fluorides in a sodium nitrate melt and choosing a crucible material for working with their solution melts

I. I. Buchinskaya[1✉], A. V. Ivchenko[2]

[1]Shubnikov Institute of Crystallography, Crystallography and Photonics Federal Research Center, Russian Academy of Sciences, 59 Leninskii prospect, Moscow 119333, Russian Federation

[2]Lomonosov Moscow State University, Faculty of Chemistry, 1-3 Leninskiye Gory, GSP-1, Moscow 119991, Russian Federation

Abstract

Sodium nitrate is a promising medium for the preparation of nanoparticles of some inorganic fluorides and for studying low-temperature phase equilibria in fluoride systems. In our study, we investigated the possibilities of carrying out long-term (hundreds of hours) experiments with MF_2–$NaNO_3$ (M = Ca, Sr).

We performed an experimental evaluation of the solubility of calcium (CaF_2) and strontium SrF_2 fluorides in a melt of sodium nitrate $NaNO_3$ in the temperature range of 320–500 ℃. The article demonstrates that for both fluorides it is low, but the solubility of SrF_2 is almost an order of magnitude higher than the solubility of CaF_2 and is about 1 g/100 g of $NaNO_3$ at 500 ℃. The absence of perceptible oxidative processes and the low solubility of CaF_2 and SrF_2 fluorides in sodium nitrate make it possible to synthesize solid solutions based on them in this medium. The article also considers the possibility of using crucibles made of glazed ceramics, glass-carbon, and aluminium for working with MF_2–$NaNO_3$ (M = Ca, Sr) melt solutions. It is shown that glass-carbon and aluminium react with the $NaNO_3$–SrF_2 melt solution to form strontium carbonate and several oxide phases, respectively.

It is recommended to use glazed ceramics as a crucible material for long-term solution-melt processes. The aluminium crucible showed high resistance to the $NaNO_3$ melt without dissolved fluorides.

Keywords: Calcium fluoride, Strontium fluoride, Sodium nitrate, Solubility, Solution melt, Powder X-ray diffraction analysis

For citation: Buchinskaya I. I., Ivchenko V. A. Solubility of calcium and strontium fluorides in a sodium nitrate melt and choosing a crucible material for working with their solution melts. *Condensed Matter and Interphases*. 2023;25(1): 14–19. https://doi.org/10.17308/kcmf.2023.25/10971

Для цитирования: Бучинская И. И., Ивченко В. А. Растворимость фторидов кальция и стронция в расплаве нитрата натрия и выбор материала тигля для работы с их раствор-расплавами. *Конденсированные среды и межфазные границы*. 2023;25(1): 14–19. https://doi.org/10.17308/kcmf.2023.25/10971

✉ Irina I. Buchinskaya, e-mail: buchinskayaii@gmail.com

1. Introduction

Sodium nitrate melt is a promising medium for the preparation of nanoparticles of certain inorganic fluorides by means of molten salt synthesis (MSS) [1–4], as well as for studying low-temperature phase equilibria in fluoride systems [4, 5]. The MSS method for the production of nanofluorides has a large number of advantages over the deposition from aqueous solutions method. They include a fast reaction speed, the possibility to conduct synthesis in the air, and the possibility to use available equipment. Nitrates of alkali metals have been used in a number of studies as melt media for the preparation of inorganic fluorides.

In [6], ScF_3 (the most refractory one of the simple inorganic fluorides) was synthesised from precursors of $Sc(NO_3)_3$ and NH_4HF_2 in a $NaNO_3–KNO_3$ reaction medium for 0.5 hours at 310 °C. Micro- and nanocrystals of $NaBiF_4:Er^{3+}/Yb^{3+}$ were synthesised from low-temperature salt melts in NH_4NO_3 [7], and CaF_2 was synthesised in a mixture of 53 wt% KNO_3, 7 wt% $NaNO_3$, and 40 wt% $NaNO_2$ [8]. Upconversion luminophores $NaYF_4$ and $LiYF_4$ were synthesised using eutectic melts $NaNO_3–KNO_3$, $NaNO_3–LiNO_3$, $KNO_3–LiNO_3$, and $NaNO_3–KNO_3–LiNO_3$ for 2 hours at 400 °C. The best result was obtained in a $NaNO_3–KNO_3$ eutectic melt. When salt media containing $LiNO_3$ were used, a tetragonal $LiYF_4$ was produced mixed with a rhombic $Y_6O_5F_8$ [9]. The MSS method was also used to synthesise CeF_3 and $CeF_3:Tb^{3+}$ particles at a low temperature in $NaNO_3$ and KNO_3 melts [10].

The above given data demonstrates that a sodium nitrate melt is an effective reaction medium since it is water-soluble and non-toxic, has high stability, and does not contaminate synthesised fluorides with oxygen.

The choice of the crucible material for the experiments, however, is problematic. It should be resistant to both NO_3^- and F^- ions. This problem has not been discussed in the existing literature. Researchers often provide detailed descriptions of their experiments, but do not mention the material of the crucible (for instance, [6, 7], although it is of great importance. [4, 5] used glazed porcelain crucibles, and [8, 10] used alumina crucibles (Al_2O_3).

There is also literature data on the effective growth if $NaNO_3$ single crystals from a melt in aluminium crucibles [11]. The best material for working with the melts of inorganic fluorides is graphite, which does not interact with the melt and is not wetted by it. However, the crystallisation of fluorides from the melt is performed in vacuum or in inert and fluorinating environment, i.e. graphite crucible does not interact with oxygen. At low temperatures (up to 400 °C) graphite is hardly oxidized in the air. At higher temperatures, the oxidation process depends on a large number of factors, including the composition of the atmosphere, porosity, and the crystalline quality. The processes occurring in the $C–NaNO_3$ system (taken in a molar ratio from 5:1 to 1:4) were studied using a derivatograph in [12]. The study demonstrated that the components interacted at temperatures significantly higher than the melting point of $NaNO_3$. Depending on the ratio of the components, derivatograms demonstrated the beginning of a noticeable reaction at 380–420 °C. The approximate range for the salt melt synthesis of fluorides is the interval of stability of $NaNO_3$ from the melting point to the decomposition temperature (~310–500 °C). When using carbon crucibles, a temperature of ~380 °C is acceptable. [13] demonstrated the stability of SrF_2 and CaF_2 fluorides in the $NaNO_3$ melt in a glass-carbon crucible at 330 °C for 1 hour.

The purpose of our study was to analyse the suitability of three materials (glass-carbon, aluminium, and glazed porcelain) for long-term experiments with $MF_2–NaNO_3$ (M = Ca, Sr) solution melts. We assumed that the stability of the crucible material would depend on the amount of dissolved fluorides (the number of F^- ions in the melt). Therefore, we first had to use available methods to evaluate the solubility of SrF_2 and CaF_2 in the $NaNO_3$ melt.

2. Experimental

The initial materials were CaF_2 in the form of fragments of optical crystal produced by Vavilov State Optical Institute and SrF_2 in the form of crystalline boules preliminary melted from a 99.995 wt% (Sigma-Aldrich) reagent in a CF_4, $NaNO_3$ fluorinating environment (analytical reagent grade).

The solubility of fluorides in a sodium nitrate melt was assessed using two methods. 1) A MF_2 single crystal of a particular mass was put into

a crucible with a certain amount of the sodium nitrate melt and thermostated until the solution melt became saturated. During this stage, glazed porcelain and glass-carbon crucibles were used. The experiments demonstrated that the solution melt became saturated in 2 hours. Then the crystal was removed from the melt, the remaining nitrate was washed off with bidistilled water, and the crystal was weighed. The change in the mass of the crystal corresponded to the amount of fluoride dissolved in the melt at the set temperature. It was used to calculate the solubility. 2) MF_2 crystals were thermostated in the $NaNO_3$ melt. A sample of the melt was then taken with a scoop made from the same material as that of the crucible. The sample was cooled to room temperature and dissolved in bidistilled water. It was then washed three times until sodium nitrate was completely removed. The precipitate was filtered, dried, and weighed.

The initial reagents and the reaction products were controlled with the X-ray diffraction (XRD) method. The XRD was performed using a MiniFlex 600 powder X-ray diffractometer (Rigaku, Japan) using CuK_α (40 kV, 15 mA, $Ni–K_\beta$-filter) radiation in the angular range 2θ from 10° to 100° at 0.02° intervals and a scanning rate of 2°/min. The phases were identified using a PXDRL software (Rigaku, Japan) based on the ICDD PDF-2 database (2017 edition).

The morphology of the interaction products was studied using a POLAM L-213M optical microscope and scanning energy-dispersive microscopy (SEM) performed on a Scios scanning electron microscope (FEI, USA). The images were registered in a backscattered electrons mode using a T1 in-lens solid state detector (FEI, USA).

When conducting long-term experiments in a $NaNO_3$ melt, it is of utmost importance that there is no interaction with the material of the crucible [5]. To study the resistivity of various materials to the solution melt, we performed the following experiment. Samples with a molar ratio MF_2:$NaNO_3$ = 1:5 (M = Ca, Sr) were put into glass-graphite and glazed porcelain crucibles; $Ca_{0.5}Sr_{0.5}F_2$:$NaNO_3$ = 1:5. The samples were put into two crucibles made from 0.22μm aluminium foil together with pure $NaNO_3$ used as a reference. The samples were previously ground in a jasper mortar. All the

crucibles were put in a muffle furnace and held in the air at a temperature of 410±5 °C for ~760 hours. After the annealing the content of the crucibles was washed with bidistilled water to remove $NaNO_3$.

3. Results and discussion

3.1. Solubility of CaF_2 and SrF_2 in the $NaNO_3$ melt

The obtained measurements of the solubility of fluorides in sodium nitrate were very low. The generalised results are experiments presented in Table 1. We should note that the solubility of SrF_2 in the studied temperature range is almost an order of magnitude higher than that of CaF_2. The solubility of CaF_2 was determined using only the first method based on the change in the mass of the crystal. It was not possible to filter the precipitate of CaF_2 due to its insignificantly small amount. Due to the evaluative nature of the analysis of solubility, without specialised equipment the obtained data varied greatly. However, the results obtained using two methods in both porcelain and glass-graphite crucibles are in satisfactory agreement with each other.

Table 1. Results of the experiments conducted to measure the solubility of CaF_2 and SrF_2 in a $NaNO_3$ melt

MF_2 T, °C	Solubility, g/100 g $NaNO_3$	
	CaF_2	SrF_2
350±10	–	0.35±0.14
450±20	~0.04	0.84±0.37
500±20	~0.14	1.03±0.19

*The solubility of CaF_2 below 450 °C could not be reliably recorded

When a glass-carbon crucible was used, the precipitate was visible even after 10 hours of thermostating of the melt with the SrF_2 crystal at temperatures of about 400 °C. SEM and XRD analysis demonstrated that besides strontium fluoride it contained a considerable amount of strontium carbonate increasing with a longer time of annealing and at higher temperatures. The results are shown in Fig.1a-c. Micrographs 1b and 1c demonstrate crystals of various morphology: small cubic crystals (probably SrF_2) and larger needle crystals (probably $SrCO_3$).

Condensed Matter and Interphases / Конденсированные среды и межфазные границы   2023;25(1): 14–19

I. I. Buchinskaya, A. V. Ivchenko   Solubility of calcium and strontium fluorides in a sodium nitrate melt...
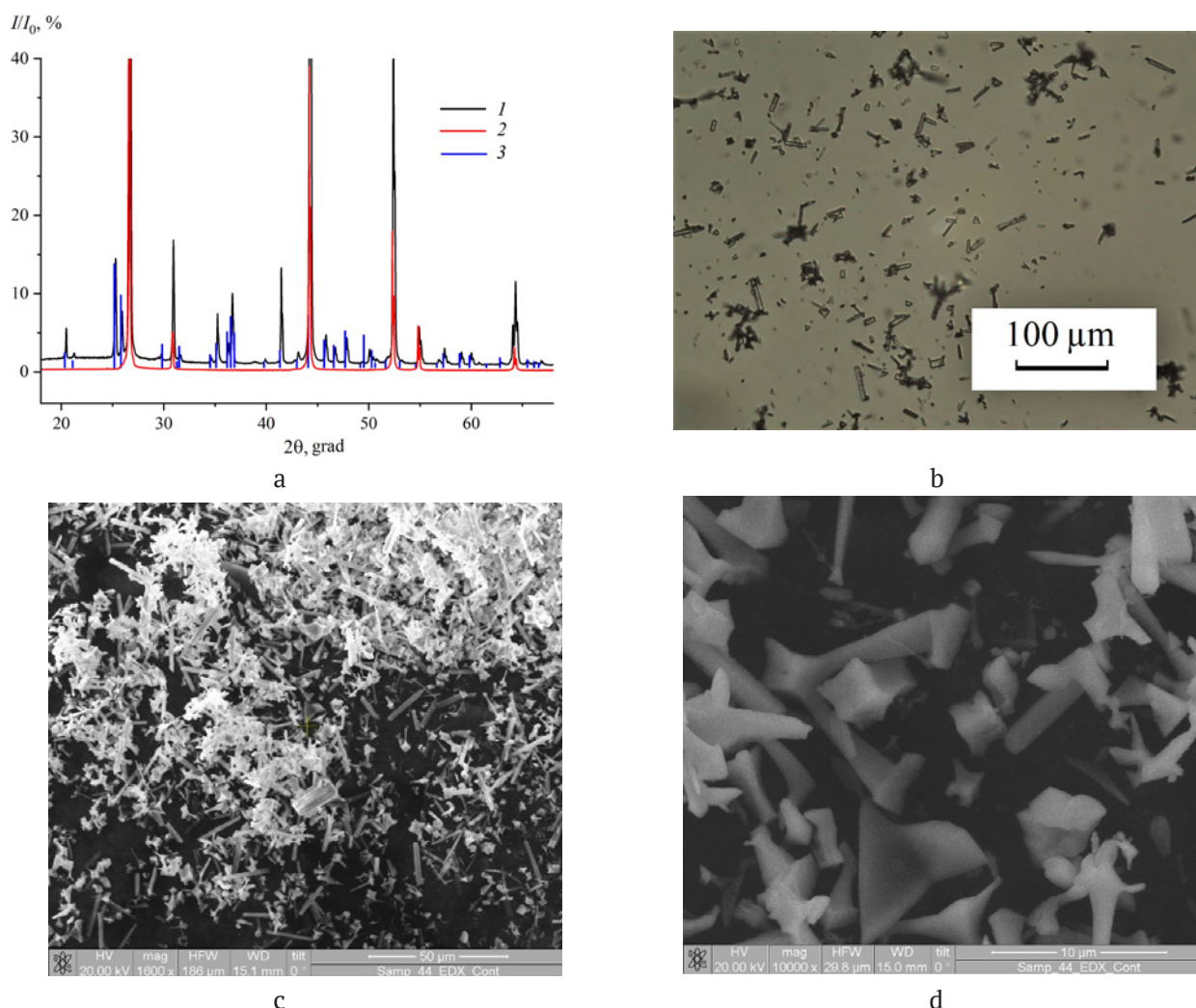
Fig. 1. Analysis of the precipitate after experiments with SrF_2–$NaNO_3$ composition in a glass-graphite crucible. XRD results: *1* – diffraction pattern of the sample, *2* – diffraction pattern of the initial reagent SrF_2, *3* – $SrCO_3$ (PDF No. 00-005-0418) (a). Photograph of the precipitate in an optical (b) microscope and electron (c, d) microscopes at different magnifications

3.2. Assessment of the crucible materials

As a result of annealing of melt solutions in a muffle furnace in the air at a temperature of 410±5 °C for ~760 hours, a $SrCO_3$ precipitate, as expected, formed in the near bottom part of the ingot from the glass-graphite crucible with c SrF_2–$NaNO_3$. When dissolving the CaF_2–$NaNO_3$ ingot from the glass-graphite crucible we also observed a very fine powder which could not be centrifuged and filtered due to its small amount. It might have been calcium carbonate.

CaF_2–$NaNO_3$ and SrF_2–$NaNO_3$ systems did not demonstrate any other phases besides the initial components in glazed porcelain crucibles.

Al foil crucibles proved to be ineffective. They transformed into a fragile substance grey at the top and pink at the bottom where it interacted directly with the melt solution. The diffraction patterns of the grey and the pink parts did not differ significantly. The XRD demonstrated that there was no metallic Al and cubic CaF_2 and SrF_2 based fluoride phases in the product. It also registered a large amount of $NaNO_3$ and probably $Na_{0.67}Al_6O_{9.33}$ oxides (card PDF No. 01-070-7114), and a Al_2O_3 modification (card PDF No. 00-012-0539). Fig. 2 demonstrates the diffraction pattern of the sample after washing with bidistilled water. $Na_{0.67}Al_6O_{9.33}$ and iota-Al_2O_3 spectra are imposed on the diffraction pattern. There are also unidentified peaks.

The reference Al foil crucible with pure $NaNO_3$ did not change visibly. The foil remained shiny

Condensed Matter and Interphases / Конденсированные среды и межфазные границы   2023;25(1): 14–19

I. I. Buchinskaya, A. V. Ivchenko   Solubility of calcium and strontium fluorides in a sodium nitrate melt...
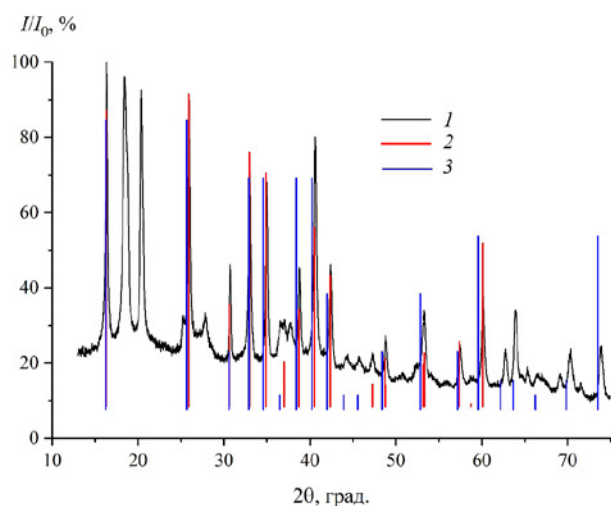
Fig. 2. *1* – X-ray diffraction pattern of reaction products of Al foil with $Ca_{0.5}Sr_{0.5}F_2$–$NaNO_3$ melt solution in the air; *2* – $Na_{0.67}Al_6O_{9.33}$ (PDF No. 01-070-7114); *3* – iota-Al_2O_3 (PDF No. 00-012-0539)

without any oxidation traces. The sodium nitrate ingot was colourless and transparent.

4. Conclusions

Calcium fluoride demonstrates significant solubility in a sodium nitrate melt, which is up to 0.14 g/100 g $NaNO_3$ at a temperature of ~500 °C. The solubility of strontium fluoride is an order of magnitude higher and reaches 1.03±0.19 g/100 g $NaNO_3$. The difference in the behaviour of the two fluorides might be the cause of a large difference in the morphology of crystals of both pure phases and solid solutions based on them and obtained in nitrate salt melts [14]. The absence of a visible oxidation process and low solubility of CaF_2 and SrF_2 fluorides in sodium nitrate make the latter a very promising medium for synthesising inorganic fluorides by means of the MSS method.

Glazed porcelain crucibles are preferable for working with MF_2–$NaNO_3$ (M = Ca, Sr) melt solutions. Carbonate impurities are observed in glass-graphite crucibles, and Al crucibles are destroyed as a result of oxidation.

Aluminium demonstrates high resistance to the sodium nitrate melt and is a good material for crucibles used with the melt.

Author contributions

Buchinskaya I. I. – problem statement, scientific supervision of research, X-ray phase analysis, text writing, discussion, conclusions.

Ivchenko V. A. – carrying out the experiment, analysis of the results, text writing, conclusions.

Conflict of interests

The authors declare that they have no known competing financial interests or personal relationships that could have influenced the work reported in this paper.

References

1. Gupta S. K., Mao Y. Recent Developments on Molten Salt Synthesis of Inorganic Nanomaterials: A Review *Journal of Physical Chemistry C*. (2021);125(12): 6508**–6533.** https://doi.org/10.1021/acs.jpcc.0c10981

2. Ding M., Lu C., Cao L., et al. Molten salt synthesis of tetragonal LiYF4:Yb³⁺/Ln³⁺ (Ln = Er, Tm, Ho) microcrystals with multicolor upconversion luminescence. *CrystEngComm*. (2013);15(30): 6015–6021. https://doi.org/10.1039/C3CE40477C

3. Fedorov P. P. Alexandrov A. A. Synthesis of Inorganic Fluorides in Molten Salt Fluxes and Ionic Liquid Mediums. *Journal of Fluorine Chem*. (2019);227: 109374. https://doi.org/10.1016/j.jfluchem.2019.109374

4. Fedorov P. P., Alexandrov A. A., Bragina A. G., ... Ivanov V. K. Preparation of Ba₁₋ₓLaₓF₂₊ₓ solid solution from nitrate melt. *Russian Journal of Inorganic Chemistry*. 2022;67(6): 861–867. https://doi.org/10.1134/S0036023622060079

5. Fedorov P. P., Alexandrov A. A., Voronov V. V. Mayakova M. N., Baranchikov A. E., Ivanov V. K. Low-temperature phase formation in the SrF₂–LaF₃ system *Journal of the American Ceramic Society*. (2021);104(6): 2836–2848. https://doi.org/10.1111/jace.17666

6. Hu L., Chen J., Fan L., Deng J., Yu R., Xing X. Rapid Molten Salt Synthesis of Isotropic Negative Thermal Expansion ScF₃. *Journal of the American Ceramic Society*. (2014);97(4): 1009–1011. https://doi.org/10.1111/jace.12855

7. Huang X., Jiang L., Xu Q., Li X., He A. Low-temperature molten-salt synthesis and upconversion of novel hexagonal NaBiF₄:Er³⁺/Yb³⁺ micro-/nanocrystals. *RSC Advances*. (2017);7: 41190–41203. https://doi.org/10.1039/c7ra05479c

8. Ha J.-W., Sohn E.-H., In J. P., Lee S.-B. Preparartion of CaF₂ microspheres by thermal decomposition of trifluoroacetate precursor in molten salt medium. *Materials Letters*. (2017);209: 357–359. https://doi.org/10.1016/j.matlet.2017.08.029

9. Pornpatdetaudom T., Serivalsatit K. Effect of Molten Salts on Synthesis and Upconversion Luminescence of Ytterbium and Thulium-Doped Alkaline Yttrium Fluorides. *Key Engineering Materials*. (2018);766: 34–39. https://doi.org/10.4028/www.scientific.net/kem.766.34

Condensed Matter and Interphases / Конденсированные среды и межфазные границы   2023;25(1): 14–19

I. I. Buchinskaya, A. V. Ivchenko   Solubility of calcium and strontium fluorides in a sodium nitrate melt...

10. Li X., Zhang W., Dong L., Liu D., Qi Z. Low temperature molten salt synthesis of CeF_3 and CeF_3:Tb^{3+} phosphors with efficient luminescence properties. *Journal of Luminescence*. (2019);205: 122–128. https://doi.org/10.1016/j.jlumin.2018.08.067

11. Avetissov I. Ch., Sadovskiy A. P., Sukhanova E. A., Orlova G. Yu., Belogorokhov I. A., Zharikov E. V. Perfection of $NaNO_3$ single crystals grown by axial vibrational control technique in Czochralski configuration. *Journal of Crystal Growth*. (2012);360: 167–171, https://doi.org/10.1016/j.jcrysgro.2011.10.018

12. Zarubitskii O. G., Dmitruk B. F., Zakharchenko N. F. Interaction of graphite with hydroxide-salt melts. *Russian Journal of Applied Chemistry*. 2006;79(4): 525 - 528. https://doi.org/10.1134/S1070427206040033

13. Buchinskaya I. I. Behavior of metal difluorides MF_2 (M = Ca, Sr, Ba, Cd, Pb) in sodium nitrate melt. *Russian Journal of Inorganic Chemistry*. (2022);67(8): 1248–1252. https://doi.org/10.1134/S0036023622080046

14. Fedorov P. P., Mayakova M. N., Alexandrov A. A., Voronov V. V., Kuznetsov S. V., Baranchikov A. E., Ivanov V. K. The melt of sodium nitrate as a medium for synthesis of fluorides. *Inorganics*. (2018);6(2): 38–55. https://doi.org/10.3390/inorganics6020038

Information about the authors

Irina I. Buchinskaya, Research Fellow at the Laboratory of Growth Technologies, Synthesis and Growth of Crystals, Shubnikov Institute of Crystallography, Crystallography and Photonics Federal Research Center, Russian Academy of Sciences (Moscow, Russian Federation).

https://orcid.org/0000-0002-4658-5695
buchinskayaii@gmail.com

Victoria Al. Ivchenko, 2nd year student of the Faculty of Chemistry, Lomonosov Moscow State University (Moscow, Russian Federation).

https://orcid.org/0000-0002-5821-2909
ranuncu1@yandex.ru

Translated by Yulia Dymant
Edited and proofread by Simon Cox

Original articles

Molecular beam epitaxy of metamorphic buffer for InGaAs/InP photodetectors with high photosensitivity in the range of 2.2–2.6 um

E. I. Vasilkova[1]✉, E. V. Pirogov[1], M. S. Sobolev[1], E. V. Ubiyvovk[2], A. M. Mizerov[1], P. V. Seredin[3]

*[1]Saint Petersburg National Research Academic University of the Russian Academy of Sciences,
Khlopina str., 8k3, lit. A, Saint Petersburg 194021, Russian Federation*

*[2]Saint Petersburg State University,
Universitetskaja nab., 7–9, Saint Petersburg 199034, Russian Federation*

*[3]Voronezh State University,
1 Universitetskaya pl., Voronezh 394018, Russian Federation*

Abstract

The present work is concerned with finding optimal technological conditions for the synthesis of heterostructures with a metamorphic buffer for InGaAs/InP photodetectors in the wavelength range of 2.2–2.6 um using molecular beam epitaxy. Three choices of buffer structure differing in design and growth parameters were proposed.

The internal structure of the grown samples was investigated by X-ray diffraction and transmission electron microscopy. Experimental data analysis has shown that the greatest degree of elastic strain relaxation in the InGaAs active layer was achieved in the sample where the metamorphic buffer formation ended with a consecutive increase and decrease in temperature. The said buffer also had InAs/InAlAs superlattice inserts.

The dislocation density in this sample turned out to be minimal out of three, which allowed us to conclude that the described heterostructure configuration appears to be the most appropriate for manufacturing of short wavelength infrared range pin-photodetectors with high photosensitivity.

Keywords: Molecular beam epitaxy, Metamorphic buffer, Short wavelength infrared range photodetectors, X-ray diffraction analysis, Transmission electron microscopy

✉ Elena I. Vasilkova, e-mail: elenvasilkov@gmail.com

Condensed Matter and Interphases / Конденсированные среды и межфазные границы   2023;25(1): 20–26

E. I. Vasilkova et al.   Molecular beam epitaxy of metamorphic buffer for InGaAs/InP photodetectors...

1. Introduction

In the recent years short wave infrared range (SWIR) photodetectors for 1-3 um are actively investigated. This band includes several atmospheric windows, which opens a lot of opportunities for utilizing it in the satellite observation, night vision and thermal imaging devices, lidars, absorption spectroscopy of gases and liquids, including CO_2, etc. [1]. One of the well-established material systems for SWIR photodetectors is $In_xGa_{1-x}As/InP$ with $x \geqslant 0.53$. The absorption layers of $In_{0.53}Ga_{0.47}As$ composition are epitaxially grown lattice-matched to the InP substrate and can be used for detector manufacturing with 1.7 um cutoff wavelength. To further extend the operating range in the long-wave direction it is necessary to increase indium mole fraction in the active layer, which results in a compressive elastic strain being introduced. The degree of layer to substrate lattice mismatch can be as high as ~ 2 % for the detectors with operating wavelength of 2.5 um. In this case the value of dark current dramatically increases, which greatly inhibits the device's performance. Nevertheless, extended wavelength SWIR photodetectors based on the InGaAs/InP heterostructures are successfully implemented using a transition layer approach known as metamorphic buffer [2].

The idea behind the metamorphic buffer is to create either an abrupt or a smooth transition from one material's lattice constant (substrate in this case) to the lattice constant of another material being used in the active layer. Buffer design and material parameters are being chosen to prevent dislocations propagating into the active layers of the heterostructure. Aside from application in extended wavelength SWIR photodetectors this technology is also used for manufacturing of a wide variety of semiconductor structures, such as high electron mobility transistors [3], lasers [4], solar energy convertors [5].

In the course of this paper a search for optimum molecular beam epitaxy (MBE) growth conditions of a metamorphic buffer for the high sensitivity 2.2–2.6 um photodetectors with InGaAs absorption layer on InP substrates. The InGaAs solid solution with indium mole fraction x=0.83 was chosen as the active layer material. The buffer configuration was chosen to be linearly graded with a lattice mismatch "overshoot" relative to the active layer's lattice parameter, since such a buffer can compensate partial relaxation of the layer [6]. An employment of the linearly graded buffer is more effectively inhibits the dislocation propagating into the active region when compared to the step-graded buffer [7], and also allows one to achieve small surface roughness. Moreover, the lack of an abrupt composition variation in the buffer layer leads to a lesser probability of a three-dimensional growth mode [8].

The buffer and upper cap layers were formed using InAlAs solid solution. Heterojunction-based photodetectors demonstrate better performance compared to their homojunction counterparts in the same wavelength range. For example, a zero-bias resistance area product R0A increases at least an order of magnitude in the heterostructure-based design [9], which on its own contributes to the increase in detectivity [10].

The present work is concerned with finding optimal technological conditions for the synthesis of heterostructures with a metamorphic buffer for InGaAs/InP photodetectors in the wavelength range of 2.2-2.6 um using molecular beam epitaxy.

2. Experimental

In order to study the effect of metamorphic buffer growth modes on the quality of the InGaAs absorption layer and the density of threading dislocations, three heterostructures (#1, #2 and #3) were manufactured. Three samples were grown by molecular beam epitaxy on semi-insulating "epi-ready" InP (100) substrates using the industrial MPE Riber MBE49 setup. Benefits of the setup include the use of high purity materials, availability of precision growth control methods and ultra-high vacuum during synthesis, which ensures high quality structures. The possibility of abrupt interruption and subsequent continuation of the material flow to the substrate makes it possible to obtain sharp heterointerfaces, and the high temperature stability of two-zone effusion sources of group III metals and an arsenic cracking source ensures the consistency of the composition. The quality of the grown layers was controlled *in situ* by the reflection high-energy electron diffraction system (RHEED).

Condensed Matter and Interphases / Конденсированные среды и межфазные границы   2023;25(1): 20–26

E. I. Vasilkova et al.   Molecular beam epitaxy of metamorphic buffer for InGaAs/InP photodetectors...

Each test sample contained 500 nm $In_{0.83}GaAs$ active layer and InAlAs graded buffer. The design of the test structures is shown in Fig. 1.

At the beginning of the growth InP substrate was annealed, and then a smoothing 100 nm thick lattice-matched $In_{0.52}AlAs$ layer was grown. Then a 2 um $In_xAl_{1-x}As$ metamorphic buffer was formed by gradually increasing the In mole fraction from 0.52 to 0.87 with a 4 % excess in indium content relative to the active layer. Gradient buffer growth was carried out by reducing the aluminum source temperature. In addition to that, the synthesis differed for three samples in temperature conditions and the presence (or absence) of additional inserts. The metamorphic buffer in all three structures was formed at the temperature of ~ 400–410 °, the subsequent layers at ~ 490 ° with a flow ratio of group V/III materials ~ 10. Such conditions, on the one hand, can contribute to the relaxation of the crystal lattice due to the low temperature of the substrate [11, 12], and also allow the majority of dislocations to be kept in the buffer layer and reduce their spread to the upper layers. On the other hand, these growth conditions can prevent the three-dimensional growth, as would be evidenced by the point diffraction pattern.

In contrast to structure #1, sample #2 undergone a peak temperature increase to ~ 520 ° at the end of graded layer growth. Then the temperature was decreased to 100 ° for an exposure period of 20 minutes followed by a rise to 520 ° for 1 minute. Lastly, after that the active layer was deposited at a temperature of 490 °. Sample #3 was obtained using the same growth conditions as #2, but additionally contained three InAs/InAlAs superlattice inserts in the buffer layer with a spacing of 500 nm in-between.

During the metamorphic layer deposition, the growth pattern was controlled by RHEED. At the beginning of the buffer synthesis, as the In fraction increased, (1x1) surface reconstruction appeared, when the RHEED streaks thickened and blurred. However, in the process of layer growth the thickening gradually disappeared. Towards the end of the buffer growth, and then for the InGaAs layer as well, a striped diffraction pattern with rather narrow streaks was seen and (4x1) surface reconstruction occurred. Thus, during the metamorphic buffer formation, a significant improvement in the surface quality of the epitaxial layer was observed, which indicates the relaxation of the graded layer, as strain increased with thickness.

The internal structure of the obtained samples was characterized by X-ray diffraction and transmission electron microscopy (TEM). X-ray diffraction studies were carried out on a DRON-8 diffractometer with a Bartels monochromator and a sharp-focus X-ray tube with Cu$K_{\alpha 1}$ radiation, $\lambda = 0.15406$ nm. TEM studies were carried out on a Zeiss Libra 200FE microscope with a dark field detector. Samples for TEM measurements were prepared using standard thinning processes.
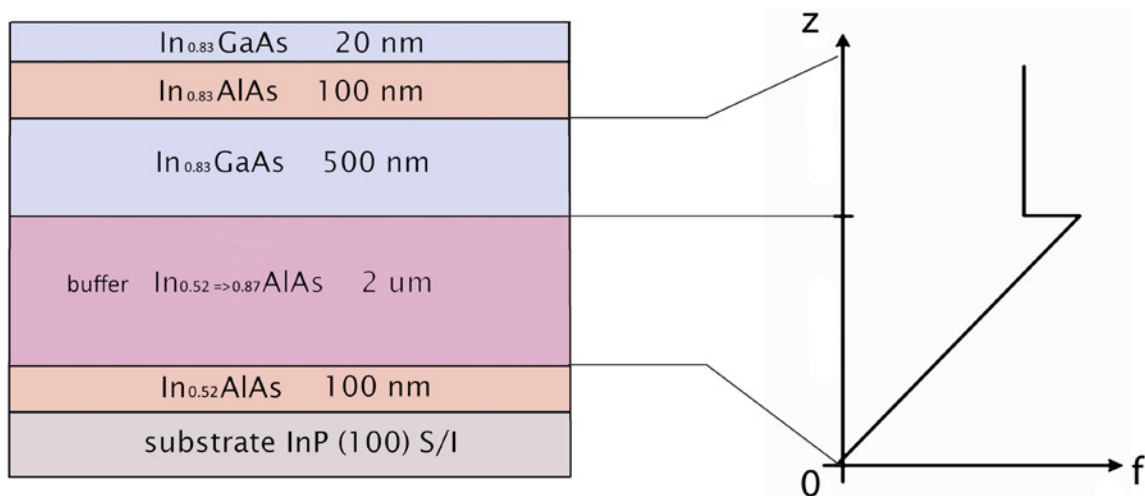
Fig. 1. Test samples layer composition and schematical representation of a graded buffer with a mismatch "overshoot" relative to absorption layer, where f – lattice mismatch, z – distance from the substrate interface

Condensed Matter and Interphases / Конденсированные среды и межфазные границы   2023;25(1): 20–26

E. I. Vasilkova et al.   Molecular beam epitaxy of metamorphic buffer for InGaAs/InP photodetectors...

3. Results and discussion

3.1. X-Ray diffraction studies

Fig. 2 shows the X-ray diffraction curves from the test structures. Each curve contains diffraction peaks from the InP substrate, InGaAs absorption layer and linearly graded metamorphic buffer positioned between the first two. To the right of the substrate peak the diffraction maximum from the InAlAs smoothing layer can be seen. In structure #3, the intensity of the diffraction maximum from the test InGaAs layer is 2.5 times higher relative to the two other samples, while the full width at half maximum of this peak is the smallest being 0.39° (versus 0.47° and 0.51° for #1 and #2, respectively). The InGaAs diffraction maximum of sample #3 nearly coincides with the calculated maximum from a completely relaxed layer of ~ 82 % In composition, which is close to the target composition. This allows us to make a conclusion that in the sample #3 the metamorphic buffer is completely relaxed and further growth of the active layer took place in the absence of internal strain. In samples #1 and #2, the peak is shifted to the left, which may be due to the presence of residual strain in the layer and thus incomplete relaxation.

3.2. TEM studies

Fig. 3 shows dark-field TEM [110] plane cross-sectional images of the experimental samples. Structural areas of linearly graded metamorphic buffer and $In_xGa_{1-x}As$ active layer with In molar fraction c x = 0.83 are indicated on the TEM images. Observed structural defects can be identifies by the two main types – misfit dislocations and threading dislocations. In Fig. 3 a), corresponding to the sample #1, a large number of threading dislocations are observed in the metamorphic buffer layer. Moreover, dislocations are also present in the absorption layer InGaAs, which is unacceptable for the device performance. The observed threading dislocations are predominantly 60-degree dislocations with Burgers vectors $b = a/2 <110>$, where a – unit cell parameter. In other words, these are dislocations parallel to [110] and [1$\underline{1}$0] directions [13]. Besides that, 90-degree threading dislocations with Burgers vectors $b = \sqrt{2}\,a\,/\,2$ can be also seen in the InGaAs active layer. Some of the dislocations spread over the entire thickness of the active and upper cap layers and propagate to the surface.

Sample #2 (see Fig. 3 b) is characterized by a lower density of threading dislocations compared
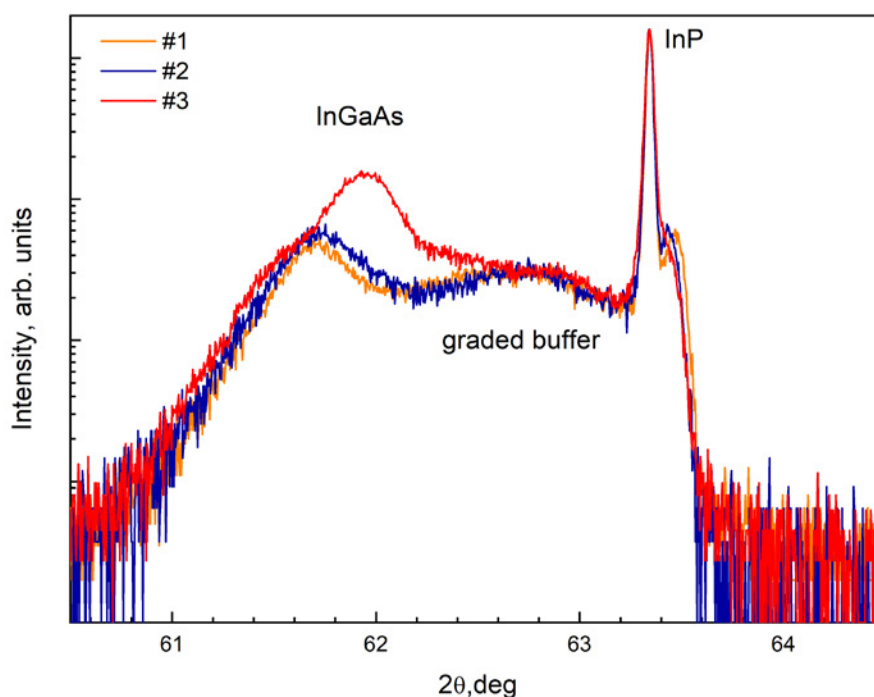
Fig. 2. X-ray diffraction curves of the test structures in relation to the symmetric InP (004) reflection

Condensed Matter and Interphases / Конденсированные среды и межфазные границы   2023;25(1): 20–26

E. I. Vasilkova et al.   Molecular beam epitaxy of metamorphic buffer for InGaAs/InP photodetectors...
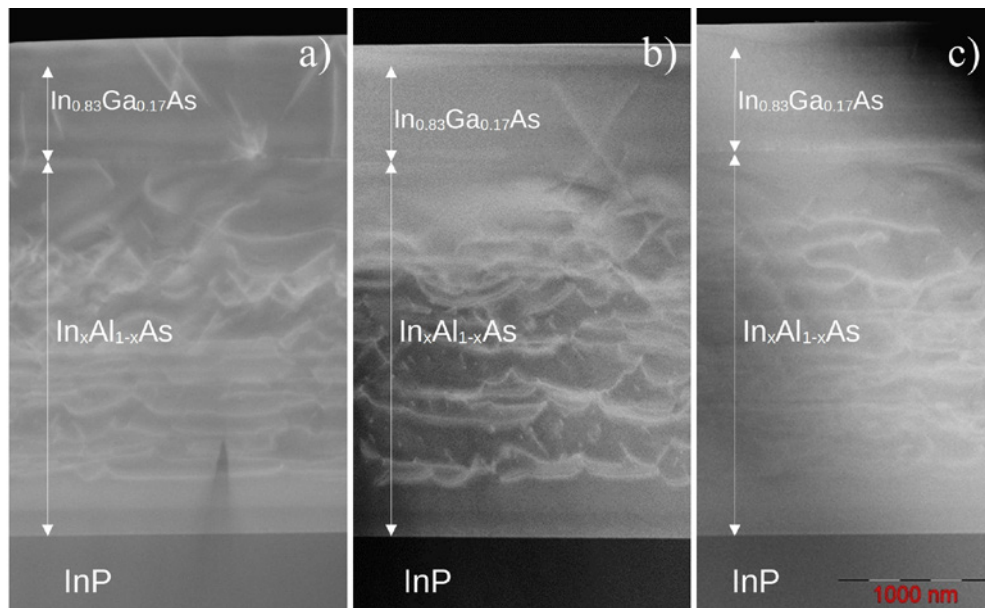
Fig. 3. TEM images of the test structures in the [110] section plane: a) sample #1, b) sample #2, c) sample #3

to sample #1. Nevertheless, one can notice the propagation of 60-degree dislocations from the metamorphic buffer to the active region. Misfit dislocations are also clearly distinguishable on the figure. The distribution of misfit dislocations over the buffer layer is almost uniform up to thicknesses of about 1500 nm. In the upper part of the buffer layer the formation of misfit dislocations stops. This result is consistent with the theoretical predictions for a metamorphic ~1400 nm thick $In_xAl_{1-x}As$ buffer (with a maximum $x = 0.87$) with a linear gradient profile [14].

Fig. 3 c) shows the TEM image of sample #3. Contrasting inserts, typical for superlattices, are distinguished in the buffer area. Moreover, threading and misfit dislocations are also observed in this sample. The threading dislocation density decreases in the direction of epitaxial growth until the dislocations finally disappear in the upper part of the buffer layer. Based on the image analysis, it can be concluded that there is a dislocation-free area in the buffer near the interface. Thus, putting InAs/InAlAs inserts in the buffer layer could be useful to inhibit the nucleation and propagation of dislocations.

4. Conclusion

In the scope of this work, we studied several various approaches to the MBE growth of linearly graded metamorphic buffers $In_xAl_{1-x}As$ for the implementation of InGaAs pin-photodetectors sensitive in 2.2–2.6 um wavelength range on InP substrates. Employing methods of internal structure analysis, such as X-ray diffraction and transmission electron microscopy, conclusions about the effectiveness of the three certain buffer designs for the formation of strain-free absorption layer were drawn. The most optimal metamorphic buffer configuration was determined. The main design feature is the inclusion of three InAs/InAlAs superlattice inserts in the metamorphic buffer with 500 nm spacings between them. At the same time, after the graded buffer growth, the temperature of the substrate was subsequently raised and lowered. It is shown that heterostructures with this buffer are characterized by the lowest of the three test structures threading dislocations density in the active layer.

Thus, the fundamental possibility of MBE synthesis of strain-free InGaAs/InP heterostructures with a metamorphic buffer was shown. The authors suggest to follow the technological parameters of the MBE process given in the text during the growth of SWIR photodetector heterostructures with high photosensitivity in the range of 2.2–2.6 um.

Condensed Matter and Interphases / Конденсированные среды и межфазные границы 2023;25(1): 20–26

E. I. Vasilkova et al. Molecular beam epitaxy of metamorphic buffer for InGaAs/InP photodetectors...

Contribution of the authors

The authors contributed equally to this article.

Conflict of interests

The authors declare that they have no known competing financial interests or personal relationships that could have influenced the work reported in this paper.

References

1. Zhang Y., Gu Y. Gas source MBE grown wavelength extending InGaAs photodetectors. *Advances in Photodiodes*. IntechOpen; 2011. https://doi.org/10.5772/13910

2. Zhang Y., Gu Y., Zhu C., Hao G., Li A., Liu T. Gas source MBE grown wavelength extended 2.2 and 2.5μm InGaAs PIN photodetectors. *Infrared Physics & Technology*. 2006;47(3): 257–62. https://doi.org/10.1016/j.infrared.2005.02.031

3. Lavrukhin D. V., Yachmenev A. E., Galiev R. R., Khabibullin R. A., Ponomarev D. S., Fedorov Y. V., Maltsev P. P. MHEMT with a power-gain cut-off frequency of f_{max} = 0.63 THz on the basis of a $In_{0.42}Al_{0.58}As/In_{0.42}Ga_{0.58}As/In_{0.42}Al_{0.58}As/GaAs$ nanoheterostructure. *Semiconductors*. 2014;48(1): 69–72. https://doi.org/10.1134/S1063782614010187

4. Kirch J., Garrod T., Kim S., ... Kuan T. S. $InAs_yP_{1-y}$ metamorphic buffer layers on InP substrates for mid-IR diode lasers. *Journal of Crystal Growth*. 2010;312(8): 1165–1169. https://doi.org/10.1016/j.jcrysgro.2009.12.057

5. Jones R. K., Hebert P., Pien P., ... Karam N. Status of 40% production efficiency concentrator cells at Spectrolab. *2010 35th IEEE Photovoltaic Specialists Conference*. 2010. p. 000189–000195.: https://doi.org/10.1109/PVSC.2010.5614535

6. Tersoff J. Dislocations and strain relief in compositionally graded layers. *Applied Physics Letters*. 1993;62(7): 693–5. https://doi.org/10.1063/1.108842

7. Chen X., Gu Y., Zhang Y. Epitaxy and device properties of InGaAs photodetectors with relatively high lattice mismatch. B: Zhong M. (ed.). In: *Epitaxy*. InTech; 2018. https://doi.org/10.5772/intechopen.70259

8. Zakaria A., King R. R., Jackson M., Goorsky M. S. Comparison of arsenide and phosphide based graded buffer layers used in inverted metamorphic solar cells. *Journal of Applied Physics*. 2012;112(2): 024907. https://doi.org/10.1063/1.4737788

9. Zhang Y. G., Gu Y., Tian Z. B., Wang K., Li A. Z., Zhu X. R., Zheng Y. L. Performance of gas source MBE-grown wavelength-extended InGaAs photodetectors with different buffer structures. *Journal of Crystal Growth*. 2009;311(7): 1881–1884. https://doi.org/10.1016/j.jcrysgro.2008.10.087

10. Burlakov I. D., Grinchenko L. Y., Dirochka A. I., Zaletaev N. B. Short wavelength infrared InGaAs detectors (a review). *Advances in Applied Physics (Uspekhi Prikladnoi Fiziki)*. 2014;2(2): 131-136. (In Russ., abstract in Eng.). Available at: https://www.elibrary.ru/item.asp?id=21505376

11. Horikawa H., Ogawa Y., Kawai Y., Sakuta M. Heteroepitaxial growth of InP on a GaAs substrate by low-pressure metalorganic vapor phase epitaxy. *Applied Physics Letters*. 1988;53(5): 397–399. https://doi.org/10.1063/1.99890

12. Kaminska M., Liliental-Weber Z., Weber E. R., George T., Kortright J. B., Smith F. W., Tsaur B., Calawa A. R. Structural properties of As-rich GaAs grown by molecular beam epitaxy at low temperatures. *Applied Physics Letters*. 1989;54(19): 1881–1883. https://doi.org/10.1063/1.101229

13. Franzosi P., Salviati G., Genova F., Stano A., Taiariol F. Misfit dislocations in InGaAs/InP mbe single heterostructures. *Journal of Crystal Growth*. 1986;75(3): 521–534. https://doi.org/10.1016/0022-0248(86)90098-9

14. Pobat D. B., Solov'ev V. A., Chernov M. Y., Ivanov S. V. Distribution of misfit dislocations and elastic mechanical stresses in metamorphic buffer InAlAs layers of various constructions. *Physics of the Solid State*. 2021;63(1): 84-89. https://doi.org/10.1134/S1063783421010170

Information about the authors

Elena I. Vasilkova, Engineer, postgraduate student at the Saint Petersburg National Research Academic University of the Russian Academy of Sciences (Saint Petersburg, Russian Federation).

https://orcid.org/0000-0002-0349-7134
elenvasilkov@gmail.com

Evgeny V. Pirogov, Researcher, Saint Petersburg National Research Academic University of the Russian Academy of Sciences (Saint Petersburg, Russian Federation).

https://orcid.org/0000-0001-7186-3768
zzzavr@gmail.com

Maxim S. Sobolev, Cand. Sci. (Phys.–Math.), Head of the Laboratory, Saint Petersburg National Research Academic University of the Russian Academy of Sciences (Saint Petersburg, Russian Federation).

https://orcid.org/0000-0001-8629-2064
sobolevsms@gmail.com

Evgeny V. Ubiyvovk, Cand. Sci. (Phys.–Math.), Senior Researcher, Saint Petersburg State University (Saint Petersburg, Russian Federation).

https://orcid.org/0000-0001-5828-4243
ubyivovk@gmail.com

Condensed Matter and Interphases / Конденсированные среды и межфазные границы   2023;25(1): 20–26

E. I. Vasilkova et al.   Molecular beam epitaxy of metamorphic buffer for InGaAs/InP photodetectors...

Andrey M. Mizerov, Cand. Sci. (Phys.–Math.), Leading Researcher, Saint Petersburg National Research Academic University of the Russian Academy of Sciences, (Saint Petersburg, Russian Federation).

https://orcid.org/0000-0002-9125-6452

andreymizerov@rambler.ru

Pavel V. Seredin, Dr. Sci. (Phys.–Math.), Full Professor, Chair of department, Department of Solid State Physics and Nanostructures, Voronezh State University,(Voronezh, Russian Federation).

https://orcid.org/0000-0002-6724-0063

paul@phys.vsu.ru

Original articles

Research article
https://doi.org/10.17308/kcmf.2023.25/10943

Dispersed copper (I) oxide particles encapsulated by polylactide

M. P. Danilaev[1]✉, N. V.Dorogov[1], S. V. Drobushev[1], S. A. Karandashov[1], M. A. Klabukov[1], V. A. Kuklin[1.2]

*[1]Kazan National Research Technical University named after A. N. Tupolev – KAI,
10 K. Marx str., Kazan 420111, Republic of Tatarstan, Russian Federation*

*[2]Kazan Federal University,
18 Kremlevskay str., Kazan 420018, Republic of Tatarstan, Russian Federation*

Abstract

One of the approaches for the production of polymer composite materials with a biocidal effect is based on the use of dispersed particles of some metal oxides as a filler (for example, copper oxide or zinc oxide). Such an approach allows not only providing a biocidal effect, but also increasing such mechanical characteristics as the modulus of elasticity, hardness, and abrasion resistance. The mechanical characteristics of such polymer composite materials can be controlled by formation of a sheath (for example, from polylactide) of a given thickness on the surfaces of dispersed particles. Polylactide is a biodegradable polymer, widely used as coating material for particles with biocidal properties. The parameters of the methods for forming a polylactide sheath are determined by the sheath's thickness and the sheath's adhesion to the particle surface. The purpose of the study was to determine the parameters of the polymer sheath's formation on the surfaces of dispersed submicron copper oxide (I) particles during coacervation of polylactide from the solution.

The encapsulation of copper (I) oxide particles was carried out by the coacervation process in a solution. Polylactide was displaced from the solution in benzene by hexane in the presence of copper (I) oxide particles. It was shown that a sheath thickness of about 250 nm can be obtained by using the polylactide sheath formation method. The recommended parameters of the polylactide sheath formation method were determined: solution temperature of 35÷38 °C, hexane volume not more than 30±2 ml. The sheath had weak adhesion to particle surfaces: adhesion was determined by the roughness of the particle surface.

The mechanical characteristics of the epoxy resin ED-20 polymer composition filled with the encapsulated particles were considered in the study. The increase in the mechanical properties of the polymer composition with encapsulated particles in comparison with the samples of polymer composition with non-encapsulated particles was revealed. That can indicate the increased adhesion of encapsulated particles to such polymer matrix.

Keywords: Encapsulation, Dispersed particles of copper (I) oxide, Polylactide

✉ Maxim P. Danilaev, e-mail: danilaev@mail.ru

Condensed Matter and Interphases / Конденсированные среды и межфазные границы   2023;25(1): 27–36

M. P. Danilaev et al.   Dispersed copper (I) oxide particles encapsulated by polylactide

1. Introduction

One of the main factors hindering the widespread use of polymer composite materials in tropical climates is their insufficiently high resistance to the simultaneous action of such external factors as high temperature, humidity, intense solar and UV radiation, and the destructive effect of microorganisms [1–4]. Thus, in [5, 6] a monotonous decrease in the mechanical characteristics of natural fibre reinforced polymer composites with was noted as a result of moisture absorption and hygrometric ageing of the composite. It was shown in [7] that the use of glass fibre reinforced epoxy composites as insulators, although promising, is limited by the destruction of this material caused by simultaneous exposure to air moisture, temperature, and high voltage. This causes the appearance and increase of cracks, starting from the surface of the material, which, in turn, leads to a decrease in its performance. Moreover, it was noted that one of the main reasons for the destruction of the composite is the destruction at the interface between the filler and the polymer matrix. The destructive effect of microorganisms is predominant for a number of polymeric materials, including polymer compositions based on epoxy resins or polyethylene [8, 9].

A promising approach to reducing the degradation rate of polymer composite materials is the use of dispersed functional fillers. Thus, in [10], the results of a comparative analysis of several approaches to increasing the resistance of cycloaliphatic epoxy resin coatings were presented and the expediency of using finely dispersed fillers in the composition was substantiated. The use of highly dispersed functional fillers with a biocidal effect, for example, silver or copper oxide particles, allows not only to increase the resistance of the polymer composite to biodegradation [11], but also to improve some of its mechanical characteristics, including hardness, modulus of elasticity, and increase resistance to abrasion [12–16]. The possibility of controlling of the mechanical characteristics of such polymer composites by creating and changing the thickness of the polymer sheath on the surfaces of the filler particles is known [12, 13].

Polylactide (PLA) is widely used as a polymer sheath material for particles with biocidal properties. For example, particles encapsulated by PLA were obtained for the production of temperature sensors [17, 18], for targeted delivery of ferrimagnetic particles in the treatment of oncological diseases [19] or targeted delivery of drugs after PLA degradation [20], for the protection of polymer composites based on epoxy resins [21, 22] from some fungi species.

The creation of a PLA sheath on particle surfaces is a non-trivial task. For example, when forming a PLA sheath by the polymerization of lactide on the surfaces of dispersed particles [21], the question of determining the mechanical properties of the sheath remains open. This is due to the complexity of determining the parameters of the formed polymer (molecular weight, modulus of elasticity, etc.), which are necessary for assessing the mechanical properties of the composite. In addition, the acids present in the solution during the formation of the sheath contribute to the destruction of certain types of particles. Thus, when copper oxide particles interact with acids, copper salts are formed. The use of evaporation methods, evaporator emulsification, or coacervation processes overcome this disadvantage. The mechanical properties of the sheath in this case will be close to the mechanical properties of the original PLA polymer. However, the issues of sheath adhesion to particle surfaces and the determination of the possible range of changes in the sheath thickness remain open. These issues can only be resolved experimentally: by selecting the parameters of the technological process for the formation of such a sheath [20].

The purpose of this study was to determine the parameters of the formation of the polymer sheath on the surfaces of copper oxide (I) dispersed particles during the coacervation of polylactide from a solution.

2. Experimental

2.1. Formation of a polylactide sheath on the surfaces of copper (I) oxide particles

A polylactide polymer sheath (manufactured by Natural Works LLC grade PLA 4043D) was prepared on dispersed copper(I) oxide particles (TU 6-09-765-76 analytical grade). The formation of this polymer sheath was carried out on the surfaces of dispersed Cu_2O particles in a dispersed

Condensed Matter and Interphases / Конденсированные среды и межфазные границы   2023;25(1): 27–36

M. P. Danilaev et al.   Dispersed copper (I) oxide particles encapsulated by polylactide

medium using a coacervation in a PLA solution. For this, a PLA solution in benzene (GOST 5955-75 chemically pure reagent) was prepared: a weighed portion of PLA of 0.75 ± 0.05 g was dissolved in 60 ± 2 ml of benzene during heating to (40 ± 1) °C and slow mixing on a heated magnetic stirrer (Ekros, model ES-6120) for 5–6 hours. After the PLA was dissolved in benzene, a viscous transparent solution was obtained. The homogenization of dispersed copper (I) oxide particles (m_{Cu2O}) 1 ± 0.05 g was carried out in 27 ± 2 ml of benzene using an ultrasonic bath (Daihan WUC-A01H, power 50 W) for 60 ± 10 s. After homogenization solution of PLA in benzene was added into the resulting suspension with constant mixing at a temperature of 40 ± 1 °C to the desired concentration (C_{PLA}) PLA, which was changed during the experiments. The coacervation process was initiated by the addition of a displacement solvent to the obtained solution. Hexane (TU 2631-158-44493179-13 chemically pure reagent) with a volume of 15 ± 0.5 ml was used as a displacing solvent, adding it to the solution through a dropping funnel at a rate of ω_{hex}. After the introduction of the displacement solvent, the resulting solution was stirred for 20 min. The encapsulated particles were filtered off using multilayer filter paper followed by washing in hexane.

2.2. Research methods

The thickness of the PLA sheath on the surfaces of dispersed particles of copper (I) oxide (Cu_2O) was determined based on the difference in the sizes of encapsulated and non-encapsulated particles. The sheath thickness was estimated by statistical image processing (Fig. 1) using the ImageJ software environment [23]. Images of particles, both encapsulated (Fig. 1) and not encapsulated, were obtained by scanning electron microscopy (SEM) using Carl Zeiss AURIGA Cross Beam electron microscope with an EDV Inca X-Max 80 mm². The study of the adhesion of the PLA sheath to dispersed particles was carried out using the turbidimetric method [24, 25] by analysing the deposition curves of dispersed particles in a solution. The evaluation of the adhesion of the PLA sheath to the polymer matrix was carried out by studying the mechanical characteristics of samples of

polymer composite material based on epoxy resin ED-20. Sample preparation was carried out according to the procedure described in [26]. Martens hardness was measured on a Shimadzu DUH-211S ultramicro tester according to ISO 14577-1 using a Berkovich indenter (triangular indenter with a 115° apex angle). Twenty five independent measurements were carried out in different areas of the test sample with subsequent averaging of the obtained values [12]. The measurement of the modulus of elasticity and maximum deformation was carried out in accordance with GOST 11262-80 using Shimadzu AG-X 50 kN universal desktop testing machine for physical and mechanical testing of various materials. Test parameters: bending loading rate – 7mm/min; ambient temperature – 23 ± 2 °C.

3. Results and discussion

Typical micrographs of encapsulated Cu_2O particles at different resolutions of the Carl Zeiss AURIGA Cross Beam electron microscope are shown in Fig.1. The encapsulated particles shown in Fig. 1 were obtained under the following conditions: $m_{Cu2O} = 1\pm0.05$ g, $C_{PLA} = (4.5\pm0.1)\cdot10^{-4}$ g per 100 ml of benzene, $\omega_{hex} = 15\pm1$ drops/min, hexane volume V 15 ± 0.5 ml, solution mixing time was 20 min. Statistics were performed based on at least 3 microphotographs; a sample of 800–1200 particles was used. Examples of statistical processing of microscopic studies are shown in Fig. 2, where the envelopes of the histograms of distribution of the size of the initial and encapsulated (Fig. 1) Cu_2O particles can be seen. The following designations were used in Fig. 2: N is the number of particles with a certain size, N_0 is the number of particles corresponding to the maximum in the distribution. The size distribution of the number of encapsulated particles (Fig. 2b) is shown for particles obtained under the following conditions: $m_{Cu2O} = 1\pm0.05$ g, $C_{PLA} = (4.5\pm0.1)\cdot10^{-4}$ g per 100 ml of benzene, $\omega_{hex} = 27\pm2$ drops/min, hexane volume V 27 ± 1 ml, solution mixing time 20 min. For original and encapsulated particles N_0 was ~500 ± 20.

The thickness of the polymer sheath on the surfaces of dispersed particles during its formation using the coacervation process is determined by the collision frequency (ν) of dispersed particles with PLA molecules displaced

Condensed Matter and Interphases / Конденсированные среды и межфазные границы   2023;25(1): 27–36

M. P. Danilaev et al.   Dispersed copper (I) oxide particles encapsulated by polylactide

a   b

c
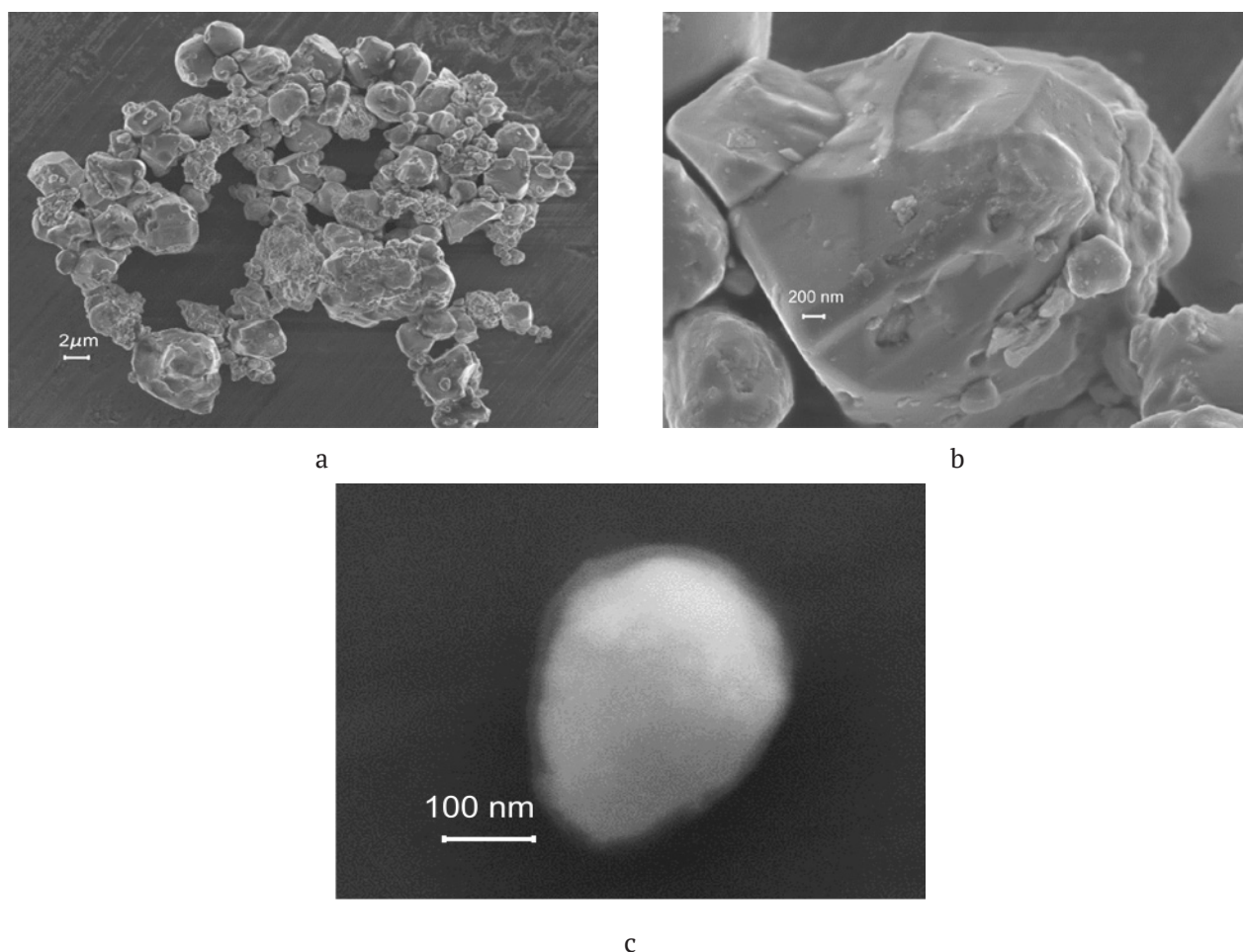
Fig. 1. Typical photomicrographs of encapsulated particles taken at various resolutions. Encapsulated particles were obtained under the following conditions: $m_{\text{Cu2O}} = 1\pm0.05\,\text{g}$, $C_{\text{PLA}} = \left(4.5\pm0.1\right)\cdot10^{-4}\,\text{g}$ per 100 ml of benzene, $\omega_{\text{hex}} = 15\pm1$ drops/min, solution mixing time 20 min, hexane volume 15±0.5 ml

a   b
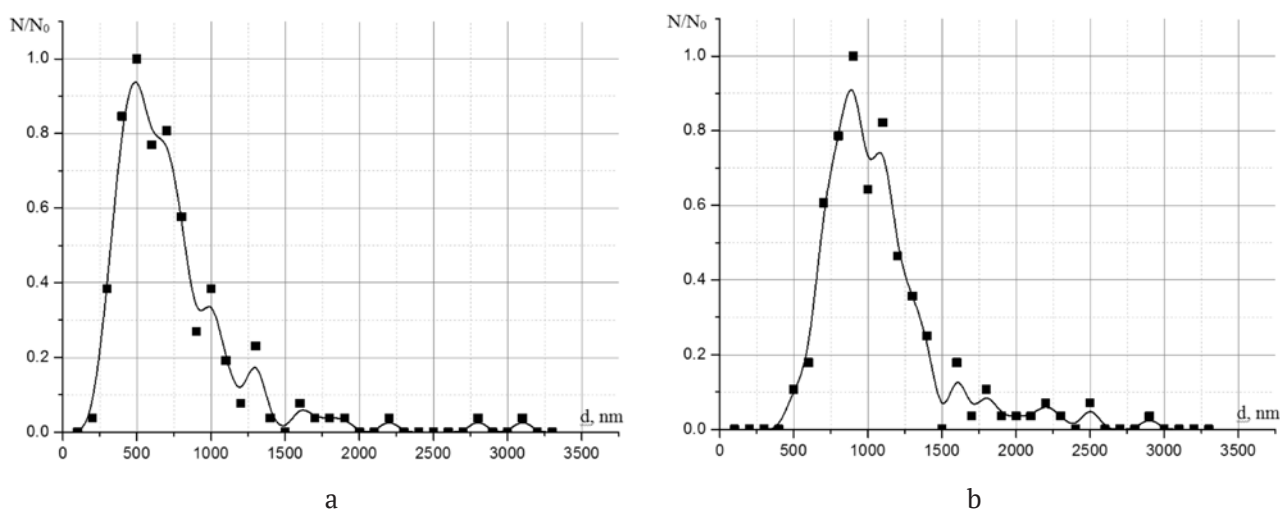
Fig. 2. Particle size distribution: a – initial particles; b – encapsulated copper (I) oxide particles, N – number of particles with a certain size, N_0 – number of particles corresponding to the maximum in the distribution

Condensed Matter and Interphases / Конденсированные среды и межфазные границы   2023;25(1): 27–36

M. P. Danilaev et al.   Dispersed copper (I) oxide particles encapsulated by polylactide

from solution with benzene, as well as by the cross section (σ) of inelastic collisions [12, 27]. For testing the technological modes of PLA sheath formation, the following parameters were considered: mixing time (t) of the suspension of dispersed Cu_2O particles with PLA solution during coacervation; the ratio of the volume of the PLA solution in benzene to the volume of the displacing solvent (hexane); temperature of the solution during the formation of the PLA sheath. Three series of experiments for the investigation of the influence of each of these parameters on the thickness of the PLA polymer sheath were carried out in the study.

In the first series of experiments, we changed the time (t) of mixing the PLA solution with dispersed particles with the uniform addition of the displacing solvent: $C_{PLA} = (4.5 \pm 0.1) \cdot 10^{-4}$ g per 100 ml of benzene, $m_{Cu2O} = 1 \pm 0.05$ g, $\omega_{hex} = 15 \pm 1$ drops/min, $T = 40 \pm 2$ °C. The mixing time varied from 20 to 110 min. The dependence of the average thickness ($2h$) of PLA sheath vs. time t is shown in Fig. 3.

Reduction of the growth rate ($\upsilon = \Delta h / \Delta t$) of the sheath thickness was probably due to a decrease in the number of PLA molecules with time (respectively, the collision frequency υ decreased) displaced from the solution by hexane due to their deposition on the surface of dispersed particles. The control in the reduction of the growth rate υ is

possible by changing the number of PLA molecules displaced from the PLA solution by changing the amount of hexane added to the solution.

In the second series of experiments for the study of the change of the volumes of the PLA solution in benzene to the volume of the displacing solvent (hexane), we changed the volume of hexane added to the solution and achieved a change in the concentration of PLA molecules: $C_{PLA} = (4.5 \pm 0.1) \cdot 10^{-4}$ g per 100 ml of benzene, $m_{Cu2O} = 1 \pm 0.05$ g, $\omega_{hex} = 27 \pm 2$ drops/min, $T = 40 \pm 2$ °C, hexane volume V was changed in the range of $(5 \div 27) \pm 1$ ml. The dependence of the average thickness ($2h$) of PLA sheaths on hexane volume V is shown in Fig. 4.

It should be noted that in the case when the volume of hexane added to the solution exceeds 30 ± 2 ml, the rate of the coacervation process increased sharply. In experiments, the formation of agglomerates of encapsulated particles, which precipitated, was observed. The use of agglomerated particles as a filler of disperse-reinforced polymeric materials does not allow obtaining reproducible mechanical properties of composites [28, 29]. This imposes a limitation on both the maximum volume of hexane added to the solution ($V < 30$ ml) and sheath thickness ($2h < 500$ nm), which can be obtained on dispersed filler particles by varying this parameter during encapsulation using this method.

Fig. 3. The dependence of polylactide sheath average thickness on the mixing time of the solution. Encapsulated particles were obtained under the following conditions: $m_{Cu2O} = 1 \pm 0.05$ g, $C_{PLA} = (4.5 \pm 0.1) \cdot 10^{-4}$ g per 100 ml of benzene, $\omega_{hex} = 15 \pm 1$ drops/min, $T = 40 \pm 2$ °C, hexane volume 15±0.5 ml, solution mixing time was changed from 20 to 110 min
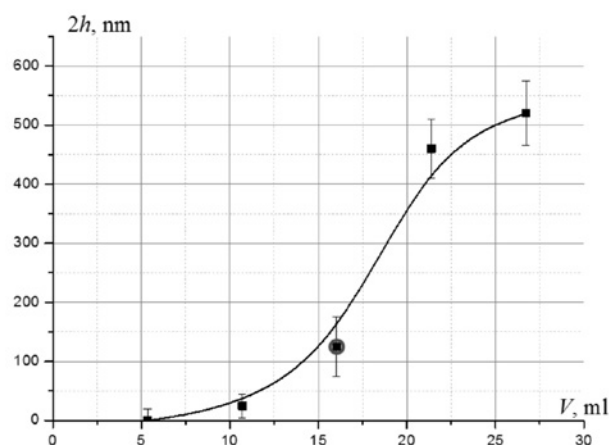
Fig. 4. The dependence of polylactide sheath average thickness on the volume of hexane added to the solution. Encapsulated particles were obtained under the following conditions: $m_{Cu2O} = 1 \pm 0.05$ g, $C_{PLA} = (4.5 \pm 0.1) \cdot 10^{-4}$ g per 100 ml of benzene, $\omega_{hex} = 27 \pm 2$ drops/min, $T = 40 \pm 2$ °C, hexane volume V was changed in the range $(5 \div 27) \pm 1$ ml, solution mixing time was 20 min

Condensed Matter and Interphases / Конденсированные среды и межфазные границы   2023;25(1): 27–36

M. P. Danilaev et al.   Dispersed copper (I) oxide particles encapsulated by polylactide

In the third series of experiments, we studied the effect of changing the temperature of the PLA solution in benzene during the formation of a sheath on the particle surfaces. These experiments were carried out under the following conditions: $C_{PLA} = (4.5 \pm 0.1) \cdot 10^{-4}$ g per 100 ml of benzene, $m_{Cu2O} = 1 \pm 0.05$ g, $\omega_{hex} = 27 \pm 2$ drops/min, hexane volume V 15 ± 1 ml, the temperature of the solution during sheath formation was changed within [25÷45]±2 °C. The upper temperature limit was limited by the temperature of PLA softening (~50 °C) [30]. At such a temperature of the solution, the probability of agglomeration of encapsulated particles due to their adhesion during collisions is high [31]. The dependence of the average value of the thickness (2h) of PLA sheath on the temperature of the solution is shown in Fig. 5.

The presence of an extremum of the curve in Fig. 5 can be explained by the fact that the solubility of PLA in benzene increases with increasing temperature starting from ~35 °C. Due to this, the amount of PLA displaced by hexane from the solution decreases and, as a result, the thickness of the polymer sheath decreases. The increase of the sheath thickness with a change in temperature from 25 °C to 35 °C is associated with an increase in collision frequency (ν) of dispersed particles with PLA molecules displaced from the
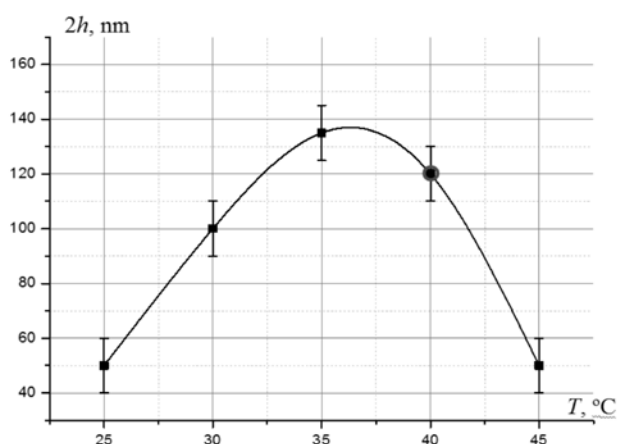
solution with benzene. Thus, the temperature ~35 °C is the most appropriate in terms of achieving the maximum thickness of the sheath. Points on the graphs (Figs. 3-5), marked with a circle, indicate the results obtained under the same conditions of the encapsulation process. The high correlation of the sheath thickness for these conditions indicates a good reproducibility of the encapsulation process. It should be noted that the change in the PLA weight in the range of $(2.25÷4.5) \cdot 10^{-4}$ g per 100 ml of benzene, as well as the weight of dispersed Cu_2O particles added to the solution in the range of (0.2÷2) g did not actually affect the thickness h of PLA sheaths under the considered conditions of the formation. Thus, the main parameters that allow to control the thickness h, are: the mixing time of the PLA solution after the addition of the displacement solvent, the ratio of the volumes of PLA solution in benzene to the volume of the displacement solvent (hexane), and the temperature of the solution during mixing.

The mechanical characteristics of a polymer reinforced with encapsulated dispersed particles are affected, among other things, by the adhesion of the polymer sheath both to dispersed particles and to the polymer matrix [12, 13]. The study of the adhesion of the PLA sheath to dispersed particles was carried out by the turbidimetric method [25, 24] by analysing the deposition curves of dispersed particles in solution (Fig. 6). The dotted lines in Fig. 6 show the equilibrium levels of optical density (D): 0.232 corresponds to curve 4; 0.135 corresponds to curve 3. Equilibrium level of optical density is the experimental value of the optical density at t = 15000 s. Sedimentation studies were carried out for the types of dispersed particles presented in Table 1.

The particle sedimentation curve (1) confirms the uneven size distribution function of the initial particles (Fig. 2a). It should be noted that, without preliminary ultrasonic treatment, significant agglomeration of the initial particles was observed. Therefore, such treatment is necessary for the encapsulation. Sedimentation curve 2 confirms the formation of PLA sheaths on the particle surfaces. The formation of a polymer sheath leads to a smoothing of the particle size distribution function (Fig. 2b), which, probably, was caused by the equalization of the particle shape due to the sheath formed on their surfaces.

Fig. 5. The dependence of the average thickness of the polylactide sheath on the solution temperature. Encapsulated particles were obtained under the following conditions: $m_{Cu2O} = 1 \pm 0.05$ g, $C_{PLA} = (4.5 \pm 0.1) \cdot 10^{-4}$ g per 100 ml of benzene, $\omega_{hex} = 27 \pm 2$ drops/min, hexane volume V was 15±0.5 ml, the temperature of the solution during the formation of the sheath was changed in the range (25÷45)±2 °C, solution mixing time was 20 min

Condensed Matter and Interphases / Конденсированные среды и межфазные границы 2023;25(1): 27–36

M. P. Danilaev et al. Dispersed copper (I) oxide particles encapsulated by polylactide

Table 1. Description of sedimented particles

Curve number	Description of particle type	The solution in which sedimentation was performed	Treatment of particles in the solution before the experiment
1	Initial copper oxide (I) particles	PLA solution in a mixture of benzene and hexane in a ratio corresponding to the encapsulation process	Ultrasonic treatment (power of 50 W) for 60±10 s. Mixing with a magnetic stirrer for 10 min.
2	Copper (I) oxide particles encapsulated by PLA: $h \sim 125$ nm	PLA solution in a mixture of benzene and hexane in a ratio corresponding to the encapsulation process	Mixing with a magnetic stirrer for 10 min.
3	Copper (I) oxide particles encapsulated by PLA: $h \sim 125$ nm	PLA solution in a mixture of benzene and hexane in a ratio corresponding to the encapsulation process	Ultrasonic treatment of the solution of particles (power of 50 W, treatment time of 10 min) for the removal of the sheath from the particle surfaces
4	Капсулированные ПЛА частицы оксида меди (I): $h \sim 125$ nm	Benzene	Mixing with a magnetic stirrer (12 h) followed by ultrasonic treatment (50 W, treatment time of 5 min) for the removal of the sheath from the particle surfaces

The sheath thickness on the surfaces of copper (I) oxide particles was not the same. The polymer sheath was formed on the surface of all initial particles with equal probability: the deposition curve *2* for the entire time interval was below the deposition curve *1*.

The shape of sedimentation curves *3* and *4* indicates that after treatment with ultrasound and treatment in a solvent, for PLA, the sheath comes off the surface of the particles. Thus, curve *3* was characterized by a significant decrease in the size of the deposited particles and an increase in the equilibrium level (indicated by the dotted line in Fig. 6) of the optical density (*D*). An increase in the equilibrium level of optical density indicates that after ultrasonic treatment, the PLA sheath is destroyed, and its parts with the density significantly lower than the density of dispersed particles, led to an additional increase in the equilibrium level of the optical density of the solution. This determined the difference in the shape of the sedimentation curves *1* and *3*. The shape of the sedimentation curve *4* indicates the complete dissolution of the PLA sheath. In this case, there was an increase in the viscosity of the liquid phase of the solution (taken into account in Fig. 6) and an increase in the sedimentation time of the dispersed particles. The increase in the viscosity of the liquid phase of the solution was taken into account according to the procedure

described in [32].

The obtained results show that the considered method of encapsulation of dispersed particles allows to ensure with equal probability the formation of a polymer sheath on copper (I) oxide particles of all sizes. In this case, the thickness (*h*) of the polymer sheath was uneven on each of the particles. The uneven thickness *h* was probably determined by the habit of the initial
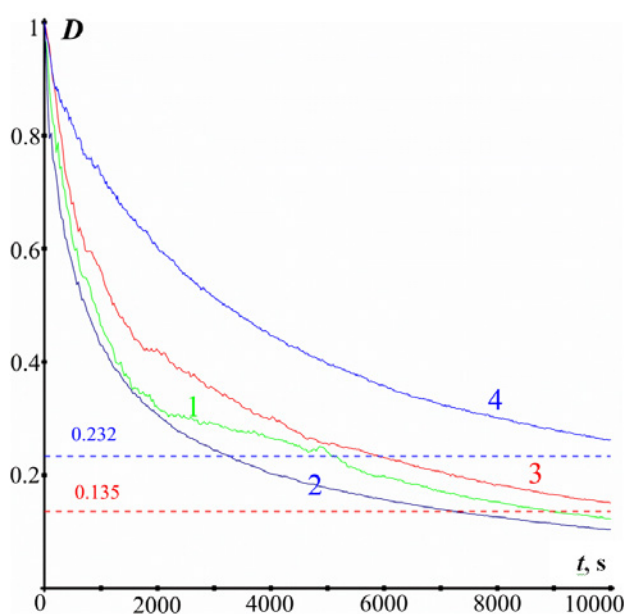
Fig. 6. Change in the optical density of solutions over time in photometric measurements. An explanation for the curve numbers are given in Table 1

Condensed Matter and Interphases / Конденсированные среды и межфазные границы 2023;25(1): 27–36

M. P. Danilaev et al. Dispersed copper (I) oxide particles encapsulated by polylactide

particles. The adhesion of the PLA sheath to the surface of the copper (I) oxide particles is weak and is determined by the surface roughness of the copper (I) oxide particles.

The study of the adhesion of the PLA sheath to the polymer matrix was carried out by comparing the mechanical characteristics of polymer composites based on epoxy resin ED-20 filled with encapsulated and non-encapsulated particles. Mechanical characteristics were studied for the following three samples: Sample 1 was without a filler, sample 2 was filled with non-encapsulated copper (I) oxide particles, sample 3 was filled with encapsulated copper (I) oxide particles. The concentration of particles in samples 2 and 3 was ~0.92±0.02 wt %. The sheath thickness on the surfaces of the encapsulated particles was ~25 ± 5 nm. The mechanical characteristics (Martens hardness HMs, N/mm^2; maximum stress σ, N/mm^2; ultimate strain ε, %) of the samples are presented in Table 2. Ten samples of each type were used in the experiment. The obtained values of mechanical characteristics were averaged. The error of the measured values of the mechanical characteristics was not higher than 15%.

Table 2. Values of the mechanical characteristics of the samples

Sample type	HMs, N/mm^2	σ, N/mm^2	ε, %
Sample 1	83.03	73.92	1.53
Sample 2	118.5	80.5	1.43
Sample 3	158.6	86.5	1.01

An increase in the average hardness and maximum stress values, and a decrease in maximum deformation for sample 3 was associated with a decrease in the mobility of matrix polymer macromolecules. This is possible with an increase in the adhesion of encapsulated particles to the matrix polymer, in contrast to unencapsulated particles [12, 13]. It should be noted that the thickness of the sheath significantly affects the mechanical properties of the composite polymer material. For the choice of the thickness of the polylactide sheath, in this case, we were guided by the results obtained in [12].

4. Conclusions

The considered method of forming a polylactide sheath on the surfaces of copper (I)

oxide particles, based on initiating the process of polylactide coacervation from a solution, allows obtaining a sheath with a thickness not higher than ~250 nm. The reason for this limitation is, in our opinion, the following factors: the process of agglomeration and subsequent sedimentation of aggregates with an increase in the concentration of the displacing solvent (hexane) by more than 30% by volume; a decrease in the number of PLA molecules in a solution after the addition of a displacing solvent during mixing. It should be noted that there is an extremum in the dependence of the sheath thickness on the temperature of the solution, observed at T = 35÷38 °C. The PLA sheath has weak adhesion to the surfaces of copper (I) oxide particles and is determined by the roughness of the surfaces of dispersed particles. An increase in the mechanical characteristics of samples of a polymer composition based on epoxy resin ED-20 filled with encapsulated particles compared to samples filled with initial particles indicates an increase in the adhesion of encapsulated particles to such a polymer matrix. Thus, the use of dispersed copper (I) oxide particles encapsulated by polylactide as a filler for epoxy resin ED-20 can not only provide increased resistance to biodegradation of such composites [33, 34], but also improves their mechanical characteristics.

Contribution of the authors

The authors contributed equally to this article.

Conflict of interests

The authors declare that they have no known competing financial interests or personal relationships that could have influenced the work reported in this paper.

References

1. Razavi M., Ogunbode E. B., Nyakuma B. B., Razavi M., Yatim J. M., Lawal T. A. Fabrication, characterisation and durability performance of kenaf fibre reinforced epoxy, vinyl and polyester-based polymer composites. *Biomass Conversion and Biorefinery.* 2021; (in press): 1–16. https://doi.org/10.1007/s13399-021-01832-z

2. Mohammed M., Chai Y. Y., Doh S. I., Lim K. S. Degradation of glass fiber reinforced polymer (GFRP) material exposed to tropical atmospheric condition. *Key Engineering Materials.* 2021;879: 265–274. https://doi.org/10.4028/www.scientific.net/kem.879.265

Condensed Matter and Interphases / Конденсированные среды и межфазные границы   2023;25(1): 27–36

M. P. Danilaev et al.   Dispersed copper (I) oxide particles encapsulated by polylactide

3. Zhang G., Gong C., Gu J., Katayama Y., Someya T., Gu J. D. Biochemical reactions and mechanisms involved in the biodeterioration of stone world cultural heritage under the tropical climate conditions. *International Biodeterioration & Biodegradation*. 2019;143(9): 104723. https://doi.org/10.1016/j.ibiod.2019.104723

4. Omazic A., Oreski G., Halwachs M., ... Erceg M. Relation between degradation of polymeric components in crystalline silicon PV module and climatic conditions: A literature review. *Solar energy materials and solar cells*. 2019;192(4): 123-133. https://doi.org/10.1016/j.solmat.2018.12.027

5. Oliveira M. S., Luz F. S., Monteiro S. N. Research progress of aging effects on fiber-reinforced polymer composites: A brief review. *Characterization of Minerals, Metals, and Materials*. 2021;2021: 505-515. https://doi.org/10.1007/978-3-030-65493-1_51

6. Mulenga T. K., Ude A. U., Vivekanandhan C. Techniques for modelling and optimizing the mechanical properties of natural fiber composites: a review. *Fibers*. 2021;9(1): 6. https://doi.org/10.3390/fib9010006

7. Ogbonna V. E., Popoola A. P., Popoola O. M., Adeosun S. O. A review on corrosion, mechanical, and electrical properties of glass fiber-reinforced epoxy composites for high-voltage insulator core rod applications: challenges and recommendations. *Polymer Bulletin*. 2021;(8): 1-28. https://doi.org/10.1007/s00289-021-03846-z

8. Murthy N., Wilson S., Sy J. C. Biodegradation of polymers. *Polymer Science: A Comprehensive Reference*. 2012;9: 547-560. https://doi.org/10.1016/B978-0-444-53349-4.00240-5

9. Lim B. K. H., Thian E. S. Biodegradation of polymers in managing plastic waste — A review. *Science of The Total Environment*. 2021;813(3): 1-25. https://doi.org/10.1016/j.scitotenv.2021.151880

10. Kondratenko Y. A., Golubeva N. K., Ivanova A. G., ... Shilova O. A. Improvement of the physicomechanical and corrosion-protective properties of coatings based on a cycloaliphatic epoxy matrix. *Russian Journal of Applied Chemistry*. 2021;94(11): 1489–1498. https://doi.org/10.1134/S1070427221110045

11. Tang S, Zheng J. Antibacterial activity of Ssilver nanoparticles: structural effects. *Advanced healthcare materials*. 2018;7(13): 1701503(1-10). https://doi.org/10.1002/adhm.201701503

12. Akhmadeev A. A., Bogoslov E. A., Danilaev M. P., Klabukov M. A., Kuklin V. A. Influence of the thickness of a polymer shell applied to surfaces of submicron filler particles on the properties of polymer compositions. *Mechanics of Composite Materials*. 2020;56(2): 241-248. https://doi.org/10.1007/s11029-020-09876-4

13. Lipatov Ju. S. *Physical chemistry of filled polymers*⁎. Moscow: Khimiya Publ.; 1977. 304 p. (In Russ.)

14. Ahmethanov R. M., Sadritdinov A. R., Zaharov V. P., Shurshina A. S., Kulish E. I Study of viscoelastic characteristics of secondary polymer raw materials in the presence of natural fillers of vegetable origin. *Condensed Matter and Interphases*. 2020;22(1): 11–17. https://doi.org/10.17308/kcmf.2020.22/2471

15. Kozlov G. V., Dolbin I. V. Transfer of mechanical stress from polymer matrix to nanofiller in dispersion-filled nanocomposites. *Inorganic Materials: Applied Research*. 2019;10(1): 226–230. https://doi.org/10.1134/S2075113319010167

16. Lavrov N. A., Kiemov Sh. N., Kryzhanovskii V. K. Tribotechnical properties of composite materials based on epoxy polymers. *Polymer Science, Series D*. 2019;12(2): 182–185. https://doi.org/10.1134/S1995421219020096

17. Bernard A., Chisholm M. H. Synthesis of core–shell (nano) particles involving TiO_2, SiO_2, Al_2O_3 and polylactide. *Polyhedron*. 2012;46(1). 1–7. https://doi.org/10.1016/j.poly.2012.07.017

18. Pfister A., Zhang G., Zareno J., Horwitz A. F., Fraser C. L Boron polylactide nanoparticles exhibiting fluorescence and phosphorescence in aqueous medium. *ACS nano*. 2008;2(6): 1252–1258. https://doi.org/10.1021/nn7003525

19. Chen F., Gao Q., Hong G., Ni J. Synthesis of magnetite core–shell nanoparticles by surface-initiated ring-opening polymerization of L-lactide. *Journal of Magnetism and Magnetic Materials*. 2008;320(13): 1921–1927. https://doi.org/10.1016/j.jmmm.2008.02.132

20. Pitukmanorom P., Yong T. H., Ying J. Y. Tunable release of proteins with polymer–inorganic nanocomposite microspheres. *Advanced Materials*. 2008;20(18): 3504-3509. https://doi.org/10.1002/adma.200800930

21. Lu X., Lv X., Sun Z., Zheng Y. Nanocomposites of poly (L-lactide) and surface-grafted TiO2 nanoparticles: Synthesis and characterization. *European Polymer Journal*. 2008;44(8): 2476–2481. https://doi.org/10.1016/j.eurpolymj.2008.06.002

22. Chee S. S., Jawaid M., Sultan M. T. H., Alothman O. Y., Abdullah L. C. Accelerated weathering and soil burial effects on colour, biodegradability and thermal properties of bamboo/kenaf/epoxy hybrid composites. *Polymer Testing*. 2019;79: 106054. https://doi.org/10.1016/j.polymertesting.2019.106054

23. Jagadeesh P., Puttegowda M., Mavinkere Rangappa S., Siengchin S. Influence of nanofillers on biodegradable composites: A comprehensive review. *Polymer Composites*. 2021;42(11): 5691–5711. https://doi.org/10.1002/pc.26291

24. Hussien S. M. R. H., Sakhabutdinov A., Anfinogentov V., Danilaev M., Kuklin V., Morozov O.

Condensed Matter and Interphases / Конденсированные среды и межфазные границы   2023;25(1): 27–36

M. P. Danilaev et al.   Dispersed copper (I) oxide particles encapsulated by polylactide

Mathematical model for measuring the concentration of nanoparticles in a liquid during sedimentation. *Karbala International Journal of Modern Science*. 2021;7(2): 160–167. https://doi.org/10.33640/2405-609X.2973

25. Danilaev M. P., Drobyshev S. V., Klabukov M. A., Kuklin V. A., Mironova D. A. Formation of a polymer shell of a given thickness on surfaces of submicronic particles. *Nanobiotechnology Reports*. 2021;16(2): 162–166. https://doi.org/10.1134/S263516762102004X

26. Bogomolova O. Y., Biktagirova I. R., Danilaev M. P., Klabukov M. A., Polsky Y. E., Pillai S., Tsentsevitsky A. A. Effect of adhesion between submicron filler particles and a polymeric matrix on the structure and mechanical properties of epoxy-resin-based compositions. *Mechanics of Composite Materials*. 2017;53(1): 117–122. https://doi.org/10.1007/s11029-017-9645-0

27. Danilaev D. P., Danilaev M. P., Dorogov N. V. The capsulation process effectiveness in multiphase gas flows. *Scientific and Technical Volga region Bulletin*. 2015;(3): 34–37. (In Russ., abstract in Eng.). Available at: https://elibrary.ru/download/elibrary_23930402_24136330.pdf

28. Pinto D., Bernardo L., Amaro A., Lopes S. Mechanical properties of epoxy nanocomposites using titanium dioxide as reinforcement–a review. *Construction and Building Materials*. 2015;95: 506–524. https://doi.org/10.1016/j.conbuildmat.2015.07.124

29. Goyat M. S., Hooda A., Gupta T. K., Kumar K., Halder S., Ghosh P. K., Dehiya B. S. Role of non-functionalized oxide nanoparticles on mechanical properties and toughening mechanisms of epoxy nanocomposites. *Ceramics International*. 2021;47(16): 22316–22344. https://doi.org/10.1016/j.ceramint.2021.05.083

30. Nampoothiri K. M., Nair N. R., John R. P. An overview of the recent developments in polylactide (PLA) research. *Bioresource Technology*. 2010;101(22): 8493–8501. https://doi.org/10.1016/j.biortech.2010.05.092

31. Zhuravlev R. A., Tamova M. Yu., Agafonova E. V. *Device for the production of encapsulated products*. Patent RF No. 2665487. Publ. 08.30.2018, bul. No. 25. (In Russ.)

32. Wang C., Sun C. Liu Q. Formation, breakage, and re-growth of quartz flocs generated by non-ionic high molecular weight polyacrylamide. *Minerals Engineering*. 2020;157: 106546(1-12). https://doi.org/10.1016/j.mineng.2020.106546

33. Kumar A. P., Depan D., Tomer N. S., Singh R. P. Nanoscale particles for polymer degradation and stabilization–trends and future perspectives. *Progress in polymer science*. 2009;34(6): 479–515. https://doi.org/10.1016/j.progpolymsci.2009.01.002

34. Allsopp D., Seal K., Gaylarde J. Ch. *Introduction to biodeterioration*. 2nd edn. Cambridge University Press; 2006. p. 252.

Information about the authors

Maxim P. Danilaev, Dr. Sci. (Tech.), Professor of Electronics and Quantum Means of Information Transmission, Head of Interuniversity Interdisciplinary Laboratory, Kazan National Research Technical University named after A. N. Tupolev – KAI (Kazan, Russian Federation).

http://orcid.org/0000-0002-7733-9200
danilaev@mail.ru

Nikolay V. Dorogov, Senior Lecturer of Radiofotonics and Multimedia Technology Department, Kazan National Research Technical University named after A. N. Tupolev – KAI, (Kazan, Russian Federation).

http://orcid.org/0000-0001-6750-6629
NVDorogov@kai.ru

Sergey V. Drobushev, Engineer of "Applied Nanotechnology" center, Kazan National Research Technical University named after A. N. Tupolev - KAI, (Kazan, Russian Federation).

https://orcid.org/0000-0002-1655-4492
warlordik_009@mail.ru

Sergey A. Karandashov, Engineer of Interuniversity Interdisciplinary laboratory, Kazan National Research Technical University named after A. N. Tupolev - KAI, (Kazan, Russian Federation).

http://orcid.org/0000-0001-7608-6531
seregak2005@yandex.ru

Mikhail A. Klabukov, Head of the Material Science and Welding Laboratory, Department of Material Science, Welding and Industrial Safety, Kazan National Research Technical University named after A. N. Tupolev – KAI, (Kazan, Russian Federation).

https://orcid.org/0000-0002-9812-7725
klabukov.misha@mail.ru

Vladimir A. Kuklin, Cand. Sci. (Phys-Math.), Lead Engineer, Kazan National Research Technical University named after A. N. Tupolev – KAI, Kazan Federal University, Institute of Physics (Kazan, Russian Federation).

http://orcid.org/0000-0003-4254-5837
iamkvova@gmail.com

Original articles

Synthesising dispersed powders of CoZn ferrites for microwave absorption

D. V. Ivashenko[1]✉, D. A. Urbanovich[1], I. Y. Polyn[1], M. V. Bushinsky[2], A. V. Trukhanov[2], V. V. Pankov[1]

[1]Belarusian State University,
4 Nezavisimosti avenue, Minsk 220030, Belarus

[2]SSPA "Scientific-Practical Materials Research Centre of NAS of Belarus"
19 Pietrusia Broŭki, Minsk 220072, Belarus

Abstract

An important task of chemical materials science is to obtain materials with set parameters and to provide a reliable prediction of their properties. At the moment, an important task is to develop promising absorbing coatings based on dispersed magnetic materials. To ensure more effective use of dispersed powders of cobalt-zinc ferrite for fillers absorbing microwave radiation, we studied the changes in their magnetic properties and morphology depending on the conditions of the sol-gel synthesis.

In our study, we synthesised $Co_{0.65}Zn_{0.35}Fe_2O_4$ ferrite powders of various degree of dispersion using the sol-gel method. The samples were analysed using X-ray diffractometry. The microstructure and the morphology of the nanoparticles were studied by means of scanning electron microscopy. The ratio of the concentration of metal atoms in ferrite powders and the features of their distribution on the surface of the particles were determined by energy dispersive X-ray spectroscopy. Magnetometry was used to determine the specific saturation magnetization and the coercive force.

The study demonstrated that the main factor resulting in low values of the saturation magnetization of the cobalt ferrite nanoparticles is the formation of the magnetic dead layer on their surface. This layer is formed due to a number of factors including noncollinearity of spins, disordering of cations, defectiveness, amorphous state, and the difference in the composition occurring because the processes of reciprocal diffusion of cations during and the formation of the spinel structure during the synthesis are not complete.

The study determined the ways to reduce the size of the inactive magnetic layer by controlling the parameters of the sol-gel synthesis in order to find effective methods of obtaining ferrite powders with increased magnetization, degree of crystallinity and the intermediate particles size between a superparamagnetic and a multidomain state. Such materials can be used as fillers for coating absorbing microwave radiation.

Keywords: Cobalt-zinc ferrite, Microwave absorption, Sol-gel synthesis, Nanoparticles

✉ Ivashenko D. V., e-mail: ivashenkodm@gmail.com

Condensed Matter and Interphases / Конденсированные среды и межфазные границы   2023;25(1): 37–46

D. V. Ivashenko et al.   Synthesising dispersed powders of CoZn ferrites for microwave absorption

1. Introduction

Ferrites are used in a large number of industries, but they are also actively used as microwave absorption materials. Recently, manufacturers have also focused on nanosized powders, which are used in biomedical diagnostics and medicine [1, 2]. However, we should point out that the use of highly dispersed magnetic particles as, for instance, absorbers of electromagnetic radiation or electronic components for creating magnetic fields can be rather difficult. The problem lies in the fact that, when using such particles, the saturation magnetization of nanosized magnetic materials is often lower than that of bulk samples [3, 4]. A decrease in the saturation magnetization of ferrites following the transition to the nanosized state, is explained by a violation of the magnetic order in the subsurface layer of the particles. In this case, the magnetic moments of magnetically active atoms demonstrate the state of spin glasses [5, 6]. The size of such surface layers with noncollinear spins calculated as a result of measuring the dependence of the specific saturation magnetization on the specific surface area of the powders is 1–2 nm [7]. It is this layer, called the magnetic dead layer, that causes a decrease in magnetization. The magnetization decreases, as compared with the magnetization of the bulk material, because a large number of atoms constituting nanoparticles are located in the subsurface layer. Moreover, as a result of the propagation of the inactive magnetic layer to the whole particle following a decrease in its size, the particle acquires superparamagnetic properties [8]. The magnetic moment of such particles can change its direction randomly depending on the temperature. When there is no external magnetic field, the mean magnetization of superparamagnetic particles equals zero. A decrease in the magnetization obviously affects the consumer performance of the material [9, 10]. Thus, at the moment, superparamagnetism observed in nanoparticles above the blocking temperature is one of the main obstacles for the creation of high-density magnetic memory devices [11, 12].

In our study, we synthesised $Co_{0.65}Zn_{0.35}Fe_2O_4$ ferrite powders of various degrees of dispersion using the sol-gel method. We used a fixed ratio of the cobalt-zinc ferrite with a spinel structure because this composition has the highest specific saturation magnetization [13, 14]. The sol-gel method was used because it enabled us to control the microstructure of ferrite powders during the synthesis [15–18].

The purpose of our study was to develop control parameters for the sol-gel synthesis in order to identify effective methods for obtaining ferrite powders with increased magnetization, degree of crystallinity and the intermediate particles size between a superparamagnetic and a multidomain state. The material obtained as a result, can be used as a filler for coatings absorbing microwave radiation.

2. Experimental

To obtain a $Co_{0.65}Zn_{0.35}Fe_2O_4$ cobalt-zinc ferrite, a sol was formed by mixing a citric acid solution and a solution of metal nitrates. All the initial reagents were of analytical grade. The solution of metal nitrates was obtained by dissolving $Co(NO_3)_2 \cdot 6H_2O$, $Zn(NO_3)_2 \cdot 6H_2O$, $Fe(NO_3)_3 \cdot 9H_2O$ with a stoichiometric ratio of metal ions Co:Zn:Fe = 0.65:0.35:2.0 and the total concentration $C(Me) = 0.3$ mol/dm³ in distilled water. The aqueous solution of citric acid with the concentration $C(C_6H_8O_7) = 0.9$ mol/dm³ was obtained by dissolving $C_6H_8O_7 \cdot H_2O$ in distilled water. The sol was formed by adding the citric acid solution to the solution of metal nitrates with vigorous stirring for 4 hours. By adding a 25% ammonia solution we obtained a neutral mixture with pH = 7. By heating at 90 °C the sol was transformed into a gel formed due to a significant increase in the volume concentration of the dispersed phase. As a result of the following thermal treatment (at 90 °C) we obtained a glass-shaped gel which was heated at 450 °C for 5 hours in order to remove any traces of carbon. The synthesised powder was washed with distilled water and dried in air. During the last stage, the powder was thermally treated at 500, 700, 900, and 1150 °C for 2 hours.

The samples were analysed using several physical and chemical methods.

X-ray diffraction patterns of the powder samples were registered using a DRON-2.0 diffractometer with CoK_α-radiation ($\lambda = 0.178896$ nm) and a Ni monochromator. Scanning was carried out in the range of angles $2\theta = 20–80°$.

Condensed Matter and Interphases / Конденсированные среды и межфазные границы   2023;25(1): 37–46

D. V. Ivashenko et al.   Synthesising dispersed powders of CoZn ferrites for microwave absorption

The microstructure and the morphology of the nanoparticles were studied by means of scanning electron microscopy using a LEO 1455 VP microscope. For this, a thin layer of the powder suspension was deposited on sitall plates. Simultaneously the ratio of the concentration of metal atoms in ferrite powders and the features of their distribution on the surface of the particles were determined by energy dispersive X-ray spectroscopy (EDX-analysis).

The specific saturation magnetization and the coercive force were studied using the Cryogen Free Measurement System by Cryogenic Ltd.

The sizes of coherent scattering regions (CSR) corresponding to the size of the crystallites of the obtained ferrite were determined by the broadening of diffraction reflections (Scherrer method).

The following expressions was used to perform calculations according to the Scherrer method:

$$\beta = \frac{K\lambda}{D\cos\theta} \Rightarrow \cos\theta = \frac{K\lambda}{D}\frac{1}{\beta}, \qquad (1)$$

where β is the width of the reflection at half height, rad; D is the size of the CSR, nm; K is the dimensionless particle drag coefficient (the Scherrer constant), λ is the wavelength of X-ray radiation, nm; and θ is the diffraction angle, rad.

Coefficient K may vary depending on the shape of the particles. For spherical particles K is usually assumed to be 0.9, while for cubic crystals the Scherrer constant can be calculated for each reflection using the following formula:

$$K = \frac{6|h|^3}{\sqrt{h^2 + k^2 + l^2}(6h^2 - 2|hk| + |kl| - 2|hl|)}, \qquad (2)$$

where h, k, and l are Miller indices.

Lattice parameter a for a cubic cell is determined using the ratio:

$$a = d\sqrt{h^2 + k^2 + l^2}, \qquad (3)$$

where d is the interplanar distance.

The shortest distance between the magnetic ions in tetrahedral (A) and octahedral (B) nodes of the lattice, also called the jump distance, considering the lattice constant was calculated using the following ratios [19]:

$$L_A = \frac{a\sqrt{3}}{4}, \qquad (4)$$

$$L_A = \frac{a\sqrt{2}}{4}. \qquad (5)$$

The theoretical X-ray density can be determined based on the X-ray diffraction patterns using the ratio [19] and taking into account the fact that each unit cell in the spinel structure consists of eight formula units,

$$N = \sum \frac{8M}{N_A \cdot a^3}, \qquad (6)$$

where M is the molecular weight of the ferrite, N_A is Avogadro number, and a^3 is the unit cell volume.

3. Results and discussion

Fig. 1 demonstrates X-ray diffraction patterns of $Co_{0.65}Zn_{0.35}Fe_2O_4$ powders annealed at various temperatures. The study determined that when the sol-gel method is used, the phase with a spinel structure forms directly after the synthesis without any additional thermal treatment. Iron-citrate complexes are formed at higher concentrations of citric acid (2:1), and their compositions depend significantly on the pH of the solution. In this case, citric acid is used as a chelating agent.

Diffraction peaks of the cubic spinel are indexed as crystallographic planes: (111), (220), (311), (222), (400), (422), (511), and (440), which corresponds to the face-centred cubic crystal structure (JCPDS 22-1086) with the space group Fd-$3m$. Intensive reflections of the sample annealed at 900 °C demonstrate that $Co_{0.65}Zn_{0.35}Fe_2O_4$ nanoparticles are well-crystallized at this temperature. The average size of the crystallites of the obtained dispersed powders calculated using the Scherrer equation is given in Table 1. The study demonstrated that at higher annealing temperatures the perfection of the structure, crystallinity, and the size of the particles improve. In this case, not only does the intensity of the characteristic X-ray reflections of the spinel grow, but their broadening decreases for the annealing temperature range of 200–500 °C. This also indicates an increase in the size of the crystallites, a decrease in the degree of their defectiveness, a decrease in the inhomogeneity of the composition, and an increase in the degree of crystallinity. For instance, the average size

Condensed Matter and Interphases / Конденсированные среды и межфазные границы   2023;25(1): 37–46

D. V. Ivashenko et al.   Synthesising dispersed powders of CoZn ferrites for microwave absorption
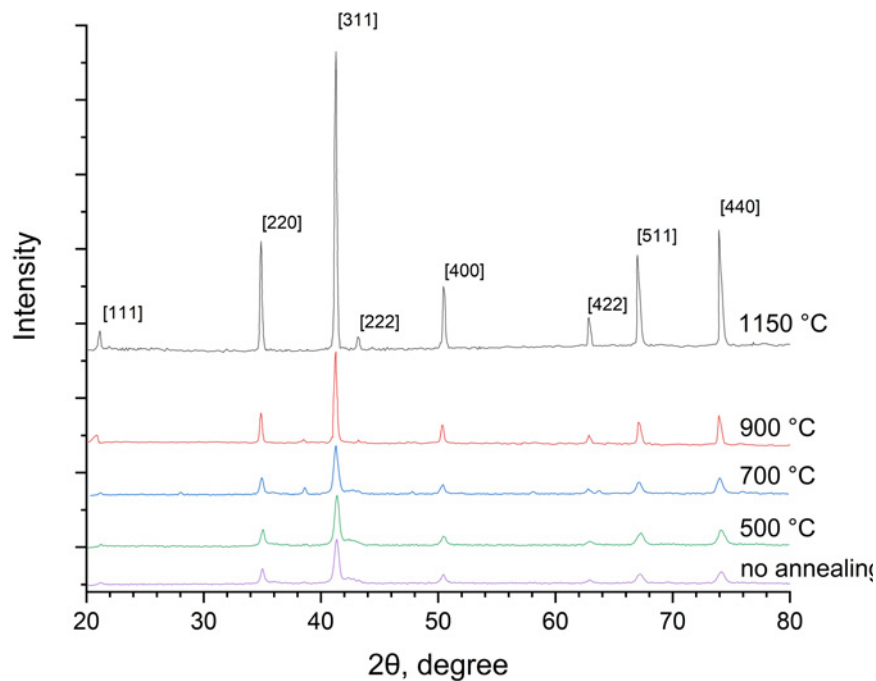
Fig. 1. X-ray diffraction patterns of the obtained powders

Table 1. Calculated and observed size of the crystallites

Annealing temperature, °C	Crystallite size by average peak, nm	Crystallite size by reflection (311), nm	Particle size (SEM), nm
0	20.8	20.6	–
500	20.6	21.0	40
700	23.5	21.3	80
900	63.8	59.4	150
1150	77.0	89.1	900

of crystallites for the CoZn ferrite obtained by the sol-gel method changed from 20 to 77 nm when annealed at 500 and 1150 °C. Some studies attribute such a growth of crystallites following an increase in the annealing temperature to the so-called Ostwald ripening effect [20, 21]. The analysis of the X-ray diffraction patterns demonstrated that when the temperature of annealing decreases after the synthesis, the background of the spectrum grows, and its reference line rises. This means that the particles are not fully crystallised and the fraction of the amorphous phase close to the crystal material increases. Obviously, this has a negative effect

on the magnetic properties of the samples, for instance, on the specific saturation magnetization [22]. The study demonstrated that the lattice constants of these samples varied from 8.401 to 8.420 Å. They were calculated for the cubic phase of the spinel. The calculated jump distance and the length of the bond for tetrahedral (A) and octahedral (B) nodes of the lattices of the studied samples are given in Table 2. We should note that the X-ray density of the obtained samples tends to decrease. This can be explained by the redistribution of cations in the sublattices and changes in the degree of crystallinity.

Fig. 2 presents SEM images of the powders annealed at various temperatures. The images of the microstructure demonstrate that the powders annealed at low temperatures consist of dispersed aggregated and agglomerated particles of a nearly spherical shape. When the temperature of annealing increases, we observe the formation of larger particles which are slightly faceted and agglomerated. The agglomeration of particles can be caused by magneto-dipole interaction decreasing with an increase in the annealing temperature and the growth of the particles. After annealing at 900 °C, the images of the powders showed that the particles increased in size and acquired an ellipsoid shape. When the

Condensed Matter and Interphases / Конденсированные среды и межфазные границы   2023;25(1): 37–46

D. V. Ivashenko et al.   Synthesising dispersed powders of CoZn ferrites for microwave absorption

Table 2. Calculation of the parameters of the crystal lattice

Annealing temperature, °C	Lattice constant a, Å	Jump length at tetrahedral lattice sites, Å	Jump length at octahedral lattice sites, Å	Radiographic density, g/cm³
0	8.401	3.64	2.97	5.30
500	8.401	3.64	2.97	5.30
700	8.412	3.64	2.97	5.29
900	8.416	3.64	2.98	5.28
1150	8.420	3.65	2.98	5.27
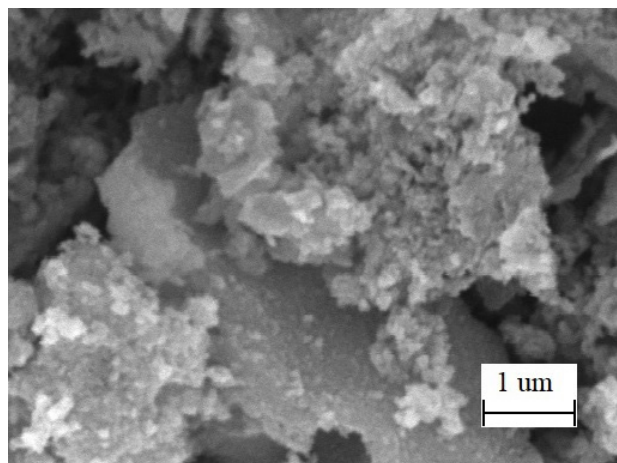
a
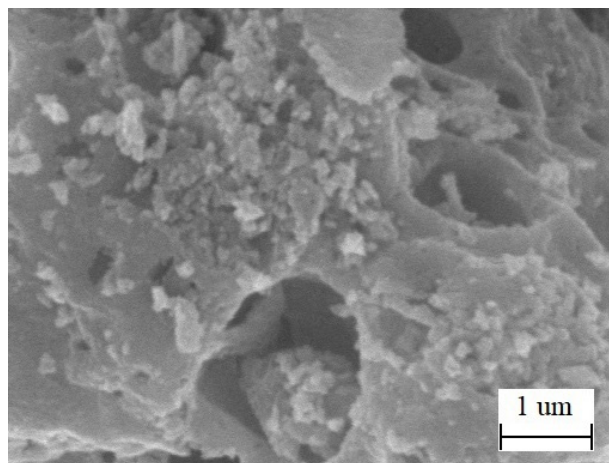
b
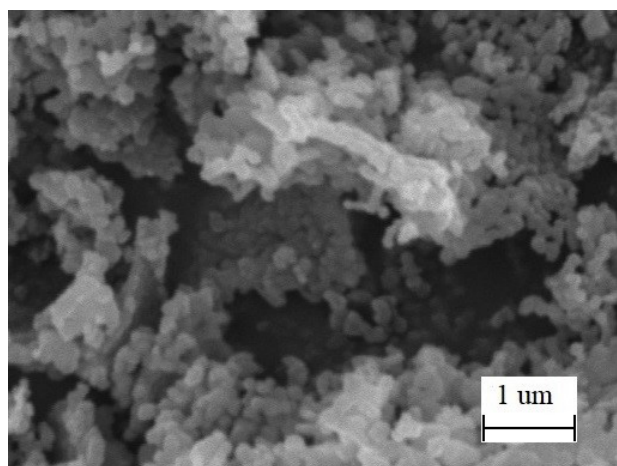
c
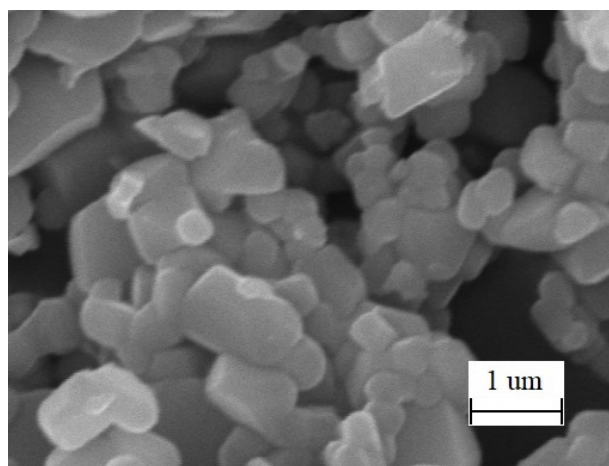
d

Fig. 2. SEM images of CoZn ferrite powders annealed at 500 °C (a), 700 °C (b), 900 °C (c), and 1150 °C (d)

annealing temperature was further increased to 1150 °C, the particles grew rapidly to 1 µm. The start of the crystallisation of the samples with tetrahedral faceting was observed. The growth of the particles, presumably, proceeds according to the Ostwald ripening mechanism. [20, 21].

Since the average size of the crystallites is about 30 nm, the particles annealed at

high temperatures include several separate crystallites. The number of crystallites in one particle decreases at lower annealing temperatures reaching 1. The samples annealed at lower temperatures have a morphology of irregular shape and are agglomerated.

To determine the ratio of metal ions in the synthesised CoZn ferrite, we performed energy

Condensed Matter and Interphases / Конденсированные среды и межфазные границы   2023;25(1): 37–46

D. V. Ivashenko et al.   Synthesising dispersed powders of CoZn ferrites for microwave absorption

dispersive X-ray spectroscopy of the sample annealed at 700 °C. The analysis determined that the amount of iron, cobalt, zinc, and oxygen corresponds to the formula $Co_{0.64}Zn_{0.35}Fe_{2.01}O_4$, which is in agreement with the target composition.

To determine the magnetic properties of the powders, we analysed the field dependences of the specific magnetization in the magnetic field $H = \pm 4$ T. Magnetization curves presented in Fig. 3 indicate the presence of the magnetic order in the analysed samples. Based on the changes in the specific magnetization of the particles of the Co-Zn ferrite depending on the strength of the external magnetic field, we can conclude that the magnetization curves of the samples annealed at 900 and 1150 °C reach the saturation region, when the strength of the magnetic field is over 3 T. This could mean that the type of the magnetic order is close to the ferrimagnetic. The study determined that the slope of the obtained curves and the saturation magnetization increase significantly following the growth of the annealing temperature. This can be interpreted as an indication of a significant decrease in the size of the inactive magnetic layer on the surface of the nanoparticles. Besides the noncollinearity of spins, this layer can also have a composition different from that of the nucleus of the particle because the process of

reciprocal diffusion of cations during the spinel synthesis is not complete. We can assume that disordering of cations and defectiveness can also take place in this layer. We should also remember the possibility that the formation of the spinel structure can be incomplete. This is indicated by broad reflections of the spinel phase on the X-ray diffraction patterns, which indicates the existence of different compositions of the material with different lattice constants. The existence of an amorphous material in this layer during certain synthesis stages is also possible.

Despite the fact that an increase in the annealing temperature (as determined for the sol-gel method) results in the growth of the specific magnetization of the CoZn ferrites, it does not reach the values characteristic for bulk samples, yet alone for single crystals (~98 $A \cdot m^2 \cdot kg^{-1}$) for $Co_{0.65}Zn_{0.35}Fe_2O_4$ [23]. This is also explained by the existence of the inactive magnetic layer on the surface of the nanoparticles, since a decrease in its fraction following an increase in the annealing temperature and a decrease in the surface area of the nanopowders during thermal treatment results in a significant increase in the saturation magnetization of the highly dispersed material.

As demonstrated by the study, a decrease in the size of the nanoparticles to several nanometres results in their transition to the
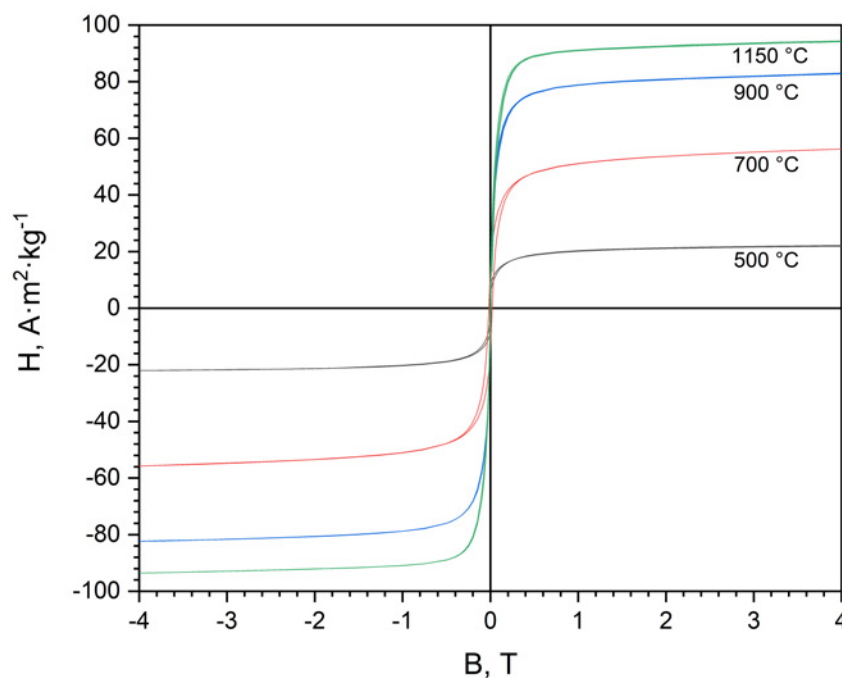
Fig. 3. Magnetization curves for the annealed CoZn ferrite powders

Condensed Matter and Interphases / Конденсированные среды и межфазные границы   2023;25(1): 37–46

D. V. Ivashenko et al.   Synthesising dispersed powders of CoZn ferrites for microwave absorption

superparamagnetic state due to the propagation of the magnetic dead layer over the whole particle. According to the literature data, the critical size of the cobalt ferrite nanoparticles for the transition to the superparamagnetic state lies within the range of up to 10 nm [24]. There is also a critical size value below which the particles become single-domain. If a ferrimagnetic particle has a domain structure, i.e. is multidomain, its remagnetization proceeds due to the displacement of the domain borders. In this case, the coercive force is low and grows with a decrease in the size of the particles. The coercive force is at maximum when the particles are single-domain. An increase in H_C during the transition to the single-domain structure is connected with a different remagnetization mechanism, namely the transition from the displacement of the borders to the coherent rotation of the magnetic order of the particle [25]. In our study, the coercive force of the powders annealed at 900 °C was 2.228 kA·m^{-1} and for the powders annealed at 1150 °C it was 3.167 kA·m^{-1}.

During the further decrease in the size of the nanoparticles following a transition from the multidomain to the single-domain state, superparamagnetism is observed. Thus, for the cobalt ferrite the critical size for the transition of the particles to the single-domain state is slightly below 50 nm [26]. Therefore, when the diameter of the particles decreases in the range from 50 to 10 nm the degree of superparamagnetism for cobalt ferrite nanopowders increases. In other words, we observe the so-called blocking process [27]. The main reason why the single-domain state has the greatest energetic advantage is the fact that with a decrease in the size of the particles, the fraction of the surface energy on the domain borders increases and becomes larger that the bulk energy of the sample. [25]. When the size of the particles in the single-domain state decreases, H_C decreases. This phenomenon is explained by the influence of thermal fluctuations on the magnetic anisotropy value, which in turn is connected with the coercive force. Superparamagnetism occurs in the surface layer of the nanoparticle when the energy barrier of the magnetic anisotropy is overcome due to the thermal activation, which results in fluctuations of the magnetization in

the surface layer [28]. The residual magnetization Mr and H_C in the superparamagnetic state is zero [29].

The study demonstrated that for the cobalt-zinc ferrite obtained by means of the sol-gel method the annealing following the synthesis changes the size of the crystallites from 20 to 77 nm. At the same time the size of the particles changes from 40 to 950 nm. Taking into account the fact that the critical value for the transition to the single-domain state is 50 nm, the analysed particles of the cobalt-zinc ferrite with the size smaller than 50 nm have a certain degree of seperparamagnetism. This is true for the annealing temperatures below 700 °C.

As we mentioned before, the highest values of the coercive force correspond to the transition boundary between the multidomain and single-domain particles. With a decrease in the size, the coercive force decreases in the superparamagnetic area or in the blocking area. It is zero for superparamagnetic particles. In the latter case, the hysteresis disappears. Thus, for the annealing temperatures of 500 and 700 °C the coercive force of the studied powders was 2.992 kA·m^{-1} and 15.199 kA·m^{-1} respectively.

For lower annealing temperatures and small sizes of the crystallites we observed prominent superparamagnetic behaviour of the samples at room temperature. This indicates the presence of an abnormally large coercive force for the powder annealed at 700 °C (Table 3). This can be explained by the fact that the obtained materials are on the border between multidomain and single-domain states, when the coercive force reaches its maximum. For higher annealing temperatures, when the particles are larger, the hysteresis curves demonstrate a prominent coercive force, which indicates the presence of only an insignificant degree of superparamagnetism.

Table 3. Magnetic properties of the obtained powders

Annealing temperature, °C	Saturation magnetization, A·m^2·kg^{-1}	Coercive force, kA·m^{-1}
500	21.8	2.992
700	56.1	15.199
900	83.0	2.228
1150	94.1	3.167

Condensed Matter and Interphases / Конденсированные среды и межфазные границы   2023;25(1): 37–46

D. V. Ivashenko et al.   Synthesising dispersed powders of CoZn ferrites for microwave absorption

In this case, only a small number of particles of the size smaller than critical transit to the superparamagnetic state. This is important for obtaining the materials sensitive to microwave radiation.

For the obtained powders of the Co-Zn ferrite the specific magnetization in the 4 T field for the annealing temperatures of 900 and 1150 °C was above 80 A·m^2·kg^{-1}. The size of the particles was 150 and 950 nm respectively. A different situation was observed, when the size of the particles was significantly smaller and therefore they had a larger surface-volume ratio. In this case, several effects including the broken bonds between the atoms on the surface resulting in the random spin orientation reduce the coordination of the surface atoms and result in a decrease in the magnetiszation due to an increase in the surface anisotropy. Thus, the study demonstrated that for the particles of the Co-Zn ferrite of an average size of 40 nm the specific saturation magnetisation is 21.8 A·m^2·kg^{-1}, and for the 80 nm particles the specific saturation magnetisation is 56.1 A·m^2·kg^{-1}.

4. Conclusions

The study determined that for highly dispersed particles with a changed magnetic order and crystal structure on the surface, an inactive magnetic layer is formed. The size of the layer can reach up to 50 % of the volume of the particles. [30]. This has a negative effect on the magnetisation of the nanoparticles. Taking into account the above described facts, when developing dispersed particles which could be used as fillers for the devices interacting with microwave radiation, it is advisable to maintain the balance between high magnetic characteristics and the acceptable degree of dispersion of the particles. From the point of view of sol-gel synthesis, the obtained dependences of magnetic properties and the degree of dispersion on the thermal treatment temperature of the synthesised powders can be used to determine optimal conditions. Based on this dependence we suggested a material for absorption of microwave radiation based on the dispersed powder of the CoZn ferrite annealed at 900 °C after the sol-gel synthesis.

Contribution of the authors

The authors contributed equally to this article.

Conflict of interests

The authors declare that they have no known competing financial interests or personal relationships that could have influenced the work reported in this paper.

References

1. Houbi A., Aldashevich Z. A., Atassi Y., Telmanovna Z. B., Saule M., Kubanych K. Microwave absorbing properties of ferrites and their composites: A review. *Journal of Magnetism and Magnetic Materials*. 2021;529: 167839. https://doi.org/10.1016/j.jmmm.2021.167839

2. Yin P., Zhang L., Feng X., Wang J., Dai J., Tang Y. Recent progress in ferrite microwave absorbing composites. *Integrated Ferroelectrics*. 2020;211(1): 82–101. https://doi.org/10.1080/10584587.2020.1803677

3. Kodama R. H., Berkowitz A. E., McNiff Jr E. J., Foner S. Surface spin disorder in ferrite nanoparticles. *Journal of Applied Physics*. 1997;81(8): 5552–5557. https://doi.org/10.1063/1.364659

4. Thakur P., Taneja S., Chahar D., Ravelo B., Thakur A. Recent advances on synthesis, characterization and high frequency applications of Ni-Zn ferrite nanoparticles. *Journal of Magnetism and Magnetic Materials*. 2021;530: 167925. https://doi.org/10.1016/j.jmmm.2021.167925

5. Martinez B., Obradors X., Balcells L., Rouanet A., Monty C.. Low temperature surface spin-glass transition in γ-Fe$_2$O$_3$ nanoparticles. *Physical Review Letters*. 1998;80(1): 181. https://doi.org/10.1103/PhysRevLett.80.181

6. Leite E. S., Coaquira J. A., Viali W. R., Sartoratto P. P., De Almeida R. L., Morais P. C., Malik S. K. Spin-glass-like characteristics of extremely small γ-Fe$_2$O$_3$ nanoparticles. Journal of Physics: Conference Series. 2010;200(7): 072060. https://doi.org/10.1088/1742-6596/200/7/072060

7. El-Sayed H. M., Ali I. A., Azzam A., Sattar A. A. Influence of the magnetic dead layer thickness of Mg-Zn ferrites nanoparticle on their magnetic properties. *Journal of Magnetism and Magnetic Materials*. 2017;424: 226–232. https://doi.org/10.1016/j.jmmm.2016.10.049

8. Khah F. M., Arab A., Kiani E. The effect of thickness of the dead layer on the magnetization of Ni$_{0.5-x}$Co$_x$Zn$_{0.5}$Fe$_2$O$_4$ ferrite nanopowders and determination of optimal permeability. *Journal of Superconductivity and Novel Magnetism*. 2021;34: 2699–708. https://doi.org/10.1007/s10948-021-05976-x

9. Singh J. P., Dixit G., Srivastava R. C., Agrawal H. M., Reddy V. R., Gupta A. Observation of bulk like magnetic ordering below the blocking temperature in

Condensed Matter and Interphases / Конденсированные среды и межфазные границы   2023;25(1): 37–46

D. V. Ivashenko et al.   Synthesising dispersed powders of CoZn ferrites for microwave absorption

nanosized zinc ferrite. *Journal of magnetism and magnetic materials*. 2012;324(16): 2553–2559. https://doi.org/10.1016/j.jmmm.2012.03.045

10. Meidanchi A., Ansari H. Copper spinel ferrite superparamagnetic nanoparticles as a novel radiotherapy enhancer effect in cancer treatment. *Journal of Cluster Science*. 2021;32: 657–663. https://doi.org/10.1007/s10876-020-01832-5

11. Sharma R., Thakur P., Sharma P., Sharma V. Ferrimagnetic Ni^{2+} doped Mg-Zn spinel ferrite nanoparticles for high density information storage. *Journal of Alloys and Compounds*. 2017;704: 7–17. https://doi.org/10.1016/j.jallcom.2017.02.021

12. Harasawa T., Suzuki R., Shimizu O., Olcer S., Eleftheriou E. Barium-ferrite particulate media for high-recording-density tape storage systems. *IEEE transactions on magnetics*. 2010;46(6): 1894–1897. https://doi.org/10.1109/TMAG.2010.2042286

13. Nasrin S., Hoque S. M., Chowdhury F. U., Hossen M. M. Influence of Zn substitution on the structural and magnetic properties of $Co_{1-x}Zn_xFe_2O_4$ nano-ferrites. *IOSR Journal of Applied Physics*. 2014;6(2): 58–65. https://doi.org/10.9790/4861-06235865

14. Vinosha P. A., Manikandan A., Ceicilia A. S., Dinesh A., Nirmala G. F., Preetha A. C., Slimani Y., Almessiere M. A., Baykal A., Xavier B. Review on recent advances of zinc substituted cobalt ferrite nanoparticles: Synthesis characterization and diverse applications. *Ceramics International*. 2021;47(8): 10512–10535. https://doi.org/10.1016/j.ceramint.2020.12.289

15. Kaur P., Chawla S. K., Meena S. S., Yusuf S. M., Pubby K., Narang S. B. Modulation of physico-chemical, magnetic, microwave and electromagnetic properties of nanocrystalline strontium hexaferrite by Co-Zr doping synthesized using citrate precursor sol-gel method. *Ceramics International*. 2017;43(1): 590–598. https://doi.org/10.1016/j.ceramint.2016.09.199

16. Sajjia M., Oubaha M., Hasanuzzaman M., Olabi A. G. Developments of cobalt ferrite nanoparticles prepared by the sol–gel process. *Ceramics International*. 2014;40(1): 1147–1154. https://doi.org/10.1016/j.ceramint.2013.06.116

17. Sutka A., Mezinskis G. Sol-gel auto-combustion synthesis of spinel-type ferrite nanomaterials. *Frontiers of Materials Science*. 2012;6(2): 128–141. https://doi.org/10.1007/s11706-012-0167-3

18. Ashour A. H., El-Batal A. I., Maksoud M. A., El-Sayyad G. S., Labib S. H., Abdeltwab E., El-Okr M. M. Antimicrobial activity of metal-substituted cobalt ferrite nanoparticles synthesized by sol–gel technique. *Particuology*. 2018;40: 141–151. https://doi.org/10.1016/j.partic.2017.12.001

19. Karimi Z., Mohammadifar Y., Shokrollahi H., Asl S. K., Yousefi G., Karimi L. Magnetic and structural properties of nano sized Dy-doped cobalt ferrite

synthesized by co-precipitation. *Journal of Magnetism and Magnetic Materials*. 2014;361: 150–156. https://doi.org/10.1016/j.jmmm.2014.01.016

20. Shahbahrami B., Rabiee S. M., Shidpour R., Salimi-Kenari H. Influence of calcination parameters on the microstructure, magnetic and hyperthermia properties of Zn-Co ferrite nanoparticles. *Journal of Electroceramics*. 2022;48: 157–168. https://doi.org/10.1007/s10832-022-00281-y

21. Sakurai S., Nishino H, Futaba DN, Yasuda S, Yamada T, Maigne A, Matsuo Y, Nakamura E, Yumura M., Hata K. Role of subsurface diffusion and Ostwald ripening in catalyst formation for single-walled carbon nanotube forest growth. *Journal of the American Chemical Society*. 2012;134(4): 2148–2153. https://doi.org/10.1021/ja208706c

22. Rafeeq S. N., Ismail M. M., Sulaiman J. M. Magnetic and dielectric properties of $CoFe_2O_4$ and $Co_xZn_{1-x}Fe_2O_4$ nanoparticles synthesized using sol-gel method. *Journal of Magnetics*. 2017;22(3): 406–413. https://doi.org/10.4283/JMAG.2017.22.3.406

23. *Tables of physical quantities*. I. K. Kikoin (ed.). Moscow: Atomizdat Publ.; 1976. 1006 p. (In Russ.)

24. Karaagac O., Yildiz B. B., Köçkar H. The influence of synthesis parameters on one-step synthesized superparamagnetic cobalt ferrite nanoparticles with high saturation magnetization. *Journal of Magnetism and Magnetic Materials*. 2019;473: 262–267. https://doi.org/10.1016/j.jmmm.2018.10.063

25. Frolov G. I., Bachina O. I., Zav'yalova M. M., Ravochkin S. I. Magnetic properties of nanoparticles of 3*d* metals. *Technical Physics*. 2008;53(8): 1059–1064. https://doi.org/10.1134/s1063784208080136

26. Chinnasamy C. N., Jeyadevan B., Shinoda K., Tohji K., Djayaprawira D. J., Takahashi M., Joseyphus R. J., Narayanasamy A. Unusually high coercivity and critical single-domain size of nearly monodispersed $CoFe_2O_4$ nanoparticles. *Applied Physics Letters*. 2003;83(14): 2862–2864. https://doi.org/10.1063/1.1616655

27. Rao K. S., Nayakulu S. R., Varma M. C., Choudary G. S., Rao K. H. Controlled phase evolution and the occurrence of single domain $CoFe_2O_4$ nanoparticles synthesized by PVA assisted sol-gel method. *Journal of Magnetism and Magnetic Materials*. 2018;451: 602–608. https://doi.org/10.1016/j.jmmm.2017.11.069

28. Khader S. A., Sankarappa T. Dielectric, magnetic and ferroelectric studies in $(x)Mn_{0.5}Zn_{0.5}Fe_2O_4 + (1-x)$ $BaTiO_3$ magnetoelectric nano-composites. *Materials Today: Proceedings*. 2016;3(6): 2358–2365. https://doi.org/10.1016/j.matpr.2016.04.148

29. Saffari F., Kameli P., Rahimi M., Ahmadvand H., Salamati H. Effects of Co-substitution on the structural and magnetic properties of $NiCo_xFe_{2-x}O_4$ ferrite nanoparticles. *Ceramics International*. 2015;41(6):

Condensed Matter and Interphases / Конденсированные среды и межфазные границы   2023;25(1): 37–46

D. V. Ivashenko et al.   Synthesising dispersed powders of CoZn ferrites for microwave absorption

7352–7358. https://doi.org/10.1016/j.ceramint.2015.02.038

30. Negi D. S., Sharona H., Bhat U., Palchoudhury S., Gupta A., Datta R. Surface spin canting in Fe_3O_4 and $CoFe_2O_4$ nanoparticles probed by high-resolution electron energy loss spectroscopy. *Physical Review B.* 201730;95(17): 174444. https://doi.org/10.1103/PhysRevB.95.174444

* Translated by author of the article.

Information about the authors

Dmitry V. Ivashenko, M. S. (Chemistry), Belarusian State University (Minsk, Belarus).

https://orcid.org/0000-0002-9149-7213

ivashenkodm@gmail.com

Diana A. Urbanovich, Belarusian State University (Minsk, Belarus).

https://orcid.org/0000-0002-5452-0277

urbanovichd00@gmail.com

Ilya Y. Palyn, Belarusian State University (Minsk, Belarus).

https://orcid.org/0000-0002-1542-8427

iliapolyn@gmail.com

Maxim V. Bushinsky, Cand. Sci. (Phys.–Math.), Head of the Laboratory of Non-metallic Ferromagnets SSPA "Scientific-Practical Materials Research Centre of National Academy of Sciences of Belarus" (Minsk, Belarus).

https://orcid.org/0000-0002-7234-6866

bushinsky@physics.by

Alexey V. Trukhanov, Dr. Sci. (Phys.–Math.), Deputy General Director for Research and Innovation SSPA "Scientific-Practical Materials Research Centre of National Academy of Sciences of Belarus" (Minsk, Belarus).

https://orcid.org/0000-0002-4387-8214

truhanov86@mail.ru

Vladimir V. Pankov, Dr. Sci. (Chem.), Professor at Department of Physical Chemistry, Belarusian State University (Minsk, Belarus). https://orcid.org/0000-0001-5478-0194

pankov@bsu.by

Translated by Yulia Dymant
Edited and proofread by Simon Cox
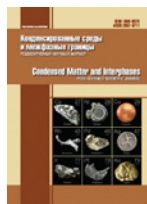
Condensed Matter and Interphases

Original articles

Phase equilibria in the Cu₂SnSe₃–Sb₂Se₃–Se system

E. N. Ismayilova✉, L. F. Mashadiyeva, I. B. Bakhtiyarly, M. B. Babanly

*Institute of Catalysis and Inorganic Chemistry n.a. M. Nagiyev of the Azerbaijan National Academy of Sciences,
113 H. Javid av., Baku Az1143, Azerbaijan*

Abstract

Complex copper-tin and copper-antimony chalcogenides are of great interest for the development of new environmentally friendly and inexpensive thermoelectric materials. Recently, these compounds have been drawing more interest due to the possibility of increasing their thermoelectric performance with various cationic and anionic substitutions. In this article, we continued the study of multi-component systems based on the copper chalcogenides and presented the results of the study of phase equilibria in the Cu_2SnSe_3–Sb_2Se_3–Se system. The study was conducted using differential thermal analysis and powder X-ray diffraction.

Based on the experimental data, a projection of the liquidus surface and three polythermal cross sections of the phase diagram were plotted. We determined the regions of primary crystallisation of the phases and the nature and temperatures of non-variant and monovariant equilibria.

It was established that the liquidus surface consisted of two primary crystallisation regions based on Cu_2SnSe_3 and Sb_2Se_3 phases. The primary crystallisation region of elementary selenium was degenerate. A large immiscibility region of two liquid phases was found in the system.

Keywords: Phase diagram, Liquidus surface, Copper-antimony-tin selenides

✉ Elnara N. Ismailova, e-mail: ismayilova818@mail.ru

Condensed Matter and Interphases / Конденсированные среды и межфазные границы   2023;25(1): 47–54

E. N. Ismayilova et al.   Phase equilibria in the Cu₂SnSe₃–Sb₂Se₃–Se system

1. Introduction

Copper-tin and copper-antimony chalcogenides form good basic phases for the development of materials with different functional properties [1–5]. Many of these phases are synthetic analogues of natural copper chalcogenide minerals, such as tetrahedrite, colusite, famatinite, etc., and they are of great interest for the development of new environmentally friendly and inexpensive thermoelectric materials. Studies showed that some of them demonstrated highly effective thermoelectric properties in the medium temperature range (600÷800 K), and their presence was primarily due to the specific features of the crystal structure [6-10]. Recently, these compounds have been garnering more interest due to the possibility of increasing their thermoelectric performance with various cationic and anionic substitutions [11–22]. Moreover, these substitutions can be both homovalent and heterovalent. For instance, in [16–22] it was shown that Sn-containing famatinites $Cu_3Sb_{1-x}Sn_xS_4$ and tetrahedrites $Cu_{12-x}Sn_xSb_4S_{13}$ could be obtained where heterovalent substitution of Sb^{5+} for Sn^{4+} resulted in the increased thermoelectric performance.

It is known that we need reliable data on the phase equilibria of the corresponding systems in order to determine the conditions for the directed synthesis of compounds and nonstoichiometric phases based on them, as well as to grow single crystals [23, 24]. In some previous works [25-28], we conducted similar comprehensive studies of complex systems based on copper and silver chalcogenides, in which we found new phases of variable compositions.

In [29, 30] we studied Cu_3SbSe_4–$SnSe_2(GeSe_2)$ systems in order to discover new phases of variable compositions based on the selenide analogue of the famatinite mineral. It was found that the solubility based on Cu_3SbSe_4 was up to 20 mol %. In the regions with lower content of Cu_3SbSe_4 phase equilibria had a complex nature. According to [29], it was associated with the stability of the Cu_2GeSe_3–Sb_2Se_3–Se concentration triangle, which led to a formation of four-phase regions in the Cu_2Se–$GeSe_2$–Sb_2Se_3–Se tetrahedron: Cu_3SbSe_4+Cu_2GeSe_3+Sb_2Se_3+Se и Cu_2GeSe_3+Sb_2Se_3+$GeSe_2$+Se. A similar situation is observed in the Cu_3SbSe_4-$SnSe_2$ system [30].

The goal of the present work was to determine the nature of phase equilibria in the Cu_2SnSe_3-Sb_2Se_3-Se concentration triangle, which play a decisive role in the formation of the complete picture of phase equilibria in the Cu_2Se-$SnSe_2$-Sb_2Se_3-Se subsystem. In previous works [31-35], other independent subsystems Cu_2Se-$SnSe$-Sb_2Se_3 and Cu_2Se-$SnSe_2$-Sb_2Se_3 of the Cu-Sn-Sb-Se quaternary system were studied, and a number of polythermal and isothermal sections as well as a projection of the liquidus surface were plotted.

1.1. Starting compounds

The starting compound Sb_2Se_3 of the studied system melts congruently at 863 K and forms a degenerate eutectic with selenium at 493 K [36]. Antimony selenide Sb_2Se_3 crystallises in the orthorhombic lattice (space group *Pnma*): a = 11.7938(9) Å, b = 3.9858(6) Å, and c = 11.6478(7) Å, z = 4 [37].

Cu_2SnSe_3 compound melts congruently at 968 K has a polymorphic transition at 948 K [38, 39]. The high-temperature modification crystallises in a cubic structure with the parameter of the lattice a = 5.6877 Å [38, 40], while the low-temperature modification crystallises in the monoclinic structure (space group *Cc*) with the parameters of the unit cell a = 6.9670±3 Å, b = 12.0493±7 Å, c = 6.9453±3 Å, β = 109.19(1)°; z = 4 [41, 42]. This compound forms a state diagram of the eutectic type with the Sb_2Se_3 compound with insignificant mutual solubility (not more than 2%) of the initial components. The coordinates of the eutectic point were 72 mol % Sb_2Se_3 and 769 K [31]. The Cu_2SnSe_3–6Se boundary system forms a *T-x* diagram with a degenerate eutectic equilibrium at 493 K and a wide region of immiscibility (37–95 mol % Se) at 910 K [39].

2. Experimental

2.1. Synthesis

Simple high-purity substances by Evochem Advanced Materials GMBH (Germany) were used for the experiments: copper granules (Cu-00029; 99.9999%), antimony granules (Sb-00002; 99.999%), tin granules (Sn-00005; 99.999%), and selenium granules (Se-00002; 99.999%). Starting compounds Cu_2SnSe_3 and Sb_2Se_3 were synthesised by melting simple substances in stoichiometric proportions in vacuumed to ~10^{-2} Pa and

Condensed Matter and Interphases / Конденсированные среды и межфазные границы   2023;25(1): 47–54

E. N. Ismayilova et al.   Phase equilibria in the Cu$_2$SnSe$_3$–Sb$_2$Se$_3$–Se system

sealed quartz ampoules at temperatures 50° higher than the melting temperatures of the synthesised compounds. The Cu$_2$SnSe$_3$ compound was synthesised in a two-zone sloping furnace. The temperature of the lower "hot" zone was 1050 K, and the temperature of the upper "cold" zone was 900 K, which is slightly lower than the boiling point of selenium (958 K [43]). After the overall reaction of selenium, the ampoule with a sample was placed completely into the hot zone of the furnace and kept at this temperature for 3–4 hours. After the synthesis, the ampoule with Cu$_2$SnSe$_3$ was cooled to room temperature in the switched-off furnace.

The individuality of the synthesised compounds Cu$_2$SnSe$_3$ and Sb$_2$Se$_3$ was controlled using differential thermal analysis (DTA) and powder X-ray diffraction (XRD). The obtained melting point values and parameters of crystal lattices of all synthesised compounds within the measure of inaccuracy (±3 K and ±0.0003 Å) were similar to the above mentioned literature data.

Approximately 30 alloys were prepared in accordance with the studied sections together with additional alloys in order to conduct the experiments through melting the initial compounds in vacuum. The DTA data for cast non-homogenised alloys showed that their crystallisation from melts was completed at ~490 K. Therefore, the cast alloys obtained by quick cooling of melts were first annealed at 650 K for 200 hours, and then at 450 K for 300 hours. This was done in order to achieve the state as similar to the equilibrium as possible.

2.2. Research methods

DTA was conducted in the range of temperatures from room temperature to 1100 K with a heating rate of 10 K·min^{-1} on a 404 F1 PEGASUS SYSTEM differential scanning calorimeter (NETZSCH). The measurement results were processed using the NETZSCH Proteus Software. The temperature measurement accuracy was within ±2 K.

X-ray phase analysis was performed at room temperature on a D8 ADVANCE diffractometer (BRUKER) with Cu$K\alpha_1$ radiation. The XRD patterns were indexed using Topas V3.0 Software Bruker.

3. Results and discussion

XRD of the selected alloys showed that they consisted of a three-phase mixture Cu$_2$SnSe$_3$+Sb$_2$Se$_3$+Se. A powder diffraction pattern of the alloy of the 1/6Cu$_2$SnSe$_3$-1/5Sb$_2$Se$_3$-Se system with the 4:4:2 ratio of the initial components, respectively, is presented in Fig. 1 as an example. It can be seen that the diffraction pattern of the alloy consists of a set of reflection lines of Cu$_2$SnSe$_3$, Sb$_2$Se$_3$, and grey crystalline selenium.
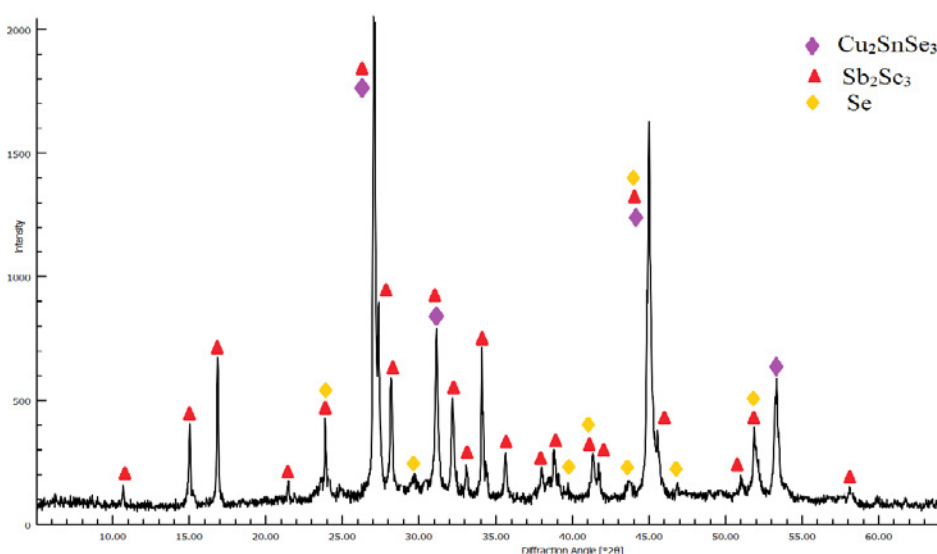
Fig. 1. Powder diffraction pattern of the alloy of the 1/6Cu$_2$SnSe$_3$–1/5Sb$_2$Se$_3$–Se system with the 4:4:2 ratio of the initial components, respectively

Condensed Matter and Interphases / Конденсированные среды и межфазные границы   2023;25(1): 47–54

E. N. Ismayilova et al.   Phase equilibria in the Cu$_2$SnSe$_3$–Sb$_2$Se$_3$–Se system

3.1. Liquidus surface

The liquidus surface of the Cu$_2$SnSe$_3$-Sb$_2$Se$_3$-Se system (Fig. 2) consists of two main and one degenerate sections. Region 1 corresponds to primary crystallisation of α_1 and α_2 phases based on two crystalline modifications of Cu$_2$SnSe$_3$, while region 2 corresponds to primary crystallisation of β-solid solutions based on Sb$_2$Se$_3$. The third region corresponds to elemental selenium and was degenerate in the corresponding angle of the concentration triangle.

A typical feature of the system is that the immiscibility region existing on the side
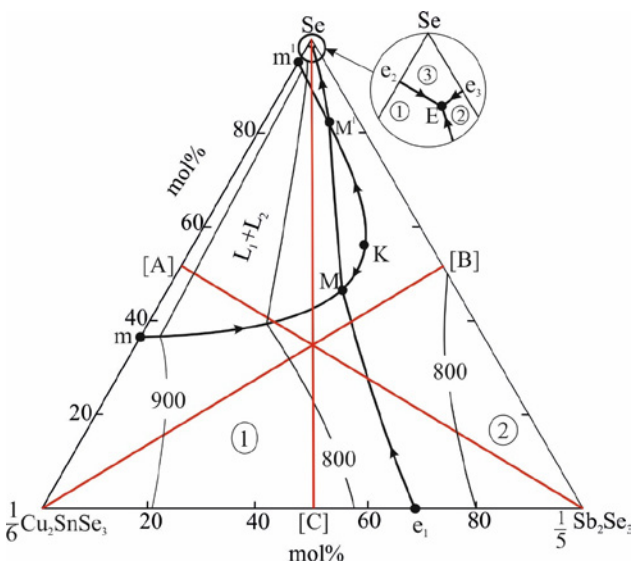
Fig. 2. Liquidus surface of the Cu$_2$SnSe$_3$–Sb$_2$Se$_3$–Se system. Primary crystallisation fields: *1* – α (solid solution based on Cu$_2$SnSe$_3$); *2* – β (solid solution based on Sb$_2$Se$_3$); *3* – Se. Red lines are the studied polythermal sections

quasi-binary section of Cu$_2$SnSe$_3$–Se (contour mm^1 at 910 K) suddenly penetrates inside the triangle forming a wide region (mMKM^{1}m^1) of immiscibility of two liquid phases (L$_1$+L$_2$). As Fig. 2 shows, this region crosses the curve coming out from the eutectic point (e$_1$) of the Cu$_2$SnSe$_3$–Sb$_2$Se$_3$ system and takes a part of the liquidus surface of β-phase (MKM^1). In the MM^1 interval the eutectic curve crosses the immiscibility region, and the eutectic equilibrium L ↔ α+β turns into a non-variant monotectic equilibrium L ↔ L$_2$+α+β.

All non-variant and monovariant phase equilibria observed in the system, including side systems, are presented in Table 1. Fig. 2 and Table 1 show that the conjugated curves mM и mM^1 limiting the immiscibility region reflect the process of crystallisation of α-phase while the conjugated curves MK and KM^1 reflect the monovariant crystallisation of β-phase upon monotectic reactions.

The process of crystallisation in the system completes with the formation of a triple eutectic mixture α$_2$+β+Se (E; 490 K). Eutectic points e$_2$ and e$_3$ on boundary quasi-binary systems as well as point E and eutectic curves e$_2$E и e$_3$E are degenerate. This part of the phase diagram is presented in Fig. 2 as an enlarged view (representative scale).

3.2. Polythermal sections

We will consider three polythermal sections of the phase diagram perpendicular to side systems in the context of Fig. 2 and Table 1 to obtain a better visual description of the crystallisation processes in the system, especially those

Table 1. Non-variant and monovariant phase equilibria in the Cu$_2$SnSe$_3$–Sb$_2$Se$_3$–Se system

Point or curve in fig. 2	Equilibrium	Composition, mol %		T, K
		0,2Sb$_2$Se$_3$	Se	
m(m^1)	L$_1$ ↔ L$_2$+α	-	36(95)	910
e$_1$	L ↔ α+β	68	-	769
e$_2$	L ↔ α+Se	-	>99	493
e$_3$	L ↔ β+Se	<1	>99	491
M(M^1)	L$_1$ ↔ L$_2$+α+β	35(13)	45(82)	730
E	L ↔ α+β+Se	<1	>98	490
e$_1$M	L$_1$ ↔ α+β			769-730
M^{1}E	L$_2$ ↔ α+β			730-490
e$_2$E	L ↔ α+Se			493-490
e$_3$E	L ↔ α+Se			491-490
mM(m^{1}M^1)	L$_1$ ↔ L$_2$+α			910-730
KM(KM^1)	L$_1$ ↔ L$_2$+β			750-730

Condensed Matter and Interphases / Конденсированные среды и межфазные границы   2023;25(1): 47–54

E. N. Ismayilova et al.   Phase equilibria in the Cu₂SnSe₃–Sb₂Se₃–Se system

Fig. 3. Phase diagram of the [A]-0.2Sb₂Se₃ system. [A] – alloy of the Cu₂SnSe₃–6Se system with the composition 1:1

Fig. 4. Phase diagram of the [B]–1.6Cu₂SnSe₃ system. [B] – alloy of the 1/5Sb₂Se₃–Se side system with the composition 1:1

below the liquidus surface and the region of immiscibility.

Section [A]–0,2 Sb₂Se₃ (where [A] is an alloy of the Cu₂SnSe₃–6Se side system corresponding to the composition 1:1). This section crosses the region of immiscibility and the liquidus surface of α and β phases (Fig. 3). The two-phase region $L_1 + L_2$ is limited by the region of L-liquid solution with a dotted line. The curves below the regions L_1+L_2, $L+\alpha$ and $L+\beta$ reflect the monovariant mM (m^1M^1) monotectic (0–28 mol % 0.2Sb₂Se₃) and eutectic e_1M (28–99 mol % 0.2Sb₂Se₃) equilibria. As a result of these processes, three-phase regions $L_1+L_2+\alpha$ и $L_1+\alpha+\beta$ are formed in Fig. 3.

At 730 K, the non-variant monotectic equilibrium M is implemented in the system, and this reaction is completed with the formation of a three-phase region $L_2+\alpha+\beta$. Finally, the horizontal line corresponding to 490 K represents the crystallisation of the ternary eutectic (E).

Section 1/6Cu₂SnSe₃–[B] (Fig. 4) (where [B] is an alloy of the 1/5Sb₂Se₃-Se side system corresponding to the composition 1:1). This section does not pass through the immiscibility region. The liquidus consists of 3 curves of primary crystallisation of two modifications of Cu₂SnSe₃ (α_1 and α_2 phases) and β-phase based on Sb₂Se₃. The formation of solid solutions based on two modifications Cu₂SnSe₃ is accompanied by the lowered temperature of the polymorphic transition of this compound and establishment of a monovariant metatectic reaction $\alpha_1 \leftrightarrow L+\alpha_2$.

The corresponding three-phase region is located in a very narrow range of temperatures and is separated by a dotted line. This part of the phase diagram is presented in Fig. 2 as an enlarged view (representative scale). The comparison of this diagram with Fig. 3 shows that the curves below liquidus also reflect monotectic equilibria. In the range of compositions 0–30; 30–80 and 80–95 mol % [B] monovariant reactions process according to mM, e_1M, and KM, which leads to the formation of regions ($L_1+L_2+\alpha$), ($L_1+\alpha+\beta$), and ($L_1+L_2+\beta$) in Fig. 4. With lower temperatures, crystallisation continues in accordance with non-variant monotectic reaction M (730 K) and ends with a non-variant eutectic process E (490 K).

Section [C]–Se (Fig. 5) (where [C] is an alloy of the 1/6Cu₂SnSe₃–1/5Sb₂Se₃ side system corresponding to the composition 1:1). This section is almost completely located in the region of primary crystallisation of the α-phase, and in the concentration range of 40–90 at. % Se (el.) it passes through the region of immiscibility of two liquids. In the range of compositions of 0-40 at. % Se (el.) α-phase crystallises from the liquid phase L_1 based on selenides, while in the range of >90 at. % Se (el.) crystallises from the liquid phase L_2 based on selenium. Monovariant and non-variant processes occurring below liquidus can be easily determined in the context of Fig. 2.

Condensed Matter and Interphases / Конденсированные среды и межфазные границы   2023;25(1): 47–54

E. N. Ismayilova et al.   Phase equilibria in the Cu₂SnSe₃–Sb₂Se₃–Se system
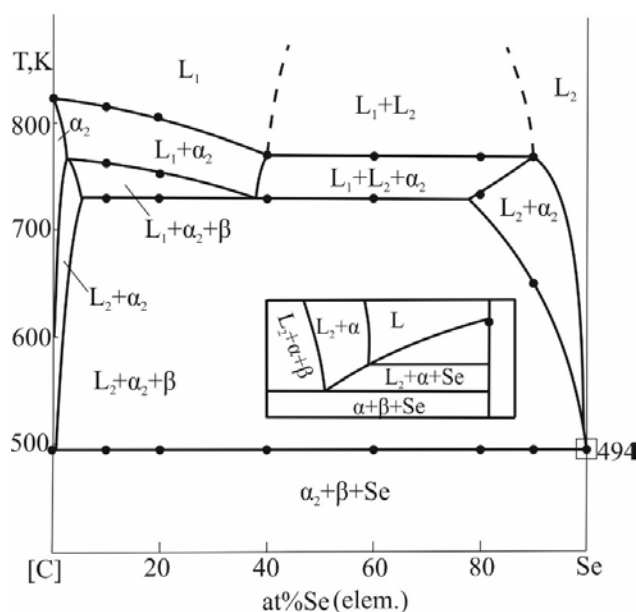
Fig. 5. Phase diagram of the [C]–Se system. [C] – alloy of the $1/6Cu_2SnSe_3–1/5Sb_2Se_3$ side system corresponding to the composition 1:1

4. Conclusions

Thus we obtained the complete picture of phase equilibria in the Cu_2SnSe_3-Sb_2Se_3-Se system. It was established that it is a quasiternary plane corresponding to the quaternary system. The liquidus surface consisted of three primary crystallisation fields α and β of solid solutions based on Cu_2SnSe_3 и Sb_2Se_3, respectively, as well as of elemental selenium. The region of crystallisation of elemental selenium was degenerate in the corresponding angle of the concentration triangle. A formation of a wide region of immiscibility permeating from the Cu_2SnSe_3–Se side system inside the Cu_2SnSe_3–Sb_2Se_3-Se concentration triangle was a typical feature of the studied system.

Author contributions

E. N. Ismayilova – research concept, conducting research, synthesis of compounds, article writing, discussion of results. L. F. Mashadiyeva – analysis of scientific literature, discussion of results. I. B. Bakhtiyarly – discussion of results. M. B. Babanly – research concept, final conclusions.

Conflict of interests

The authors declare that they have no known competing financial interests or personal relationships that could have influenced the work reported in this paper.

References

1. Alonso-Vante N. *Chalcogenide materials for energy conversion. Pathways to oxygen and hydrogen reactions*. Springer Cham; 2018. 226 p. https://doi.org/10.1007/978-3-319-89612-0

2. *Applications of Chalcogenides: S, Se, and Te.* Ahluwalia G. K. (ed.). Cham. Springer, 2016. 461 p. https://doi.org/10.1007/978-3-319-41190-3

3. *Chalcogenides: Advances in research and applications*. Nova P. W. (ed.). 2018. 111 p.

4. Peccerillo E., Durose K. Copper–antimony and copper–bismuth chalcogenides—Research opportunities and review for solar photovoltaics. *MRS Energy & Sustainability*. 2018;5(1): 1–59. https://doi.org/10.1557/mre.2018.10

5. Sanghoon X. L., Tengfei L. J., Zhang L. Y-H. *Chalcogenide. From 3D to 2D and beyond*. Elsevier; 2019. 398 p.

6. Suekun K., Takabatake T. Research update: Cu–S based synthetic minerals as efficient thermoelectric materials at medium temperatures. *APL Materials*. 2016;4: 104503. https://doi.org/10.1063/1.4955398

7. Chetty R., Bali A., Mallik R. C. Tetrahedrites as thermoelectric materials: an overview. *Journal of Materials Chemistry C*. 2015;3(48): 12364–12378. https://doi.org/10.1039/c5tc02537k

8. Kim F. S., Suekuni K., Nishiate H., Ohta M., Tanaka H. I., Takabatake T. Tuning the charge carrier density in the thermoelectric colusite. *Journal of Applied Physics*. 2016;119(17): 175105. https://doi.org/10.1063/1.4948475

9. Powell A. V. Recent developments in Earth-abundant copper-sulfide thermoelectric materials. *Journal of Applied Physics,* 2019;126(10): 100901. https://doi.org/10.1063/1.5119345

10. Mikuła A., Mars K., Nieroda P., Rutkowski P. Copper chalcogenide-copper tetrahedrite composites – a new concept for stable thermoelectric materials dased on the chalcogenide system. *Materials*. 2021;14(10): 2635. https://doi.org/10.3390/ma14102635

11. Sobolev A. V., Presniakov I. A., Nasonova D. I., Verchenko V. Yu., Shevelkov, A. V. Thermally-activated electron exchange in $Cu_{12-x}Fe_xSb_4S_{13}$ (x = 1.3, 1.5) tetrahedrites: a Mössbauer study. *The Journal of Physical Chemistry C*. 2017;121(8): 4548–4557. https://doi.org/10.1021/acs.jpcc.6b12779

12. Sun F.-H., Dong J., Dey S., ... Li J.-F. Enhanced thermoelectric performance of $Cu_{12}Sb_4S_{13}$–δ tetrahedrite via nickel doping. *Science China Materials*. 2018;61(9): 1209–1217. https://doi.org/10.1007/s40843-018-9241-x

13. Deng S., Jiang X., ... Tang X. The reduction of

Condensed Matter and Interphases / Конденсированные среды и межфазные границы   2023;25(1): 47–54

E. N. Ismayilova et al.   Phase equilibria in the Cu_2SnSe_3–Sb_2Se_3–Se system

thermal conductivity in Cd and Sn co-doped Cu_3SbSe_4-based composites with a secondary-phase CdSe. *Journal of Materials Science*, 2020;56(7): 4727–4740. https://doi.org/10.1007/s10853-020-05586-3

14. Zhao D., Wu D., Bo L. Enhanced thermoelectric properties of Cu_3SbSe_4 compounds via gallium doping. *Energies*. 2017;10(10): 1524. https://doi.org/10.3390/en10101524

15. Liu G., Li J., Chen K., ... Li, L. Direct fabrication of highly-dense $Cu_2ZnSnSe_4$ bulk materials by combustion synthesis for enhanced thermoelectric properties. *Materials & Design*. 2016;93: 238–246. https://doi.org/10.1016/j.matdes.2015.12.172

16. Liu M., Qin X., Liu C. Substitution site selection and thermoelectric performance-enhancing mechanism of $Cu_{12}Sb_4S_{13}$ doped with Pb/Ge/Sn. *Physica Status Solidi B*. 2022;259: 2100275–2100278. https://doi.org/10.1002/pssb.202100275

17. Chen K., Di Paola C., Laricchia S., ... Bonini N. Structural and electronic evolution in the Cu_3SbS_4–Cu_3SnS_4 solid solution. *Journal of Materials Chemistry C*. 2020;8(33): 11508–11516. https://doi.org/10.1039/d0tc01804j

18. Nasonova D. I., Sobolev A. V., Presniakov I. A., Andreeva K. D., Shevelkov A. V. Position and oxidation state of tin in Sn-bearing tetrahedrites $Cu_{12-x}Sn_xSb_4S_{13}$. *Journal of Alloys and Compounds*, 2019;778: 774–778. https://doi.org/10.1016/j.jallcom.2018.11.168

19. Wei T.-R., Wang H., Gibbs Z. M., ... Li J.-F. Thermoelectric properties of Sn-doped *p*-type Cu_3SbSe_4: a compound with large effective mass and small band gap. *Journal of Materials Chemistri A*. 2014;2(33): 13527–13533. https://doi.org/10.1039/c4ta01957a

20. Tippireddy S., Prem Kumar D. S., Karati A., ... Mallik R. C. Effect of Sn substitution on the thermoelectric properties of synthetic tetrahedrite. *ACS Applied Materials and Interfaces*. 2019;116(24): 21686–21696. https://doi.org/10.1021/acsami.9b02956

21. Chen K., Di Paola C., Du B., ... Reece, M. Enhanced thermoelectric performance of Sn-doped Cu_3SbS_4. *Journal of Materials Chemistry C*. 2018;6(31): 8546–8552. https://doi.org/10.1039/c8tc02481b

22. Pi J.-H., Lee G.-E., Kim I.-H. Effects of Sn-doping on the thermoelectric properties of famatinite. *Journal of Electronic Materials*. 2019;49(5): 2755–2761. https://doi.org/10.1007/s11664-019-07710-9

23. Babanly M. B., Chulkov E. V., Aliev Z. S., Shevel'kov A. V., Amiraslanov I. R. Phase diagrams in materials science of topological insulators based on metal chalcogenides. *Russian Journal of Inorganic Chemistry*. 2017;62(13): 1703–1729. https://doi.org/10.1134/s0036023617130034

24. Imamaliyeva S. Z., Babanly D. M., Tagiev D. B., Babanly M. B. Physicochemical aspects of development of multicomponent chalcogenide phases having the Tl_5Te_3 structure: A Review. *Russian Journal of Inorganic Chemistry*. 2018;13: 1703–1027. https://doi.org/10.1134/s0036023618130041

25. Alverdiyev I. J., Aliev Z. S., Bagheri S. M., Mashadiyeva L. F., Yusibov Y. A., Babanly M. B. Study of the $2Cu_2S+GeSe_2 \leftrightarrow Cu_2Se+GeS_2$ reciprocal system and thermodynamic properties of the $Cu_8GeS_{6-x}Se_x$ solid solutions. *Journal of Alloys and Compounds*. 2017;691: 255–262. doi: https://doi.org/10.1016/j.jallcom.2016.08.251

26. Mashadiyeva L. F., Kevser J. O., Aliev I. I., Yusibov Y. A., Taghiyev D. B., Aliev Z. S., Babanlı M. B. The Ag_2Te-$SnTe$-Bi_2Te_3 system and thermodynamic properties of the $(2SnTe)_{1-x}(AgBiTe_2)_x$ solid solutions series. *Journal of Alloys and Compounds*. 2017;724: 641–648. https://doi.org/10.1016/j.jallcom.2017.06.338

27. Mashadiyeva L. F., Kevser J. O., Aliev I. I., Yusibov Y. A., Taghiyev D. B., Aliev Z. S., Babanlı M. B. Phase equilibria in the Ag_2Te-$SnTe$-Sb_2Te_3 system and thermodynamic properties of the $(2SnTe)_{12x}(AgSbTe_2)_x$ solid solution. *Phase Equilibria and Diffusion*. 2017;38(5): 603–614. https://doi.org/10.1007/s11669-017-0583-2

28. Bagheri S. M., Alverdiyev I. J., Aliev Z. S., Yusibov Y. A., Babanly M. B. Phase relationships in the $1.5GeS_2+Cu_2GeSe_3 \leftrightarrow 1.5GeSe_2+Cu_2GeS_3$ reciprocal system. *Journal of Alloys and Compounds*. 2015;625: 131–137. https://doi.org/10.1016/j.jallcom.2014.11.118

29. Ismayilova E. N., Baladzhayeva A. N., Mashadiyeva L. F. Phase equilibria along the Cu_3SbSe_4-$GeSe_2$ section of The Cu-Ge-Sb-Se. *New Materials, Compounds and Applications*. 2021;5(1): 52–58. Режим доступа: http://jomardpublishing.com/UploadFiles/Files/journals/NMCA/V5N1/Ismayilova_et_al.pdf

30. Ismayilova E. N. X-ray study of phase equilibria of the Cu_3SbSe_4-$SnSe_2$. *News of Azerbaijan Higher Technical Educational Institutions*. 2021;23(5): 21–25. Режим доступа: https://zenodo.org/record/7621101

31. Ostapyuk T. A., Yermiychuk I. M., Zmiy O. F., Olekseyuk I. D. Phase equilibria in the quasiternary system Cu_2Se–$SnSe_2$–Sb_2Se_3. *Chemistry of Metals and Alloys*. 2009;2: 164–169. https://doi.org/10.30970/cma2.0100

32. Ismayilova E. N., Mashadieva L. F. Фазовые равновесия в системе Cu_2Se-$SnSe$-Sb_2Se_3 по разрезу $SnSe$-Cu_3SbSe_3. Конденсированные среды и межфазные границы. 2018;20(2): 218–221. https://doi.org/10.17308/kcmf.2018.20/553

33. Ismailova E. N., Mashadieva L. F., Bakhtiyarly I. B., Babanly M. B. Phase equilibria in the Cu_2Se–$SnSe$–$CuSbSe_2$ system. *Russian Journal of Inorganic Chemistry*. 2019;64(6): 801–809. https://doi.org/10.1134/S0036023619060093

34. Ismailova E. N, Bakhtiyarly I. B, Babanly M. B. Refinement of the phase diagram of the $SnSe$-Sb_2Se_3 system. *Chemical Problems*. 2020;18(2): 250-256.

Condensed Matter and Interphases / Конденсированные среды и межфазные границы   2023;25(1): 47–54

E. N. Ismayilova et al.   Phase equilibria in the Cu_2SnSe_3–Sb_2Se_3–Se system

https://doi.org/10.32737/2221-8688-2020-2-250-256

35. Ismayilova E. N., Mashadiyeva L. F., Bakhtiyarly I. B., Babanly M. B. Phase equilibria in the Cu_2Se-$SnSe$-Sb_2Se_3 system. *Azerbaijan Chemical Journal*. 2022;1: 73–82. https://doi.org/10.32737/0005-2531-2022-1-73-82

36. *Binary alloy phase diagrams - second edition*. T. B. Massalski, H. Okamoto, P. R. Subramanian, L. Kacprzak (eds.). Ohio, USA: ASM International, Materials Park; 1990. 3589 p.

37. Voutsas G. P., Papazoglou A. G., Rentzeperis P. J., Siapkas D. The crystal structure of antimony selenide, Sb_2Se_3. *Zeitschrift für Kristallographie - Crystalline Materials*. 1985;171: 261–268. https://doi.org/10.1524/zkri.1985.171.14.261

38. Parasyuk O. V., Olekseyuk I. D., Marchuk O. V. The Cu_2Se–$HgSe$–$SnSe_2$ system. *Journal of Alloys and Compounds*. 1999; 287(1-2): 197–205. https://doi.org/10.1016/S0925-8388(99)00047-X

39. Babanly M. B., Yusibov Yu. A., Abishov V. T. *Three-component chalcogenides based on copper and silver**. Baku: BSU Publ.; 1993. 342 p. (In Russ.).

40. Sharma B.B., Ayyar R., Singh H. Stability of the Tetrahedral Phase in the $A^{I}_2 B^{IV} C^{VI}_3$ Group of Compounds. *Physica Status Solidi A*. 1977;A40(2): 691–697. https://doi.org/10.1002/pssa.2210400237

41. Marcano G., Chalbaud L., Rincón C., Sánchez P. G. Crystal growth and structure of the semiconductor Cu_2SnSe_3. *Materials Letters*. 2002;53(3): 151–154. https://doi.org/10.1016/s0167-577x(01)00466-9

42. Delgado G. E., Mora A. J., Marcano G., Rincon C. Crystal structure refinement of the semiconducting compound Cu_2SnSe_3 from X-ray powder diffraction data. *Materials Research Bulletin*. 2003;38: 1949–1955. https://doi.org/10.1016/j.materresbull.2003.09.017

43. Emsley J. *The Elements*. Oxford University Press; 1998. 300 p.

* Translated by author of the article.

Information about of authors

Elnara N. Ismailova, PhD student, Researcher, Institute of Catalysis and Inorganic Chemistry of the National Academy of Sciences of Azerbaijan (Baku, Azerbaijan).

https://orcid.org/0000-0002-1327-1753

ismayilova818@mail.ru

Leyla F. Mashadiyeva, PhD in Chemistry, Senior Researcher, Institute of Catalysis and Inorganic Chemistry of the National Academy of Sciences of Azerbaijan (Baku, Azerbaijan).

https://orcid.org/0000-0003-2357-6195

leylafm76@gmail.com

Ikhtiyar B. Bakhtiyarly, Dr. Sci. (Chem.), Professor, Head of laboratory, Institute of Catalysis and Inorganic Chemistry of the National Academy of Sciences of Azerbaijan (Baku, Azerbaijan).

https://orcid.org/0000-0002-7765-0672

ibbakhtiarli@mail.ru

Mahammad B. Babanly, Dr. Sci. (Chem.), Professor, Associate Member of the Azerbaijan National Academy of Sciences, Executive Director of the Institute of Catalysis and Inorganic Chemistry, Azerbaijan National Academy of Sciences (Baku, Azerbaijan).

https://orcid.org/0000-0001-5962-3710

babanlymb@gmail.com

Condensed Matter and Interphases

Original articles

Thermochemical characteristics of the formation of aqueous solutions of imino acids

T. A. Krysanova[1]✉, D. L. Kotova[1], E. G. Davydova[2], V. A. Krysanov[1]

[1]*Voronezh State University,
1 Universitetskaya pl., Voronezh 394018, Russian Federation*

[2]*Voronezh State Technical University,
84 ul. 20-letiya Oktyabrya, Voronezh 394006, Russian Federation*

Abstract

The calorimetry methods are an important source of thermodynamic information in the physicochemistry of solutions of biologically active substances, including amino acids. The goal of the work was to prepare a thermodynamic description of the formation of an aqueous solution of heterocyclic imino acids, proline and hydroxyproline, that have different structures and sizes of the side radical, in a wide range of concentrations, which can be used for a qualitative analysis of changes occurring in their solutions.

Thermochemical measurements of the formation of an aqueous solution of imino acids in the concentration range $1.0 \cdot 10^{-3} – 40.0 \cdot 10^{-3}$ mol/kg was performed on a MID-200 differential heat-conducting microcalorimeter at 293 K. The equilibrium moment in the solution formation was determined by the output of the thermokinetic curve to the zero line. The enthalpy of the formation of an aqueous solution of imino acids was calculated by the integration of the time dependence of thermal power.

It is shown that the increase in the equilibrium time, the increase in the maximum heat flow, and the decrease in the rate of change of the heat flow during the dissolution of hydroxyproline is due to the formation of intra and intermolecular bonds in the Hypro structure with the participation of the OH group. The difference in the structure of imino acids is reflected in the sign of the thermal effect and the form of the concentration dependence of the enthalpy of formation of aqueous solutions. The exoeffect of proline dissolution is due to the stabilisation of the water structure influenced by imino acid.

Keywords: Imino acids, Aqueous solutions, Thermochemical characteristics

✉ Tatiana A. Krysanova, takrys@yandex.ru

Condensed Matter and Interphases / Конденсированные среды и межфазные границы   2023;25(1): 55–60

T. A. Krysanova et al.   Thermochemical characteristics of the formation of aqueous solutions of imino acids

1. Introduction

Among all the diversity of thermodynamic properties in chemistry of solutions of biologically active substances, much attention is paid to the study of thermochemical characteristics [1–4]. Calorimetry methods are often used as a source of thermodynamic information in the physicochemistry of solutions. Amino acids are among the most important biologically active substances. Thermodynamic description of the process of formation of an aqueous solution of amino acids that have different structures and sizes of the side radical in a wide range of concentrations are also of great interest. The course of the dependence isotherm of the integral heat of dissolution on the concentration of the dissolved substance can be used for a qualitative analysis of changes occurring in the solution. Heterocyclic amino acid (proline) and its derivative (4-hydroxyproline) are contained in the connective tissue protein called collagen. They stabilise the secondary structure of the polyproline helix and play an important metabolic role in the body. In this work we present the results of the study of thermochemical properties of the formation of aqueous solutions of imino acids, specifically proline and hydroxyproline.

2. Experimental

Heterocyclic amino acids proline (pyrrolidine-2-carboxylic acid) (Pro) and hydroxyproline (L-4-hydroxypyrrolidine-α-carboxylic acid) (Hyp), which belong to imino acids, were chosen as the objects of study. Their carbon skeleton forms a cyclic compound that includes an amino group. Imino acids can be found in an aqueous solution as a bipolar ion (Fig. 1) [8].

(Pro$^\pm$)   (Hypro$^\pm$)
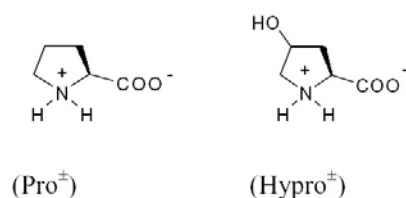
Fig. 1. Structure of amino acids

The samples of amino acids produced by Reanal (Hungary) and bidistilled water with specific electrical conductivity of not more than $1.4\cdot10^{-6}$ (Ohm/cm)$^{-1}$ were used for the study.

Solubility in water at 298 K was 162.3 g/100 ml for Pro and 36.1 g/100 ml for Hyp. Thermochemical measurements of the formation of an aqueous solution of imino acids in the concentration range $1.0\cdot10^{-3}$–$40.0\cdot10^{-3}$ mol/kg were conducted on a MID-200 differential heat-conducting microcalorimeter at 293 ± 1 K [9,10]. The sensitivity of the microcalorimeter was $5\cdot10^{-3}$ W. An amino acid sample weighed with an accuracy of ±0.0002 g was placed in a thin-walled ampoule which was immersed in 50.0 cm^3 of water and thermostated in an adiabatic calorimeter for 24 hours. Then the ampoule was broken with a special stock, and a weighed portion of amino acid was poured into the solvent. The equilibrium moment in the solution formation was determined by the output of the thermokinetic curve to the zero line. The enthalpy of the formations of Pro and Hyp aqueous solutions were calculated by the integration of the time dependence of thermal power. The values of standard deviation and the confidence interval were $4.43\cdot10^{-3}$ and $5.12\cdot10^{-3}$, respectively, for five independent measurements with the confidence interval 0.95 and Student's coefficient 2.78 [11].

A series of measurements of the thermal effect of potassium chloride dissolution in water at 298 K, which is used as a standard substance in calorimetry for calibration of devices, was performed in order to assess the accuracy and reliability of the obtained calorimetric measurements [12]. We used a weighed portion of potassium chloride weighing 1.0642 ± 0.0002 g based on the final concentration of the solution which was 0.278 mol/1000 g of water. As a result of five independent measurements, the obtained value of enthalpy of the formation of an aqueous solution KCl upon infinite dilution was 17.34 ± 0.28 kJ/mol, and it corresponds well with the data provided in [13].

3. Results and discussion

The thermodynamic parameter of the formation of an aqueous solution of amino acids in the whole concentration region is determined by the sum of the main effects, including endothermic effect, caused by the displacement of amino acid molecules from their distance in the molecular crystal lattice to the average distance between them in the solution

Condensed Matter and Interphases / Конденсированные среды и межфазные границы   2023;25(1): 55–60

T. A. Krysanova et al.   Thermochemical characteristics of the formation of aqueous solutions of imino acids

of this concentration, and exothermic effect of hydration, which is presented as a sum of a number of endo and exoeffects [1]. The formation of an aqueous solution of proline in the selected region of concentration, unlike hydroxyproline and such previously studied amino acids as phenylalanin, histidine, and cystine [6, 7, 14], is accompanied by heat production (Fig. 2).

The exothermic effect of the hydration process caused by a number of endo and exoeffects prevails over the energy consumption for the destruction of the proline crystal lattice and the structure of water [12]. The introduction of a hydroxyl group into the structure of the hydroxyproline molecule is reflected in a change of the thermal effect sign and in the nature of the concentration dependence of the enthalpy of dissolution of imino acids.

Thermokinetic curves of the formation of an aqueous solution of proline and hydroxyproline representing the energy of the process as a function of time are presented in Figs. 3 and 4. Maximum intensity of the thermal effect ($W_{max.}$) for imino acids in the studied concentration region was observed during the initial period of dissolution (2-4 min) and increased linearly with the growth of concentration. The dissolution of hydroxyproline is characterised by great values of $W_{max.}$ (Fig. 5). However, in case of hydroxyproline, unlike proline, we observed a smaller value of the rate of change in the heat flow and its linear dependence on concentration (Fig. 6). The differences in the rates of change in the heat
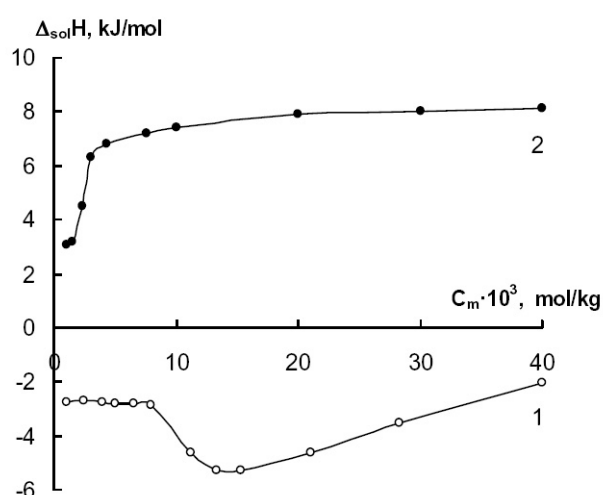
Fig. 2. Concentration dependence of enthalpy of formation of aqueous solutions of proline (*1*) and hydroxyproline (*2*)

flow of the dissolution process (υ_{Pro} and υ_{Hypro}) increased with an increase in the concentration of the obtained solution of imino acids.

The isotherm of proline dissolution (Fig. 2) has an extreme nature. The presence of a maximum on the isotherm was apparently caused by the competition between the effects of hydrophobic stabilisation of the water structure influenced by a non-polar radical and the destruction of its structure influenced by the zwitterionic group of the imino acid. The presence of absorption bands at 1609, 1643, and 3174 cm^{-1}, as well as at 1625 and 3152 cm^{-1} on an IR spectrum of the initial samples confirms the previous data [13] on the formation of COO^{-}...NH$_3^+$ bonds in the structure of amino acids.
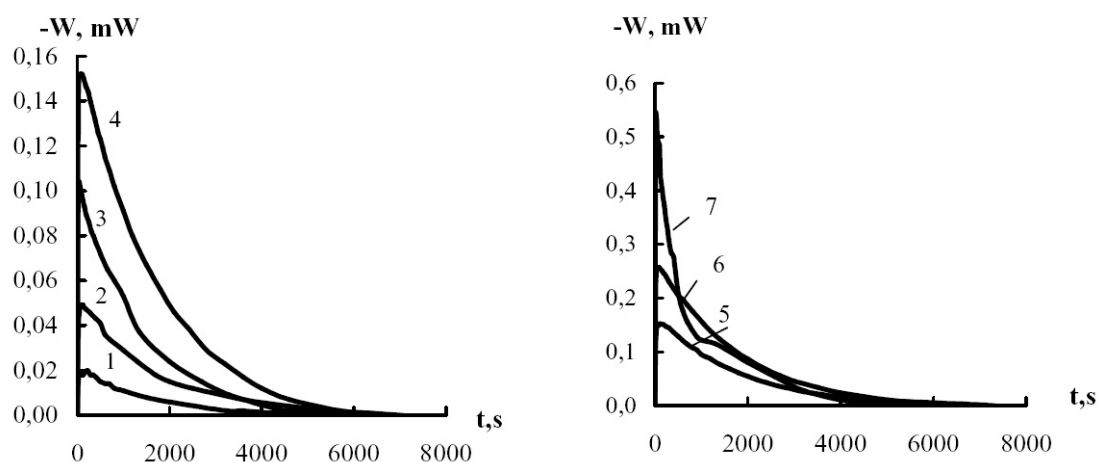
Fig. 3. Thermokinetic curves of formations of aqueous solutions of proline with concentrations: *1* – 2.5·10^{-3}, *2* – 5·10^{-3}, *3* – 8·10^{-3}, *4* – 10·10^{-3}, *5* – 15·10^{-3}, *6* – 20·10^{-3}, *7* – 40·10^{-3} mol/kg

Condensed Matter and Interphases / Конденсированные среды и межфазные границы   2023;25(1): 55–60

T. A. Krysanova et al.   Thermochemical characteristics of the formation of aqueous solutions of imino acids
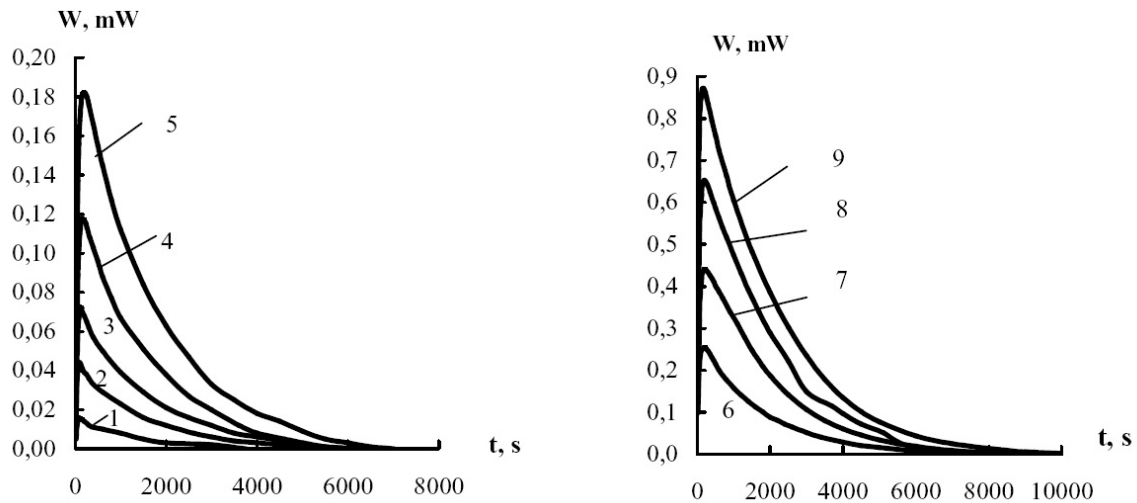
Fig. 4. Thermokinetic curves of formations of aqueous solutions of hydroxyproline with concentrations: *1* – $1 \cdot 10^{-3}$, *2* – $2.5 \cdot 10^{-3}$, *3* – $3 \cdot 10^{-3}$, *4* – $5 \cdot 10^{-3}$, *5* – $8 \cdot 10^{-3}$, *6* – $10 \cdot 10^{-3}$, *7* – $20 \cdot 10^{-3}$, *8* – $30 \cdot 10^{-3}$, *9* – $40 \cdot 10^{-3}$ mol/kg
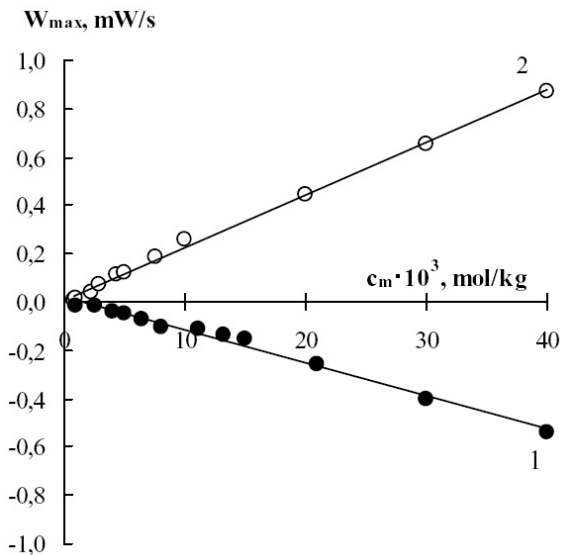
Fig. 5. Concentration dependence of the maximum value of the heat flux during the formation of a solution of hydroxyproline (*1*) and (*2*) proline
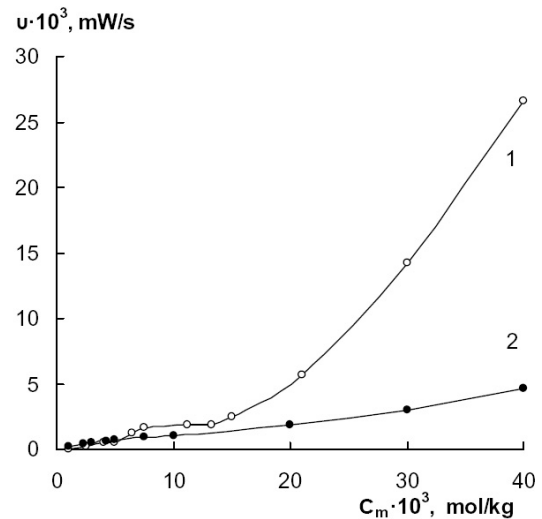
Fig. 6. Concentration dependence of the rate of change in the heat flow of the process of dissolution of proline (*1*) and hydroxyproline (*2*)

In the region of concentrations $\leqslant 8.0 \cdot 10^{-3}$ mol/kg, the independence of the value of the integral heat of dissolution from the concentration was observed. It can be assumed that in this region of concentrations the influence of proline on the water structure showed to a smaller degree [13]. The growth of exothermicity of the formation of solution in the region of concentrations ($8.0 \cdot 10^{-3}$– $15.2 \cdot 10^{-3}$ mol/kg) was caused by an increase in the hydrophobic component of hydration, meaning an increase in the stabilisation of the water structure under the influence of a non-polar radical of an amino acid [1, 15, 16]. Authors of [15]

considered this phenomenon as a violation of the dynamic structure of water. The process of amino acid dissolution is characterised by a change in the nature of the concentration dependence of the enthalpy of dissolution with an increase in the concentration of the obtained solution by more than $15.2 \cdot 10^{-3}$ mol/kg. Upon reaching the maximum stabilisation of the water structure influenced by the hydrocarbon radical of proline, the solvent molecules were reoriented under the influence of the formed imino acid associates due to the hydrophobic interaction of side radicals as well as to the direct pair interaction of zwitterionic

groups [1, 17]. It should be taken into account that proline's hydrophobic hydration ability decreased with an increase in concentration.

The isotherm of hydroxyproline dissolution (Fig. 2) belongs to the type with a continuously increasing endothermicity with a growth in concentration [12]. The solvent's structure is damaged due to the participation of an OH group in the formation of H-bonds with water molecules. The endoeffect of the formation of an aqueous solution of hydroxyproline was caused by the participation of the OH group in the formation of H-bonds with water molecules. The participation of the OH group in the formation of hydrogen bonds with water molecules was confirmed by the absorption bands at 3194 and 2495 cm^{-1} [18]. The positive contribution of the OH group to the enthalpy value increased in proportion to the concentration in the region of solution concentrations $1.5 \cdot 10^{-3} - 5.0 \cdot 10^{-3}$ mol/kg, The isotherm is characterised by a slight change in the enthalpy value in case of a concentration of more than $5.0 \cdot 10^{-3}$ mol/kg, The ability of hydroxyproline to form associates increases with an increase in the concentration of the solution, which suggests an increased role of hydrophobic hydration.

The stability of the values of enthalpies of dissolution for imino acids in the region of proline concentrations of $1.0 \cdot 10^{-3} - 8.0 \cdot 10^{-3}$ mol/kg and $1.0 \cdot 10^{-3} - 1.5 \cdot 10^{-3}$ mol/kg of hydroxyproline allowed attributing the obtained enthalpy value to the maximum dilution condition. In this region of concentrations the state of amino acids probably corresponds to the smallest change in the water structure. The value of the enthalpy of dissolution upon infinite dilution was calculated using an extrapolation of thermodynamic functions to zero solution concentration [12, 19]. The values of maximum enthalpy of dissolution were 2.85 ± 0.04 kJ/mol for proline and 3.20 ± 0.12 kJ/mol for hydroxyproline.

4. Conclusions

Therefore, the established differences in the nature of changes in thermokinetic characteristics, the sign of the thermal effect, and the form of dissolution isotherms for proline and hydroxyproline can be explained by the differences in the structural organisation of the solvent in different concentration zones.

Contribution of the authors

The authors contributed equally to this article.

Conflict of interests

The authors declare that they have no known competing financial interests or personal relationships that could have influenced the work reported in this paper.

References

1. Abrosimov V. K., Agafonov A. V., Antin E. V., Berezin B. D., Berezin M. B., Vyugin A. I., Ivanov E. V., Kulikov G. S., Lapshev P. V., Lomova T. N., Novoselov N. P., Sashina E. S., Chumakova R. V. *Biologically active substances in solutions. Structure, thermodynamics, reactivity**. Moscow: Nauka Publ., 2001. 403 p. (In Russ.)

2. *Biochemical thermodynamics*. M. Jones (ed.). Amsterdam, New York: Elsevier; 1988. 408 p.

3. Lytkin A. I., Chernikov V. V., Krutova O. N., Smirnova D. K. Standard enthalpy of dissolution of crystalline DL – valyl – DL - leucine in water and aqueous solutions of KOH. *Russian Journal of Physical Chemistry A*. 2019;93: 1699–1702. https://doi.org/10.1134/S0036024419090115

4. Ryzhkina I. S., Murtazina L. I., Kiseleva Yu. V., Konovalov A. I. Properties of supramolecular nanoassociates formed in aqueous solutions of biologically active compounds in low or ultra-low concentrations. *Doklady Physical Chemistry*. 2009;428(2): 196–200. https://doi.org/10.1134/S0012501609100029

5. Badelin V. G., Smirnov V. I., Mezhevoy I. N. Effect of the molecular structure on the enthalpies of hydration of amino acids and oligopeptides. *Russian Journal of Physical Chemistry A*. 2002;76(7): 1168–1171. Available at: https://www.elibrary.ru/item.asp?id=44546289

6. Bekeneva A. V., Kustov A. V., Korolev V. P. The enthalpy of solution of phenylalanine in water. *Journal of Physical Chemistry*. 2004; 78 (11):1927. *Russian Journal of Physical Chemistry A*. 2004;78(11): 1697–1700. Available at: https://www.elibrary.ru/item.asp?id=13461990

7. Kotova D.L., Beilina D.S., Krysanova T.A. Thermochemical characteristics of the dissolution of histidine. *Russian Journal of Physical Chemistry A*. 2004;78(3): 375–377. Available at: https://www.elibrary.ru/item.asp?id=13462463

8. Gurskaya G.V. *Structure of amino acids**. Moscow: Nauka Publ.; 1966. 159 p. (In Russ.)

9. Amelin V. N., Leikin Yu. A. *Calorimetry of ion processes**. Voronezh: VSU Publ.; 1991. 102 p. (In Russ.)

10. Perelygin I. S., Kimtis L. L., Chizhik V. I., ... Krestov G.A. *Experimental methods of solution chemistry.*

Condensed Matter and Interphases / Конденсированные среды и межфазные границы   2023;25(1): 55–60

T. A. Krysanova et al.   Thermochemical characteristics of the formation of aqueous solutions of imino acids

Spectroscopy and calorimetry. Moscow: Nauka Publ.; 1995. 380 p. (In Russ.)

11. Doerffel K. *Statistik in der analytischen Chemie*. Leipzig: Dt. Verl. für Grundstoffindustrie; 1984. 256 p.

12. Mishchenko K. P., Poltoratsky M. L. *Issues of thermodynamics and structure of aqueous solutions and non-aqueous solutions of electrolytes**. Leningrad: Khimiya Publ.; 1976. 327 p. (In Russ.)

13. Parker V. B. *Tables of chemical and thermodynamic properties*. Wach.: MS Depart of Commerce Nat.. Bur. of Stand. NSRDS – NBS 2. 1982. p. 319.

14. Kotova D. L., Rozhnova O. I., Selemenev V. F., Peregudov Yu. S. Thermochemical characteristics of dissolution of cysteine in water. *Russian Journal of Physical Chemistry A*. 2000;74(12): 2071–2072. Available at: https://www.elibrary.ru/item.asp?id=13356491

15. Reichard C. Solvents and solvent effects in organic chemistry. Weinheim: VCH, Cop.; 1988. 534 p.

16. Wilson K., Walker J. *Principles and techniques of biochemistry and molecular biolog*y. Cambridge University Press; 2010. https://doi.org/10.1017/CBO9780511841477

17. Belousov V. P., Panov M. Yu. *Thermodynamics of dilute solutions**. Leningrad: Khimiya Publ.; 1982. 240 p. (In Russ.)

18. Vasiliev A. V., Grinenko E. V., Shchukin A. O., Fedulina T. G. *Infrared spectroscopy of organic and natural compounds: textbook.** St. Petersburg: SPbGLTA Publ.; 2007. 54 p. (In Russ.)

19. Hamburg Yu. D. *Chemical thermodynamics: textbook**. Moscow: Laboratoriya znanii. Publ.; 2016. 237 p. (In Russ.)

* Translated by author of the article

Information about the authors

Tatiana A. Krysanova, Cand. Sci. (Chem.), Associate Professor of the Department of Analytical Chemistry, Voronezh State University (Voronezh, Russian Federation).

https://orcid.org/0000-0003-1720-6358

takrys@yandex.ru

Diana L. Kotova, Dr. Sci. (Chem.), Full Professor of the Department of Analytical Chemistry, Voronezh State University (Voronezh, Russian Federation).

https://orcid.org/0000-0002-6060-088X

Ekaterina G. Davydova, Cand. Sci. (Chem.), Associate Professor of the Department of Chemistry and Chemical Technology of Materials, Voronezh State Technical University (Voronezh, Russian Federation).

https://orcid.org/0000-0001-6658-0835

davkat@mail.ru

Vyacheslav A. Krysanov, Cand. Sci. (Chem.), Associate Professor of the Department of Physical Chemistry, Voronezh State University (Voronezh, Russian Federation).

https://orcid.org/0000-0002-6580-1939

krysanov@chem.vsu.ru

Original articles

Formation during glycine-nitrate combustion and magnetic properties of YFe$_{1-x}$Ni$_x$O$_3$ nanoparticles

E. I. Lisunova[1], N. S. Perov[2], V. O. Mittova[3], Bui Xuan Vuong[4], Nguyen Anh Tien[5],
B. V. Sladkopevtsev[1✉], Yu. A. Alekhina[2], V. F. Kostryukov[1], I. Ya. Mittova[1]

[1]Voronezh State University,
1 Universitetskaya pl., Voronezh, 394018, Russian Federation

[2]Lomonosov Moscow State University
1, building 2 Leninskie Gory, Moscow 119991, Russian Federation

[3]Teaching University Geomedi
4 st. King Solomon II str. 0114, Tbilisi, Georgia

[4]Faculty of Natural Sciences Education, Saigon University,
273 An Duong Vuong St., Ward 3, District 5, Ho Chi Minh City, Vietnam

[5]Faculty of Chemistry, Ho Chi Minh City University of Education,
Ho Chi Minh City 700000, Vietnam

Abstract

The synthesis of FeO$_3$ and YFe$_{1-x}$Ni$_x$O$_3$ (x = 0.1; 0.15; 0.2; 0.3; 0.5) nanocrystals was performed under the conditions of a self-propagating wave of glycine-nitrate combustion and their characterization and determination of the effect of Ni^{2+} doping of yttrium ferrite on the magnetic properties of nanopowders.

The technology for the synthesis of yttrium orthoferrite nanoparticles (with and without doping with Ni^{2+} ions) by the glycine-nitrate combustion method at a ratio of G/N = 1 and 1.5 without adding a gelling agent to the reaction mixture and using ethylene glycol/glycerol is described. For the characterization of nanopowders based on YFeO$_3$, the following were determined: phase composition and crystal structure (X-ray diffraction (XRD) method); size and structure of nanocrystal particles (transmission electron microscopy (TEM)); elemental composition of the samples (local X-ray spectral microanalysis (LXSMA)); magnetic characteristics (field dependences of specific magnetization).

Thermal annealing of the synthesized samples at 800°C for 60 min led to the formation of the o-YFeO$_3$ main phase. Undoped samples of yttrium orthoferrite were characterized by a particle diameter in the range of 5-185 nm, depending on the gelling agent used. YFe$_{1-x}$Ni$_x$O$_3$ particles had a predominantly round shape with a size of 24 to 31 nm; the non-monotonic dependence of the average particle diameter on the dopant content was revealed: as the amount of dopant added increased, the average crystallite size tended to decrease. Nanopowders of undoped yttrium orthoferrite exhibit antiferromagnetic behaviour of magnetic susceptibility with temperature. The change in the magnetic properties of the nickel-doped YFeO$_3$ nanocrystalline powders was due to the incorporation of Ni^{2+} into the Fe^{3+}position, which led to the formation of a material with more pronounced soft magnetic properties at a substitution degree of 0.1. Samples with high degrees of substitution (x = 0.15 and 0.3) were also characterized by paramagnetic behaviour at temperatures above 100 K.

Keywords: Nanocrystals, Yttrium orthoferrite, Nickel, Doping, Glycine-nitrate combustion

✉ Boris V. Sladkopevtsev, e-mail: dp-kmins@yandex.ru

Condensed Matter and Interphases / Конденсированные среды и межфазные границы   2023;25(1): 61–71

E. I. Lisunova et al.   Formation during glycine-nitrate combustion and magnetic properties of YFe$_{1-x}$Ni$_x$O$_3$...

1. Introduction

The preparation of nanocrystalline perovskite-like orthoferrites of rare-earth elements (REE), as well as solid solutions and composite materials based on them, is now one of the most intensively developing areas of research of material science [1–5]. Interest in this class of inorganic substances is mainly due to the possibility of using the properties of REE orthoferrites as multiferroics, which are practically important for use in data storage, gas sensors, and fuel cells [6–8].

One of the brightest representatives of this class is YFeO$_3$, which possesses a variety of important properties (multiferroic, semiconductor, photocatalyst in the visible light region, etc.) and is complemented by the economic feasibility of using materials based on it due to the highest prevalence of yttrium among the entire series of rare earth elements [9–11]. YFeO$_3$ nanopowders can be obtained by co-deposition [12], hydrothermal synthesis [13], sol-gel technology, and other methods [14, 15].

The tendency of nanoparticles to agglomerate is an important factor affecting the size of clusters in a solution and, hence, their physicochemical properties [15–18]. Recently, the method for obtaining complex oxide systems in a combustion wave and, in particular, glycine-nitrate combustion method (GNC) has been actively used. GNC allows to ensure high chemical homogeneity of substances by mixing the initial components at the molecular level at relatively low temperatures [19–22]. The main advantage of this method is the achievement of a narrow particle size distribution, therefore GNC is actively used for the synthesis of nanocrystalline YFeO$_3$ [23, 24]. However, the influence of gelling agents on the process of formation of yttrium orthoferrite nanocrystals (with and without doping) under the conditions of a self-propagating wave of glycine-nitrate combustion, their size, structure, and magnetic properties of the resulting composition still remains unexplored.

Particular attention is paid to the study of the magnetic properties of yttrium orthoferrite doped with doubly charged cations [25 – 28]. For example, it was shown in [29] that the doping of YFeO$_3$ with cobalt provides an increase in the magnetic permeability of the material and a broadening of the hysteresis loop, caused by an increase in the angularity of the magnetic moments of atoms in antiferromagnets. Therefore, the cation of the transition element Ni^{2+} with defective d–shell was chosen for the doping of yttrium ferrite. Due to the similarity in physicochemical properties and dimensional parameters according to the system of Shannon radii (r(Ni^{2+}) = 0.69 Å), nickel, most probably, should occupy the positions of iron in the ferrite lattice (r(Fe^{3+}) = 0.65 Å) [30].

In this regard, the aim of the study was the synthesis of YFeO$_3$ and YFe$_{1x}$Ni$_x$O$_3$ nanocrystals under the conditions of a self-propagating wave of glycine-nitrate combustion, their characterization and determination of the influence of doping of yttrium ferrite with Ni^{2+} on the magnetic properties of nanopowders.

2. Experimental

The starting materials were pure iron (III) and yttrium nitrates – Fe(NO$_3$)$_3$·9H$_2$O (pure) and Y(NO$_3$)$_3$·6H$_2$O (chemically pure), glycine (aminoacetic acid) C$_2$H$_5$NO$_2$ (analytical grade), the amount of which in relation to metal nitrates G/N varied from 1 to 1.5. In the general case, polyatomic alcohols are used as gelling agents. Due to the use of polyatomic alcohols the polyesterification of chelates occurs; in this study, chemically pure glycerol C$_3$H$_5$(OH)$_3$ and ethylene glycol C$_2$H$_4$(OH)$_2$, were used as gelling agents. As a result, a uniform distribution of Y (III) and Fe (III) metal ions is achieved in the initial precursor, during subsequent heat treatment of the precursor a complex oxide powder, corresponding to the main phase of YFeO$_3$ is formed.

The procedure for the synthesis of nanocrystals was as follows. The Y(NO$_3$)$_3$·6H$_2$O, Fe(NO$_3$)$_3$·9H$_2$O

Condensed Matter and Interphases / Конденсированные среды и межфазные границы   2023;25(1): 61–71

E. I. Lisunova et al.   Formation during glycine-nitrate combustion and magnetic properties of YFe$_{1-x}$Ni$_x$O$_3$...

and $C_2H_5NO_2$ were dissolved in 200 ml of distilled water. In addition to glycine, ethylene glycol or glycerol was added to the solution of metal nitrates. The amount of gelling agent was changed depending on the main components, G/N = 1 and G/N = 1.5, respectively. The boiling was performed for 120 minutes. The resulting gel was subjected to thermal heating, as a result of which the self-sustaining exothermic reaction involving glycine (aminoacetic acid) developed. The final product (in powder form) was annealed in a muffle furnace at 800°C for 60 minutes. These thermal annealing parameters were chosen based on our previous results on the co-deposition of nickel-doped YFeO$_3$ nanocrystals [31]. It was also shown that under these conditions, the formation of a single-phase yttrium orthoferrite product with a perovskite structure and particle sizes up to 160 nm occurs. A further increase in the temperature and time of annealing is undesirable, since it leads to coarsening of particles and their agglomeration.

The phase composition and crystal structure of the synthesized samples were determined by X-ray diffraction (XRD, diffractometer Thermo ARL X'tra (CuK$_\alpha$ radiation, λ = 0.154018 nm, 2θ = 20–70°, step = 0.02°). The particle size was determined using the transmission electron microscopy (TEM, Carl Zeiss LIBRA 120). For the determination of the elemental composition of the samples, electron probe X-ray microanalysis (EPMA, JEOL-6580LV scanning electron microscope with an INCA 250 energy-dispersive microanalysis system) was used.

Measurements of the temperature dependences of the magnetic susceptibility up to helium temperatures were carried out using the PPMS (Physical Properties Measurement System). The same installation was used to measure the hysteresis loops of sample 5 (see below) with ferrimagnetic ordering in fields up to 6.4 MA/m. The magnetic properties of the remaining samples were measured using LakeShore vibrating magnetometer model 7407. The samples were sealed in polyethylene capsules about 4x4 mm in size and laminated for the prevention of the movement of powder particles during measurements. The capsules were fixed on the magnetometer holder with a Teflon tape. The magnetic field during measurements was applied in the plane of the capsule. The measurements were carried out in a cryostat at temperatures of 100 and 300 K.

3. Results and discussion

As can be seen from the XRD data (Fig. 1) thermal annealing at a temperature of 800°C for 60 minutes of undoped samples, synthesized under the conditions of glycine-nitrate combustion with the ratio G/N = 1 without adding a gelling agent to the reaction mixture (diffraction pattern 1) and with the addition of ethylene glycol at ratios G/N = 1 and G/N = 1.5 (diffraction patterns 2 and 3), led to the formation of yttrium orthoferrite powders. At the same time, for both G/N = 1 and for G/N = 1.5 using glycerol as a gelling agent, in addition to the main YFeO$_3$ phase (cards No.: 48-0529 and 39-1489), the presence of Y$_2$O$_3$ impurities (card No: 20-1412) was established, as can be seen from diffraction patterns 4 and 5 in Figs. 1 (see Table 1).

On diffraction patterns of yttrium ferrite samples (Fig. 2, beginning of numbering in Fig. 1, diffraction patterns 6 and 7), doped with Ni^{2+}, under conditions of glycine-nitrate combustion at G/N = 1 without the use of gelling agents, followed by thermal annealing at 800 °C for 60 minutes, peaks of the main yttrium orthoferrite phase were observed (cards No.: 48-0529 and 39-1489). In addition to reflections of the main phase, diffraction patterns No. 6 and 7 contain one impurity peak of yttrium oxide with insignificant intensity (card No. 20-1412). When glycerol (Fig. 2, diffraction patterns No. 8 and No. 9) and ethylene glycol (Fig. 2, diffraction patterns No. 10 and No. 11) were used, the presence of the main phase of yttrium orthoferrite and an insignificant number of peaks of Y$_2$O$_3$ oxide was observed (Fig. 2).

The determination of the particle size of YFe$_{1-x}$Ni$_x$O$_3$ nanopowders (x = 0.1; 0.15; 0.2; 0.3; 0.5), based on the broadening of X-ray diffraction lines (calculated using Scherrer equation) and transmission electron microscopy, provided the following results (Table 2). The calculation using Scherrer equation (XRD) showed that with an increase x from 0.1 to 0.3 D_{av} of nanocrystals varies from 27±2 nm to 47±4 nm, respectively (XRD). As follows from the TEM data, nickel-doped yttrium ferrite nanoparticles with a nominal degree of doping x = 0.15 at G/N = 1.5 with the addition
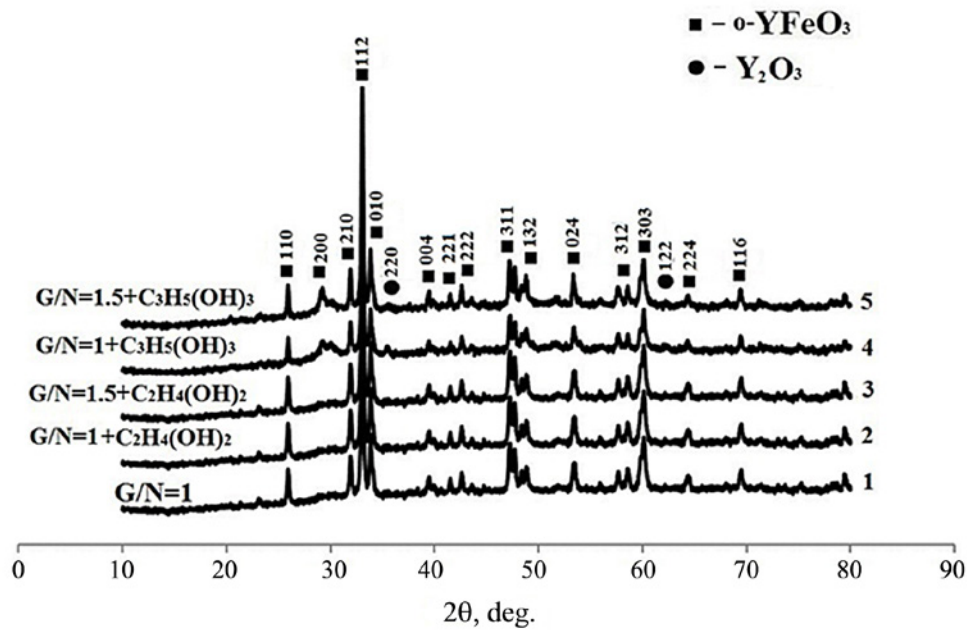
Fig. 1. X-ray diffraction patterns of YFeO$_3$ powders, obtained by the glycine-nitrate method, with a different ratio of G/N components and various gelling agents after thermal annealing at 800°C, 60 min: *1* – G/N = 1 without the addition of a gelling agent; *2, 3* – G/N = 1 and 1.5, respectively, gelling agent – ethylene glycol C$_2$H$_4$(OH)$_2$; *4, 5* – G/N = 1 and 1.5, gelling agent – glycerol C$_3$H$_5$(OH)$_3$
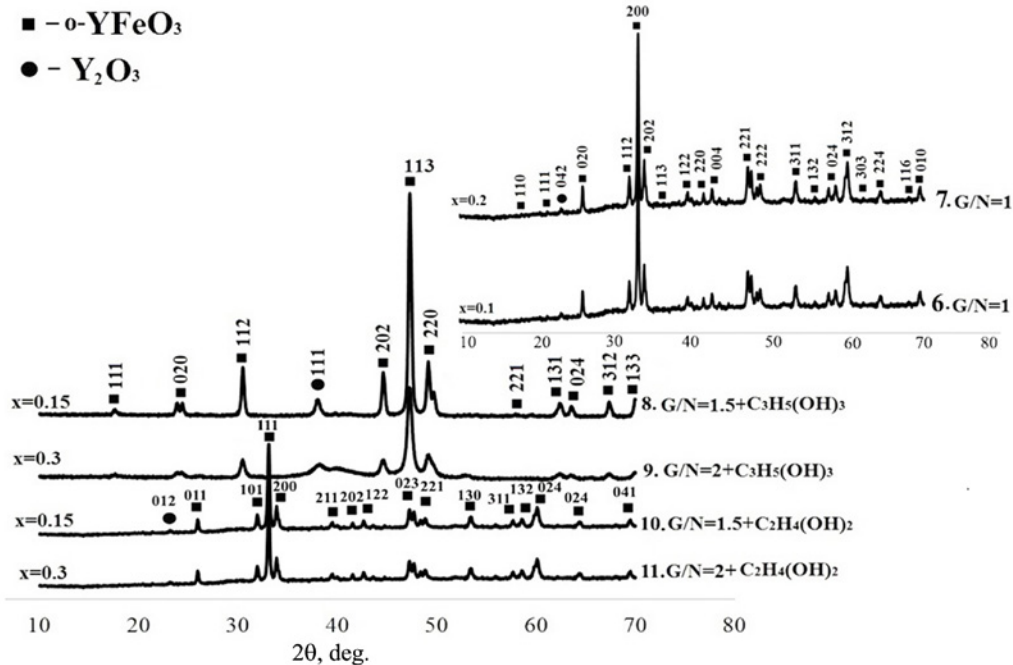
Fig. 2. X-ray diffraction patterns of powders thermally annealed at 800°C, 60 min: *6* – YFe$_{1-x}$Ni$_x$O$_3$ (*x* = 0.1) at G/N = 1 without the addition of a gelling agent; *7* – YFe$_{1-x}$Ni$_x$O$_3$ (*x* = 0.2) at G/N = 1 without the addition of a gelling agent; *8* – YFe$_{1-x}$Ni$_x$O$_3$ (*x* = 0.15) at G/N = 1.5, gelling agent – glycerol C$_3$H$_5$(OH)$_3$; *9* – YFe$_{1-x}$Ni$_x$O$_3$ (*x* = 0.3) at G/N = 2, gelling agent – glycerol C$_3$H$_5$(OH)$_3$; *10* – YFe$_{1-x}$Ni$_x$O$_3$ (*x* = 0.15) at G/N = 1.5, gelling agent – ethylene glycol C$_2$H$_4$(OH)$_2$; *11* – YFe$_{1-x}$Ni$_x$O$_3$ (*x* = 0.3) at G/N = 2, gelling agent – ethylene glycol C$_2$H$_4$(OH)$_2$

Condensed Matter and Interphases / Конденсированные среды и межфазные границы   2023;25(1): 61–71

E. I. Lisunova et al.   Formation during glycine-nitrate combustion and magnetic properties of YFe$_{1-x}$Ni$_x$O$_3$...

Table 1. Results of X-ray phase analysis of YFeO$_3$ and YFe$_{1-x}$Ni$_x$O$_3$ nanopowders

№	Composition	G/N	Gelling agent	Additional phase
1	YFeO$_3$	1	–	–
2	YFeO$_3$	1	C$_2$H$_4$(OH)$_2$	–
3	YFeO$_3$	1.5	C$_2$H$_4$(OH)$_2$	–
4	YFeO$_3$	1	C$_3$H$_5$(OH)$_3$	Y$_2$O$_3$
5	YFeO$_3$	1.5	C$_3$H$_5$(OH)$_3$	Y$_2$O$_3$
6	YFe$_{0.9}$Ni$_{0.1}$O$_3$	1	–	Y$_2$O$_3$
7	YFe$_{0.8}$Ni$_{0.2}$O$_3$	1	–	Y$_2$O$_3$
8	YFe$_{0.85}$Ni$_{0.15}$O$_3$	1.5	C$_3$H$_5$(OH)$_3$	Y$_2$O$_3$
9	YFe$_{0.7}$Ni$_{0.3}$O$_3$	2	C$_3$H$_5$(OH)$_3$	Y$_2$O$_3$
10	YFe$_{0.85}$Ni$_{0.15}$O$_3$	1.5	C$_2$H$_4$(OH)$_2$	Y$_2$O$_3$
11	YFe$_{0.7}$Ni$_{0.3}$O$_3$	2	C$_2$H$_4$(OH)$_2$	Y$_2$O$_3$

a   b
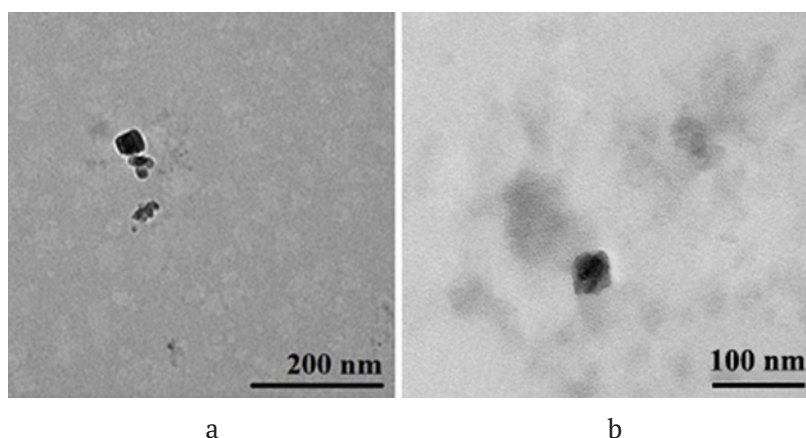
Fig. 3. TEM images (a, b) of YFe$_{1-x}$Ni$_x$O$_3$ powder (x = 0.15), in the ratio G/N = 1.5, gelling agent – C$_2$H$_4$(OH)$_2$ (a, Sample No. 10) and C$_3$H$_5$(OH)$_3$ (b, sample No. 8), annealing – 800°C, 60 min

of ethylene glycol (Fig. 3a) and glycerol (Fig. 3b) were characterized predominantly by a spherical shape, their diameter was in the range from 4 to 50 nm (Fig. 3).

As can be seen from Table 2 the data obtained show the non-monotonic nature of the dependence D_{av} from the content of the dopant. As the amount of added dopant increased, the average crystallite size tends to decrease; such a decrease may be caused by the peculiarities of the chemical structure of gelling agents (ethylene glycol/glycerol).

The results of the study of the elemental composition by the local X-ray spectral microanalysis are shown in Table 3.

Determination of the elemental composition of the samples showed that the actual content of each element in them is quite close to their nominal composition (Table 4).

The field dependences of the magnetization of undoped samples synthesized without the use of a gelling agent and with the addition of ethylene glycol are shown in Figs. 4–5. Samples in a field of 1270 kA/m at T = 100 K (Fig. 4a) and 300 K (Fig. 4b) do not reach magnetic saturation (flip transition). The field dependences of the specific magnetization are straight lines (the noise on the dependences was primarily associated with the smallness of measured magnetization values), the maximum measured values of the magnetization for these samples in a field of 1270 kA/m were in the range of 0.25–0.36 A m^2/kg at a temperature of 100 K and 0.12–0.30 A m^2/kg at a temperature of 300 K (Table 5). The magnetic properties of the samples were comparable to those for the pure YFeO$_3$ phase, synthesized by the deposition method [32]. The specific magnetization of pure YFeO$_3$ phase in a magnetic field of the same

Condensed Matter and Interphases / Конденсированные среды и межфазные границы   2023;25(1): 61–71

E. I. Lisunova et al.   Formation during glycine-nitrate combustion and magnetic properties of YFe$_{1-x}$Ni$_x$O$_3$...

Table 2. Average diameter of YFe$_{1-x}$Ni$_x$O nanocrystals (x = 0.1; 0.15; 0.2; 0.3) after annealing at 800 °C for 60 min

Method of determination	D_{av}, nm					
	sample № 6 (x = 0.1)	sample № 7 (x = 0.2)	sample № 8 (x = 0.15)	sample № 10 (x = 0.15)	sample № 9 (x = 0.3)	sample № 11 (x = 0.3)
XRD	27±2	40±4	24±2	40±4	47±4	26±2
TEM	31±3	26±2	17±5	31±2	24±9	28±5

Table 3 Results of X-ray microanalysis and the determination error of the content of elements in YFe$_{1-x}$Ni$_x$O$_3$ samples obtained by glycine-nitrate combustion, after thermal annealing at 800 °C, 60 min

Sample №	Nominal composition of samples	Elemental composition, at %				
	x	Y	Ni	Fe	O	C
6	0.1	15.9±1.8	0.8 ±0.1	11.9±0.6	55.0±3.4	16.0±1.0
7	0.2	13.1±1.6	2.3±0.2	10.9±0.6	58.6±3.8	15.1±1.0
8	0.15	10.1±1.4	3.1±0.2	6.8±0.4	63.0±4.5	17.0±1.2
9	0.3	10.1±1.4	3.1±0.2	6.8±0.4	61.0±4.5	19.0±1.2
10	0.15	18.4±1.8	1.1±0.1	14.2±0.6	50.9±2.8	15.3±0.9
11	0.3	18.4±1.8	1.3±0.1	14.2±0.6	50.8±2.8	15.3±0.9

a   b
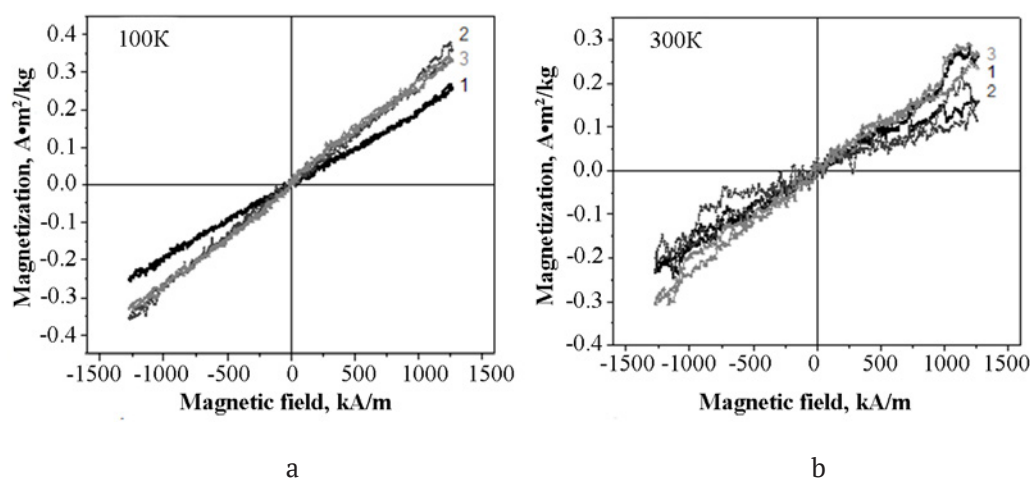
Fig. 4. Hysteresis loops at a) 100 K and b) 300 K of YFeO$_3$ samples (annealing at 800°C, 60 min) synthesized at component ratios: G/N = 1 without the addition of a gelling agent (*1*) and G/N = 1 and 1.5 with the addition of ethylene glycol (*2, 3*)

value was J = 0.242 A m^2/kg. In the given range of magnetic fields and temperatures, the material exhibits paramagnetic behaviour. In this case, the temperature dependences of the magnetization indicate the existence of an antiferromagnetic type of ordering at low temperatures. The linear approximation of the curve section crosses the abscissa axis in the region of negative values, which indicates the presence of an antiferromagnetic type (Fig. 5b). The maximum of the direct dependence of the susceptibility, corresponding to the Neel temperature, can be observed at temperatures below 2 K, however,

the existence of local ordering can be observed up to 100 K.

According to the literature data, yttrium ferrite is a weak ferromagnet, which demonstrates the phenomenon of spin reorientation - rotation of the antiferromagnetism axis under the action of a magnetic field [15]. The magnetic properties of undoped sample 5, synthesized with the addition of glycerol as a gelling agent at G/N = 1.5, in a wide range of magnetic fields demonstrated the presence of a wide hysteresis loop, which is characteristic of materials with an antiferromagnetic type of ordering with an

Condensed Matter and Interphases / Конденсированные среды и межфазные границы   2023;25(1): 61–71

E. I. Lisunova et al.   Formation during glycine-nitrate combustion and magnetic properties of YFe$_{1-x}$Ni$_x$O$_3$...

a

b
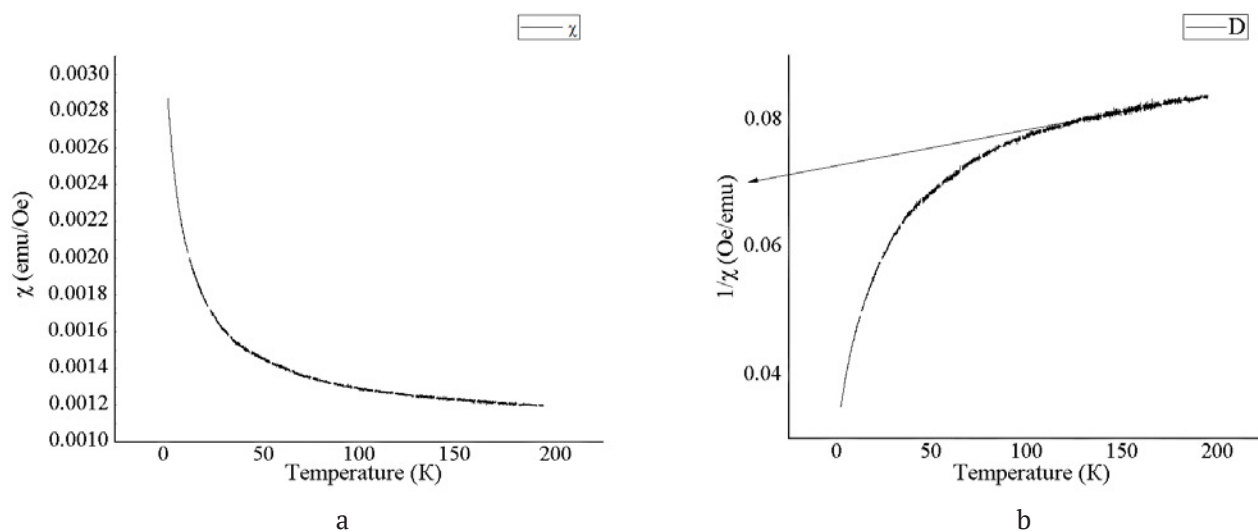
Fig. 5. Temperature dependence of magnetic susceptibility (a) and inverse susceptibility (b) for sample 1 from Table 5 (for samples 2 and 3, the dependences were similar)

uncompensated magnetic moment (Fig. 6). At 2 K, the field dependences of the magnetization also show a waisted hysteresis loop, which indicates a more expressed spin reorientation phenomenon [15]. It should also be noted that for the samples synthesized using glycerol, the formation of an impurity phase of yttrium oxide was observed.

The hysteresis of the field dependences was also observed for a sample of yttrium orthoferrite with a low degree of nickel doping. For a sample with a degree of substitution $x = 0.1$ at G/N = 1 without the addition of a gelling agent to the reaction system, hysteresis behaviour, indicating the presence of an uncompensated magnetic

moment was observed in the range of magnetic fields up to 1270 kA/m (Fig. 7, Table 6). In this case, in the region of magnetic fields with a strength of about 1000 kA/m, an inflection in the field dependence of the magnetization was observed, the appearance of which may indicate the onset of the spin reorientation process, but the process itself can be observed only when stronger magnetic fields were applied. The absence of magnetic saturation of the samples in the presented range of magnetic fields also should be noted. At the same time, the coercive force in the given partial cycles was about 50–80 kA/m (both at 300 K and at 100 K), which is an order of magnitude lower than the
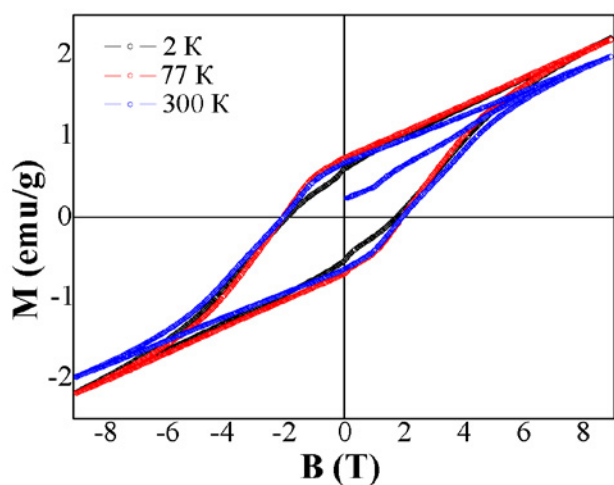
Fig. 6. Hysteresis loops of sample 5 synthesized with glycerol at different temperatures. At 2 K (black line) there was a tendency to transition to the antiferro-magnetic state
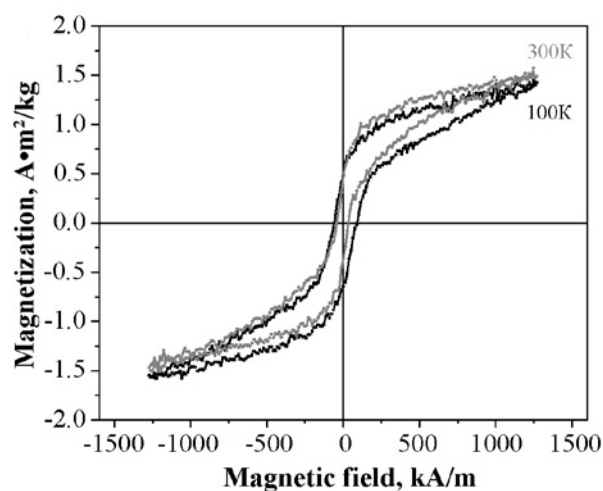
Fig. 7. Hysteresis loops of sample 6 with nominal composition YFe$_{0.9}$Ni$_{0.1}$O$_3$ (annealing at 800 °C, 60 min) at G/N = 1 without the addition of a gelling agent

Condensed Matter and Interphases / Конденсированные среды и межфазные границы   2023;25(1): 61–71

E. I. Lisunova et al.   Formation during glycine-nitrate combustion and magnetic properties of YFe$_{1-x}$Ni$_x$O$_3$...

coercive force of the undoped sample measured under similar conditions (about 520–550 kA/m). Thus, the doping of yttrium ferrite with nickel to a small extent allows obtaining materials with a softer magnetic behaviour of the uncompensated magnetic moment and smaller spin reorientation fields.

For samples with high degrees of substitution ($x = 0.15$, $x = 0.3$) and obtained using glycerol and ethylene glycol as gelling agents in the range of magnetic fields up to 1270 kA/m, paramagnetic

behaviour was observed at temperatures above 100 K with a susceptibility of about 10^{-5}-10^{-6} (Fig. 8).

Other YFe$_{1-x}$Ni$_x$O$_3$ ($x = 0.15$ and 0.3) samples No. 8 and 9, synthesized using glycerol as a gelling agent in the ratio G/N = 1.5 and 2, respectively, as well as YFe$_{1-x}$Ni$_x$O$_3$ ($x = 0.15$ and 0.3) samples No. 10 and 11, obtained with the addition of ethylene glycol in the same ratio G/N = 1.5 and 2, demonstrated paramagnetic behaviour.

Thus, during the formation of yttrium orthoferrite nanopowders (with and without

a   b
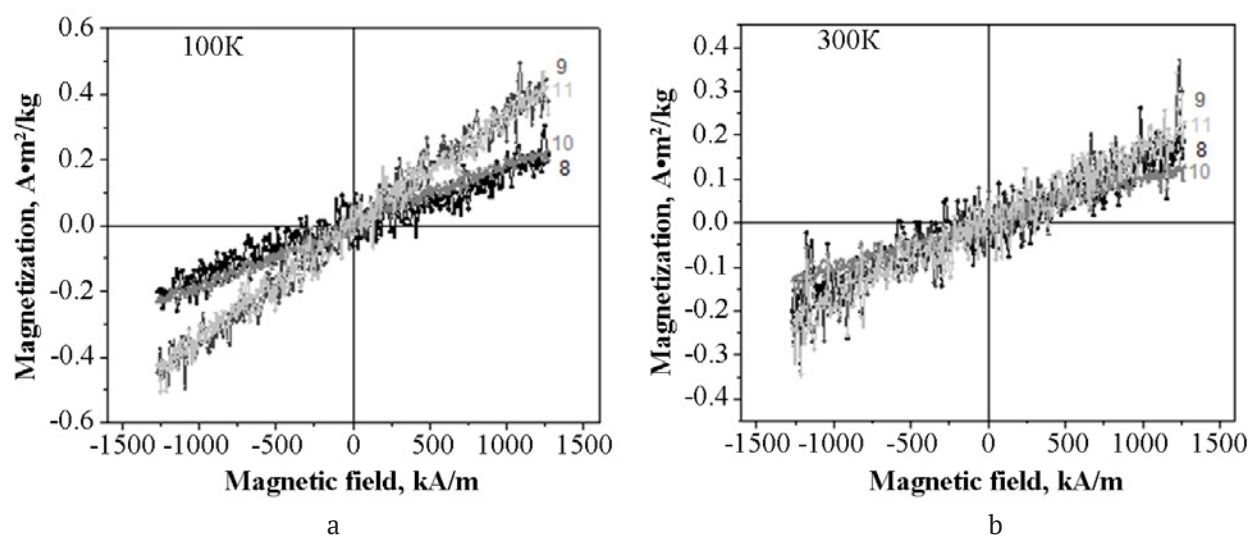
Fig. 8. Field dependences of the magnetization for samples thermally annealed at 800°C, 60 min: *8* – nominal composition YFe$_{0.85}$Ni$_{0.15}$O$_3$ at G/N = 1 with the addition of glycerol, *9* – nominal composition YFe$_{0.7}$Ni$_{0.3}$O$_3$ at G/N = 2 with the addition of glycerol, *10* – nominal composition YFe$_{0.85}$Ni$_{0.15}$O$_3$ at G/N = 1.5 with the addition of ethylene glycol, *11* – nominal composition YFe$_{0.7}$Ni$_{0.3}$O$_3$ at G/N = 2 with the addition of ethylene glycol

Table 4 Results of X-ray microanalysis for YFe$_{1-x}$Ni$_x$O$_3$ samples obtained by glycine-nitrate combustion after thermal annealing in 800 °C mode, 60 min

Sample №	G/N	Gelling agent	x	Nominal composition	Real composition of samples
6	1	-	0.1	YFe$_{0.9}$Ni$_{0.1}$O$_3$	YFe$_{0.92}$Ni$_{0.08}$O$_3$
7	2	-	0.2	YFe$_{0.8}$Ni$_{0.2}$O$_3$	YFe$_{0.83}$Ni$_{0.17}$O$_3$
8	1.5	C$_3$H$_5$(OH)$_3$	0.15	YFe$_{0.85}$Ni$_{0.15}$O$_3$	YFe$_{0.75}$Ni$_{0.25}$O$_3$
9	2	C$_3$H$_5$(OH)$_3$	0.3	YFe$_{0.7}$Ni$_{0.3}$O$_3$	YFe$_{0.69}$Ni$_{0.31}$O$_3$
10	1.5	C$_2$H$_4$(OH)$_2$	0.15	YFe$_{0.85}$Ni$_{0.15}$O$_3$	YFe$_{0.79}$Ni$_{0.21}$O$_3$
11	2	C$_2$H$_4$(OH)$_2$	0.3	YFe$_{0.7}$Ni$_{0.3}$O$_3$	YFe$_{0.73}$Ni$_{0.27}$O$_3$

Table 5 Magnetic characteristics of undoped YFeO$_3$ nanopowders (annealing at 800°C, 60 min), measured at 100 and 300 K

№	G/N	Gelling agents	Particle size (TEM), nm	J(100K), A·m^2/kg	J(300K), A·m^2/kg
1	1	–	~5-145	0.26	0.23
2	1	C$_2$H$_4$(OH)$_2$	~5-150	0.36	0.16
3	1.5	C$_2$H$_4$(OH)$_2$	~20-185	0.33	0.26

Condensed Matter and Interphases / Конденсированные среды и межфазные границы   2023;25(1): 61–71

E. I. Lisunova et al.   Formation during glycine-nitrate combustion and magnetic properties of YFe$_{1-x}$Ni$_x$O$_3$...

Table 6 Magnetic characteristics in the field of 1270 kA/m of YFe$_{1-x}$Ni$_x$O$_3$ nanopowders (x = 0.1; 0.15; 0.3) after thermal annealing at 800°C, 60 min, measured at 100 and 300 K

№	G/N	Gelling agents	Particle size (TEM), nm	J(300K), A·m^2/kg	J(100K), A·m^2/kg
6	1	–	5-100	0.066	0.145
8	1.5	C$_3$H$_5$(OH)$_3$	5-35	0.1	0.09
9	2	C$_3$H$_5$(OH)$_3$	4-55	0.128	0.133
10	1.5	C$_2$H$_4$(OH)$_2$	5-50	0.056	0.42
11	2	C$_2$H$_4$(OH)$_2$	4-70	0.176	0.092

doping) under the conditions of a self-propagating wave of glycine-nitrate combustion in the region of the stoichiometric parameter G/N from 1 to 2, materials that exhibit different magnetic properties were formed. Fine adjustment of the magnetic characteristics by changing the G/N ratio of components and using various gelling agents in the synthesis of nanocrystals is possible.

4. Conclusions

Yttrium orthoferrite nanocrystals (with and without doping) were synthesized under glycine–nitrate combustion conditions at G/N = 1 and 1.5 without adding a gelling agent to the reaction mixture and using ethylene glycol/glycerol. It was established that thermal annealing for an hour at 800 °C led to the formation of the main phase of o-YFeO$_3$. For undoped yttrium orthoferrite samples, a particle diameter of the order of 5–185 nm was characteristic, depending on the gelling agent (TEM) used. The study of the magnetic characteristics demonstrated that YFeO$_3$ samples, synthesized with the use of ethylene glycol as a gelling agent, were characterized by antiferromagnetic behaviour up to extremely low temperatures (below 2 K), and the use of glycerol as a gelling agent in a similar process led to the formation of particles with an uncompensated magnetic moment, most probably caused by the weak ferromagnetism of yttrium ferrite, which exhibits a magnetically hard response. In the case of yttrium orthoferrite doped with Ni^{2+}, under the same conditions, particles were characterized by a predominantly rounded shape with a size of 24 to 31 nm (TEM). Changes in the magnetic properties of YFeO$_3$ nanocrystalline powders doped with nickel was due to the incorporation of Ni^{2+} (r(Ni^{2+}) = 0.69 Å) in the position of Fe^{3+} (r(Fe^{3+}) = 0.645 Å), which led to the formation of a material with more expressed soft magnetic properties at a degree of substitution of 0.1. Samples with higher degrees of substitution also exhibited paramagnetic behaviour at temperatures above 100 K.

Author contributions

The authors contributed equally to this article.

Conflict of interests

The authors declare that they have no known competing financial interests or personal relationships that could have influenced the work reported in this paper.

References

1. Saukhimov A. A., Hobosyan M. A., Dannangoda G. C., Zhumabekova N. N., Almanov G. A., Kumekov S. E., Martirosyan K. S. Solution-combustion synthesis and magnetodielectric properties of nanostructured rare earth ferrites. *International Journal of Self-Propagating High-Temperature Synthesis*. 2015;24(2): 63–71. https://doi.org/10.3103/S1061386215020065

2. Popkov V. I., Almjasheva O. V., Gusarov V. V. The investigation of the structure control possibility of nanocrystalline yttrium orthoferrite in its synthesis from amorphous powders. *Russian Journal of Applied Chemistry*. 2014;87(10): 1417–1421. https://doi.org/10.1134/S1070427214100048

3. Nguyen A. T., Nguyen V. Y., Mittova I. Ya., Mittova V. O., Viryutina E. L., Hoang C. Ch. T., Nguyen Tr. L. T., Bui X. V., Do T. H. Synthesis and magnetic properties of PrFeO$_3$ nanopowders by the co-precipitation method using ethanol. *Nanosystems: Physics, Chemistry, Mathematics*. 2020;11(4): 468–473. https://doi.org/10.17586/2220-8054-2020-11-4-468-473

4. Nguyen A. T., Phan Ph. H. Nh., Mittova I. Ya., Knurova M. V., Mittova V. O. The characterization of nanosized ZnFe$_2$O$_4$ material prepared by coprecipitation. *Nanosystems: Physics, Chemistry, Mathematics*. 2016;7(3): 459–463. https://doi.org/10.17586/2220-8054-2016-7-3-459-463

Condensed Matter and Interphases / Конденсированные среды и межфазные границы 2023;25(1): 61–71

E. I. Lisunova et al. Formation during glycine-nitrate combustion and magnetic properties of YFe$_{1-x}$Ni$_x$O$_3$...

5. Sherstyuk D. P., Starikov A. Yu., Zhivulin V. E., Zherebtsov D. A., Gudkova S. A., Perov N. S., Alekhina Yu. A., Astapovich K. A., Vinnik D. A., Trukhanov A. V. Effect of Co content on magnetic features and SPIN states in Ni – Zn spinel ferrites. *Ceramics International*. 2021;47(9): 12163–12169. https://doi.org/10.1016/j.ceramint.2021.01.063

6. Serrao C. R., Sahu J. R., Ramesha K., Rao C. N. R. Magnetoelectric effect in rare earth ferrites, LnFe$_2$O$_4$. *Journal of Applied Physics*. 2008;104(1): 16102. https://doi.org/10.1063/1.2946455

7. Xu C., Yang Y., Wang S., Duan W., Gu B., Bellaiche L. Anomalous properties of hexagonal rare-earth ferrites from first principles. *Physical Review B*. 2014;89: 205122. https://doi.org/10.1103/PhysRevB.89.205122

8. Kanhere P., Chen Z. A review on visible light active perovskite-based photocatalysts. *Molecules*. 2014;19: 19995–20022. https://doi.org/10.3390/molecules191219995

9. Ahmad T., Lone I. H., Ansari S. G., Ahmed J., Ahamad T., Alshehri S. M. Multifunctional properties and applications of yttrium ferrite nanoparticles prepared by citrate precursor route. *Materials and Design*. 2017;126: 331–338. https://doi.org/10.1016/j.matdes.2017.04.034

10. Jabbarzare S., Abdellahi M., Ghayour H., Chami A., Hejazian S. Mechanochemically assisted synthesis of yttrium ferrite ceramic and its visible light photocatalytic and magnetic properties. *Journal of Alloys and Compounds*. 2016;688: 1125–1130. https://doi.org/10.1016/j.jallcom.2016.07.123

11. Suthar L., Bhadala F., Roy M. Structural, electrical, thermal and optical properties of YFeO$_3$, prepared by SSR and sol – gel route: a comparative study. *Applied Physics A*. 2019;125: 452. https://doi.org/10.1007/s00339-019-2743-1

12. Nguyen A. T., Pham V. N. T., Nguyen T. T. L., Mittova V. O., Vo Q. M., Berezhnaya M. V., Mittova I. Ya., Do Tr. H., Chau H. D. Crystal structure and magnetic properties of perovskite YFe$_{1x}$Mn$_x$O$_3$ nanopowders synthesized by co-precipitation method. *Solid State Sciences*. 2019;96: 105922. https://doi.org/10.1016/j.solidstatesciences.2019.06.011

13. Popkov V. I., Almjasheva O. V. Formation mechanism of YFeO$_3$ nanoparticles under the hydrothermal condition. *Nanosystems: Physics, Chemistry, Mathematics*. 2014;5(5): 703–708. Available at: https://www.elibrary.ru/item.asp?id=22415667

14. Berezhnaya M. V., Al'myasheva O. V., Mittova V. O., Nguyen A. T., Mittova I. Ya. Sol-gel synthesis and properties of Y$_{1-x}$Ba$_x$FeO$_3$ nanocrystals. *Russian Journal of General Chemistry*. 2018;88(4): 626–631. https://doi.org/10.1134/S1070363218040035

15. Popkov V. I., Almjasheva O. V., Semenova A. S., Kellerman D. G., Nevedomskiy V. N., Gusarov V. V. Magnetic properties of YFeO$_3$ nanocrystals obtained by different soft-chemical methods. *Journal of Materials Science: Materials in Electronics*. 2017;28; 7163–7170. https://doi.org/10.1007/s10854-017-6676-1

16. Shobana M. K., Kwon H., Choe H. Structural studies on the yttrium-doped cobalt ferrite powders synthesized by sol-gel combustion method. *Journal of Magnetism and Magnetic Materials*. 2012;324: 2245–2248. https://doi.org/10.1016/j.jmmm.2012.02.110

17. Nguyen T. A., Pham V. N. T., Le H. T., Chau D. H., Mittova V. O., Nguyen L. T. Tr., Dinh D. A., Nhan Hao T. V., Mittova I. Ya. Crystal structure and magnetic properties of LaFe$_{1x}$Ni$_x$O$_3$ nanomaterials prepared via a simple co-precipitation method. *Ceramics International*. 2019;45: 21768–21772. https://doi.org/10.1016/j.ceramint.2019.07.178

18. Lima E., De Biasi E., Mansilla M. V., Saleta M. E., Granada M., Troiani H. E., Rechenberg H. R., Zysler R.D. Heat generation in agglomerated ferrite nanoparticles in an alternating magnetic field. *Journal of Physics D: Applied Physics*. 2012;46: 045002. https://doi.org/10.1088/0022-3727/46/4/045002

19. Bachina A., Ivanov V. A., Popkov V. I. Peculiarities of LaFeO$_3$ nanocrystals formation via glycine-nitrate combustion. *Nanosystems: Physics, Chemistry, Mathematics*. 2017;8(5): 647–653. https://doi.org/10.17586/2220-8054-2017-8-5-647-653

20. Martinson K. D., Kondrashkova, I. S., Popkov V. I. Synthesis of EuFeO$_3$ nanocrystals by glycine-nitrate combustion method. *Russian Journal of Applied Chemistry*. 2017;90(8): 1214–1218. https://doi.org/10.1134/S1070427217080031

21. Popkov V. I., Almjasheva O. V., Nevedomskyi V. N., Panchuk V. V., Semenov V. G., Gusarov V. V. Effect of spatial constraints on the phase evolution of YFeO$_3$-based nanopowders under heat treatment of glycine-nitrate combustion products. *Ceramics International*. 2018;44: 20906–20912. https://doi.org/10.1016/j.ceramint.2018.08.097

22. Lebedev L. A., Tenevich M. I., Popkov V. I. The effect of solution-combustion mode on the structure, morphology, and size-sensitive photocatalytic performance of MgFe$_2$O$_4$ nanopowders. *Condensed Matter and Interphases*. 2022;24(4): 496–503. https://doi.org/10.17308/kcmf.2022.24/10645

23. Popkov V. I., Almjasheva O. V., Nevedomskiy V. N., Sokolov V. V., Gusarov V. V. Crystallization behavior and morphological features of YFeO$_3$ nanocrystallites obtained by glycine-nitrate combustion. *Nanosystems: Physics, Chemistry, Mathematics*. 2015;6(6): 866–874. https://doi.org/10.17586/2220-8054-2015-6-6-866-874

24. Popkov V. I., Almyasheva O. V. Yttrium orthoferrite nanopowders formation under glycine-nitrate combustion conditions. *Journal of Applied Chemistry*. 2014;87(2): 167–171. https://doi.org/10.1134/S1070427214020074

Condensed Matter and Interphases / Конденсированные среды и межфазные границы   2023;25(1): 61–71

E. I. Lisunova et al.   Formation during glycine-nitrate combustion and magnetic properties of YFe$_{1-x}$Ni$_x$O$_3$...

25. Nguyen A. T., Chau H. Nguyen A. T., Chau H. O., Huong D. T., Mittova I. Ya. Structural and magnetic properties of YFe$_{1-x}$Co$_x$O$_3$ (0.1<x<0.5) perovskite nanomaterials synthesized by coprecipitation method. *Nanosystems: physics, chemistry, mathematics*. 2018;9(3): 424–429. https://doi.org/10.17586/2220-8054-2018-9-3-424-429

26. Nguyen A. T., Mittova I. Ya., Solodukhin D. O., Al'myasheva O. V., Mittova V. O., Demidova S. Yu. Sol-gel formation and properties of nanocrystals of solid solutions Y$_{1x}$Ca$_x$FeO$_3$. *Journal of Inorganic Chemistry*. 2014;59(2): 40–45. https://doi.org/10.7868/S0044457X14020159

27. Pomiro F., Gil D. M., Nassif V., Paesano A., Gomez M. I., Guimpel J., Sanchez R. D., Carbonio R. E. Weak ferromagnetism and superparamagnetic clusters coexistence in YFe$_{1x}$co$_x$O$_3$ (0 ⩽ x ⩽ 1) perovskites. *Materials Research Bulletin*. 2017;94: 472–482. https://doi.org/10.1016/j.materresbull.2017.06.045

28. Tomina E. V., Kurkin N. A., Maltsev S. A. Microwave synthesis of yttrium orthoferrite and doping with nickel. *Condensed Matter and Interphases*. 2019;21(2): 306–312. https://doi.org/10.17308/kcmf.2019.21/768

29. Tomina E. V., Darinsky B. M., Mittova I. Ya., Churkin V. D., Boikov N. I., Ivanova O. B. Microwave-assisted synthesis of YCo$_x$Fe$_{1-x}$O$_3$ nanocrystals. *Inorganic materials*. 2019;55(4): 390–394. https://doi.org/10.1134/S0002337X19040158

30. Shannon R.D. Revised effective ionic radii and systematic studies of interatomic distances in halides and chalcogenides. *Acta Crystallographica Section A*. 1976; A32(5): 751–767. https://doi.org/10.1107/S0567739476001551

31. Nguyen A. T., Pham V., Chau D. H., Mittova V. O., Mittova I. Ya., Kopeychenko E. Nguyen A. T., Pham V., Chau D. X., Nguyen A.T. P. Effect of Ni substitution on phase transition, crystal structure and magnetic properties of nanostructured YFeO$_3$ perovskite. *Journal of Molecular Structure*. 2020;1215: 12829. https://doi.org/10.1016/j.molstruc.2020.128293

32. Berezhnaya M. V., Mittova, I. Ya., Perov N. S., Al'myasheva O. V., Nguyen A. T., Mittova V. O., Bessalova V. V., Viryutina E. L. Production of zinc-doped yttrium ferrite nanopowders by the sol-gel method. *Russian Journal of Inorganic Chemistry*. 2018;63(6): 742–746. https://doi.org/10.7868/S0044457X18060077

Author information

Evgenia I. Lisunova, PhD student of the Department of Materials Science and the Industry of Nanosystems, Voronezh State University (Voronezh, Russian Federation).

https://orcid.org/0000-0002-8657-2135
kopejchenko00@mail.ru

Nikolai S. Perov, Dr. Sci. (Phys.–Math.), Professor, Head of the Department of Magnetism, Faculty of Physics, Lomonosov Moscow State University (Moscow, Russian Federation).

https://orcid.org/0000-0002-0757-4942
perov@magn.ru

Valentina O. Mittova, PhD, Professor of the Scientific-Research Institute of Experimental and Clinical Medicine, Laboratory of Molecular Medicine, Teaching University Geomedi (Tbilisi, Georgia).

https://orcid.org/0000-0002-9844-8684
valentina.mittova@geomedi.edu.ge

Boris V. Sladkopevtsev, Cand. Sci. (Chem.), Associate Professor of the Department of Materials Science and Nanosystem Technologies, Voronezh State University (Voronezh, Russian Federation).

https://orcid.org/0000-0002-0372-1941
dp-kmins@yandex.ru

Xuan Vuong Bui, PhD in Chemistry, Lecturer of the Faculty of Natural Sciences Education, Saigon University (Ho Chi Minh City, Vietnam).

https://orcid.org/0000-0002-3757-1099
bxvuong@sgu.edu.vn

Anh Tien Nguyen, PhD in Chemistry, Chief of Inorganic Chemistry Department, Ho Chi Minh City University of Education (Ho Chi Minh City, Vietnam).

https://orcid.org/0000-0002-4396-0349
tienna@hcmue.edu.vn

Yulia A. Alekhina, Researcher of the Department of Magnetism, Faculty of Physics, Lomonosov Moscow State University n (Moscow, Russian Federation).

https://orcid.org/0000-0003-1776-5782
Ya.alekhina@physics.msu.ru

Viktor F. Kostryukov, Dr. Sci. (Chem.), Associate Professor, Associate Professor of the Department of Materials Science and the Industry of Nanosystems, Voronezh State University (Voronezh, Russian Federation).

https://orcid.org/0000-0001-5753-5653
vc@chem.vsu.ru

Irina Ya. Mittova, Dr. Sci. (Chem.), Professor of the Department of Materials Science and the Industry of Nanosystems, Voronezh State University (Voronezh, Russian Federation).

https://orcid.org/0000-0001-6919-1683
imittova@mail.ru

Original articles

Activity and stability of PtCo/C electrocatalysts for alcohol oxidation

D. K. Mauer✉, S. V. Belenov, A. Yu. Nikulin, N. V. Toporkov

Southen Federal University,
105/42 Bolshaya Sadovaya str., Rostov-on-Don 344006, Russian Federation

Abstract

This study considers the liquid-phase synthesis of PtCo/C catalysts based on CoO_x/C composite carriers with different mass fractions of metals and Pt:Co ratios. The purpose of the article is to study the activity of PtCo/C electrocatalysts of various compositions in the oxidation reactions of methanol and ethanol and to compare their characteristics with their commercial PtRu/C and Pt/C analogues.

PtCo/C catalysts were synthesised with Pt:Co ratios of 1:1 and 3:1. The specific active surface of the obtained PtCo/C materials was determined, their activity in the oxidation reactions of methanol and ethanol and their resistance to poisoning by intermediate products of alcohol oxidation were studied. The structural and electrochemical characteristics of the obtained PtCo/C catalysts were studied by X-ray diffraction, cyclic voltammetry, and chronoamperometry. It was found that PtCo/C materials with a mass fraction of platinum close to 20% are the most active and stable as compared to their commercial PtRu/C and Pt/C analogues.

The presented results show that PtCo/C catalysts are a promising material for direct alcohol fuel cells.

Keywords: Methanol fuel cells, Ethanol fuel cells, Electrocatalysis, Ethanol oxidation reaction, Methanol oxidation reaction, Bimetallic catalysts

✉ Vladislav, S. Menshikov, e-mail: men.vlad@mail.ru

Condensed Matter and Interphases / Конденсированные среды и межфазные границы   2023;25(1): 72–84

D. K. Mauer et al.   Activity and stability of PtCo/C electrocatalysts for alcohol oxidation

1. Introduction

In recent years, fuel cell (FE) technologies, which use various alcohols as fuel, are being intensively developed. This is associated with the fact that they are highly efficient, low-emission, and easy to transport and refuel [1–5]. However, currently, such devices have a number of serious shortcomings, primarily associated with slow multistage methanol (MOR) or ethanol (EOR) oxidation reactions [6,7] and catalysts' insufficient stability and resistance to CO poisoning [8, 9]. Today, the most common catalysts for low-temperature hydrogen-air and alcohol fuel cells are platinum nanoparticles deposited on carbon black [2, 9]. However, pure platinum on a carbon carrier is not a very effective catalyst for MOR and EOR due to a rapid poisoning of its surface with CO and other products of alcohol oxidation [8–10]. Therefore, there is a need to search catalysts that would have a higher tolerance to the intermediate products of the oxidation reaction of alcohols.

One of the most promising approaches to improving the performance of catalysts is obtaining bimetallic catalysts by doping Pt with transition d-metals, such as: Co, Ni, Fe, Cu, etc. [11–16]. Increased activity of bimetallic platinum-containing electrocatalysts can be explained by geometric factors (decreased interatomic distance in the crystal lattice) [17], a change in the energy of the platinum d-orbitals [18], and a change in the surface morphology of the nanoparticles [19] associated with a selective dissolution of the alloying component [16]. It should be noted that currently the most effective bimetallic catalysts for MOR are PtRu/C catalysts [3]. However, they are quite costly since they contain precious metals.

It is known that Toyota uses PtCo/C catalysts in their Mirai cars [20], which proves that such systems are commercially promising. Hence, we assume that PtCo/C can also be effective for MOR and EOR. For example, the authors of [21] demonstrated that a PtCo alloy with a developed structure has a noticeably better activity in MOR in terms of mass activity, electrochemical surface area (ESA), the potential for the methanol oxidation onset, and durability as compared to Pt_3Co, Pt/C, and PtRu/C catalysts. The authors of [22] claim that nanoparticles obtained by the hydrothermal synthesis of PtCo in the form of concave nanocrosses whose dimensions exceed 20 nm demonstrate high activity and stability in MOR. The comparison of PtCo/C, PtNi/C, and Pt/C catalysts in operation [23] revealed that both bimetallic catalysts show higher characteristics of stability and activity in MOR as compared to the commercial catalyst. It should also be noted that the PtCo/C catalyst has increased stability as compared to PtNi/C. It is necessary to emphasise that it is highly challenging to develop catalysts for ethanol oxidation due to a complex oxidation mechanism and a large number of intermediate products [24]. That is why multicomponent platinum-containing catalysts are often used for EOR: PtRuNi/C, PtSnRh/C, PtSn/C, CoPtAu [25–27]. The use of PtCo/C catalysts in EOR is currently under study. A number of studies have been dedicated to the activity of such catalysts in EOR [28-31]. In [28], the authors found that PtCo and PtMn electrocatalysts obtained by electrodeposition on titanium foil show the greatest activity in the methanol and ethanol oxidation reactions as compared to pure platinum. The authors of [29] studied the activity of a number of PtCo nanoparticles deposited on graphene with an atomic Pt:Co ratio of 1:1, 1:7, and 1:44 and a size of particles of 1 to 3 nm. In this study, it was found that all Pt:Co catalysts demonstrate increased activity and stability in EOR as compared to platinum nanoparticles on graphene, and the catalyst with a Pt:Co ratio of 1:7 has the best characteristics. The paper [30] compared the activity in EOR of PtCo/C materials obtained by various methods of synthesis. PtCo/C catalysts prepared with ethylene glycol and sodium borohydride used as reducing agents were found to be the most active. In [31] it was shown that catalysts in the form of Pt_1Co_1 nanowires obtained by hydrothermal synthesis demonstrate 3.69 times higher mass activity in EOR than pure Pt.

Thus, doping platinum with some d-metals is a well-known method that significantly improves the characteristics of electrocatalysts in MOR and EOR. We believe that PtCo/C catalysts may be promising materials for direct alcohol fuel cells.

Hence, the purpose of this study was to study the characteristics of PtCo/C catalysts of various compositions obtained from composite

Condensed Matter and Interphases / Конденсированные среды и межфазные границы 2023;25(1): 72–84

D. K. Mauer et al. Activity and stability of PtCo/C electrocatalysts for alcohol oxidation

CoO$_x$/C carriers and to compare them with their commercial PtRu/C and Pt/C analogues.

2. Experimental

Platinum-cobalt catalysts were obtained by borohydride synthesis from CoO$_x$/C carriers with a cobalt oxide content of 8% and 25% as it had been described in an earlier published study [32]. The composition and structure of CoO$_x$/C carriers were also presented earlier [32]. Materials obtained from the carrier with a mass fraction of cobalt oxide of 8% were designated as PC2 (PtCo composition) and PC3 (Pt$_3$Co composition) materials with a mass fraction of oxide of 25% were designated as PC1 (PtCo composition).

The mass fraction of metals in the obtained samples was determined by thermogravimetry based on the weight of the unburned residue. For this, a weighed portion of the studied sample was placed in a pre-calcined crucible with a constant mass and heat treated at 800 °C for 40 min. When calculating the mass fraction of Pt and PtCo, the formation of Co$_3$O$_4$ oxide was taken into account.

The Pt:Co ratio in the obtained samples was determined by X-ray fluorescence analysis (XRF) using a RFS-001 spectrometer (Research Institute of Physics, Southern Federal University, Russia). The conditions of the analysis were as follows: the X-ray tube voltage: 50 kV; current: 150 μA; anode material: molybdenum; spectrum acquisition time: 300 s. X-ray fluorescence spectra were recorded and processed using the UniveRS software (Southern Federal University, Russia).

The XRD phase composition (XRD) and the average size of crystallites were determined by powder X-ray diffraction using an ARL X'TRA diffractometer (Cu K_α). The conditions of the experiment were as follows: room temperature, an angle range of 2θ from 15 to 55 degrees. The average crystallite size was determined using the Scherrer formula [33]:

$D = K\lambda/(FWHM \cos \theta)$,

where $K = 0.98$ is the Scherrer constant, λ is the wavelength of monochromatic radiation in Å, FWHM is the full width of the peak at half maximum (in radians), D is the average crystallite size, nm; θ is the reflection angle in radians.

The electrochemical behaviour of the catalysts was studied by cyclic voltammetry (CV) and chronoamperometry using a VesaSTAT 3 potentiostat. For this study, we used a rotating disk electrode and a three-electrode cell, a platinum wire was used as a counter electrode, and a silver chloride electrode was used as a reference electrode. All potentials in this study are relative to a reversible hydrogen electrode (RHE). A weighed portion of the catalyst with a mass of 0.0060 g was placed in a mixture of 100 μl of 0.5% Nafionalcohol solution and 900 μl of isopropyl alcohol (extra pure grade). The resulting suspension was homogenised in ultrasound for 30 minutes, while making sure that the water temperature did not rise above 20 °C. Then it was stirred on a vibrating platform for 30 minutes. After that, a 6 μl aliquot of ink was applied to the end of the disk electrode and dried while rotating at room temperature.

Surface standardisation was carried out in 0.1 M electrolyte solution (Sigma Aldrich HClO$_4$) saturated with argon at atmospheric pressure, in the range of potentials of 0.04–1.20 V at a sweep rate of 100 mV/s. The electrochemical surface area was determined by the formula:

$ESA(CO_{ad}) = Q_{CO}/Rm1000$,

where Q_{CO} is the amount of electricity spent on the oxidation of the chemisorbed CO monolayer on the voltammogramme measured at a sweep rate of 20 mV/s under similar conditions [5]; R is the amount of electricity spent on the oxidation of CO (420 μC/cm^2); and m is the mass of Pt on the electrode (g).

Catalysts' activity in MOR was evaluated in 0.1 M HClO$_4$ with the addition of a methanol solution to achieve a concentration of 0.5 M CH$_3$OH. CV were recorded in the same way as in the case of ESA. To evaluate the activity, the following generally accepted parameters were used [5]: Q_{CH3OH}, the amount of electricity used for the oxidation of methanol in the forward sweep of the potential; I_{max}, the maximum current density in the forward sweep of the potential, and $E_{initial}$, the potential for the oxidation onset of the direct anodic peak. To evaluate the tolerance of materials to CO, a chronoamperometry was used to evaluate the values of currents at the initial and final moment of the experiment. To do this, current decay curves were recorded at a constant potential of 0.6 V for 30 minutes. δ_{CO} coefficient

Condensed Matter and Interphases / Конденсированные среды и межфазные границы   2023;25(1): 72–84

D. K. Mauer et al.   Activity and stability of PtCo/C electrocatalysts for alcohol oxidation

(coefficient of long-term CO poisoning) was used to express CO tolerance in quantitative terms [34]

TEM analysis of the catalysts' composition and microstructure was carried out using a FEI Tecnai G2 F20S-TWIN TMP microscope with an EDAX attachment operating at an accelerating voltage of 200 kV. Electrocatalyst powders (0.5 mg) were placed in 1 ml of heptane to prepare samples for TEM analysis. The suspension was then dispersed by ultrasound, after which a drop of suspension was applied to a copper grid coated with a thin layer of amorphous carbon. The eZAF (MThin) software algorithm implemented in the EDAX TEAM software was used to calculate the concentrations of the elements with due account of their peak intensities and the exit cross-section of their secondary X-ray emission for the lines of each element at each point of the map.

3. Results and discussion

To study the effect of the composition and structure of PtCo/C catalysts on their activity in the oxidation reaction of alcohols, liquid-phase synthesis was used to obtain PtCo/C catalysts of different mass fractions of the metal component and Pt:Co ratios. X-ray diffraction patterns of the obtained PtCo/C materials (Fig. 1) had peaks related to the phases of carbon C (002) and platinum Pt (111) and Pt (200). It should be noted

that all reflections on the XRD patterns were characterised by a significant broadening, which is associated with the nanodispersed structure of the material. Also, all bimetallic materials were characterised by a shift of Pt (111) and Pt (200) peaks from the angles characteristic of the platinum phase (2θ = 39.8 and 46.3 degrees) towards higher values for angles 2θ. This fact is associated with a decreased lattice parameter (Table 1) due to the formation of solid Pt:Co and Pt:Ru solutions. The value of the crystal lattice parameter for solid solutions of the obtained PtCo/C materials was used to calculate the composition of solid Pt:Co solutions according to Vegard's law [35] (Table 1).

The XRD data with regard to reflection broadening and the Scherrer formula were used to calculate the average size of crystallites. As a result, for PC2, PC3, and JM20 catalysts, the calculated value was between 2.3 and 2.8 nm (Table 1), and for PtRu/C and PC1 catalysts it was 3.2 and 3.3 nm, respectively. According to the results of the XRF, the atomic metal ratios for all PtCo/C materials appeared to be close to those specified at the stage of synthesis (Table 1). However, it should be noted that the composition calculated according to Vegard's law differed significantly from the XRF data, which may be due to the incomplete entry of cobalt into the solid
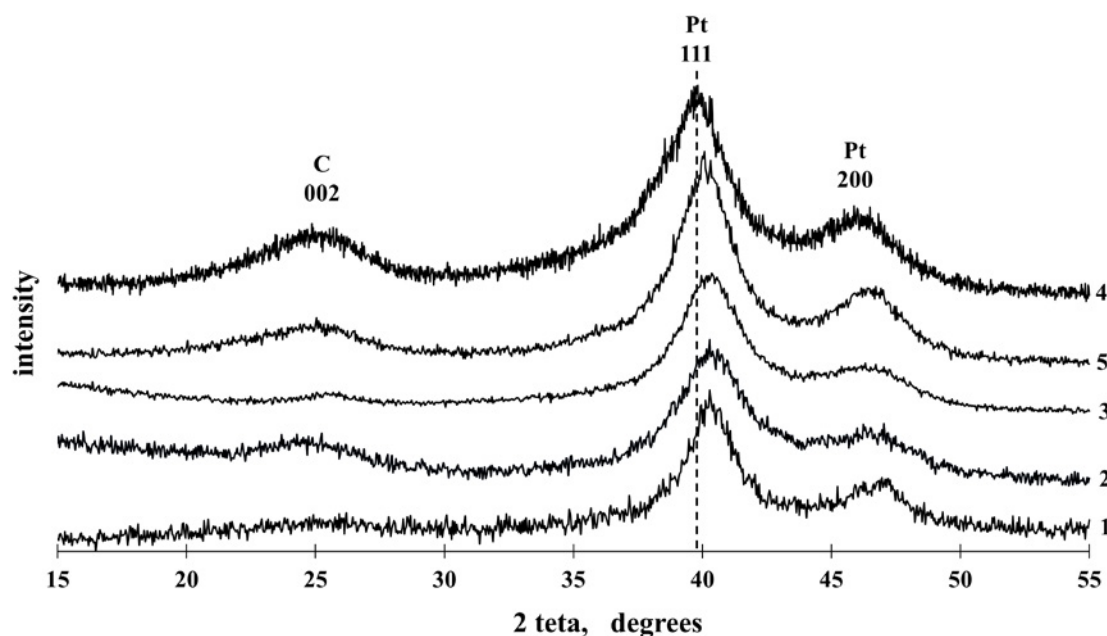
Fig. 1. X-ray diffraction patterns of platinum-containing materials: *1* – PC1; *2* – PC2; *3* – PC3; *4* – commercial Pt/C (JM20) sample; *5* – commercial PtRu/C sample

Condensed Matter and Interphases / Конденсированные среды и межфазные границы   2023;25(1): 72–84

D. K. Mauer et al.   Activity and stability of PtCo/C electrocatalysts for alcohol oxidation

Table 1. Characteristics of PC materials obtained from CoO_x/C carriers

Materials	M-Loading (Pt), ω %	Metal Composition (According to XRF)	Metal Composition (According to XRD)	Lattice Parameter of the Metal Component, Å	Average crystallite size (XRD) Pt, nm
PC1	30±0.6	$Pt_{1.1}Co_1$	$Pt_{7.1}Co$	3.875	3.3±0.3
PC2	14±0.3	$Pt_{1.6}Co_1$	$Pt_{6.9}Co$	3.876	2.6±0.2
PC3	18±0.4	$Pt_{3.2}Co_1$	$Pt_{6.9}Co$	3.876	2.8±0.2
JM20	20±0.4	–	–	3.923	2.3±0.2
PtRu/C	40±0.8	Pt_1Ru_1	–	3.851	3.2±0.3

solution with platinum (Table 1). It should be noted that despite the difference in Pt:Co ratios in the obtained PtCo/C materials according to the XRF data, the amount of cobalt in the solid solution was almost the same and corresponded to the composition of Pt_7Co.

The microstructure and composition of PC1 and PC2 materials were also studied by TEM. In addition, the composition of the studied samples was studied by local EDAX microanalysis (Fig. 2). TEM images of the PC2 material (Fig. 2d, e) showed a uniform distribution of particles over the surface of the carbon carrier. The diameter of single particles was in the range from 1.5 to 3.5 nm. There were also a number of large agglomerates with a size of about 10 nm. The PC1 sample was characterised by particles with the size in the range from 3 to 5 nm (Fig. 2a, b), however, this material had a large number of large agglomerates of about 20 nm. The average size of metal nanoparticles for both PC1 and PC2 materials was slightly bigger than the average size of crystallites according to XRD data. It should be noted that it is typical for Pt/C and PtM/C materials to have a smaller average size of their crystallites according to XRD data than the size of metal nanoparticles according to TEM data, which can be due to a number of reasons [36].
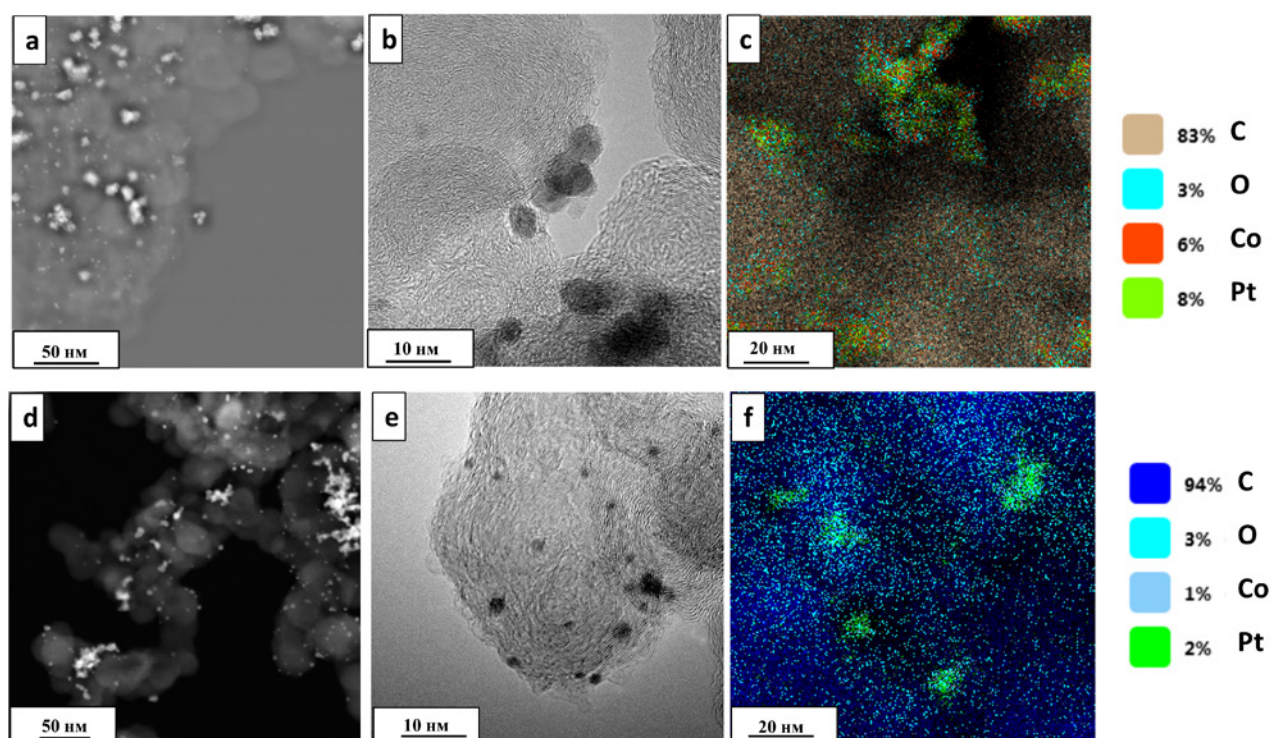
Fig. 2. TEM images of fragments of the material surface in PC1 (a, b), PC2 (d, e), and elemental mapping of fragments of PtCo/C surface in the PC1 (c), PC2 (e) samples

Condensed Matter and Interphases / Конденсированные среды и межфазные границы 2023;25(1): 72–84

D. K. Mauer et al. Activity and stability of PtCo/C electrocatalysts for alcohol oxidation

The results of elemental mapping of the surface fragments of the PC1 and PC2 materials indicated localisation of platinum and cobalt atoms in the same places (nanoparticles) (Fig. 2c, f), which also confirms the formation of bimetallic nanoparticles in the obtained materials. Local EDAX microanalysis used to determine the composition of the studied samples showed the atomic ratio of $PtCo_{1.27}$ and $PtCo_{1.05}$ for PC1 and PC2, respectively. These compositions were slightly different from the data received by the X-ray fluorescence analysis (Table 1), however, they confirmed a high content of cobalt in the obtained materials.

The CV of the obtained catalysts were characteristic of platinum-containing catalysts (Fig. 3). ESA values for all cobalt-containing catalysts determined by hydrogen adsorption/desorption were quite close (Table 2) and slightly

lower than those of the commercial JM20 sample. ESA values for PC materials were quite high and exceeded or corresponded to the materials described in [12, 37]. It should be noted that it is difficult to determine the area for PtRu/C catalysts by this method [38-39], therefore, the method of the oxidation of a chemisorbed CO monolayer was used to determine the surface area for all materials. ESA values determined by CO oxidation (Fig. 3b), which was carried out for all catalysts, are in good agreement with the data obtained for hydrogen adsorption/desorption (Table 2). Several maximums on the CO oxidation voltammogrammes may be caused by several factors , such as the formation of alloys of different compositions [40–41], the influence of various faces of platinum [42], and defects on the platinum faces [43]. All these factors may also apply to the obtained PtCo/C materials. It should
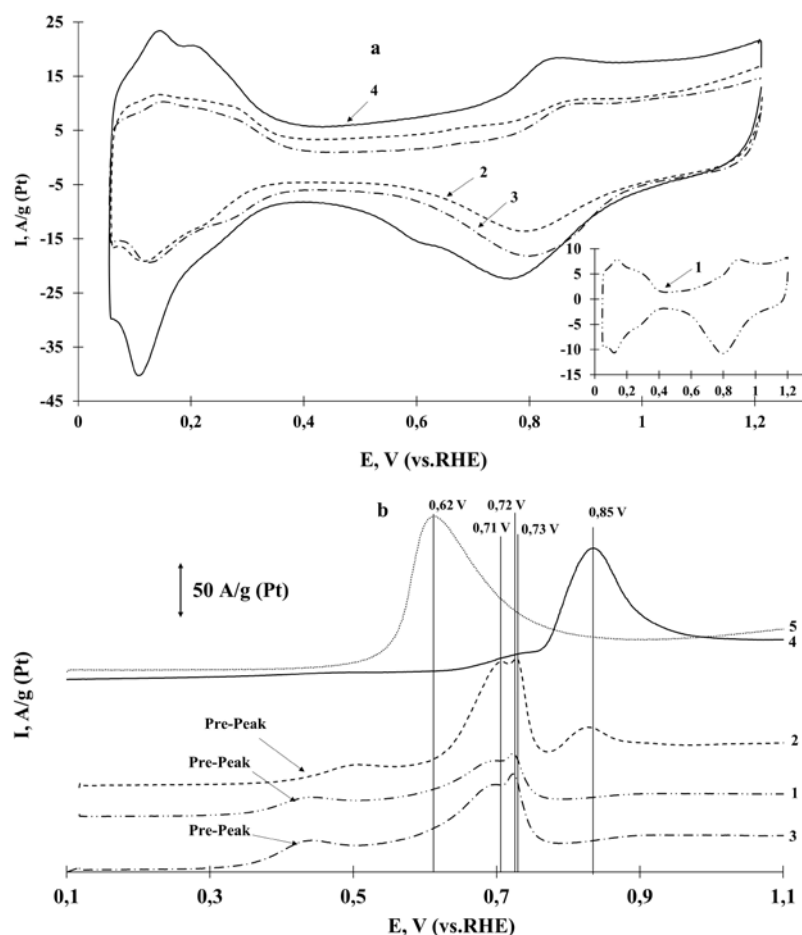
Fig. 3. Cyclic voltammogrammes (2nd cycle) (a) and fragments of cyclic voltammogrammes, including peaks of CO electrochemical desorption from the surface of nanoparticles of the studied catalysts (b): *1* – PC1; *2* – PC2; *3* – PC3; *4* – commercial Pt/C (JM20) sample; *5* – commercial PtRu/C sample. Electrolyte is 0.1 M $HClO_4$, argon atmosphere. Potential sweep rate is 40 mV/s

Condensed Matter and Interphases / Конденсированные среды и межфазные границы   2023;25(1): 72–84

D. K. Mauer et al.   Activity and stability of PtCo/C electrocatalysts for alcohol oxidation

Table 2. Parameters characterising the electrochemical behaviour of catalysts in MOR

Materials	ESA		I_{max}, A/g (Pt, PtRu)	$E_{initial}$, V	I chronoamperograms, A/g (Pt, PtRu)		δ_{CO}, %/s
	$H_{ads/des}$ m²/g(Pt)	CO m²/g(Pt)			$I_{initial}$ *	I_{final}	
PC1	52±5	45±5	563	0.57	19.3	9.5	0.039
PC2	51±5	58±5	849	0.54	32.6	17.4	0.036
PC3	53±5	47±5	834	0.55	35.4	16.6	0.041
JM20	75±7	76±7	401	0.58	20.5	17.2	0.012
PtRu/C	–	80±8	218	0.52	47.8	26.3	0.034

* – values 10 seconds after the start of the experiment.

be noted that CO oxidation for all bimetallic PtCo/C catalysts started at less positive potentials than for the commercial Pt/C material and at more positive potentials as compared to PtRu/C. At the same time, PtCo/C catalysts had a pronounced prepeak at potentials of 0.4–0.5 V. According to Petry's review [44], prepeaks in the range of potentials of 0.35–0.6 V are usually associated with the CO_{ads} oxidation in the defective sites of metal surfaces. This indirectly indicates a greater tolerance of the obtained bimetallic systems to CO poisoning as compared to the Pt/C material and makes them potentially very promising catalysts for oxidation reactions of organic substances in which CO is one of the intermediate products of the oxidation reaction [6].

The activity of the obtained catalysts in MOR was determined by the parameters of the direct peak of methanol oxidation on CV (Fig. 4a). The direct peak (0.7–1 V) was due to the oxidation of methanol molecules and their intermediates on the clean surface of platinum-containing catalysts. The PC2 and PC3 catalysts were characterised by the highest currents at the maximum, 849 and 834 A/g, respectively, which exceeded this parameter for the PC1 catalyst by 1.48 times and for the commercial JM20 and PtRu/C catalysts by 2.0 and 3.8 times. Such results correlate well with the data provided by the authors in [45]. It should be noted that PtRu/C had the lowest potential for the oxidation onset, which also indicated that it was the most active in MOR. $E_{initial}$ values for all PC materials were very close and were within the range of 0.54 to 0.57 V, which was lower than for the commercial JM20 catalyst (Table 2; Fig. 4b). From the forward sweep section of cyclic voltammogrammes, it is obvious that the PC2 material had the highest

activity in the potential range of 0.6 – 0.8 V. The PtRu/C and PC1 samples had the lowest current values at a potential of 0.6 V (Fig. 4B, inset), while the PC1 sample at potentials of 0.7 and 0.8 V was characterised by more than 2 times higher currents than the PtRu/C catalyst. An increased activity of PtCo/C materials in the MOR reaction as compared to Pt/C can be associated with both the size of metal nanoparticles and the structure of the active component and with the doping of platinum with cobalt. It should be noted that the effect of doping platinum with cobalt must not be excluded despite cobalt elution from the surface of nanoparticles. As mentioned in [45-48], the introduction of cobalt reduces the parameter of the crystal lattice and leads to a decrease in the energy of the *d*-sublevel, which leads to an increase in catalytic activity. These effects are still observed after cobalt elution from the surface of nanoparticles.

A comprehensive study of the characteristics of the studied catalysts in the oxidation reaction of alcohols requires chronoamperometric measurements at potentials close to the potential of the methanol oxidation onset, in this case at a potential of 0.6 V (Fig. 5). The highest values of $I_{initial}$ and I_{final} were characteristic of the PtRu/C catalyst. This fact agrees with the onset of CO oxidation at less positive potentials as compared to the other studied catalysts (Fig. 3). As for PC materials, the highest characteristics were shown by materials with a close mass fraction: 14 and 18 %. It should be noted that there was no dependence of the catalysts' characteristics in MOR on the catalysts' composition possibly due to the same composition of the solid PtCo solution according to XRD. What is more, the PC1 sample, which was characterised by the

Condensed Matter and Interphases / Конденсированные среды и межфазные границы   2023;25(1): 72–84

D. K. Mauer et al.   Activity and stability of PtCo/C electrocatalysts for alcohol oxidation
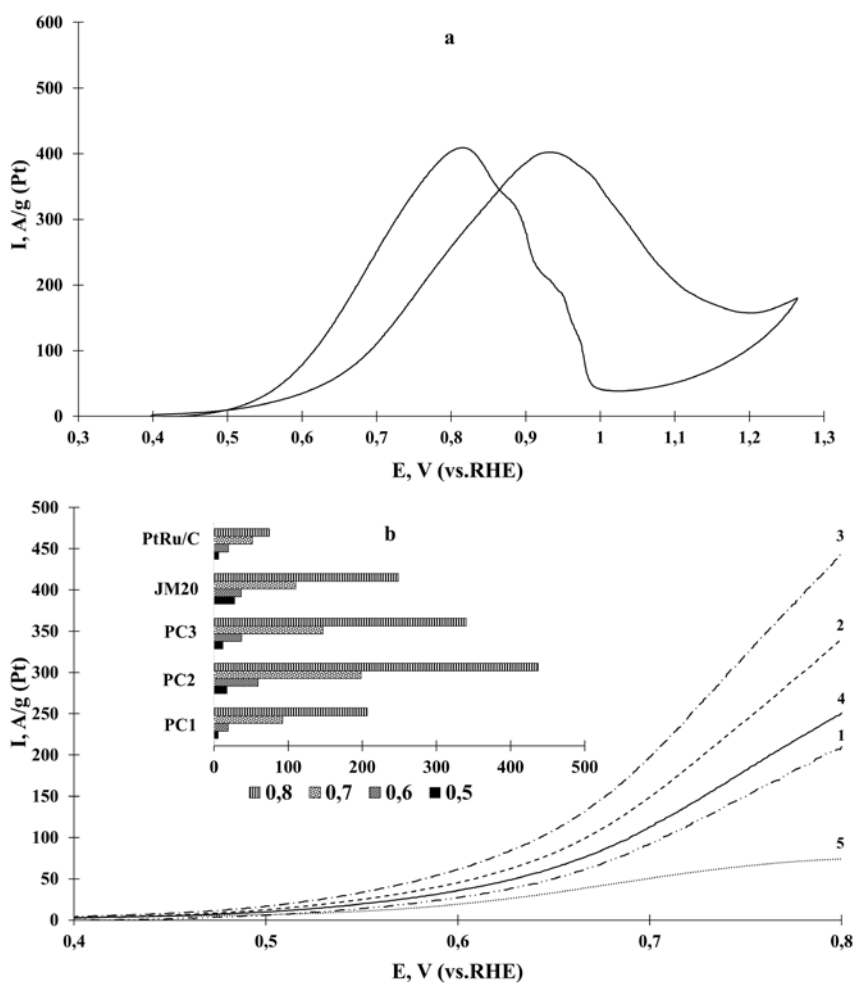
Fig. 4. Typical CV (a) and the forward sweep section of cyclic voltammogrammes in the range of potentials between 0.4 and 0.8 V (b), the values of specific currents at certain potentials (inset) for: *1* – PC1; *2* – PC2; *3* – PC3; *4* – JM20; *5* – commercial PtRu/C sample. Currents are normalised to the Pt or PtRu mass. Electrolyte is 0.1 M HClO$_4$ with 0.5 M CH$_3$OH. Ar atmosphere

Fig. 5. Chronoamperogrammes at a potential of 0.6 V for: *1* – PC1; *2* – PC2; *3* – PC3; *4* – JM20; *5* – commercial PtRu/C sample. Currents are normalised to the Pt or PtRu mass. Electrolyte is 0.1 M HClO$_4$ with 0.5 M CH$_3$OH. Ar atmosphere

Condensed Matter and Interphases / Конденсированные среды и межфазные границы   2023;25(1): 72–84

D. K. Mauer et al.   Activity and stability of PtCo/C electrocatalysts for alcohol oxidation
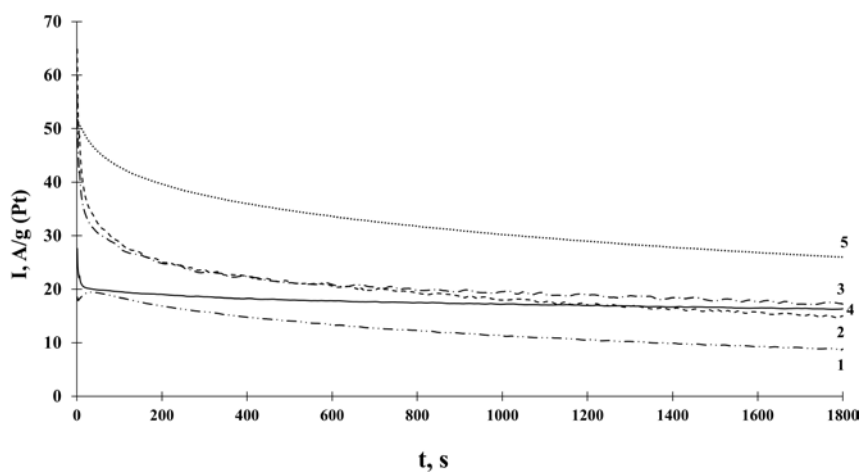
value of I_{on} close to that of the JM20 sample, degraded much more in 30 minutes and the value I_{fin} for PC1 was almost 2 times lower than for the commercial Pt/C catalyst (Fig. 5). The delta value shows the degree of material degradation during chronopotentiometry measurements. According to this value, the most stable material is the commercial Pt/C material (δ = 0.012). The other catalysts had significantly higher δ values than those of the JM20 catalyst, which indicates lower stability of both PtCo/C and PtRu/C catalysts. However, since the absolute values of $I_{initial}$ and I_{final} for PtRu/C were higher than those for JM20, this means that this catalyst is more promising.

Hence, it can be concluded that according to chronoamperometry data and the potential for the onset of CO oxidation, the most active catalyst in MOR is the commercial PtRu/C catalyst. However, PC2 and PC3 PtCo/C materials are much more superior to the commercial Pt/C catalyst.

The analysis of voltampreometry data for PtCo/C materials of the PC series revealed that they have higher characteristics at potentials above 0.5 V as compared to the commercial materials. These differences are due to the peculiarities of the methods. For example, CV data records curves with a high sweep rate, which allows assessing the activity of catalysts and their tolerance to CO. When measuring chronoamperometry, the system is observed until it reaches stationary currents, which provides information allowing to evaluate the stability of electrocatalysts and their poisoning by chemisorbed reaction products [49, 50].

Similar methods were used to study the activity of all obtained catalysts in EOR. According to cyclic voltammetry data (Fig. 6b), it can be concluded that the $E_{initial}$ value for PC materials is less positive as compared to commercial catalysts, which confirms the high activity of these catalysts
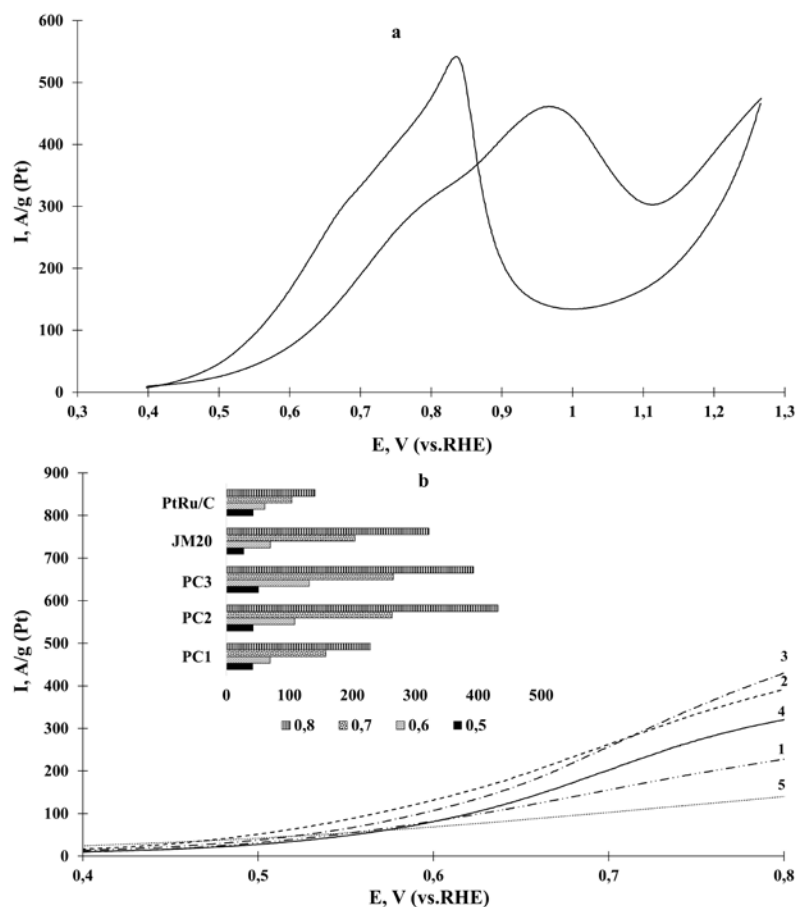
Fig. 6. Typical cyclic voltammogrammes (a) and the forward sweep section of cyclic voltammogrammes in the range of potentials between 0.4 and 0.8 V (b), the values of currents at certain potentials (inset) for: *1* – PC1; *2* – PC2; *3* – PC3; *4* – JM20; *5* – commercial PtRu/C sample. Currents are normalised to the Pt or PtRu mass. Electrolyte is 0.1 M $HClO_4$ with 0.5 M C_2H_5OH. Ar atmosphere

Condensed Matter and Interphases / Конденсированные среды и межфазные границы   2023;25(1): 72–84

D. K. Mauer et al.   Activity and stability of PtCo/C electrocatalysts for alcohol oxidation

in EOR (Table 3). At the same time, $E_{initial}$ values for all PC materials are quite close. In the case of EOR, the I_{max} value was 1.5 to 3.7 times higher for the PC2 sample than for all studied samples. It should also be noted that for the PC1 and PC3 materials, the I_{max} values were higher than for the commercial PtRu/C and JM20 catalysts (Table 3).

The analysis of the forward sweep sections of cyclic voltammogrammes in EOR allowed concluding that all catalysts but JM20 had high current values at a potential of 0.5 V. With further growth of potentials, there is a tendency to a sharp increase in currents for all PtCo/C catalysts of the PC series (Fig. 6b, inset).

According to the results of chronoamperometric (Fig. 7) measurements, the highest values of $I_{initial}$ and I_{final} were characteristic of the PC2 and PC3 materials. The PC2 material is characterised by the lowest value of δ, which indicates the highest stability of this material. It is important to emphasise that the PtRu/C catalyst exhibited characteristics close to the PC1

catalyst and inferior characteristics than the PC2 and PC3 materials. The JM20 catalyst, in turn, demonstrated the most inferior characteristics among all the studied materials.

The superior characteristics of the obtained PtCo/C materials as compared to the commercial PtRu/C sample in MOR can apparently be explained by a decreased crystal lattice parameter and electronic effects on the surface of nanoparticles caused by the influence of the subsurface solid PtCo solution [50, 51]. These effects lead to a decrease in the energy of the Pt d-sublevel. They reduce the adsorption of intermediate poisoning products on the surface of Pt and contribute to their easier removal from the surface [51, 52].

4. Conclusions

We studied the possibility of using PtCo/C materials of various compositions for the methanol and ethanol oxidation reaction. It was found that the samples of PtCo/C catalysts with a close mass fraction of platinum of 14 and 18%
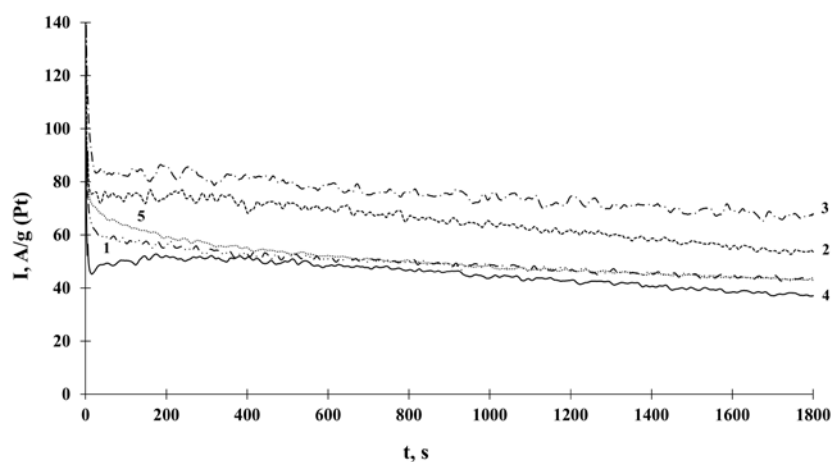
Fig. 7. Chronoamperogrammes at a potential of 0.6 V for: *1* – PC1; *2* – PC2; *3* – PC3; *4* – JM20; *5* – commercial PtRu/C sample. Currents are normalised to the Pt or PtRu mass. Electrolyte is 0.1 M $HClO_4$ with 0.5 M C_2H_5OH. Ar atmosphere

Table 3. Parameters characterising the electrochemical behaviour of catalysts in EOR

Materials	I_{max}, A/g (Pt, PtRu)	$E_{initial}$, V	I chronoamperograms, A/g (Pt, PtRu)		δ_{CO}, %/c
			$I_{initial}$ *	I_{final}	
PC1	460	0.53	61.6	43.6.	0.022
PC2	867	0.54	83.4	67.6	0.015
PC3	563	0.52	75.3	53.6	0.022
JM20	454	0.58	48.0	37.3	0.017
PtRu/C	234	0.59	68.7	43.7	0.027

* – values 10 seconds after the start of the experiment

Condensed Matter and Interphases / Конденсированные среды и межфазные границы 2023;25(1): 72–84

D. K. Mauer et al. Activity and stability of PtCo/C electrocatalysts for alcohol oxidation

and different compositions of PtCo/C and Pt$_3$Co/C are characterised by similar values of activity and stability in both EOR and MOR. Increased volume of platinum in the PtCo/C material has a negative impact on the catalyst's characteristics in MOR and EOR. For example, the values of I_{max} for the PC1 sample are the lowest among all PtCo/C samples and the values of currents in the range of potentials of 0.5 to 0.8 V are about 2 times lower in MOR and 1.5 times lower in EOR. According to the comparative analysis of the commercial Pt/C and PtRu/C catalysts in the methanol oxidation reaction, the most active and stable catalyst by a combination of chronoamperometry data and $E_{initial}$ values is the PtRu/C catalyst. In the case of ethanol oxidation reaction, the PC2 and PC3 samples of PtCo/C are superior to commercial samples in all of the studied parameters. Considering the combination of characteristics of PtCo/C materials, we conclude that further research of cobalt-containing catalysts can open new opportunities for alcohol fuel cells.

Contribution of the authors

The authors contributed equally to this article.

Conflict of interests

The authors declare that they have no known competing financial interests or personal relationships that could have influenced the work reported in this paper.

References

1. Sundarrajan S., Allakhverdiev S. I., Ramakrishna. S. Progress and perspectives in micro direct methanol fuel cell. *Int J of Hydrogen Energy*. 2012;37(10): 8765–8786. https://doi.org/10.1016/j.ijhydene.2011.12.017

2. Yaroslavtsev A. B., Dobrovolsckiy Yu. A., Shaglaeve N. S., Frolova L. A., Gerasimova E. V., Sanginov E. A. Nanostructured materials developed for the low temperature fuel elements, *Russian Chemical Reviews*. 2012;81(3) 191–201. https://doi.org/10.1070/RC2012v081n03ABEH004290

3. Karim N. A., Kamarudin S. K. Introduction to direct alcohol fuel cells (DAFCs). *Direct Liquid Fuel Cells*. 2021: 49–70. https://doi.org/10.1016/B978-0-12-818624-4.00002-9

4. Wang X. X., Swihart M. T., Wu G. Achievements, challenges and perspectives on cathode catalysts in proton exchange membrane fuel cells for transportation. *Nature Catalysis*. 2019;2: 578–589. https://doi.org/10.1038/s41929-019-0304-9

5. Menshikov V. S., Novomlinsky I. N., Belenov S. V., Alekseenko A. A., Safronenko O. I., Guterman V. E. Methanol, ethanol, and formic acid oxidation on new platinum-containing catalysts. *Catalysts*. 2021;11: 1–18. https://doi.org/10.3390/catal11020158

6. Petrii O. A. The progress in understanding the mechanisms of methanol and formic acid electrooxidation on platinum group metals. *Russian Journal of Electrochemistry*. 2019;55: 1-33. https://doi.org/10.1134/S1023193519010129

7. Vigier F., Coutanceau C., Hahn F., Belgsir E. M., Lamy, C. On the mechanism of ethanol electro-oxidation on Pt and PtSn catalysts: electrochemical and in situ IR reflectance spectroscopy studies. *Journal of Electroanalytical Chemistry*. 2004;563(1): 81–89. https://doi.org/10.1016/j.jelechem.2003.08.019

8. Chen A., Holt-Hindle P. Platinum-based nano-structuredmaterials properties, and applications. *Chemical Reviews*. 2010;110(6): 3767–3804. https://doi.org/10.1021/cr9003902

9. Shi G. Y., Yano H., Tryk D. A., Watanabe M., Uchida H. A novel Pt–Co alloy hydrogen anode catalyst with superlative activity, CO-tolerance and robustness. *Nanoscale*. 2016;8: 13893–13897. https://doi.org/10.1039/c6nr00778c

10. Antolini E., Salgado J. R. C., Gonzalez E. R. The methanol oxidation reaction on platinum alloys with the first row transition metals: The case of Pt-Co and -Ni alloy electrocatalysts for DMFCs: A short review. *Applied Catalysis B: Environmental*. 2006;63(1–2): 137–149. https://doi.org/10.1016/j.apcatb.2005.09.014

11. Baronia R., Goel J., Tiwari S., Singh P. Efficient electro-oxidation of methanol using PtCo nanocata-lysts supported reduced graphene oxide matrix as anode for DMFC. *International Journal of Hydrogen Energy*. 2017;42(15): 10238–10247. https://doi.org/10.1016/j.ijhydene.2017.03.011

12. Xu Y., Yuan Y., Ma A., Wu X., Liu Y., Zhang B. Composition-tunable Pt-Co alloy nanoparticle networks: facile room-temperature synthesis and sup-portless electrocatalytic applications. *ChemPhysChem*. 2012;13: 2601–2609. https://doi.org/10.1002/cphc.201100989

13. Sorsa O., Romar H., Lassi U., Kallio T. Co-elect-rodeposited mesoporous PtM (M=Co, Ni, Cu) as an active catalyst for oxygen reduction reaction in a polymer electrolyte membrane fuel cell. *Electrochimica Acta*. 2017;230: 49–57. https://doi.org/10.1016/j.electacta.2017.01.158

14. Mohl M., Dobo D., Kukovecz A., … Ajayan P. M. Formation of CuPd and CuPt bimetallic nanotubes by galvanic replacement reaction. *The Journal of Physical Chemistry C*. 2011;115: 9403–9409. https://doi.org/10.1021/jp112128g

15. Wang X., Zhang L., Wang F., Yu J., Zhu H. Nickel-introduced structurally ordered PtCuNi/C as high performance electrocatalyst for oxygen reduction reaction. *Progress in Natural Science: Materials Inter-*

Condensed Matter and Interphases / Конденсированные среды и межфазные границы 2023;25(1): 72–84

D. K. Mauer et al. Activity and stability of PtCo/C electrocatalysts for alcohol oxidation

national. 2020;30(6): 905–911. https://doi.org/10.1016/j.pnsc.2020.10.017

16. Asset T., Chattot R., Fontana M., ... Maillard F. A Review on recent developments and prospects for the oxygen reduction reaction on hollow Pt-alloy nanoparticles. *ChemPhysChem*. 2018;19: 1552–1567. https://doi.org/10.1002/cphc.201800153

17. Jalan V. M., Taylor E. J. Importance of interatomic spacing in catalytic reduction of oxygen in phosphoric acid. *Journal of The Electrochemical Society*. 1983;130(11): 2299–2302. https://doi.org/10.1149/1.2119574

18. Toda T., Igarashi H., Uchida H., Watanabe M. Enhancement of the electroreduction of oxygen on Pt Alloys with Fe, Ni, and Co. *Journal of The Electrochemical Society*. 1999;146: 3750–3756. https://doi.org/10.1149/1.1392544

19. Munoz M., Ponce S., Zhang G. R., Etzold B. J. M. Size-controlled PtNi nanoparticles as highly efficient catalyst for hydrodechlorination reactions. *Applied Catalysis B: Environmental*. 2016;192: 1–7. https://doi.org/10.1016/J.APCATB.2016.03.038

20. Konno N., Mizuno S., Nakaji H., Ishikawa Y. Development of compact and high- performance fuel cell stack. *SAE International Journal of Alternative Powertrains*. 2015;4(1): 123–129. https://doi.org/10.4271/2015-01-1175

21. Ding J., Ji S., Wang H., Pollet B. G., Wang R. Tailoring nanopores within nanoparticles of PtCo networks as catalysts for methanol oxidation reaction. *Electrochimica Acta*. 2017;255: 55–62. https://doi.org/10.1016/j.electacta.2017.09.159

22. Li Z., Jiang X., Wang X., ... Tang Y. Concave PtCo nanocrosses for methanol oxidation reaction. *Applied Catalysis B: Environmental*. 2020;270: 119135–119160. https://doi.org/10.1016/j.apcatb.2020.119135

23. Xu C., Hou J., Pang X., Li X., Zhu M., Tang B. Nanoporous PtCo and PtNi alloy ribbons for methanol electrooxidation. *International Journal of Hydrogen Energy*. 37(14), 10489–10498. https://doi.org/10.1016/j.ijhydene.2012.04.041

24. Flórez-Montaño J., García G., Guillén-Villafuerte O., Rodríguez J. L., Planes G. A., Pastor E. Mechanism of ethanol electrooxidation on mesoporous Pt electrode in acidic medium studied by a novel electrochemical mass spectrometry set-up. *Electrochimica Acta*. 2016;209: 121–131. https://doi.org/10.1016/j.electacta.2016.05.070

25. Bonesi A., Garaventa G., Triaca W., Castro Luna A. Synthesis and characterization of new electrocatalysts for ethanol oxidation. *International Journal of Hydrogen Energy*. 2008;33(13): 3499–3501. https://doi.org/10.1016/j.ijhydene.2007.12.056

26. Parreira L. S., Antoniassi R. M., Freitas I. C., de Oliveira D. C., Spinacé E. V., Camargo P. H. C., dos Santos M. C. MWCNT-COOH supported PtSnNi electrocatalysts for direct ethanol fuel cells: Low Pt content, selectivity and chemical stability. *Renewable Energy*. 2019;143: 1397–1405. https://doi.org/10.1016/j.renene.2019.05.067

27. Li J., Jilani S. Z., Lin H., ... Sun S. Ternary CoPtAu nanoparticles as a general catalyst for highly efficient electro-oxidation of liquid fuels. *Angewandte Chemie*. 2019;*131*(33): 11651–11657. https://doi.org/10.1002/ange.201906137

28. Xu C., Su Y., Tan L., Liu Z., Zhang J., Chen S., Jiang S. P. Electrodeposited PtCo and PtMn electrocatalysts for methanol and ethanol electrooxidation of direct alcohol fuel cells. *Electrochimica Acta*. 2009;54(26): 6322–6326. https://doi.org/10.1016/j.electacta.2009.05.088

29. Kepenienė V., Tamašauskaitė-Tamašiūnaitė L., Jablonskienė J., Vaičiūnienė J., Kondrotas R., Juškėnas R., Norkus E. Investigation of graphene supported platinum-cobalt nanocomposites as electrocatalysts for ethanol pxidation. *Journal of The Electrochemical Society*. 2014;161(14): F1354–F1359. https://doi.org/10.1149/05901.0217ecst

30. Mondal A., De A., Datta J. Selective methodology for developing PtCo NPs and performance screening for energy efficient electro-catalysis in direct ethanol fuel cell. *International Journal of Hydrogen Energy*. 2019;44(21): 10996–11011. https://doi.org/10.1016/j.ijhydene.2019.02.146

31. Zhai X., Wang P., Wang K., Li J., Pang X., Wang X., Li Z. Facile synthesis of PtCo nanowires with enhanced electrocatalytic performance for ethanol oxidation reaction. *Ionics*. 2020;26(6): 3091–3097. https://doi.org/10.1007/s11581-019-03419-1

32. Mauer D., Belenov S., Guterman V., ... Safronenko O. Gram-scale synthesis of CoO/C as base for PtCo/C high-performance catalysts for the oxygen reduction reaction. *Catalysts*. 2021;11(12): 1539–1558. https://doi.org/10.3390/catal11121539

33. Langford J. I., Wilson A. J. C. Scherrer after sixty years: a survey and some new results in the determination of crystallite size. *Journal of Applied Crystallography*. 1978;11(2): 102–103. https://doi.org/10.1107/S0021889878012844

34. Guo J. W., Zhao T. S., Prabhuram J., Chen R., Wong C.W. Preparation and characterization of a PtRu/C nanocatalyst for direct methanol fuel cells. *Electrochimica Acta*. 2005;51(4): 754–763. https://doi.org/10.1016/j.electacta.2005.05.056

35. Jenkins R., Snyder R. L. *Introduction to X-Ray powder diffractometry*. John Wiley & Sons; 1996. 432 p.

36. Favilla P. C., Acosta J. J., Schvezov C. E., Sercovich D. J., Collet-Lacos J. R. Size control of carbon-supported platinum nanoparticles made using polyol method for low temperature fuel cells. *Chemical Engineering Science*. 2013;101: 27–34. https://doi.org/10.1016/j.ces.2013.05.067

Condensed Matter and Interphases / Конденсированные среды и межфазные границы   2023;25(1): 72–84

D. K. Mauer et al.   Activity and stability of PtCo/C electrocatalysts for alcohol oxidation

37. Hu S., Wang Z., Chen H., Wang S., Li X., Zhang X., Shen P. K. Ultrathin PtCo nanorod assemblies with self-optimized surface for oxygen reduction reaction. *Journal of Electroanalytical Chemistry*. 2020;870, 114194–114201. https://doi.org/10.1016/j.jelechem.2020.114194

38. Huang T., Zhang D., Xue L., Cai W.-B., Yu A. A facile method to synthesize well-dispersed PtRuMoOx and PtRuWOx nanoparticles and their electrocatalytic activities for methanol oxidation. *Journal of Power Sources*. 2009;192(2): 285–290. https://doi.org/10.1016/j.jpowsour.2009.03.037

39. Kuo C.-W., Lu I-T., Chang L.-C., ... Lee J.-F. Surface modification of commercial PtRu nanoparticles for methanol electro-oxidation. *Journal of Power Sources*. 2013;240: 122–130. https://doi.org/10.1016/j.jpowsour.2013.04.001

40. Rudi S., Cui C., Gan L., Strasser P. Comparative study of the electrocatalytically active surface Aareas (ECSAs) of Pt alloy nanoparticles evaluated by H_{upd} and CO-stripping voltammetry. *Electrocatalysis*. 2014;5: 408–418. https://doi.org/10.1007/s12678-014-0205-2

41. Van der Vliet D. F., Wang C., Li D., ... Stamenkovic V. R. Unique electrochemical adsorption properties of Pt-skin surfaces. *Angewandte Chemie International Edition*. 2012;51(3): 3139–3142. https://doi.org/10.1002/anie.201107668

42. de la Fuente J. L. G., Rojas S., Martínez-Huerta M. V., Terreros P., Peña M. A., Fierro J. L. G. Functionalization of carbon support and its influence on the electrocatalytic behaviour of Pt/C in H_2 and CO electrooxidation. *Carbon*. 2006;44: 1919–1929. https://doi.org/10.1016/j.carbon.2006.02.009

43. Travitsky N., Ripenbein T., Golodnitsky D., Rosenberg Y., Burshtein L., Peled E. Pt-, PtNi- and PtCo-supported catalysts for oxygen reduction in PEM fuel cells. *Journal of Power Sources*. 2006;161: 782–789. https://doi.org/10.1016/j.jpowsour.2006.05.035

44. Li X., Liu Y., Zhu J., Tsiakaras P., Shen P. K. Enhanced oxygen reduction and methanol oxidation reaction over self-assembled Pt-M (M = Co, Ni) nano-flowers. *Journal of Colloid and Interface Science*. 2022;607: 1411–1423. https://doi.org/10.1016/j.jcis.2021.09.060

45. Yang H. Platinum-based electrocatalysts with core-shell nanostructures. *Angewandte Chemie International Edition*. 2011;50(12): 2674. https://doi.org/10.1002/anie.201005868

46. Paulus U. A., Wokaun A., Scherer G. G., Schmidt T. J., Stamenković V., Marković N. M., Ross P. N. Oxygen reduction on high surface area Pt-based alloy catalysts in comparison to well defined smooth bulk alloy electrodes. *Electrochimica Acta*. 2002;47(22-23): 3787. https://doi.org/10.1016/s0013-4686(02)00349-3

47. Xing Z., Li J., Wang S., Su C., Jin H. Structure engineering of $PtCu_3$/C catalyst from disordered to ordered intermetallic compound with heat-treatment for the methanol electrooxidation reaction. *Nano Research*. 2022;15: 3866–3871. https://doi.org/10.1007/s12274-021-3993-8

48. Petrii O. A. Pt–Ru electrocatalysts for fuel cells: a representative review. *Journal of Solid-State Electrochemistry*. 2008;12(5): 609–642. https://doi.org/10.1007/s10008-007-0500-4

49. Tolmachev Y. V., Petrii O. A. Pt–Ru electrocatalysts for fuel cells: developments in the last decade. *Journal of Solid-State Electrochemistry*. 2017;21: 613–639. https://doi.org/10.1007/s10008-016-3382-5

50. Castagna R. M., Sieben J. M., Alvarez A. E., Duarte M. M. E. Electrooxidation of ethanol and glycerol on carbon supported PtCu nanoparticles. *International Journal of Hydrogen Energy*. 2019;44: 5970–5982. https://doi.org/10.1016/j.ijhydene.2019.01.090

51. Fang B., Feng L. PtCo-NC catalyst derived from the pyrolysis of Pt-incorporated ZIF-67 for alcohols fuel electrooxidation. *Acta Physico-Chimica Sinica*. 2020;36(7): 1905023. https://doi.org/10.3866/PKU.WHXB201905023

Information about the authors

Dmitry D. Mauer, Researcher at the Department of Electrochemistry, Southern Federal University (Rostov-on-Don, Russian Federation).

https://orcid.org/0000-0002-1658-2426
dima333000@yandex.ru

Sergey V. Belenov, Cand. Sci. (Chem.), Research Fellow at the Department of Electrochemistry, Southern Federal University (Rostov-on-Don, Russian Federation).

https://orcid.org/0000-0003-2980-7089
serg1986chem@mail.ru

Aleksey Y. Nikulin, Researcher at the Department of Electrochemistry, Southern Federal University (Rostov-on-Don, Russian Federation).

chemistnik@yandex.ru

Toporkov N. Vasilyevich, trainee researcher, Research Institute of Physics Department of Analytical Instrumentation, Southern Federal University (Rostov-on-Don, Russian Federation).

ntoporkov@sfedu.ru.

Original articles

Hydrogen permeability of the Pd–Pb system foil of various composition

N. B. Morozova[1]✉, A. I. Dontsov[1,2], A. I. Fedoseeva[1], A. V. Vvedenskii[1]

[1]Voronezh State University,
1 Universitetskaya pl., Voronezh 394018, Russian Federation

[2]Voronezh State Technical University,
84 ul. 20-Letiya Oktyabrya, Voronezh 394006, Russian Federation

Abstract

The purpose of the study was identification of the role of the chemical composition of Pd, Pb-alloys based of palladium in the processes of injection and extraction of atomic hydrogen.

The objects of study were Pd-Pb alloy foils with a lead content of 3, 5, 7, 9, and 11 at. %, representing the β-phase of the solid solution. Samples with a thickness of 40 to 62 µm were obtained by cold rolling. Hydrogen permeability was studied by cyclic voltammetry and two-stage cathode-anode chronoamperometry in deaerated solutions of 0.1 M H_2SO_4. The obtained results were processed according to a mathematical model developed for electrodes of semi-infinite thickness.

The dependence of the hydrogen permeability coefficient, as well as the rate constants of the processes of injection and extraction of atomic hydrogen, on the chemical composition of the alloy has been revealed. It was found that the Pd–Pb alloy with a lead content of 5 at.% demonstrates the highest values of hydrogen permeability compared with samples of the same crystal structure, since the rate constant of atomic hydrogen injection is very sensitive to the alloy structure. The latter confirms that the phase-limiting transition of atomic hydrogen into the alloy is the rate-determining stage, at least in the initial period of time.

Keywords: Solid solution of Pd-Pb systems, Atomic hydrogen, Phase boundary transition, Alloy structure, Hydrogen permeability, Cathode injection, Anode extraction

✉ Morozova Natalya Borisovna, e-mail: mnb@chem.vsu.ru

Condensed Matter and Interphases / Конденсированные среды и межфазные границы   2023;25(1): 85–94

N. B. Morozova et al.   Hydrogen permeability of the Pd–Pb system foil of various composition

1. Introduction

Now, one of the promising areas is the development of materials for portable electronic sensors based on palladium alloys and their oxides [1–3]. Methods for the synthesis of such materials are not expensive and are compatible with planar technologies of the microelectronic industry [4, 5].

An analysis of literature sources indicates that metal oxide semiconductors based on palladium alloys have a significant advantage in detecting gases with oxidizing properties (ozone, nitrogen dioxide) compared to materials with n-type of conductivity, in particular tin (IV) oxide SnO_2, which is widely used for the detection of reducing gases [6]. However, the process of interaction of palladium alloys and metal oxide semiconductors based on them with reducing gases remains not fully understood.

Also, one of the important areas of hydrogen energetics is the production of high-purity hydrogen using membranes based on palladium and its alloys. Hydrogen is widely used as fuel for ecological transport and in power plants, as well as in industries such as micro- and nanoelectronics and reduction metallurgy [7–9]. Effective palladium membranes should have not only high specific hydrogen permeability and corrosion resistance, but also high plasticity [10, 11]. The forecasting of hydrogen permeability is an important step in the design of fused membranes for hydrogen separation. Hydrogen permeability in alloys is determined by the diffusion coefficient of hydrogen and its solubility. Since in modern technologies the consumption of high-purity hydrogen is in great demand, reduction of the cost of its production becomes necessary. Therefore, the transition from pure metals to alloys is one of the effective ways for reducing the cost of membranes. In addition, doping palladium with such chemical elements as Pb, Ru, Cu, Y, and Ag can increase the durability of the membrane [12–15].

The Pd-Pb system exhibits limited solubility over the entire range of compositions and temperatures. The investigated samples of alloys of the Pd-Pb system with a lead content of up to 14 at. % are substitutional solid solutions [16]. It was also shown in [17] that the Pd–Pb system has a fairly wide range of α-solubility compared to other binary palladium compounds. An analysis of the research results [12] showed that the addition of lead to palladium-based alloys leads not only to an increase in their hydrogen permeability, but also to an increase in corrosion resistance, strength, and plasticity. The fact that binary Pb–Pd alloys have an excellent ability to accumulate atomic hydrogen is also important [18].

The aim of this research was investigation of the role of the chemical composition of palladium-based Pd,Pb alloys in the processes of injection and extraction of atomic hydrogen.

2. Experimental

The studies were carried out on foils made of palladium-lead solid solution with a Pb content 3, 5, 7, 9, and 11 at. % obtained by cold rolling. The foil thickness of the Pd-Pb system ranged from 40 to 62 μm.

The studied samples were made in an electric arc furnace in a purified helium environment at a slight overpressure [12]. Pd–Pb systems were fused with lead and palladium with a purity of 99.95 wt. %. Each ingot was subjected to remelting 2–3 times, which allowed ensuring the uniformity of the composition. Then, the flat samples were melted from the original ingots for subsequent rolling into foil. The chemical composition of the alloy was controlled by scanning electron microscopy (SEM, Jeol-6510, Japan). The structure and phase composition of Pd,Pb samples were studied by X-ray diffractometry (ARL X'TRA, Switzerland).

For obtaining foil of a given thickness, the annealed samples were subjected to cold rolling followed by vacuum annealing at 950°C for 3 h, and then rolling on a four-high rolling mill in 10 passes with intermediate vacuum annealing at 900 °C for 30–90 min. The use of this technology allows to obtain foils with a uniform fine-grained structure of a solid solution with an FCC lattice. The electrode made of spectrally pure graphite, onto which metal samples, previously degreased with ethyl alcohol were deposited using a conductive graphite glue, was used for electrochemical measurements.

The studies were carried out in a glass three-electrode cell with the cathode and anode spaces separated by a thin section. The working solution was aqueous 0.1 M H_2SO_4 (extra pure

Condensed Matter and Interphases / Конденсированные среды и межфазные границы   2023;25(1): 85–94

N. B. Morozova et al.   Hydrogen permeability of the Pd–Pb system foil of various composition

grade), prepared using a bidistillate. Solutions were deaerated with chemically pure argon for 30 min. Platinated platinum Pt(Pt) was used as an auxiliary electrode. Copper sulphate reference electrode (0.1M $CuSO_4$ +0.1M H_2SO_4) was connected to the working electrode with a Luggin capillary and a thin section.

Electrochemical measurements were performed by cyclic voltammetry and two-stage cathode-anode chronoamperometry using an IPC-Compact potentiostat. Before obtaining the polarization dependences, the working electrode was subjected to preliminary preparation, for the removal of the products of oil annealing used in rolling, as well as for standardization of the surface condition. The preparation included preliminary polarization of the electrode for 500 s at the initial potential E_{pp} = 0.21 V, followed by cycling over a wide range of potentials. First, the potential was scanned from E_p to the cathode region E_c = -0.13 V, then the scanning direction was changed to the anode region up to E_a = 1.55 V and again returned to E_{pp}. The potential scan rate was 5 mV/s. According to this scheme, the samples were cycled four times without preparation of the electrode surface and changing the solution. Potentiodynamic curves (forward and reverse) were obtained in the same range of potentials at dE/dt = 5 mV/s.

The potential E_{pp} = 0.21 V was applied to the working electrode for 500 s before obtaining each two-stage cathode-anode i,t-curve. The curve corresponding to the cathode current transients was recorded at the hydrogenation potential E_c = −0.13 V, the hydrogenation potential values were the same for all studied samples. The duration of the hydrogenation process t_c of electrodes was changed from 1 to 10 s. Then the potential was switched to the hydrogen ionization potential E_p^a determined based on the anodic peak in the cyclic voltammogram. The current transients was recorded until it reached a constant value, which usually occurred within 500 s. After that, without turning off the cell

and without removing the electrode from the cell, the pre-polarization potential E_{pp} was again applied and the procedure with another time t_c was repeated. The hydrogenation time used in the study t_c = 10 s removed the possibility of palladium hydrides being formed.

All potentials are provided for a standard hydrogen electrode, and the current values are given per single unit of the visible surface.

3. Results and discussion

Hydrogen permeability depends on many factors, such as the roughness, structure, substructure, and phase composition of metal systems. Diffraction patterns of the studied Pd,Pb alloys with different lead content are shown in Fig. 1. The orientation of the (200) and (220) faces was most pronounced in alloys with a lead content of 3, 5, 9, and 11 at. %. This orientation is characteristic of cold-rolled samples due to grain elongation during rolling. The texture (111) and (311) was characteristic for an alloy with a lead content of 7 at. %. As can be seen from Fig. 1, the orientation of the faces of Pd-7 at. % Pb alloy was close to the orientation for pure palladium obtained under the same conditions.

The values of the crystal lattice parameters for alloys of the Pd−Pb system, obtained at different pretreatment temperatures in a vacuum are shown in Table 1 [12].

As can be seen from the data in the Table, an increase in the lead content in the alloy of the Pd−Pb system from 3 to 11 at. % results in a nonlinear change in the period of the crystal lattice, which reached a minimum at X_{Pb} = 5 at. %.

The production of thin metal alloys by cold rolling involves the use of organic oils. Subsequent annealing of rolled samples at temperatures of 900 and 950 °C results in the formation of annealing products on the surface of the alloys. The presence of such products manifested itself on the anodic branches of the potentiodynamic curves as a suppression of the ionization peak of atomic hydrogen and

Table 1. Lattice parameter of Pd–Pb alloys during vacuum heat treatment [12]

t, °C	X_{Pb}, at.%				
	3	5	7	9	11
25	3.9080±0.0005	3.9027±0.0007	3.9286±0.0007	3.9422±0.0003	3.9480±0.0002
200	3.9168±0.0005	3.9114±0.0013	3.9369±0.0002	3.9511±0.0010	3.9567±0.0006

Condensed Matter and Interphases / Конденсированные среды и межфазные границы 2023;25(1): 85–94

N. B. Morozova et al.   Hydrogen permeability of the Pd–Pb system foil of various composition
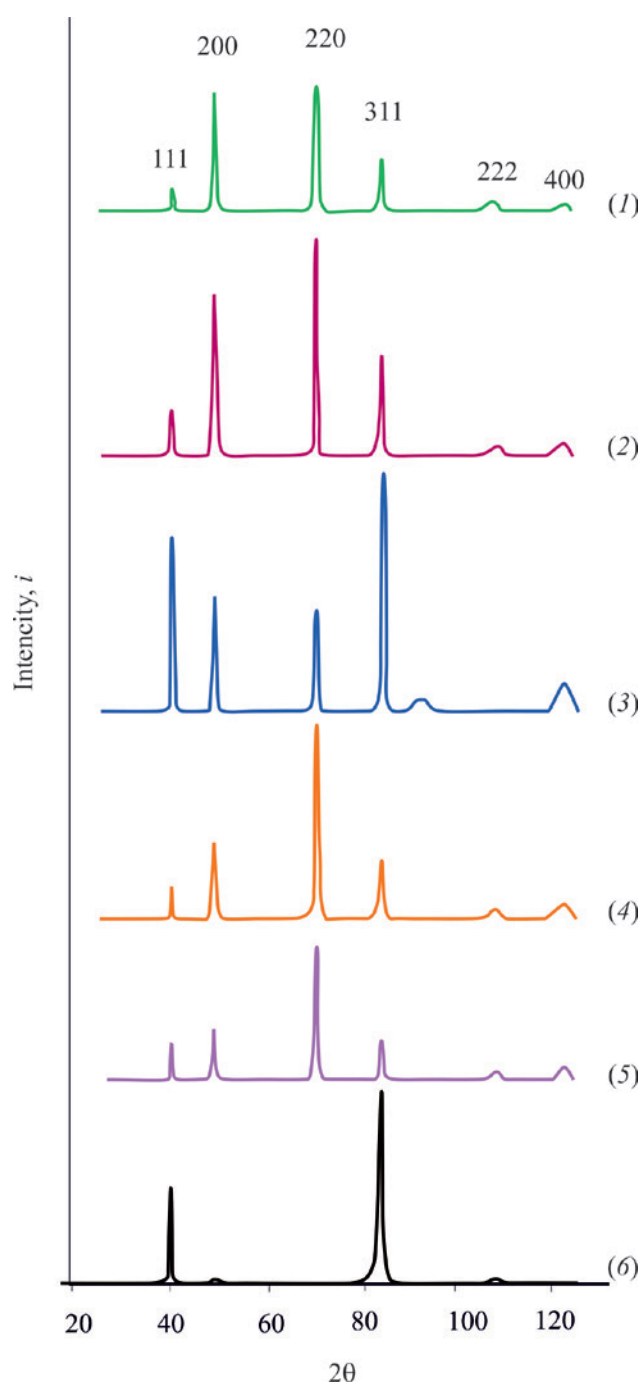
Fig. 1. X-ray diffractograms of Pd-Pb alloys foil with lead content: 3(*1*), 5 (*2*), 7 (*3*), 9 (*4*), 11 at. % (*5*) and Pd (*6*)

Fig. 2. Cyclic voltammograms for Pd-7 alloy foil at.% Pb obtained in 0.1 M H_2SO_4 at *dE/dt* = 5 mV/s; *1-4* – cycle numbers

atomic hydrogen ionization peak, and results in the disappearance of the oxidation peak. Five or more scan cycles did not lead to any noticeable changes in the obtained results.

Thus, the cyclic voltammetry method not only turned out to be sensitive to contamination of the surface of metal samples, but also allowed additional surface cleaning to be performed.

Cyclic voltammograms obtained on the foil electrodes of the Pd–Pb system with different lead content are shown in Fig. 3. The comparison of cyclic voltammograms revealed that 3 at.% of lead in the alloy results in a sharp increase in the ionization peak of atomic hydrogen compared to pure palladium. However, an increase in the concentration of lead to 11 at. % results in a decrease in the ionization rate of atomic hydrogen. The cathodic branch of the curve at a potential of ~0.65 V had a peak related to the reduction of surface palladium oxides, presumably PdO. The position and amplitude of this peak were practically independent of the lead concentration in the alloy. The observed maximum cathode current corresponds to the process of evolution of molecular hydrogen.

For the calculation of the hydrogen permeability parameters two-stage cathode-anode chronoamperograms of samples of the Pd-Pb system were used (Fig. 4). Their general view was similar for all alloys, however, as

the appearance of a peak in the potential range from 1.00 to 1.20 V (Fig. 2). This peak, which was clearly visible both in the first and second cycles of voltammograms, was probably associated with the oxidation of oil annealing products on the surface of the rolled foil. Further cycling of the potential significantly increased the height of the

Condensed Matter and Interphases / Конденсированные среды и межфазные границы   2023;25(1): 85–94

N. B. Morozova et al.   Hydrogen permeability of the Pd–Pb system foil of various composition

Fig. 3. Cyclic voltammograms for foil alloys of the Pd-Pb system with X_{Pb} = 3 (1), 5 (2), 7 (3), 9 (4), 11 (5) at. % and palladium (6) obtained in 0.1 M H_2SO_4 at dE/dt = 5 mV/s

the hydrogenation time increased, a gradual increase in anodic and cathodic currents was observed. It should be noted that if the nature of the declines on the anode and cathode i,t-curves for alloys with X_{Pb} up to 7 at. % was quite sharp, for alloys with a lead content of 9 and 11 at. %, the currents decrease more smoothly, which may be due to a change in the mechanism of the process.

As in the case of rather slow cyclic voltammograms, the pulsed cathodic and

anodic current transients with an increase in lead content up to X_{Pb} = 7 at. % first increased and then decreased. Therefore, the addition of Pb to the palladium crystal lattice in an amount of more than 7 at. % results in the suppression of both the intercalation process and the ionization of atomic hydrogen.

Using the results presented in [19], and taking into account the thickness of the studied samples, further processing of the experimental data was carried out using a mathematical model describing the injection and extraction of atomic hydrogen for electrodes of semi-infinite thickness [20]. This model assumes that during the period of hydrogenation t_c = 10 s, there is no through penetration of atomic hydrogen into the foil. In this case, according to [20], for the studied samples, the cathode current transients i_c is described by the equation:

$$i_c(t) = i_c^\infty + F\overleftarrow{k}\left(c_{\bar{H}}^s(\eta_c) - c_{\bar{H}}^e\right) \cdot \exp\left(\frac{\overleftarrow{k}^2 t}{D_H}\right) \text{erfc}\,\frac{\overleftarrow{k}t^{1/2}}{D_H^{1/2}}. \quad (1)$$

Here i_c^∞ is the maximum cathodic current, D_H is the diffusion coefficient of atomic hydrogen in the solid phase, $\overrightarrow{k}$ is the efficient rate constant of atomic hydrogen extraction, $\Delta c_{\bar{H}} = (c_{\bar{H}}^s(\eta^c) - c_{\bar{H}}^e)$ is the change in the concentration of atomic hydrogen $\bar{H}$ in the surface layer of the metal phase $c_{\bar{H}}^e$, and $c_{\bar{H}}^s$ is the equilibrium molar concentration $\bar{H}$ in the bulk and in the near-

Рис. 4. Двухступенчатые катодно-анодные хроноамперограммы, полученные в 0.1 M H_2SO_4 для фольги системы Pd–Pb с содержанием свинца 5 (а) и 11 ат. % (б)
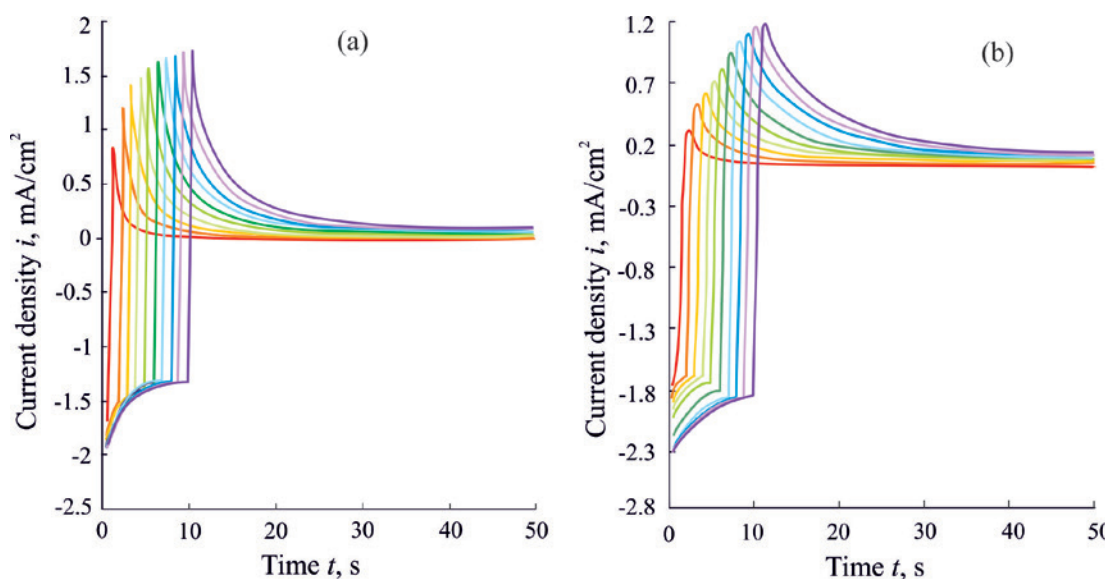
Condensed Matter and Interphases / Конденсированные среды и межфазные границы   2023;25(1): 85–94

N. B. Morozova et al.   Hydrogen permeability of the Pd–Pb system foil of various composition

surface layer of the film, respectively, and η_c is the cathodic overvoltage.

For short times when $t \leqslant 3$ s, and the parameter $\dfrac{\overleftarrow{k}t^{1/2}}{D_H^{1/2}} \ll 1$, equation (1) describes the initial period of the cathodic current transients, when the phase boundary kinetics mode is reached:

$$i_c(t) = i_c(0) - F\overleftarrow{k}\left[c_H^s(\eta_c) - c_H^e\right]\frac{2\overleftarrow{k}t^{1/2}}{\pi^{1/2}D_H^{1/2}}. \qquad (2)$$

In case when $\dfrac{\overleftarrow{k}t^{1/2}}{D_H^{1/2}} \gg 1$, which means that the limiting stage is the solid-phase diffusion H, equation (1) is transformed:

$$i_c(t) = i_c^\infty + \frac{FK_D}{\pi^{1/2}t^{1/2}}. \qquad (3)$$

Here $K_D = \Delta c_{\overline{H}} \cdot D_H^{1/2}$ is the coefficient that makes it possible to estimate the permeability of hydrogen into the metal in the case when the values $\Delta c_{\overline{H}}$ and D_H cannot be determined separately.

The linearisation of cathodic chronoamperograms obtained at $t_c = 10$ s, allowed to isolate two linear segments (Fig. 5). Their location, both at short and longer times, strongly depends on the concentration of palladium in the alloy. At the same time, the slopes of the obtained dependences not significantly differed from each other. This suggests that with an increase in the concentration of lead in the Pd,Pb-alloy, the mechanism of hydrogen insertion/ionization does not change.

Diffusion and kinetic parameters obtained from the linear dependences of the cathodic current transients are presented in Table 2:

Analysing the obtained parameters, we can conclude that the hydrogen permeability parameter K_D grows with an increase in the concentration of lead in the palladium crystal lattice, reaching a maximum value in the alloy with $X_{Pb} = 7$ at. %. A further increase in the lead content in the alloy results in a non-systematic change in the parameters.

The comparison of similar characteristics on Pd-Pb samples with pure palladium revealed that even small additions of lead to the palladium crystal lattice results in the suppression of the processes of incorporation and ionization of atomic hydrogen in the alloy. At the same time, the calculated values of the parameters determined for the alloy with $X_{Pb} = 7$ at. %, almost coincide with the values corresponding to palladium.

It should be noted that the effective rate constant of the extraction $\overrightarrow{k}$ for all the studied alloys remain practically unchanged within the experimental error. At the same time, the effective rate constant of the process of injection of atomic hydrogen $\overleftarrow{k}$ varied with the change in lead content in the alloy. As in the case of hydrogen permeability, these characteristics were maximal for an alloy containing 7 at. % Pd. As a consequence, the adsorption equilibrium constant K changed in the same way.
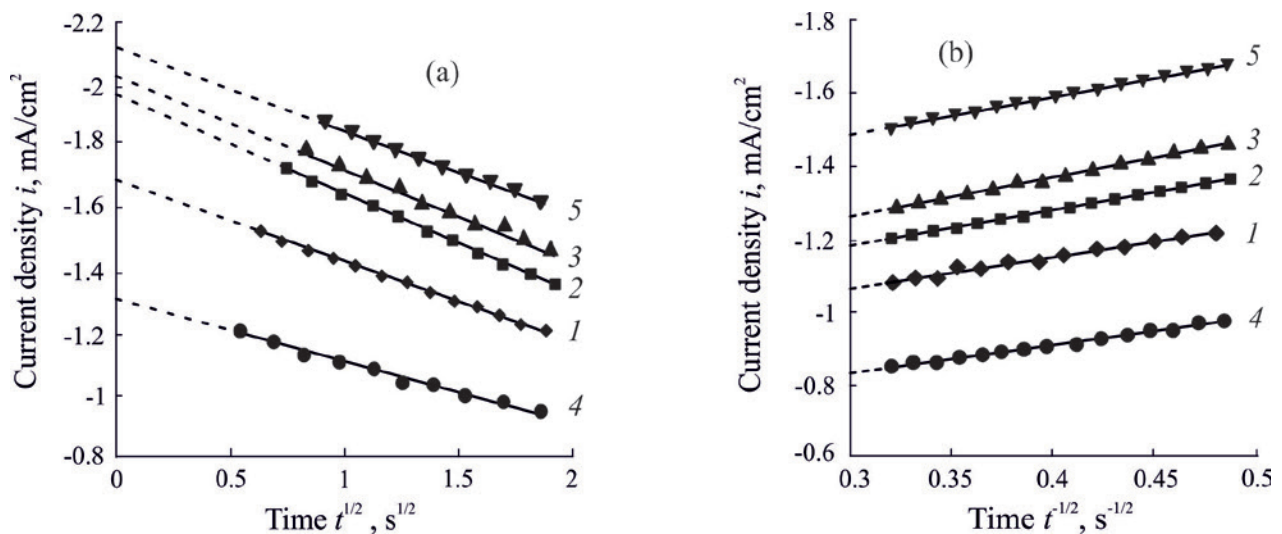
Fig. 5. Linearised cathodic potentiostatic current transients curves for Pd-Pb alloy samples with $X_{Pb} = 3$ (*1*), 5 (*2*), 7 (*3*), 9 (*4*), eleven (*5*) at. % for different time sections: a) $t = 0$-3 s; b) $t = 4$-10 s

Condensed Matter and Interphases / Конденсированные среды и межфазные границы   2023;25(1): 85–94

N. B. Morozova et al.   Hydrogen permeability of the Pd–Pb system foil of various composition

Table 2. Characteristics of cathode injection and anode extraction of atomic hydrogen obtained both on the foil of the Pd-Pb system with different lead content and on Pd [21]

X_{Pb}, at. %	$K_D \cdot 10^8$, mol/cm²·s^{1/2}	$\overleftarrow{k} \times 10^8$, mol/cm²·s	$\overleftarrow{k} \times 10^4$, cm/s	$K \cdot \times 10^5$, mol/cm³
0	2.06 ± 0.76	1.88 ± 0.47	2.43 ± 0.86	5.57 ± 2.24
3	1.07 ± 0,01	1.12 ± 0.04	3.77 ± 0.05	3.32 ± 0.02
5	1.40 ± 0.01	1.35 ± 0.01	3.07 ± 0.05	4.36 ± 0.01
7	2.02 ± 0.01	1.79 ± 0.01	3.24 ± 0.13	5.63 ± 0.01
9	0.65 ± 0.01	0.58 ± 0.05	3.21 ± 0.02	1.84 ± 0.01
11	1.64 ± 0.01	1.66 ± 0.01	3.05 ± 0.02	5.08 ± 0.01

The values $\overleftarrow{k}$ and $\overrightarrow{k}$ determined in these experiments are important characteristics of the phase-boundary exchange process. The most favourable orientation of a metal sample for surface processes is the (311) crystal face, which manifests itself in an alloy with X_{Pb} = 7 at. %. However, based on the obtained results, we can conclude that the results on hydrogen permeability for an alloy with 7 at. % cannot be compared with data for alloys of other compositions due to the different structure of the alloy. On the other hand, there was a non-monotonic decrease in both the diffusion and kinetic parameters of hydrogen permeability for alloys with X_{Pb} >7 at. %. In this regard, it should be noted that the alloy used in the study with X_{Pb} = 11 at. % had additional deformations associated with the folds of the sample. The latter could lead to an increase in the hydrogen permeability parameter.

The theoretical model developed for samples of semi-infinite thickness adequately describes the processes of cathodic injection and anodic extraction of atomic hydrogen on the studied alloys of the Pd–Pb system with different lead content. In particular, the complete anode current transients of step chronoamperograms is adequately described by the equation:

$$i_a(\tau) = i_a^\infty - \frac{F[c_H^s(\eta_c) - c_H^e]}{\pi^{1/2} t^{1/2}} D_H^{1/2} \times$$
$$\times \left(1 - \frac{\overleftarrow{k} \pi^{1/2} t^{1/2}}{D^{1/2}}\right) \exp\frac{\overleftarrow{k}^2 \tau}{D_H} \text{erfc} \frac{\overleftarrow{k}\tau}{D_H^{1/2}}. \tag{4}$$

Here $\tau = t - t_c$. In the anodic chronoamperogram (4), it is not possible to identify the sections corresponding to the phase boundary transition and diffusion processes separately. Therefore, the processes of injection and extraction of atomic hydrogen were considered only within the framework of the solid-phase diffusion kinetics regime. We assumed that, at sufficient times, these processes are limited only by solid-phase diffusion of atomic hydrogen in a metal sample. Taking into account this assumption, the section of the anode i,t-curve at $t > 50$ s was well linearised in the coordinates $i_a - [1/\tau^{1/2} - 1/t^{1/2}]$ according to the equation:

$$i_a(\tau) = i_a^\infty - \frac{FK_D}{\pi^{1/2}}\left(\frac{1}{\tau^{1/2}} - \frac{1}{t^{1/2}}\right). \tag{5}$$

The value of the hydrogen permeability coefficient K_D can also be found from the slope of the chronocoulograms plotted in coordinates $q_a(\tau) - [\tau^{1/2} + t_c^{1/2} - t^{1/2}]$ according to the equation:

$$q_a(\tau) \approx i_a^\infty \tau + \frac{2FK_D}{\pi^{1/2}}\left[\tau^{1/2} + t_c^{1/2} - t^{1/2}\right]. \tag{6}$$

The parameters of the injection and extraction processes of atomic hydrogen, determined using the linear dependences of the anode current transients, are presented in Table 3.

One can see from these data, the hydrogen permeability coefficient calculated based on the anode current transients was somewhat overestimated compared to K_D calculated based on cathode current transients (Fig. 6). Possibly,

Table 3. Hydrogen permeability coefficients calculated from anodic chronoamperograms and chronocoulograms for Pd-Pb system foils with different lead content

X_{Pb}, at.%	3	5	7	9	11
K_D $(i_a) \times 10^8$, mol/cm²·s^{1/2}	3.01 ± 0.04	4.41 ± 0.01	14.27 ± 0.30	1.49 ± 0.02	8.08 ± 0.30
K_D $(q_a) \times 10^8$, mol/cm²·s^{1/2}	4.86 ± 0.02	4.54 ± 0.02	7.11 ± 0.15	16.33 ± 0.05	23.87 ± 0.09

Condensed Matter and Interphases / Конденсированные среды и межфазные границы   2023;25(1): 85–94

N. B. Morozova et al.   Hydrogen permeability of the Pd–Pb system foil of various composition
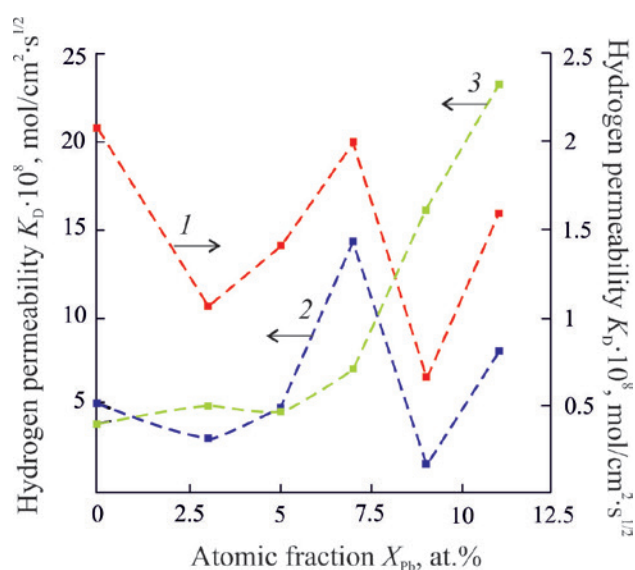
Fig. 6. Dependence of K_D on the composition of the alloy, found from the cathode (*1*) and anodic chrono-amperograms (*2*) and chronocoulograms (*3*)

this phenomenon is due to the effect of dilatation of the crystal lattice of palladium-based alloys. It should be noted that the nature of the K_D dependencies determined based on the cathode and anode chronoamperograms (Fig. 6) on the composition of the alloy was almost the same. At the same time, the K_D values, calculated based on chronocoulograms, non-linearly increase with an increase in the lead content in the alloy. The reasons for this discrepancy are not yet clear.

Lead additives strengthen palladium. Out of the studied alloys, a sample with a lead content of 11 at. % had higher hardness (HV) and higher tensile strength (σ_B) than the other samples [12]. As a result, this sample was more prone to the formation of macrodefects, which adversely affect the hydrogen permeability. In addition, this composition is close to peritectic for the Pd–Pb system, which can also affect the electrochemical behaviour of the sample.

Based on the presented X-ray patterns (Fig. 1), we can conclude that the alloy containing 7 at. % Pb is very similar to pure palladium by crystallographic orientation. Therefore, a comparison of the hydrogen permeability of alloys with a Pb content of 7 and 11 at. % with alloys of other compositions is incorrect. Therefore, among Pd,Pb alloys with a lead content of 3, 5, and 9 at.%, the alloy with X_{Pb} = 5 at.% was characterized by the highest hydrogen permeability. In this case,

alloys of the same crystallographic orientation were considered.

The data obtained are consistent with the results presented in [12]. However, the indicated values of hydrogen permeability, obtained using the physical method of the calibrated volume, did not reveal a noticeable effect based on the orientation of the crystal face. At the same time, the electrochemical method of non-stationary chronoamperometry used in this study turned out to be sufficiently sensitive to the structural state of the sample surface.

4. Conclusions

1. The injection and extraction of atomic hydrogen of the studied Pd-Pb samples of different compositions, obtained by cold rolling, is adequately described by a mathematical model developed for electrodes of semi-infinite thickness.

2. Potentiodynamic and chronoamperometric dependences for alloys of the Pd-Pb system with lead content X_{Pb} ⩽ 11 at. % showed that small additions of lead to palladium did not change the kinetics of hydrogen evolution. An alloy with a lead content of 5 at. % demonstrated the best hydrogen permeability among the alloys of the Pb–Pd system, considering samples with the same structure.

3. It was established that when lead is added in an amount of up to 7 at. % into the crystal lattice of palladium, both the atomic hydrogen ionization rate and hydrogen permeability increased. However, a further increase in the lead content in the alloy results in suppression of the process. At the same time, the addition of lead results in a decrease in the hydrogen permeability constant K_D, as well as the effective rate constant of atomic hydrogen injection $\vec{k}$ compared to pure palladium.

4. The electrochemical method of chronoampe-rometry turned out to be quite sensitive to the structural state of the sample surface. The alloy structure especially affected the phase-boundary exchange stage, which was reflected in the effective rate constant of atomic hydrogen injection.

Contribution of the authors

The authors contributed equally to this article.

Condensed Matter and Interphases / Конденсированные среды и межфазные границы   2023;25(1): 85–94

N. B. Morozova et al.   Hydrogen permeability of the Pd–Pb system foil of various composition

Conflict of interests

The authors declare that they have no known competing financial interests or personal relationships that could have influenced the work reported in this paper.

References

1. Marikutsa A. V., Rumyantseva M. N., Gaskov A. M., Samoylov A. M. Nanocrystalline tin dioxide: Basics in relation with gas sensing phenomena. Part I. Physical and chemical properties and sensor signal formation, *Inorganic Materials*, 2015;51(13): 1329–1347. https://doi.org/10.1134/s002016851513004x

2. Ryabtsev S. V., Shaposhnik A. V., Samoylov A. M., Sinelnikov A. A., Soldatenko S. A., Kuschev S. B., Ievlev V. M. Thin films of palladium oxide for gas sensors. *Doklady Physical Chemistry*. 2016;470(2): 158–161. https://doi.org/10.1134/S0012501616100055

3. Ievlev V. M., Ryabtsev S. V., Shaposhnik A. V., Samoylov A. M., Kuschev S. B., Sinelnikov A. A. Ultrathin films of palladium oxide for oxidizing gases detecting, *Procedia Engineering*, 2016;168: 1106–1109. https://doi.org/10.1016/j.proeng.2016.11.357

4. Marikutsa A. V., Rumyantseva M. N., Gaskov A. M., Samoylov A. M. Nanocrystalline tin dioxide: Basics in relation with gas sensing phenomena part II. Active centers and sensor behavior. *Inorganic Materials*. 2016;52(13): 1311–1338. https://doi.org/10.1134/S0020168516130045

5. Ryabtsev S. V., Ievlev V. M., Samoylov A. M., Kuschev S. B., Soldatenko S. A., Microstructure and electrical properties of palladium oxide thin films for oxidizing gases detection. *Thin Solid Films*. 2017;636: 751–759. https://doi.org/10.1016/j.tsf.2017.04.009

6. Korotcenkov G., Cho B. K. Ozone measuring: What can limit application of SnO$_2$-based conductometric gas sensors? *Sensors and Actuators B*. 2012;161(1): 28–44. https://doi.org/10.1016/j.snb.2011.12.003

7. Slovetsky D. I., Chistov E. M., Roshan N. R. Production of pure hydrogen. *Mezhdunarodnyj nauchnyj zhurnal al'ternativnaja jenergetika i jekologija*. 2004;1(9): 43–46. (In Russ., abstract in Eng). Available at: https://www.elibrary.ru/item.asp?id=9336911

8. Yan F., Xu L., Wang Y. Application of hydrogen enriched natural gas in spark ignition IC engines: from fundamental fuel properties to engine performances and emissions *Journal of Renewable and Sustainable Energy Reviews*. 2018;82(1): 1457–1488. https://doi.org/10.1016/j.rser.2017.05.227

9. Cappelletti A., Martelli F. Investigation of a pure hydrogen fueled gas turbine burner. *International Journal of Hydrogen Energy*. 2017;42(15): 10513–10523. https://doi.org/10.1016/j.ijhydene.2017.02.104

10. Adhikari S., Fernando S. Hydrogen membrane separation techniques. *Industrial & Engineering Chemistry Research*. 2006;45(3): 875-881. https://doi.org/10.1021/ie050644l

11. Paglieri S. N., Way J. D. Innovations in palladium membrane research. *Separation and Purification Methods*. 2002;31(1): 1–169. https://doi.org/10.1081/SPM-120006115

12. Gorbunov S. V., Penkina T. N., Roshan N. R., Chustov E. M., Burkhanov G. S., Kannykin S. V. Palladium–lead alloys for the purification of hydrogen-containing gas mixtures and the separation of hydrogen from them. *Russian Metallurgy (Metally)*. 2017;(1): 54–59. https://doi.org/10.1134/S0036029517010050

13. Ievlev V. M., Roshan N. R., Belonogov E. K., Kushev S. B., Kannikin S. V., Maksimenko A. A., Dontsov A. I., Glazunova Y. I. Hydrogen permeability of foil of Pd-Cu, Pd-Ru and Pd-In-Ru alloys received by magnetron sputtering *Condensed Matter and Interphases*. 2012;14(4): 422-427. (In Russ., abstract in Eng.). Available at: https://www.elibrary.ru/item.asp?id=18485336

14. Iwaoka H., Ide T., Arita M., Horita Z. Mechanical property and hydrogen permeability of ultrafine-grained Pd–Ag alloy processed by high-pressure torsion. *International Journal of Hydrogen Energy*. 2017;42(38): 24176–24182. https://doi.org/10.1016/j.ijhydene.2017.07.235

15. Sakamoto Y., Chen F. L., Kinari Y. Permeability and diffusivity of hydrogen through Pd-Y-In(Sn, Pb) alloy membranes. *Journal of Alloys and Compounds*. 1994;205(1–2): 205–210. https://doi.org/10.1016/0925-8388(94)90790-0

16. Vassiliev V., Mathon M., Gambino M., Bros J. P. The Pd-Pb system: excess functions of formation and liquidus line in the range $0<X_{Pd}>0.60$ and $600<T<1200$ K. *Journal of Alloys and Compounds*. 1994;215(1-2): 141–149. https://doi.org/10.1016/0925-8388(94)90831-1

17. Durusell Ph., Feschotte P. The binary system Pd-Pb. *Journal of Alloys and Compounds*. 1996;236(1-2) 195–202. https://doi.org/10.1016/0925-8388(95)02056-X

18. Gierlotka W., Dębski A., Terlicka S., Saternus M., Fornalczyk A., Gąsior W. On the Pb-Pd system. Calorimetric studies and ab-initio aided thermodynamic calculations. *Journal of molecular liquid*. 2020;316: 113806. https://doi.org/10.1016/j.molliq.2020.113806

19. Fedoseeva A. I., Morozova N. B., Dontsov A. I., Kozaderova O. A., Vvedenskii A. V. Cold-rolled binary palladium alloys with copper and ruthenium: injection and extraction of atomic hydrogen. *Russian Journal of Electrochemistry*. 2022;58(9): 812–822. https://doi.org/10.1134/S1023193522090051

20. Morozova N. B., Vvedenskii A. V., Beredina I. P. The phase-boundary exchange and the non-steady-state diffusion of atomic hydrogen in Cu–Pd and

Condensed Matter and Interphases / Конденсированные среды и межфазные границы   2023;25(1): 85–94

N. B. Morozova et al.   Hydrogen permeability of the Pd–Pb system foil of various composition

Ag–Pd alloys. I. Aanalysis of the model. *Protection of metals and physical chemistry of surfaces*. 2014;50(6): 699–704. https://doi.org/10.1134/S2070205114060136

21. Morozova N. B., Vvedensky A. V., Beredina I. P. The phase-boundary exchange and the non-steady-state diffusion of atomic hydrogen in Cu-Pd and Ag-Pd alloys. II. Experimental data. *Protection of metals and physical chemistry of surfaces*. 2015; 51(1): 72–80. https://doi.org/10.1134/S2070205115010098

Information about of authors

Natalia B. Morozova, Cand. Sci. (Chem.), Associate Professor at the Department of Physical Chemistry, Voronezh State University (Voronezh, Russian Federation).

https://orcid.org/0000-0003-4011-6510

mnb@chem.vsu.ru

Alexey I. Dontsov, Cand. Sci. (Phys.–Math.), Associate Professor at the Department of Materials Science and Industry of Nanosystems, Voronezh State University; Associate Professor at the Department of Physics, Voronezh State Technical University, Voronezh, Russian Federation; Senior Researcher.

https://orcid.org/0000-0002-3645-1626

dontalex@mail.ru

Anastasia I. Fedoseeva, 4th year post-graduate student at the Department of Physical Chemistry, Voronezh State University (Voronezh, Russian Federation).

https://orcid.org/0000-0002-6041-7460

Kanamepsp@yandex.ru

Alexander V. Vvedenskii, Dr. Sci. (Chem.), Professor, Professor at the Department of Physical Chemistry, Voronezh State University (Voronezh, Russian Federation).

https://orcid.org/0000-0003-2210-5543

alvved@chem.vsu.ru

Original articles

Simulation of the molecular dynamics of the passage of liposome with cinnarizine through the blood-brain barrier

Yu. A. Polkovnikova✉

Voronezh State University,
1 Universitetskaya pl., Voronezh 394018, Russian Federation

Abstract

Liposomal preparations have a number of advantages: they protect the cells of the body from the toxic effects of drugs; prolong the action of the drug introduced into the body; protect medicinal substances from degradation; promote the manifestation of targeted specificity due to selective penetration from blood into tissues; change the pharmacokinetics of drugs, increasing their pharmacological effectiveness; make it possible to create a water-soluble form of a number of medicinal substances, thereby increasing their bioavailability. In this work, studies were carried out for the development of the method for determining the degree of inclusion of cinnarizine used as a corrector of cerebrovascular accidents into liposomes from soy lecithin. The aim of this study was to determine the distance between the membranes of endotheliocytes, which is critical for the passage of a liposome through the blood-brain barrier.

A simulation of changes in the structure of a liposome with cinnarizine located between two cell membranes was carried out using the molecular dynamics method at various distances between the membranes. A square planar fragment of a bilayer phospholipid membrane was assembled using the Internet service Charmm-GUI->Input Generator->Martini Maker->BilayerBuilder (http://www.charmm-gui.org/?doc=input/mbilayer). Geometry optimization and molecular dynamics simulation were performed in Gromacs 2019 using Martini 2.2 force field. According to the results of the simulation of coarse-grained molecular dynamics, a liposome from purified soy lecithin with cinnarizine adsorbed on its inner and outer surface is able to maintain integrity, being between the membranes of endotheliocytes at a distance between membranes of more than 8 nm. When the distance between the membranes of endothelial cells is less than 8 nm, the liposome with cinnarizine located between the endotheliocytes can lose its structural integrity due to fusion with the endothelial cell membrane.

As a result of the studies, the distance between the membranes of endotheliocytes was established, at which point the liposome with cinnarizine, located between endotheliocytes, can lose its structural integrity due to fusion with the endothelial cell membrane.

Keywords: Molecular dynamics, Liposomes, Cinnarizine, Blood-brain barrier

✉ Yulia A. Polkovnikova, email: juli-polk@mail.ru

Condensed Matter and Interphases / Конденсированные среды и межфазные границы   2023;25(1): 95–102

Yu. A. Polkovnikova   Simulation of the molecular dynamics of the passage of liposome with cinnarizine...

1. Introduction

The tasks of targeted delivery of drugs, as well as increasing their bioavailability, are among the priorities in pharmacology. Currently, the development of a new generation of drugs based on liposomes is of strategic importance, since it will solve many problems associated with the targeted delivery of drugs [1]. Liposomes attract researchers as model systems for studying the mechanisms of functioning of biomembranes, as promising delivery vehicles for bioactive molecules and drugs, and also due to the possibility of wide use of liposomal forms of drugs for the treatment of various diseases [2]. Thus, the development of liposomal forms for the treatment of cerebrovascular diseases is relevant [3,4]. Currently, various groups of drugs are used for this purpose, including calcium channel blockers, one of the most widely used and economically available drug is cinnarizine [5–11]. Numerous studies of the drug have confirmed its effectiveness in diseases such as cerebral atherosclerosis without severe focal symptoms and an ischemic stroke. It is used after a haemorrhagic stroke and traumatic brain injury, with dyscirculatory encephalopathy [12].

One of the scenarios for the penetration of liposomes through the blood-brain barrier is their passage between endotheliocytes [13, 14]. Such a scenario becomes possible under pathological conditions, when the permeability of the tight junction between endotheliocytes of the blood-brain barrier increases due to an increase in the width of the gap between the membranes of adjacent cells [15].

The goal of the study was to determine the distance between endotheliocyte membranes, which is critical for the passage of a liposome through the blood-brain barrier.

2. Experimental

For the study of the process of passage of liposomes through the blood-brain barrier between endothelial cells, we simulated changes in the structure of a liposome with cinnarizine located between two cell membranes using the molecular dynamics method at different distances between the membranes. A spherical fragment of the system obtained by simulation of the molecular dynamics of liposome formation in the presence of cinnarizine was used as the initial structure. This fragment contained a liposome with a diameter of 14.7 nm with cinnarizine (125) molecules adsorbed on the inner and outer surfaces, as well as water molecules (Fig. 1).

Next, using the internet service Charmm-GUI-> Input Generator->Martini Maker->BilayerBuilder (http://www.charmm-gui.org/?doc=input/ mbilayer) [16–19], a square flat fragment of a bilayer phospholipid membrane was assembled. The composition of this fragment was set based on the literature data on the composition of the cytoplasmic membrane of the endotheliocyte [20]. Also, on both sides of the membrane, layers of water molecules with the amount of Na^+ ions necessary to neutralize the negative charge of anionic phospholipids were placed (Table 1).

The liposome was placed in an aqueous environment and aligned with the endotheliocyte cell membrane model on both sides of the liposome. The initial distance between the membranes was 15.2 nm (151.81 Å) (Table 2).

Next, geometry optimization and molecular dynamics simulation were carried out in the Gromacs 2019 program using the Martini 2.2 force field [21]. During the simulation, periodic boundary conditions were used along all coordinate axes. The geometry of the system was preliminarily optimized by the gradient method. Next, thermodynamic balancing was carried out using thermodynamic balancing (310 K) and barostatting (Berendsen barostat, 1 atm) [22, 23]. The simulation step in the process of thermodynamic balancing varied from a lower (0.5 fs) to the higher (4 fs). Next, molecular dynamics simulation was carried out for 700 ns with a step of 5 fs (Table 3).

The molecular dynamics of this system was simulated in the same way with a reduced distance between the membranes. For the reduction of the distance, some of the water molecules were removed from the space between the membranes.

3. Results and discussion

The simulation results with indication of the distance between the membranes are shown in Table 4.

The spatial structures of the states of the studied system during 700 nanoseconds of molecular dynamics simulation after

Condensed Matter and Interphases / Конденсированные среды и межфазные границы   2023;25(1): 95–102

Yu. A. Polkovnikova   Simulation of the molecular dynamics of the passage of liposome with cinnarizine...
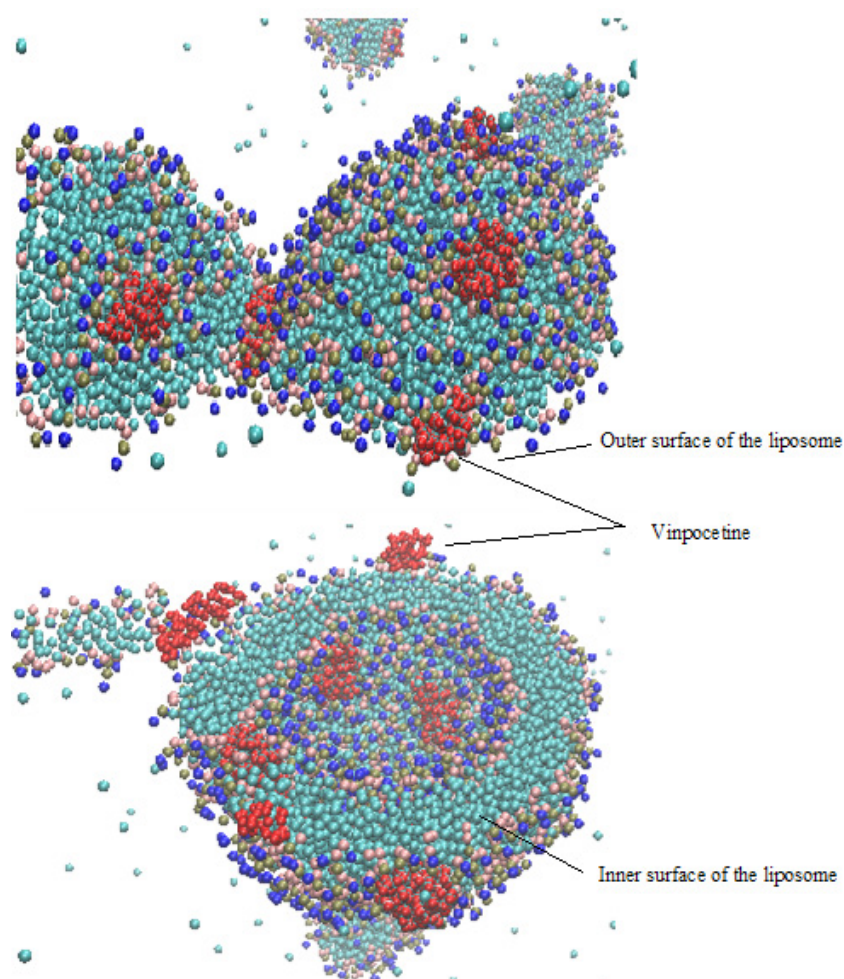
Fig. 1. Adsorption of cinnarizine molecules on the inner and outer surfaces of the liposome

Table 1. Composition of the endotheliocyte cell membrane model

Component	Abbreviation	Number of molecules
Dioleyl-phosphatidylcholine	DOPC	78
Dipalmitoyl-phosphatidylcholine	DPPC	368
Palmitoyl-oleyl-phosphatidylcholine	POPC	226
Dioleyl-phosphatidylethanolamine	DOPE	42
Dipalmitoylphosphatidylethanolamine	DPPE	72
Palmitoyl-oleyl-phosphatidylethanols	POPE	56
Dioleyl-phosphatidylserine	DOPS	14
Dipalmitoylphosphatidylserine	DPPS	12
Palmitoyl-oleyl-phosphatidylserine	POPS	14
Dipalmitoyl-phosphoinositol	DPPI	34
Palmitoyl-oleyl-phosphoinositol	POPI	52
Dipalmitoyl-sphingomyelin	DPSM	184
Palmitoyl-oleyl-sphingomyelin	POSM	98
Cholesterol	CHOL	534
Water	–	49972
Na$^+$ ion	–	126

Condensed Matter and Interphases / Конденсированные среды и межфазные границы   2023;25(1): 95–102

Yu. A. Polkovnikova   Simulation of the molecular dynamics of the passage of liposome with cinnarizine...

Table 2. The composition of the simulated "liposome-cinnarizine-cell membranes" system

Component	Abbreviation	Number of molecules
Dilinoleoyl-phosphatidylcholine	DIPC	714
Dioleyl-phosphatidylcholine	DOPC	156
Dipalmitoyl-phosphatidylcholine	DPPC	736
Palmitoyl-oleyl-phosphatidylcholine	POPC	681
Dioleyl-phosphatidylethanolamine	DOPE	84
Dipalmitoylphosphatidylethanolamine	DPPE	144
Palmitoyl-oleyl-phosphatidylethanols	POPE	112
Dioleyl-phosphatidylserine	DOPS	28
Dipalmitoylphosphatidylserine	DPPS	24
Palmitoyl-oleyl-phosphatidylserine	POPS	28
Dipalmitoyl-phosphoinositol	DPPI	68
Palmitoyl-oleyl-phosphoinositol	POPI	104
Dipalmitoyl-sphingomyelin	DPSM	368
Palmitoyl-oleyl-sphingomyelin	POSM	196
Cholesterol	CHOL	1068
Water	-	213136
Na^+ ion	-	126
Cl^- ion		250
Cinnarizine-cation	-	125

Table 3. Stages of simulation of the "liposome-cinnarizine-cell membrane" system

Stage	Trigger type	Number of steps	Step, fs	Duration, ns	Barostat/tensiostat	Thermostat
1	Geometry optimization	10000				
2	Molecular dynamics	2000000	0.5	1	Berendsen, semi-isotropic, 1 atm in z and 1 atm x and y, time constant 6 ps	Speed scaling, time constant 1 ps, temperature 310 K
3	Molecular dynamics	5000000	1	5	Berendsen, semi-isotropic, 1 atm in z and 1 atm x and y, time constant 6 ps	Speed scaling, time constant 1 ps, temperature 310 K
4	Molecular dynamics	200000000	4	800	Berendsen, semi-isotropic, 1 atm in z and 1 atm x and y, time constant 6 ps	Nose-Hoover, time constant 5 ps, temperature 310 K
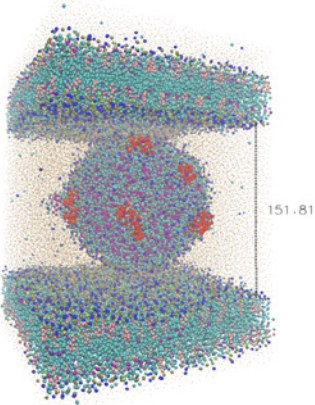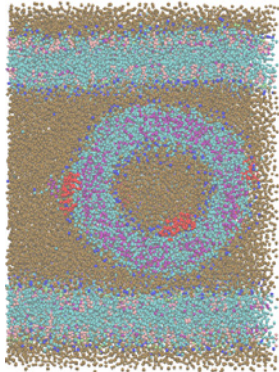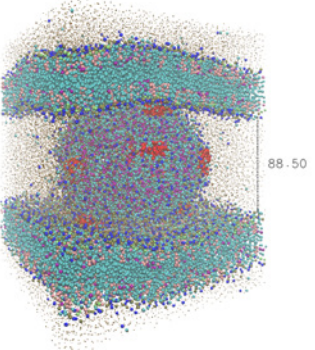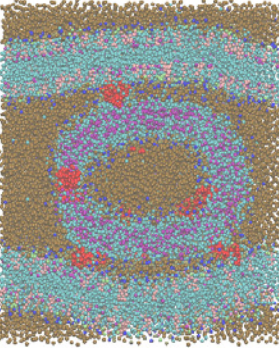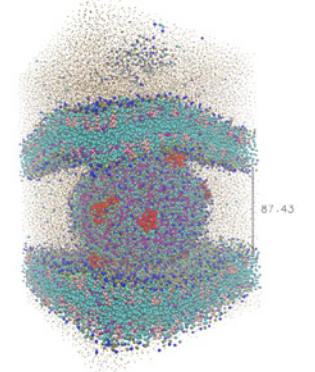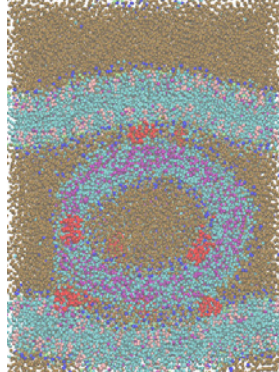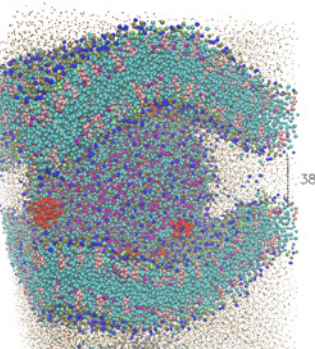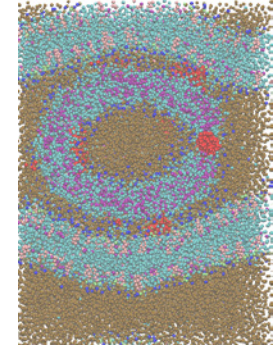
thermodynamic balancing for the system with the smallest distance between membranes (3.8 nm) are shown in Table 5. At a distance between membranes of 3.8 nm, the liposome fuses with the cell membrane. Fusion begins with the adhesion of the liposome to the surface of the cell membrane (200 ns) and the formation of a bridge between the liposome and the cell membrane (300–400 ns). Next, the semi-fusion of the liposome with the cell membrane occurs:

the outer layers of the membranes of the liposome and the cell (700 ns) are merged.
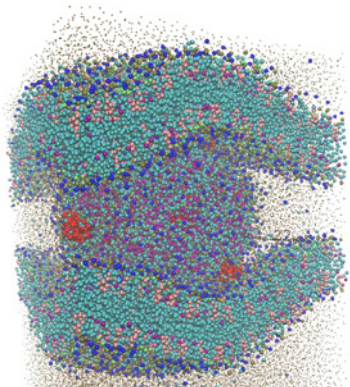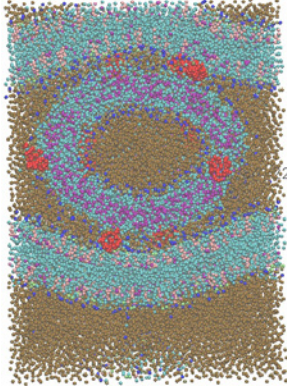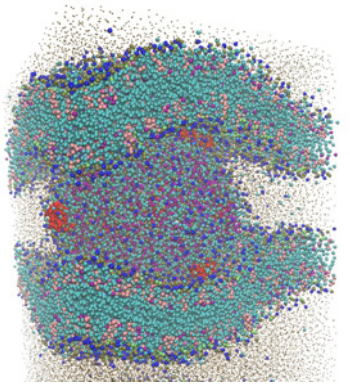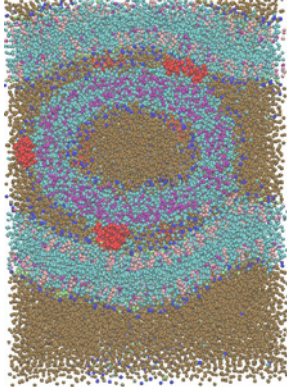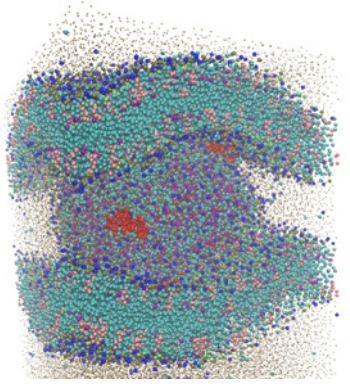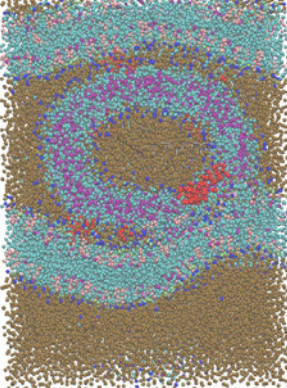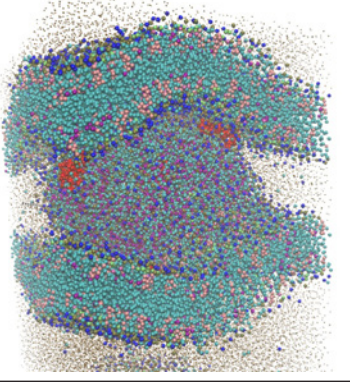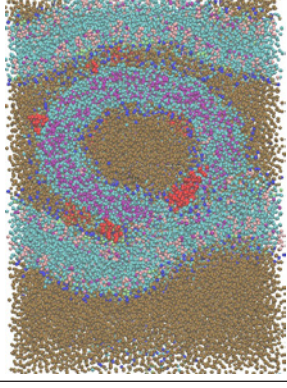
4. Conclusions

1. According to the results of simulation of coarse-grained molecular dynamics, a liposome from purified soy lecithin with cinnarizine adsorbed on its inner and outer surface is able to maintain integrity, being between the membranes of endotheliocytes

Condensed Matter and Interphases / Конденсированные среды и межфазные границы   2023;25(1): 95–102

Yu. A. Polkovnikova   Simulation of the molecular dynamics of the passage of liposome with cinnarizine...
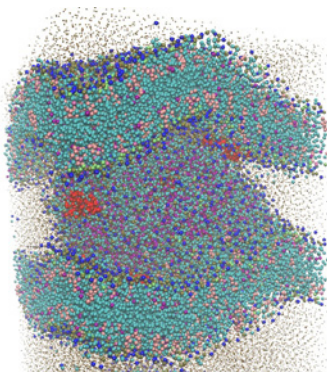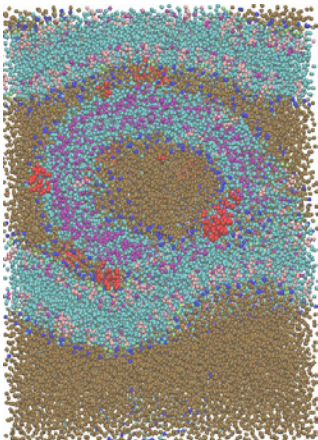
Table 4. Simulation of the molecular dynamics of the "liposome-cinnarizine-cell membranes" system at different distances between the membranes

Distance between membranes, nm	System status	
15.2		
8.9		
8.7		
3.8		

Condensed Matter and Interphases / Конденсированные среды и межфазные границы   2023;25(1): 95–102

Yu. A. Polkovnikova   Simulation of the molecular dynamics of the passage of liposome with cinnarizine...

Table 5. Simulation of the molecular dynamics of the "liposome-cinnarizine-cell membrane" system for a system with a distance between membranes of 3.8 nm

Time, ns	System state
1	2
100	
200	
400	
600	

Condensed Matter and Interphases / Конденсированные среды и межфазные границы   2023;25(1): 95–102

Yu. A. Polkovnikova   Simulation of the molecular dynamics of the passage of liposome with cinnarizine...

End of table 5

| 700 | | |

at a distance between the membranes of more than 8 nm.

2. The results of simulation of coarse-grained molecular dynamics also demonstrate that if the distance between endotheliocyte membranes is less than 8 nm, a liposome with cinnarizine located between endotheliocytes can lose its structural integrity due to fusion with the endotheliocyte membrane.

Conflict of interests

The author declares that they have no known competing financial interests or personal relationships that could have appeared to influence the work reported in this paper.

References

1. Hou G., Niu J., Song F., Liu Z., Liu S. Studies on the interactions between ginsenosides and liposome by equilibrium dialysis combined with ultrahigh performance liquid chromatography-tandem mass spectrometry. *Journal of Chromatography B*. 2013;923–924: 1–7. https://doi.org/10.1016/j.jchromb.2013.01.035

2. Sariev A. K., Abaimov D. A., Seyfulla R. D. Drug bioavailability improvement by means of nanopharmacology: pharmacokinetics of liposomal drugs. *Experimental and Clinical Pharmacology*. 2010;11: 34–38. (In Russ.). https://doi.org/10.30906/0869-2092-2010-73-11-34-38

3. Kamchatnov P. R., Salnikova G. S., Mikhailova N. A. Chronic disorders of bran blood circulation and possibilities of their pharmacological correction. *Zhurnal Nevrologii i Psikhiatrii imeni S.S. Korsakova*. 2012;112(6): 72–75. (In Russ.). Available at: https://www.elibrary.ru/item.asp?id=17912111

4. Dolgova I. N., Starodubtsev A. I. The chronic cerebrovascular pathology in young patients. *Medical Bulletin of the North Caucasus*. 2011;1:26–29. (In Russ., abstract in Eng.). Available at: https://med-click.ru/uploads/files/docs/hronicheskaya-tserebrovaskulyarnaya-patologiya-u-patsientov-molodogo-vozrasta.pdf

5. Glukhova O. E. Liposome Drug Delivery System across Endothelial Plasma Membrane: Role of Distance between Endothelial Cells and Blood Flow Rate. *Molecules*.2020;25:1875. DOI: https://doi.org/10.3390/molecules25081875

6. Jo S., Kim T., Iyer V.G., Im W. CHARMM-GUI: A Web-based Graphical User Interface for CHARMM. *Journal of Computational Chemistry*. 2008;29: 1859–1865. https://doi.org/10.1002/jcc.20945

7. Qi Y., Ingólfsson H. I., Cheng X., Lee J., Marrink S. J., Im W. CHARMM-GUI Martini Maker for Coarse-Grained Simulations with the Martini Force Field. *Journal of Chemical Theory and Computation*. 2015;1: 4486–4494. https://doi.org/10.1021/acs.jctc.5b00513

8. Tian Y., Shen S, Gu L., Zhou J., Li Y., Zheng X. Computer-aided design of glucoside brain-targeted molecules based on 4PYP. *Journal of Molecular Graphics and Modelling*. 2021;103: 107819. https://doi.org/10.1016/j.jmgm.2020.107819

9. Dar K. B., Bhat A. H., Amin S., ... Ganie S. A. Modern computational strategies for designing drugs to curb human diseases: a prospect. *Current Topics in Medicinal Chemistry*. 2018;18(31): 2702–2719. https://doi.org/10.2174/1568026619666190119150741

10. Scholtz A. W., Hahn A., Stefflova B., ... Weisshaar G. Efficacy and safety of a fixed combination of Cinnarizine 20 mg and Dimenhydrinate 40 mg vs Betahistine Dihydrochloride 16 mg in patients with peripheral vestibular vertigo: a prospective, multinational, multicenter, double-blind, randomized,

Condensed Matter and Interphases / Конденсированные среды и межфазные границы   2023;25(1): 95–102

Yu. A. Polkovnikova   Simulation of the molecular dynamics of the passage of liposome with cinnarizine...

non-inferiority clinical trial. *Clinical Drug Investigation*. 2019;39(11): 1045–1056. https://doi.org/10.1007/s40261-019-00858-6

11. Ivanova L., Nikolov R., Tsikalova P., Nikolova M. Experimental rheoencephalographic studies on the effect of the cinnarizin analogue As2 on cerebral circulation. *Acta Physiol Pharmacol Bulg*. 1979;5(2):47–52.

12. Asadi P., Zia Ziabari S. M., Majdi A., Vatanparast K., Naseri Alavi S. A. Cinnarizine/betahistine combination vs. the respective monotherapies in acute peripheral vertigo: a randomized triple-blind placebo-controlled trial. *European Journal of Clinical Pharmacology*. 2019;75(11): 1513-1519. https://doi.org/10.1007/s00228-019-02741-x

13. Sethi S., Mangla B., Kamboj S., Rana V. A. QbD approach for the fabrication of immediate and prolong buoyant cinnarizine tablet using polyacrylamide-g-corn fibre gum. *International Journal of Biological Macromolecules* 2018;117: 350–361. https://doi.org/10.1016/j.ijbiomac.2018.05.178

14. Maghsoodi M., Nokhodchi A., Oskuei M. A., Heidari S. Formulation of Cinnarizine for stabilization of its physiologically generated supersaturation. *AAPS PharmSciTech*. 2019;20(3): 139. https://doi.org/10.1208/s12249-019-1338-7

15. Wang X., Liu W., Du K. Palaeontological evidence of membrane relationship in step-by-step membrane fusion. *Molecular Membrane Biology*. 2011;28: 115–122. https://doi.org/10.3109/09687688.2010.536169

16. Hsu P-C., Bruininks B. M. H., Jefferies D., ... Im W. CHARMM-GUI Martini Maker for modeling and simulation of complex bacterial membranes with lipopolysaccharides. *Journal of Computational Chemistry*. 2017;15: 38(27):2354–2363. https://doi.org/10.1002/jcc.24895

17. van Hoogevest P., Wendel P. A. The use of natural and synthetic phospholipids as pharmaceutical excipients. *European Journal of Lipid Science and Technology*. 2014;116: 1088–1110. https://doi.org/10.1002/ejlt.201400219

18. Marrink S. J., Risselada H. J., Yefimov S., Tieleman D. P., de Vries, A. H. The MARTINI force field: Coarse grained model for biomolecular simulations. *Journal of Physical Chemistry B*. 2007;111: 7812–7824. https://doi.org/10.1021/jp071097f

19. Berendsen H. J. C., Postma J. P. M., van Gunsteren W. F., Di Nola A., Haak J. R. Molecular dynamics with coupling to an external bath. *The Journal of Chemical Physics*. 1984;81(8): 3684–3690. https://doi.org/10.1063/1.448118

20. Cansella M., Gouygoub J.-P., Jozefonvicza J., Letourneura D. Lipid composition of cultured endothelial cells in relation to their growth. *Lipids*. 1997;32: 39–44. https://doi.org/10.1007/s11745-997-0006-3

Information about the authors

Yulia A. Polkovnikova, Cand Sci. (Pharmacy), Associate Professor at the Department of Pharmaceutical Technology and Pharmaceutical Chemistry, Faculty of Pharmacy, Voronezh State University (Voronezh, Russian Federation).

https://orcid.org/0000-0003-0123-9526

juli-polk@mail.ru

Original articles

Research article

Study of semi-polar gallium nitride grown on m-sapphire by chloride vapor-phase epitaxy

P. V. Seredin[1]✉, **N. A. Kurilo**[1], **Ali O. Radam**[1], **N. S. Builov**[1], **D. L. Goloshchapov**[1], **S. A. Ivkov**[1],
A. S. Lenshin[1], **I. N. Arsentiev**[2], **A. V. Nashchekin**[2], **Sh. Sh. Sharofidinov**[2], **A. M. Mizerov**[3],
M. S. Sobolev[3], **E. V. Pirogov**[3], **I. V. Semeykin**[4]

[1]Voronezh State University,
1 Universitetskaya pl., Voronezh 394018, Russian Federation

[2]Ioffe Institute,
26 Politekhnicheskaya str., Sankt-Petersburg 194021, Russian Federation

[3]Federal State Budgetary Institution of the Highest Education and Science «Sankt-Petersburg National Research Academic University of Russian Academy of Sciences»,
8 Khlopina, str., Bd. 3, A, Sankt-Petersburg 194021, Russian Federation

[4]Research Institute of Electronic Technology,
5 Staryh Bolshevikov str., Voronezh 394033, Russian Federation

Abstract

In this study, we analyzed the result of the influence of the non-polar plane of a sapphire substrate on the structural, morphological, and optical properties and Raman scattering of the grown epitaxial GaN film.

It was found that selected technological conditions for the performed chloride-hydride epitaxy let us obtain the samples of structurally qualitative semi-polar wurtzite gallium nitride with (11¯22) orientation on m-sapphire. Using a set of structural and spectral methods of analysis the structural, morphological, and optical properties of the films were studied and the value of residual bi-axial stresses was determined. A complex of the obtained results means a high structural and optical quality of the epitaxial gallium nitride film.

Optimization of the applied technological technique in the future can be a promising approach for the growth of the qualitative GaN structures on m-sapphire substrates.

✉ Pavel V. Seredin, e-mail: paul@phys.vsu.ru

Condensed Matter and Interphases / Конденсированные среды и межфазные границы   2023;25(1): 103–111

P. V. Seredin et al.   Study of semi-polar gallium nitride grown on m-sapphire by chloride vapor-phase epitaxy

1. Introduction

The growing interest in $A_{III}N$ semiconductors is caused by the capabilities of these compounds ensuring their application as a basis for the development of a wide range of new devices forming the backbone of the electronic component base[1].

Epitaxial $A_{III}N$ films in several cases are grown on affordable alien substrates (sapphire, silicon, silicon carbide) having wurtzite hexagonal modification. Nitrides from the third group Periodic table are polar materials meaning that they lack inversion symmetry.

The lack of inversion symmetry in the hexagonal crystal lattices of $A_{III}N$ compounds stipulates their polarization properties which are extremely important while considering the mechanisms of recombination in light emitting devices, for characterizing 2D electron gas in microwave transistors and other applications.

Large values of piezoelectric constants in the conditions of strong misfit stresses in III-N heterostructures result in the large values of piezofields (< 10^7 V/cm) and, hence, in a considerable spatial separation of charge carriers in the quantum-size heterostructures. This effect is widely used in microwave transistors based on AlGaN to obtain 2D electron gas with enhanced mobility. On the other hand, such separation in heterostructures with quantum wells (QW) is accompanied not only by the red shift of the effective width of the band gap but results in a decrease of the radiative recombination as well, due to a decrease of overlapping the electron and hole wave functions (Stark effect) [2–4].

That is why nowadays along with the studies of the synthesis features of the polar $A_{III}N$ compounds active investigations are performed concerning the development of technological approaches for the epitaxial synthesis of high-quality non-polar or semi-polar $A_{III}N$ compounds [5, 6].

To perform epitaxial synthesis of $A_{III}N$ nitride films with different orientations various technologies are used: molecular beam epitaxy (MBE), vapor phase epitaxy from metal-organic compounds VPE-MOS) and chloride vapor-phase epitaxy (Cl-VPE). The latter makes it possible to synthesize $A_{III}N$ layers with the highest growth rate and it proves to be the most advanced technology for the fabrication of bulk $A_{III}N$ layers of high quality [7–14].

In this work, the results of the study for GaN/AlN heterostructure are presented and obtained with the use of a set of structural-spectroscopic methods. The structure was grown on the substrate of m-Al_2O_3 by the Cl-VPE technique.

2. Experimental

Optimal technological conditions used in this work for growing AlN and GaN layers were determined in the series of preliminary experiments concerning the synthesis of AlN and GaN compounds by the Ch-VPE technique on the substrates of c-sapphire (Al_2O_3), silicon (Si), and silicon carbide (SiC/Si). It was also experimentally determined that the use of buffer AlN layers allows for avoiding the appearance of cracks in the process of growth of the main GaN layer considerably reduces the values of elastic deformations as well as it can specify the crystallographic direction of growth. For example, in [15] the authors managed to grow a semi-polar GaN layer in the direction of [101⁻3] on the substrate of the Si (100) plane with the use of an oriented buffer layer of AlN layer with a thickness of 600 nm in the direction of [101⁻2], [101⁻3] plane. While performing a series of experiments related to the deposition of the buffer AlN layers on the substrates of sapphire and Si optimal temperatures of the substrates in the range of 1080–1100°C were determined. The optimal temperature for deposition of the buffer AlN layer on sapphire substrate proved to be equal to T = 1080 °C, while for silicon it was equal to T = 1100°C. More detailed information on the epitaxial growth of AlN on the substrate of silicon is presented in [16].

In the present work, the growth of GaN/AlN heterostructure using the Ch-VPE method was performed on the substrate of m-sapphire (m-Al_2O_3) in two stages. In the first stage of deposition of the buffer, the AlN layer was performed at the temperature of T = 1080 °C. The time of deposition for the buffer layer was equal to 3 minutes. In the second stage deposition of the main GaN layer was realized on the buffer AlN layer at the temperature of T = 1050 °C.

Diagnostics of the samples were made with the use of a set of structural-spectroscope methods of analysis.

Condensed Matter and Interphases / Конденсированные среды и межфазные границы   2023;25(1): 103–111

P. V. Seredin et al.   Study of semi-polar gallium nitride grown on m-sapphire by chloride vapor-phase epitaxy

Microscopic studies were performed with the use of a scanning electron microscope (SEM) JSM-7001F (Jeol) and scanning probe microscope Femtoscan-001 (NT MDT).

X-ray diffraction data were obtained at room temperature with the use of diffractometer DRON-4-07 employing characteristic radiation of the cobalt tube.

Micro-Raman scattering spectra were obtained with the use of Raman microscope RamMix 532 employing laser excitation with the wavelength of 532 nm.

Photoluminescence spectra of the samples were obtained with the unit for measuring of photoluminescence and optical reflection Accent RPM Sigma. The studies were made at room temperature under laser excitation with a wavelength of 266 nm and W = 5 W/cm^2.

3. Results and discussion

Fig. 1 depicts an SEM image of the cross-section (cleavage) for the GaN/AlN/m-Al$_2$O$_3$ heterostructure. SEM data made it possible to determine not only the nominal thickness of the Ch-VPE grown AlN and GaN layers (presented in Fig. 1), but also to estimate qualitatively the features in the development of the layers morphology during the process of their growth by Ch-VPE technique. From Fig. 1 it is seen that AlN and GaN in the obtained heterostructures were grown in the form of a continuous layer. Buffer AlN layer was characterized by rather rough morphology while in the growth of the main GaN layer a gradual change of morphology occurred from the rough one observed near the

GaN/AlN interface to more smooth morphology of the GaN layer. One should also note the lack of microcracks for both cases.

Images of the surface microareas of GaN epitaxial film grown on the m-plane of the sapphire substrate are presented in Fig. 2. It is seen that the film morphology can be characterized as a step-wise terrace with certain features of the surface in the form of feathers (V-shaped elements), oriented along (0001) direction of a sapphire substrate. This result coincides with the known literature data not only for GaN layers[10,17,18] but also for those of α-(AlGa)$_2$O$_3$ [19] grown on an m-plane of sapphire. In the chosen conditions of the epitaxial growth merging of semi-polar{11$^-$03} faces proved to be energy efficient that just resulted in
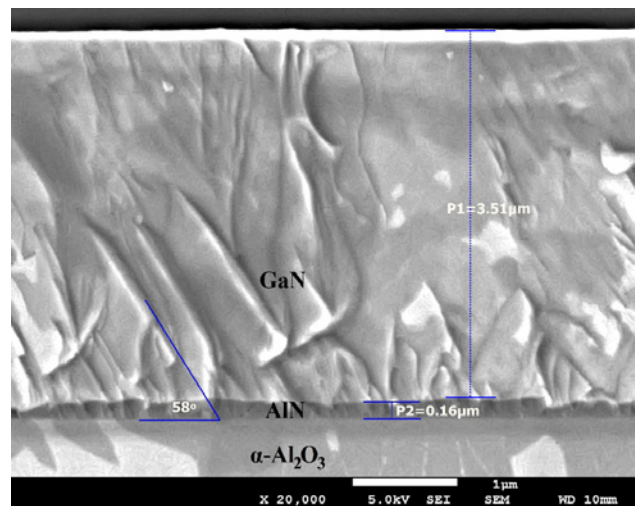
Fig. 1. SEM image of the cleavage for GaN/AlN/m-Al$_2$O$_3$ heterostructure
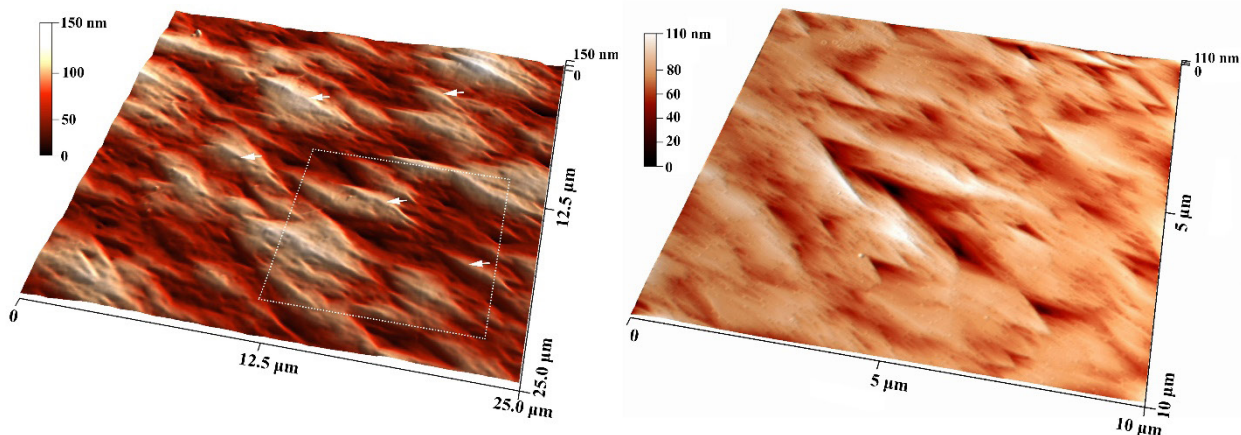
Fig. 2. AFM images of relief for microareas at the surface of GaN/AlN/m- Al$_2$O$_3$ heterostrucures

Condensed Matter and Interphases / Конденсированные среды и межфазные границы   2023;25(1): 103–111

P. V. Seredin et al.   Study of semi-polar gallium nitride grown on m-sapphire by chloride vapor-phase epitaxy

the formation of the observed surface relief [20]. This is just a coincidence with the discussions presented in [17], where semi-polar growth of GaN on m-sapphire was employed with the use of a vapor-phase deposition.

X-ray ω/2θ scan of GaN/AlN/m-Al_2O_3 heterostructure and m-Al_2O_3 substrate is given in figure 3 in the logarithmic scale of intensity. The diffraction profile is presented in the range of angles 2θ = 10–100°, where a number of the main diffraction reflexes is arranged.

The analysis demonstrates that the most intensive reflection here is related to (30$\bar{3}$0) line of a sapphire substrate. It should be noted that there are other reflections in ω/2θ scan attributed to the diffraction from m-Al_2O_3 (this range of the angles is not shown in Fig. 3), which is connected with the presence of deviation of the substrate orientation from its primary flat. As for the epitaxial film, our experiments show that in θ/2θ scan there are two reflections observed at the angles greater than those inherent for sapphire substrate, which correspond to the diffraction from the plane (11$\bar{2}$2) of wurtzite GaN and AlN layers.

Using elasticity theory [21–24] for the crystals with wurtzite crystal lattice deformation in the growth plane ε_{xx} *(along a axis)* can be determined in terms of the following relation [25]:

$$\varepsilon_{xx} = \varepsilon_{11-22} = \frac{d - d_0}{d_0} \qquad (1)$$

Here d and d_0 is the experimental interplanar spacing for the reflection 11$\bar{2}$22, d_0 – experimental interplanar spacing for the reflection of 11$\bar{2}$22 for the non-strained crystal of GaN, in accordance with the literature data d_0 = 1.3588 Å [26,27].

Next, according to the known correlation [28] it is possible to calculate bi-axial strains in the growth plane σ_{xx}:

$$\sigma_{xx} = M\varepsilon_{xx}. \qquad (2)$$

Here M is the biaxial modulus of elasticity for the crystalline material with a wurtzite crystal lattice and its value for GaN ~478.5 GPa. Calculations show that deformations in the growth plane are stretching ones (ε_{xx} ~ 0.00088, while the appearing biaxial stresses in the growth plane σ_{xx} are close to ~ 420 MPa.

It was repeatedly shown that Raman spectroscopy is a method for the determination of fine structural crystal properties and it is very sensitive to impurities, composition, crystalline structure, crystal orientation, and mechanical stresses.

Micro-Raman scattering spectra from the epitaxial heterostructure and the used m-sapphire substrate are presented in figure 4. Taking into account sample orientation and in accordance with the selection rule in the Raman spectrum of semi-polar GaN several maxima are observed that can be attributed to the phonon modes $A_1(TO)$, $E_1(TO)$, E_2^{high} for the crystal with a wurtzite

Fig. 3. X-ray ω/2θ scan of GaN/AlN/m-Al_2O_3 heterostructure

Condensed Matter and Interphases / Конденсированные среды и межфазные границы   2023;25(1): 103–111

P. V. Seredin et al.   Study of semi-polar gallium nitride grown on m-sapphire by chloride vapor-phase epitaxy
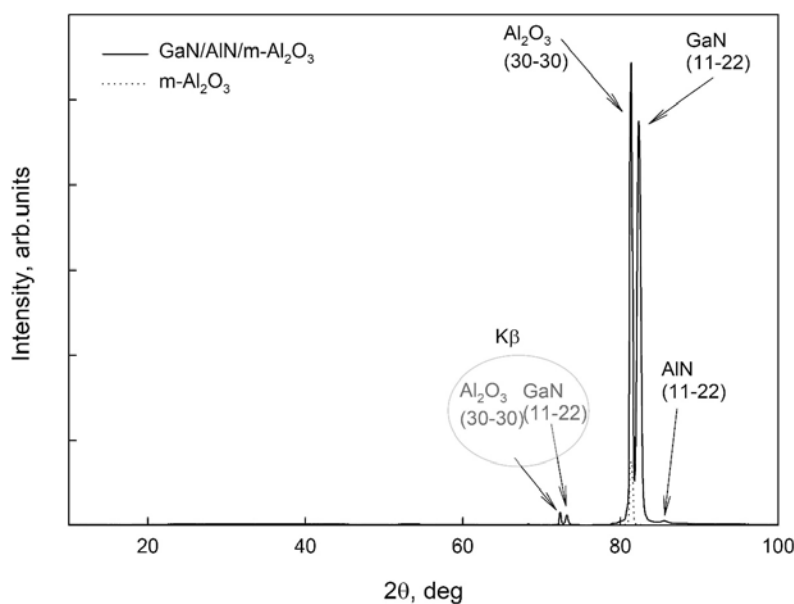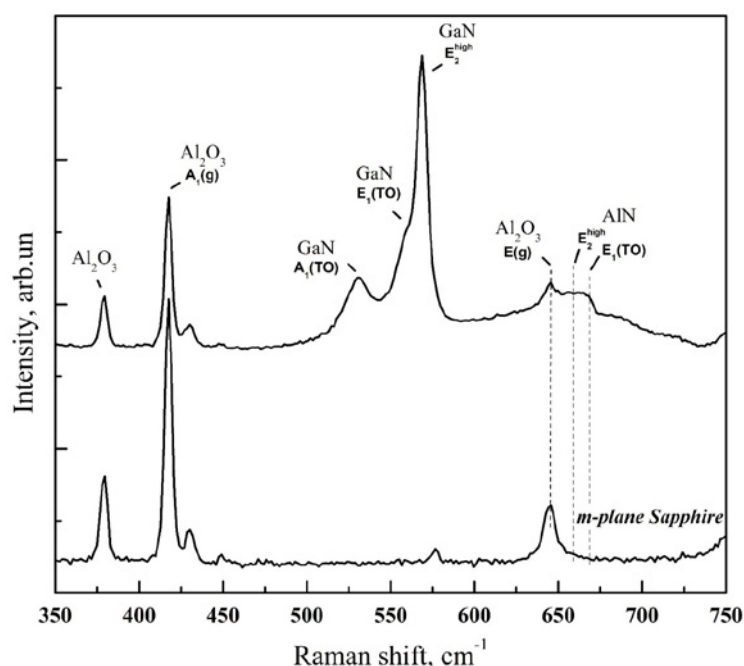
Fig. 4. Raman spectra from the epitaxial GaN/AlN/m-Al$_2$O$_3$ heterostructure and sapphire substrate.

structure [29]. Maxima in the scattering Raman spectra at 370, 417, 644 cm^{-1} represent typical characteristic combination-active modes of sapphire (Al$_2$O$_3$) with symmetry A$_{1g}$ and E$_{1g}$ [30].

Moreover, in the spectrum of the sample, there are two low-intensive vibrations in the range of 655 and 670 cm^{-1}. They can be attributed to the mode of E$_2^{high}$ AlN, the strong among the allowed modes in the films of wurtzite AlN films, for the geometry of backscattering employed in our experiment $z(xy)z'$, and E$_1$(TO) mode of AlN, respectively [31, 32].

It is known that the intensity and full width at the half maximum (FWHM) of the phonon mode E$_2^{high}$ in GaN represents the structural quality of the crystals in the epitaxial film. GaN films with a high dislocation density usually demonstrate the spectrum with a greater full width at the half maximum[29]. Based on the obtained results on micro-Raman scattering FWHM of the phonon mode E$_2^{high}$ in the spectrum it is ~7 cm^{-1}. Comparison with the results of similar previous works shows that the width of E$_2^{high}$ mode in the Raman spectrum of semi-polar (11$\bar{2}$2) GaN was noticeably greater and it was within the 9.5–12 cm^{-1} range.

The presence of a narrow peak of E$_2^{high}$ in GaN and an intensive peak of E$_1$(TO) in the Raman spectra indicate that high-quality semi-polar (11$\bar{2}$2) GaN films were obtained in fact, almost without their deformation.

Estimation of the structural quality of the epitaxial film, namely, the value of stresses in the GaN layer, can be obtained based on the determination of the main maximum shift in the Raman spectrum.

The value of biaxial stress for semi-polar GaN film grown on m-sapphire can be estimated according to the following formula:

$$\Delta\omega = k\sigma \tag{3}$$

where где s – is a value of residual biaxial stresses in the epitaxial layer, k – is the coefficient of the transformation for biaxial stress into Raman shift. The transformation coefficient for the E_2^{high} mode of GaN is equal to 4.3 (cm^{-1}·GPA^{-1}) [33]. The value of biaxial stress in the GaN layer calculated from expression (3) is of ~ 117 MPa and it means effective relaxation of elastic stresses in the epitaxial GaN layer. It should be noted that the determined value of residual biaxial stresses is 2,5 times lower than that one calculated based on the results of the XRD w-scan.

The optical quality of the epitaxial layer can be assessed from photoluminescence (PL) [34–36]. Figure 5 represents the PL spectrum of the GaN layer obtained at room temperature. It is seen as the main intensive peak with a maximum

Condensed Matter and Interphases / Конденсированные среды и межфазные границы   2023;25(1): 103–111

P. V. Seredin et al.   Study of semi-polar gallium nitride grown on m-sapphire by chloride vapor-phase epitaxy
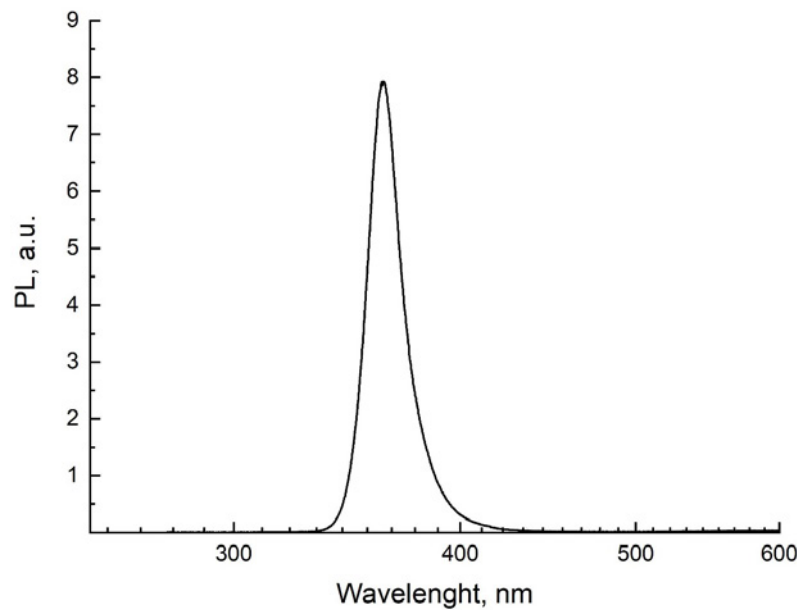
Fig. 5. PL spectrum of GaN/AlN/m-Al$_2$O$_3$ heterostructure at room temperature

localized near 3.4154 eV. The full width at half maximum of this photoluminescence peak is ~0.16 eV which is much less than the values presented earlier in the literature for GaN grown on m-sapphire. Nevertheless, the observed rather broad PL spectrum can indicate the relatively high density of defects in the grown layer [8, 9, 17].

It should be noted that no additional emission is observed in the spectrum in the low-energy range near 3.0–3.1 eV which is attributed either to highly localized excitons [9] or is connected with yellow luminescence thus indicating the quite good crystalline quality of the GaN layer.

It was repeatedly shown that PL is one more optical method providing information about residual stresses in the epitaxial film.

Quantitative level of biaxial stresses σ_{xx}, arising in GaN film, can be determined based on the fact that the band-gap width of the layer is sensitive to the deformation degree [37]. To do this the following empirical linear correlation was applied:

$$\Delta E = E_{PL} - E_0 = K_{PL}\sigma_{xx}. \qquad (4)$$

Here E_{PL} is the value of the band gap experimentally measured from the PL spectrum, E_0 is the energy of peak of the non-deformational PL at room temperature, while K_{PL} is the coefficient of the transformation of biaxial stresses into the linear shift of the material's band-gap value

in the spectrum of photoluminescence. Energy value of E_0 = 3.4180±0.0008 eV, and the value of K_{PL} = -0.017±0.0025 eV/GPa; these values are based on the results obtained in [37].

Our calculations show that the value of residual stresses in the GaN layer determined from the PL spectrum, is about ~ 150 MPa, and this is comparable with the data of Raman spectroscopy. Note, that the PL spectrum at room temperature allows for a determination of stresses in a quite thin surface GaN layer since penetration depth for selected laser radiation wavelength is up to 100 nm.

4. Conclusions

The result of the effect of non-polar m-plane in the sapphire substrate on the structural, morphological, and optical properties as well as on Raman scattering of the epitaxial GaN film grown by Ch-VPE was analyzed in our studies.

It was found that selected technological conditions of Cl-VPE epitaxy made it possible to obtain samples of structurally qualitative semi-polar wurtzite gallium nitride with (11¯22) orientation on m-sapphire. With the use of a set of structural-spectroscopic methods for analyzing various structural, morphological, and optical properties of the films and the level of residual biaxial stresses was determined as well.

Condensed Matter and Interphases / Конденсированные среды и межфазные границы   2023;25(1): 103–111

P. V. Seredin et al.   Study of semi-polar gallium nitride grown on m-sapphire by chloride vapor-phase epitaxy

Optimization of the applied technological technique can become a rather challenging approach to the growth of the qualitative GaN structures on the substrates of m-sapphire in the near future.

Contribution of the authors

The authors contributed equally to this article.

Conflict of interests

The authors declare that they have no known competing financial interests or personal relationships that could have influenced the work reported in this paper.

References

1. Hibberd M. T., Frey V., Spencer B. F., Mitchell P. W., Dawson P., Kappers M. J., Oliver R. A., Humphreys C. J., Graham D. M. Dielectric response of wurtzite gallium nitride in the terahertz frequency range. *Solid State Communications*. 2016;247: 68–71. https://doi.org/10.1016/j.ssc.2016.08.017

2. Ambacher O., Majewski J., Miskys C., Link A., Hermann M., Eickhoff M., Stutzmann M., Bernardini F., Fiorentini V., Tilak V., Schaff B., Eastman L. F. Pyroelectric properties of Al(In)GaN/GaN hetero- and quantum well structures. *Journal of Physics: Condensed Matter*. 2002;14(13): 3399–3434. https://doi.org/10.1088/0953-8984/14/13/302

3. Grahn H. T. Polarization properties of nonpolar GaN films and (In,Ga)N/GaN multiple quantum wells. *Physica Status Solidi (b)*. 2004;241(12): 2795–2801. https://doi.org/10.1002/pssb.200405040

4. Katzir S. The discovery of the piezoelectric effect. *Archive for History of Exact Sciences*. 2003;57(1): 61–91. https://doi.org/10.1007/s00407-002-0059-5

5. Xu B., Jiu L., Gong Y., Zhang Y., Wang L. C., Bai J., Wang T. Stimulated emission from semi-polar (11-22) GaN overgrown on sapphire. *AIP Advances*. 2017;7(4): 045009. https://doi.org/10.1063/1.4981137

6. Landmann M., Rauls E., Schmidt W. G., Neumann M. D., Speiser E., Esser N. GaN m -plane: Atomic structure, surface bands, and optical response. *Physical Review B*. 2015;91(3): 035302. https://doi.org/10.1103/PhysRevB.91.035302

7. Fu H., Zhang X., Fu K., Liu H., Alugubelli S. R., Huang X., Chen H., Baranowski I., Yang T.-H., Xu K., Ponce F. A., Zhang B., Zhao Y. Nonpolar vertical GaN-on-GaN $p-n$ diodes grown on free-standing (10-10) m-plane GaN substrates. *Applied Physics Express*. 2018;11(11): 111003. https://doi.org/10.7567/APEX.11.111003

8. Wang M., Xu K., Xu S. Photoluminescence and Raman Scattering signatures of anisotropic optical properties in freestanding m-, a- and c-plane GaN

substrates. *The Journal of Physical Chemistry C*. 2020;124(33): 18203–18208. https://doi.org/10.1021/acs.jpcc.0c04959

9. Maliakkal C. B., Rahman A. A., Hatui N., Chalke B. A., Bapat R. D., Bhattacharya A. Comparison of GaN nanowires grown on c-, r- and m-plane sapphire substrates. *Journal of Crystal Growth*. 2016;439:47–53. https://doi.org/10.1016/j.jcrysgro.2015.12.044

10. de Mierry P., Kriouche N., Nemoz M., Nataf G. Improved semipolar (112‾2) GaN quality using asymmetric lateral epitaxy. *Applied Physics Letters*. 2009;94(19): 191903. https://doi.org/10.1063/1.3134489

11. Seredin P. V., Lenshin A. S., Mizerov A. M., Leiste H., Rinke M. Structural, optical and morphological properties of hybrid heterostructures on the basis of GaN grown on compliant substrate por-Si(111). *Applied Surface Science*. 2019;476: 1049–1060. https://doi.org/10.1016/j.apsusc.2019.01.239

12. Boichot R., Chen D., Mercier F., Baillet F., Giusti G., Coughlan T., Chubarov M., Pons M. Epitaxial growth of AlN on (0001) sapphire: assessment of HVPE process by a design of experiments approach. *Coatings*. 2017;7(9): 136. https://doi.org/10.3390/coatings7090136

13. Hu J., Wei H., Yang S., Li C., Li H., Liu X., Wang L., Wang Z. Hydride vapor phase epitaxy for gallium nitride substrate. *Journal of Semiconductors*. 2019;40(10): 101801. https://doi.org/10.1088/1674-4926/40/10/101801

14. Seredin P. V., Goloshchapov D. L., Arsentyev I. N., Sharofidinov S., Kasatkin I. A., Prutskij T. HVPE fabrication of GaN sub-micro pillars on preliminarily treated Si(001) substrate. *Optical Materials*. 2021;117: 111130. https://doi.org/10.1016/j.optmat.2021.111130

15. Bessolov V. N., Zhilyaev Yu. V., Konenkova E. V., Poletaev N. K., Sharofidinov Sh., Shcheglov M. P. Epitaxy of gallium nitride in semi-polar direction on silicon. *Technical Physics Letters*. 2012;38(1): 9–11. https://doi.org/10.1134/S1063785012010051

16. Nikolaev V. I., Pechnikov A. I., Stepanov S. I., Sharofidinov Sh. Sh., Golovatenko A. A., Nikitina I. P., Smirnov A. N., Bugrov V. E., Romanov A. E., Brunkov P. N., Kirilenko D. A. Chloride epitaxy of β-Ga_2O_3 layers grown on c-sapphire substrates. *Semiconductors*. 2016;50(7): 980–983. https://doi.org/10.1134/S1063782616070186

17. Wu Z., Shen X., Liu C., Li K., Shen W., Kang J., Fang Z. In situ asymmetric island sidewall growth of high-quality semipolar (112‾2) GaN on m-plane sapphire. *CrystEngComm*. 2016;18(29): 5440–5447. https://doi.org/10.1039/C6CE00878J

18. Ni X., Özgür Ü., Baski A. A., Morkoç H., Zhou L., Smith D. J., Tran C. A. Epitaxial lateral overgrowth of (112‾2) semipolar GaN on (11‾00) m-plane sapphire

Condensed Matter and Interphases / Конденсированные среды и межфазные границы   2023;25(1): 103–111

P. V. Seredin et al.   Study of semi-polar gallium nitride grown on m-sapphire by chloride vapor-phase epitaxy

by metalorganic chemical vapor deposition. *Applied Physics Letters*. 2007;90(18): 182109. https://doi.org/10.1063/1.2735558

19. Jinno R., Chang C. S., Onuma T., Cho Y., ... Jena D. Crystal orientation dictated epitaxy of ultrawide-bandgap 5.4- to 8.6-eV α-(AlGa)2O3 on m-plane sapphire. *Science Advances*. 2021;7(2): eabd5891. https://doi.org/10.1126/sciadv.abd5891

20. Seredin P. V., Domashevskaya P., Arsentyev I. N., Vinokurov D. A., Stankevich A. L., Prutskij T. Superstructured ordering in $Al_xGa_{1-x}As$ and $GaxIn_{1-x}P$ alloys. *Semiconductors*. 2013;47(1): 1–6. https://doi.org/10.1134/S106378261301020X

21. Domashevskaya E. P., Seredin P. V., Lukin A. N., Bityutskaya L. A., Grechkina M. V., Arsentyev I. N., Vinokurov D. A., Tarasov I. S. XRD, AFM and IR investigations of ordered $AlGaAs_2$ phase in epitaxial $Al_xGa_{1-x}As/GaAs$ (100) heterostructures. *Surface and Interface Analysis*. 2006;38(4): 828–832. https://doi.org/10.1002/sia.2306

22. Seredin P. V., Lenshin A. S., Zolotukhin D. S., Arsentyev I. N., Nikolaev D. N., Zhabotinskiy A. V. Experimental study of structural and optical properties of integrated MOCVD GaAs/Si(001) heterostructures. *Physica B: Condensed Matter*. 2018;530: 30–37. https://doi.org/10.1016/j.physb.2017.11.028

23. Seredin P. V., Glotov A. V., Domashevskaya E. P., Arsentyev I. N., Vinokurov D. A., Tarasov I. S. Structural features and surface morphology of AlxGay-In1-x-yAszP1-z/GaAs(1 0 0) heterostructures. *Applied Surface Science*. 2013;267: 181–184. https://doi.org/10.1016/j.apsusc.2012.09.053

24. Seredin P. V., Ternovaya V. E., Glotov A. V., Len'shin A. S., Arsent'ev I. N., Vinokurov D. A., Tarasov I. S., Leiste H., Prutskij T. X-ray diffraction studies of heterostructures based on solid solutions $Al_xGa_{1-x}As_yP_{1-y}$:Si. *Physics of the Solid State*. 2013;55(10): 2161–2164. https://doi.org/10.1134/S1063783413100296

25. Li Z., Jiu L., Gong Y., Wang L., Zhang Y., Bai J., Wang T. Semi-polar (11-22) AlGaN on overgrown GaN on micro-rod templates: Simultaneous management of crystal quality improvement and cracking issue. *Applied Physics Letters*. 2017;110(8): 082103. https://doi.org/10.1063/1.4977094

26. Morkoç H. *Handbook of nitride semiconductors and devices: materials properties, physics and growth. Volume 1.* Wiley; 2008. https://onlinelibrary.wiley.com/doi/book/10.1002/9783527628438

27. Collaboration: Authors and editors of the volumes III/17A-22A-41A1a. List of frequently used symbols and abbreviations, conversion factors In: *Group IV Elements, IV-IV and III-V Compounds. Part a – Lattice Properties*. O. Madelung, U. Rössler, M. Schulz (eds.). Berlin/Heidelberg: Springer-Verlag; 2001;a: 1–7. http://materials.springer.com/lb/docs/sm_lbs_978-3-540-31355-7_2

28. Harutyunyan V. S., Aivazyan A. P., Weber E. R., Kim Y., Park Y., Subramanya S. G. High-resolution x-ray diffraction strain-stress analysis of GaN/sapphire heterostructures. *Journal of Physics D: Applied Physics*. 2001;34(10A): A35–A39. https://doi.org/10.1088/0022-3727/34/10A/308

29. Zeng Y., Ning J., Zhang J., Jia Y., Yan C., Wang B., Wang D. Raman analysis of E2 (High) and A1 (LO) phonon to the stress-free GaN grown on sputtered AlN/graphene buffer layer. *Applied Sciences*. 2020;10(24): 8814. https://doi.org/10.3390/app10248814

30. Li P. G., Lei M., Tang W. H. Raman and photoluminescence properties of α-Al_2O_3 microcones with hierarchical and repetitive superstructure. *Materials Letters*. 2010;64(2): 161–163. https://doi.org/10.1016/j.matlet.2009.10.032

31. Lughi V., Clarke D. R. Defect and stress characterization of AlN films by Raman spectroscopy. *Applied Physics Letters*. 2006;89(24): 241911. https://doi.org/10.1063/1.2404938

32. Davydov V. Yu., Kitaev Yu. E., Goncharuk I. N., Smirnov A. N., Graul J., Semchinova O., Uffmann D., Smirnov M. B., Mirgorodsky A. P., Evarestov R. A. Phonon dispersion and Raman scattering in hexagonal GaN and AlN. *Physical Review B*. 1998;58(19): 12899–12907. https://doi.org/10.1103/PhysRevB.58.12899

33. Tripathy S., Chua S. J., Chen P., Miao Z. L. Micro-Raman investigation of strain in GaN and $Al_xGa_{1-x}N/GaN$ heterostructures grown on Si(111). *Journal of Applied Physics*. 2002;92(7): 3503–3510. https://doi.org/10.1063/1.1502921

34. Seredin P. V., Glotov A. V., Ternovaya V. E., Domashevskaya E. P., Arsentyev I. N., Vavilova L. S., Tarasov I. S. Spinodal decomposition of $Ga_xIn_{1-x}AsyP_{1-y}$ quaternary alloys. *Semiconductors*. 2011;45(11): 1433–1440. https://doi.org/10.1134/S1063782611110236

35. Seredin P. V., Glotov A. V., Domashevskaya E. P., Arsentyev I. N., Vinokurov D. A., Tarasov I. S., Zhurbina I. A. The substructure and luminescence of low-temperature AlGaAs/GaAs(100) heterostructures. *Semiconductors*. 2010;44(2): 184–188. https://doi.org/10.1134/S1063782610020089

36. Seredin P. V., Lenshin A. S., Zolotukhin D. S., Arsentyev I. N., Zhabotinskiy A. V., Nikolaev D. N. Impact of the substrate misorientation and its preliminary etching on the structural and optical properties of integrated GaAs/Si MOCVD heterostructures. *Physica E: Low-dimensional Systems and Nanostructures*. 2018;97: 218–225. https://doi.org/10.1016/j.physe.2017.11.018

37. Choi S., Heller E., Dorsey D., Vetury R., Graham S. Analysis of the residual stress distribution in AlGaN/GaN high electron mobility transistors. *Journal of Applied Physics*. 2013;113(9): 093510. https://doi.org/10.1063/1.4794009

Condensed Matter and Interphases / Конденсированные среды и межфазные границы   2023;25(1): 103–111

P. V. Seredin et al.   Study of semi-polar gallium nitride grown on m-sapphire by chloride vapor-phase epitaxy

Information about the authors

Pavel V. Seredin, Dr. Sci. (Phys.-Math.), Full Professor, Chair of department, Department of Solid State Physics and Nanostructures, Voronezh State University (Voronezh, Russian Federation).

https://orcid.org/0000-0002-6724-0063

paul@phys.vsu.ru

Nikolay A. Kurilo, postgraduate student, Department of Solid State Physics and Nanostructures, Voronezh State University (Voronezh, Russian Federation).

https://orcid.org/0000-0001-7652-6912

kurilo@vsu.ru

Ali Obaid Radam, postgraduate student, Department of Solid State Physics and Nanostructures, Voronezh State University (Voronezh, Russian Federation).

Nikita S. Buylov, Cand. Sci. (Phys.-Math.), Educator, Department of Solid State Physics and Nanostructures, Voronezh State University (Voronezh, Russian Federation).

https://orcid.org/0000-0003-1793-4400

buylov@phys.vsu.ru

Dmitry L. Goloshchapov, Cand. Sci. (Phys.-Math.), Assistant Professor, Department of Solid State Physics and Nanostructures, Voronezh State University (Voronezh, Russian Federation).

https://orcid.org/0000-0002-1400-2870

goloshchapov@phys.vsu.ru

Ivkov Sergey Alexandrovich, Cand. Sci. (Phys.-Math.), Educator, Department of Solid State Physics and Nanostructures, Voronezh State University (Voronezh, Russian Federation).

https://orcid.org/0000-0003-1658-5579

ivkov@phys.vsu.ru

Alexandr S. Lenshin, Dr. Sci. (Phys.-Math.), Leading Researcher, Department of Solid State Physics and Nanostructures, Voronezh State University (Voronezh, Russian Federation).

https://orcid.org/0000-0002-1939-253X

lenshin@phys.vsu.ru

Ivan N. Arsentyev, Dr. Sci. (Eng.), Leading Researcher, Ioffe Institut, (Saint Petersburg, Russian Federation).

arsentyev@mail.ioffe.ru

Alexey V. Nashchekin, Cand. Sci. (Phys.-Math.), Senior Researcher, Ioffe Institute (Saint Petersburg, Russian Federation).

https://orcid.org/0000-0002-2542-7364

e-mail: nashchekin@mail.ioffe.ru

Shukrilo Sh. Sharofidinov, Cand. Sci. (Phys.-Math.), Researcher, Ioffe Institute (Saint Petersburg, Russian Federation).

shukrillo71@mail.ru

Andrey M. Mizerov, Cand. Sci. (Phys.-Math.), Leading Researcher, Saint Petersburg National Research Academic University of the Russian Academy of Sciences (Saint Petersburg, Russian Federation).

https://orcid.org/0000-0002-9125-6452

andreymizerov@rambler.ru

Maksim S. Sobolev, Cand. Sci. (Phys.-Math.), Acting Head of the Laboratory of Nanoelectronics, Sankt-Petersburg National Research Academic University of Russian Academy of Sciences (Saint Petersburg,, Russian Federation).

https://orcid.org/0000-0001-8629-2064

sobolevsms@gmail.com

Evgeniy V. Pirogov, Junior Researcher, Saint Petersburg National Research Academic University of Russian Academy of Sciences (Saint Petersburg, Russian Federation).

https://orcid.org/0000-0001-7186-3768

e-mail: zzzavr@gmail.com

Igor Valentinovich Semeykin, Cand. Sci. (Eng.), Technical Director, Research Institute of Electronic Technology (Voronezh, Russian Federation).

https://orcid.org/0000-0001-7186-3768

sig@niiet.ru

Original articles

Research article
https://doi.org/10.17308/kcmf.2023.25/10979

Studying the effect of modifying additives on the hydration and hardening of cement composites for 3D printing

G. S. Slavcheva, O. V. Artamonova, D. S. Babenko, M. A. Shvedova✉

Voronezh State Technical University,
84 20-Letiya Oktyabrya ul., Voronezh 394006, Russian Federation

Abstract

The development and application of multicomponent multifunctional additives for cement composites is an important research area since the use of such additives allows controlling both the rheological properties of fresh mixtures and the physical and mechanical properties of the hardened composite.

In our study, we used several additives, including metakaolin and xanthan gum together with tetrapotassium pyrophosphate and a SiO_2 based complex additive, to modify cementitious sand-based materials. We studied the peculiarities of the influence of these additives on the technological characteristics of mixtures (plasticity and shape retention) and the processes of setting, hydration, and hardening of the composite materials.

The optimal values of plasticity, for stability, acceleration of hardening were demonstrated by sand-based systems modified with a complex nanosized additive and metakaolin. The hydration products in the such systems are mainly formed from low basic hydroxides. Metakaolin also results in the formation of ettringite. These systems demonstrate the optimal time of the beginning of setting and the maximum strength gain of the modified cementitious sand-based materials at 28 days.

The optimal ratio of indicators of plasticity and shape retention of cement mixtures and the strength of composites based on them obtained by using the studied additives allows us to recommend using these additives in the innovative technologies for 3D-build printing.

Keywords: cement hardening systems, modification, modifying additives, hydration process, rheological properties, compressive strength

For citation: Slavcheva G. S., Artamonova O. V., Babenko D. S., Shvedova M. A. Studying the effect of modifying additives on the hydratation and hardening of cement composites for 3D printing. *Condensed Matter and Interphase*s. 2023;25(1): 112–124. https://doi.org/10.17308/kcmf.2023.25/10979

Для цитирования: Славчева Г. С., Артамонова О. В., Бабенко Д. С., Шведова М. А. Исследование влияния модифицирующих добавок на структурообразование и твердение цементных композитов для 3D-печати. *Конденсированные среды и межфазные границы.* 2023;25(1): 112–124. https://doi.org/10.17308/kcmf.2023.25/10979

✉ Maria A. Shvedova, e-mail: marishwedowa@mail.ru

Condensed Matter and Interphases / Конденсированные среды и межфазные границы 2023;25(1): 112–124

G. S. Slavcheva et al. Studying the effect of modifying additives on the hydration and hardening of cement...

Designations used in the article:

C – cement
W – water
S – quartz sand
SP - superplasticiser
MKL - metakaolin
XG - xanthan gum
TPPPh - tetrapotassium pyrophosphate
CNA – complex nanosized additive
PF – polypropylene fibre

1. Introduction

The emergence and development of new construction technologies, such as 3D-printing, requires improving the existing and creating new cement-based composite materials with a set of specific properties. Therefore, during the initial stage, the fresh mixtures should have specified fabricability indicators. In particular, for the innovative 3D-printing process, of fundamental importance are such fabricability indicators as plasticity, shape retention , and accelerated setting, which are required to create a structure using off-mould additive manufacturing. What is more, the resulting composite material must have good physical and mechanical properties to ensure the standard service life of the building or structure. To ensure that cement mortar has the characteristics required for 3D printing, it is important to determine the optimal composition and substantiate the use of every component [1, 2].

Cement mortars for 3D printing are highly concentrated heterogeneous disperse systems consisting of a liquid dispersion medium and a solid dispersed phase. The rheological behaviour of fresh mixtures is determined by their structure which changes during the printing process from the coagulation structure (when the mortar is mixed and transferred to the extruder) to the coagulation-crystallization structure (setting and hardening of the mixture in printed layers). We should note that an optimal composition in terms of the type of components, their dosage, chemical and mineralogical composition, dispersion, etc., allows for direct control over the properties of both the dispersed phase and the dispersion medium. This allows for control over the hydration products, and therefore the visco-plastic properties of the cement-water heterogeneous disperse system [3].

The simplest and most accessible factor for controlling the hydration process and the properties of cement composite systems for 3D printing is the use of chemical additives of various nature (inorganic and organic), morphology, and dispersion [4, 5]. An analysis of the studies published by Russian and international researchers [4–12] demonstrated that such additives can be divided into the following groups based on the technological properties acquired by cement mixtures.

– Additives accelerating the setting and hardening process and enhancing the strength properties of printed objects. These additives are usually inorganic salts of alkali metals and calcium (K_2CO_3, Li_2CO_3, Na_2SiO_3, $CaCl_2$, $NaAlO$) [11], active mineral additives (finely dispersed quartz, metakaolin) [5, 6], and industrial waste (microsilica, fly ash, and waste remaining after the enrichment of mineral resources) [7–10].

– Additives increasing plasticity. These are various types of superplasticizers (SPs), which, depending on the chemical composition and the ability to reduce water, are divided into four groups: lignosulphonates, melamine sulfonates, polyacrylates, and polycarboxylate esters. At the moment, the most commonly used superplasticizers are those based on polycarboxylate esters [4, 5].

– Additives increasing adhesion. They are redispersible polymer powders of polyethylene, polyacrylate, and vinylformamide [4].

– Disperse reinforcing components enhancing the physical-mechanical properties of printed composites. These are various types of fibres - polypropylene, glass, basalt, or steel fibres [13–15].

Each additive works according to a certain mechanism and, when added to cement mortar has a selective effect on the properties of the freshly prepared composite mixture and the final cement composite.

In this regard, it is important to study the use of complex and multicomponent modifiers which include additives of various types. Namely, in our study we considered the use of an additive accelerating the setting and hardening process, a superplasticiser enhancing the plasticity of fresh mixture, and a micro-reinforcing component contributing to the additional strengthening of the cement composite by preventing crack

Condensed Matter and Interphases / Конденсированные среды и межфазные границы   2023;25(1): 112–124

G. S. Slavcheva et al.   Studying the effect of modifying additives on the hydration and hardening of cement...

propagation during the hydration process. When choosing the composition of a polyfunctional additive we should take into account the fact that the particles of the modifying additive should have a similar crystal chemical structure with the particles of the cement clinker. This will allow them to form an optimal crystal structure of the material (a denser one, with fewer pores and voids) [16].

In our study, we analysed the effect the use of various modifying additives on the rheological properties, setting, hydration, and hardening of cementitious sand-based materials.

2. Experimental

For experimental studies, modified cement systems were obtained. Their initial components were Portland cement (C), grade CEM I 42.5 (GOST 31108-2016), process water (W) (GOST 23732-2011), and a superplasticiser (SP) based on polycarboxylate esters, grade Sika® ViscoCrete® T100. Quartz sand (S) with a fineness modulus $M_f \leq 1.25$ (GOST 8736-2014) was used as an aggregate.

The modifying additives were: metakaolin (MKL), grade VMK-45 ($Al_2O_3 \cdot SiO_2$; SiO_2 – 53 %, Al_2O_3 – 47 %), a complex additive – xanthan gum, grade FUFENG®80 (($C_{35}H_{49}O_{29}$)$_n$ ~ 91 %), together with tetrapotassium pyrophosphate ($K_4P_2O_7$ – 98 %) (XG + TPPPh), and a complex nanosized additive based on silicon dioxide (CNA)

with a composition "nanosized SiO_2 particles – superplasticiser" obtained by means of the sol-gel synthesis described in [16]. As a result of the synthesis, SiO_2 particles with an average size of 5–10 nm are formed in the system. They retain their aggregate stability for 7 days after the synthesis [16].

To perform the micro-reinforcement of cement composites, we used a polypropylene fibre (PF), grade Sika Fiber PPM-12, in the form of polymerized olefins (l = 12 mm, d = 0.022–0.034 mm; ρ = 910 kg/m³, tensile strength 300 – 400 MPa). The mass fraction of the PF with regard to the weight of the cement for all the systems was 0.5 %.

Compositions and concentrations of the initial components and the designations of the studied systems are presented in Table 1.

The concentrations of the modifying additives (MKL, XG + TPPPh, CNA) and the aggregate (S) were optimised during the preliminary research and remained constant. The concentration of the superplasticiser for each system was determined empirically in order to obtain the required consistency and bonding properties of the cement mortar.

The cement systems of the described compositions were obtained by mixing of dry components for 3 minutes. When obtaining visco-plastic mixtures, the mass ratios of C : S were 1 : 1.25. These ratios are optimal and were

Table 1. Composition and the main properties of the studied systems

№	System composition	W/C	ω_{SP}, % from the mass of cement	ω_{dmix}, % from the mass of cement	System designation
1	Cement, water, superplasticizer	0.33	0.8	0	C–W–SP
2	Cement, water, superplasticizer, quartz sand, fiber	0.28	0.8	0	C–W–SP–S–PF
3	Cement, water, superplasticizer, metacaolin, quartz sand, fiber	0.29	1	2	C–W–SP–S–MKL–PF
4	Cement, water, superplasticizer, xanthan gum, tetrapotassium pyrophosphate, quartz sand, fiber	0.28	1.2	0.2 / 0.2	C–W–SP–S–XG–TPPPh–PF
5	Cement, water, superplasticizer, complex nanoadditive based on SiO_2, quartz sand, fiber	0.26	0.7	0.01	C–W–SP–S–CNA–PF

Condensed Matter and Interphases / Конденсированные среды и межфазные границы 2023;25(1): 112–124

G. S. Slavcheva et al. Studying the effect of modifying additives on the hydration and hardening of cement...

determined experimentally based on preliminary studies [13]. The C - W - SP system and the C–W–SP–S–PF system were recognised as reference systems.

In our experiments, we used systems of the same consistency, which corresponded to the standard density of cement-water paste according to GOST 310.3-76 "Cements. Methods for determination of standard consistency, times of setting and soundness". Based on the consistency, which remained constant, we conducted experiments to determine the water content (W/C ratio) for each of the studied systems.

The rheological behaviour of the cement visco-plastic mixtures was evaluated by the methods of squeeze rheometry [17–20]. For this, we performed squeezing tests of freshly mixed cylinder samples using the INSTRON 5982 universal floor hydraulic testing system. The radius of the samples was equal to their height ($R = h_0 = 25$ mm).

The plasticity of the obtained composite mixtures was determined based on the results of the squeezing test performed at a constant strain rate of 5 mm/s [17]. The curves "load N – displacement Δ" obtained as a result of the testing were transformed into dependencies of the reduced load F^* on the relative change in sample height h_i/R:

$$F_i^* = \frac{Ph_i}{\pi R^2},$$

where $h_i = (h_0 - \Delta)$, h_0 is the initial height of the sample, Δ is the displacement at the i-th moment of time, P is the load applied to the sample. The value R was taken as a constant equal to the sample radius at the beginning of the test.

At the first point of inflexion of the obtained experimental curves, the plastic yield strength value K_i(I) was calculated:

$$K_i\left(\frac{h}{R}\right) = \frac{\sqrt{3}}{2}F^*.$$

To assess the shape retention, a compression test was performed at a constant load rate of $v = 0.5$ N/s [18, 19]. The results of experimental studies were interpreted as the "relative displacement Δ – time t", "load N – relative displacement Δ" curves, which were used to calculate the values of the structural strength of cement systems at the moments corresponding to the beginning of deformation and the beginning of cracking of the samples according to the formula:

$$\sigma = \frac{P}{\pi R^2},$$

Thus, we determined the criteria for the plasticity and form stability of cement composite mixtures under the modelled 3D printing conditions. These criteria include [19]:

– Plastic yield strength value K_i (I).

– Structural strength σ_0 at the beginning of deformation, which is responsible for the ability of the system to resist deformation under load.

– Plastic strength σ_{pl} and the value of relative plastic deformations Δ_{pl} at the beginning of cracking. They characterise the ability of the system to deform without destruction.

The setting process in the obtained cement composite systems was studied using the penetrometer method. The plastic strength (P_{pl}) was calculated using the following ratio:

$$P_{pl} = \frac{4N}{\pi d^2},$$

where N is penetration resistance of the mixture when a plunger with a standard diameter is immersed to a depth of 5 mm, kN; d is the plunger diameter, m². The method error was 10% [20].

The phase composition of the hardened cement paste was determined by powder diffraction (ARL X'TRA diffractometer with CuK_α radiation, $\lambda = 1.541788$ Å). The obtained data were processed using the PDWin 4.0 software package [21]. The value of the degree of hydration of the modified cement hardening systems was calculated based on the content of the alite phase $3CaO \cdot SiO_2$ (C_3S) by comparing their XRD patterns with the XRD pattern of the original cement clinker [22]:

$$D_h(C_3S) = \left(1 - \frac{I_{mod}}{I_0}\right) \times 100\,\%,$$

where I_{mod} is the intensity of the diffraction maximum at $d = 2.75$ Å of the C_3S phase of the samples of different compositions by types of additives and the timing of cement hydration; I_0 is the intensity of the diffraction maximum at $d = 2.75$ Å of the C_3S phase of the original cement.

Condensed Matter and Interphases / Конденсированные среды и межфазные границы   2023;25(1): 112–124

G. S. Slavcheva et al.   Studying the effect of modifying additives on the hydration and hardening of cement…

The microstructure of the cement composites was assessed using scanning electron microscopy (SEM) (Phenom XL scanning electron microscope).

The kinetics of the strength gain of the studied cement composites was determined by the destruction of sample cubes with the size of 5×5×5 cm using an INSTRON Sates 1500HDS testing machine. To ensure the statistically reliable results of physical and mechanical tests, the number of samples in the series was 6. The measurement uncertainty was 0.5%.

3. Results and discussion

3.1. Plasticity and shape retention of modified systems

Figure 1 shows the curves of the dependence of the reduced load F^* on the relative change in sample height h_i/R. The studied cement systems were characterised by two types of curves. Curves of the first type, including the C – W – SP – S – MKL – PF system, have a prominent horizontal section of plastic deformation between two points of inflexion, which means that the system is rigid. In this case, the value of the plastic yield strength value is $K_i(I) = 2.47$ kPa.

Reference systems as well as the C – W – SP – S – XG – TPPPh – PF and C – W – SP – S – CNA – PF systems belong to the second type of curves which do not have pronounced transitions between their sections. For these systems, the plastic yield strength value $K_i(I)$ is within the range of 1.06÷5.03 kPa. These systems have a good extrusion ability as a result of their plasticity and viscoelastic flow which does not destruct the structure.

As a result of the experimental investigation of shape retention of the studied systems two types of curves were obtained: "relative displacement Δ – time t" (Fig. 2a) and "relative displacement – load σ" (Fig. 2b).

The first type of curves was characterised by three sections: the "phase stability", which characterised the absence of deformations under loads; "plastic phase", which characterised the ability of the system to deform without destruction, and "cracking phase", in which microcracking occurred before the complete destruction of the structure. On the "relative displacement – load σ" curves, the moment when microcracks appeared in the systems corresponded to a sharp drop in the load.

The analysis of the results (Fig. 2, Table 2) demonstrated that all the cementitious sand-based materials with modifying additives and fibres are characterised by rational values of plasticity and shape retention , which makes it possible to perform 3D printing without defects
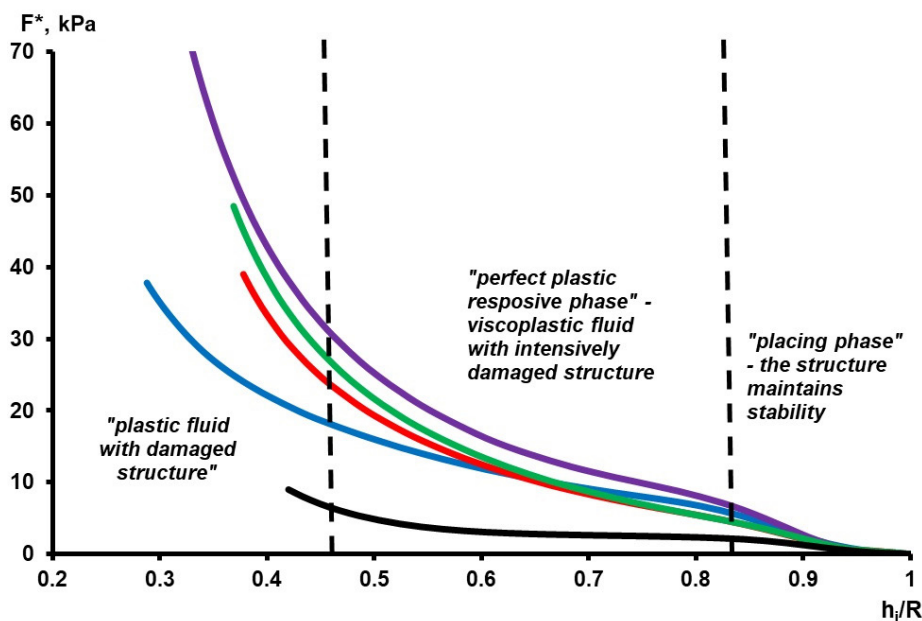
Fig. 1. Curves of the dependence of the reduced load F* on the relative change in sample height h$_i$/R. Designated: ▬ – C–W–SP; ▬ – C–W–SP–S–PF; ▬ – C–W–SP–S–MKL–PF; ▬ – C–W–SP–S–CNA–PF; ▬ – C–W–SP–S–XG–TPPPh–PF

Condensed Matter and Interphases / Конденсированные среды и межфазные границы   2023;25(1): 112–124

G. S. Slavcheva et al.   Studying the effect of modifying additives on the hydration and hardening of cement...
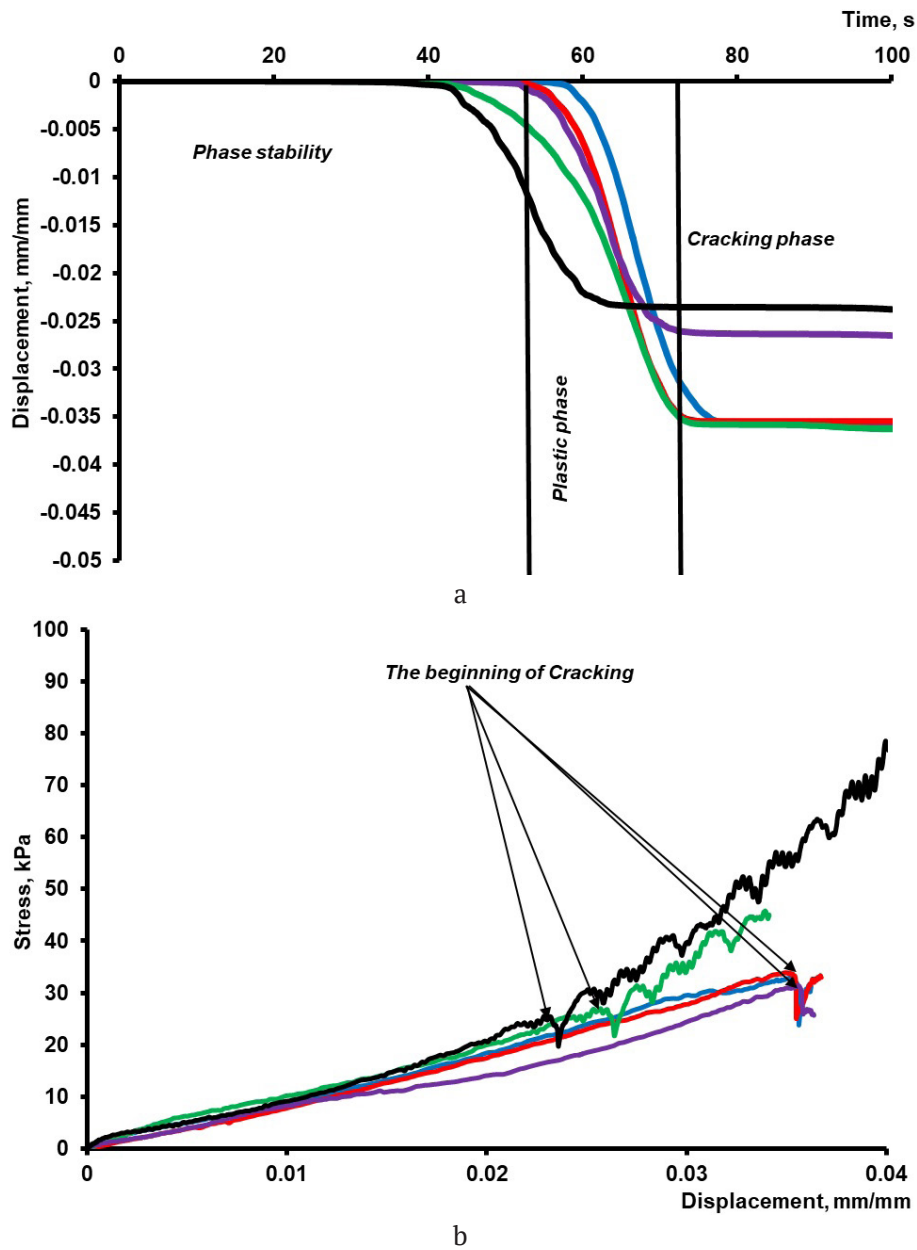
Fig. 2. Dependence curves a) displacement Δ – time *t*; b) load σ – relative displacement Δ. Designated: ▬ – C–W–SP; ▬ – C–W–SP–S–PF; ▬ – C–W–SP–S–MKL–PF; ▬ – C–W–SP–S–CNA–PF; ▬ – C–W–SP–S–XG–TPPPh–PF

and deformed layers. The best shape retention was observed in the C – W – SP – S – CNA – PF system. It demonstrated the highest values $\sigma_0 = 5.44$ kPa, and the lowest $\Delta_{pl} = 0.03$ mm/mm.

Thus, the setting, hydration and hardening processes were studied for mixtures whose compositions were optimised based on the plasticity and shape retention criteria (Table 2). They are considered to be basic mixtures for 3D printing.

3.2. Phase composition and microstructure of the studied systems

The X-ray diffraction analysis (Fig. 3, Table 3) of the reference system (C – W – SP), with the hardening process lasting 28 days, demonstrated that hydrated compounds in this system are represented mostly by highly basic calcium silicate hydroxides ($2CaO \cdot SiO_2 \cdot H_2O$), a tobermorite ($xCaO \cdot SiO_2 \cdot zH_2O$), and smaller amounts of the calcium sulphoaluminate phase

Condensed Matter and Interphases / Конденсированные среды и межфазные границы   2023;25(1): 112–124

G. S. Slavcheva et al.   Studying the effect of modifying additives on the hydration and hardening of cement...

Table 2. Rheological characteristics of the modified cement systems

System	Setting start time, τ, min	Plastic yield strength value $K_i(I)$, kPa	Structural strength σ_0, kPa	Plastic strength σ_{pl}, kPa	Relative plastic deformation Δ_{pl}, mm/mm
C–W–SP	270	1.06	1.10	45.01	0.02
C–W–SP–S–PF	135	5.03	5.03	31.64	0.044
C–W–SP–S–MKL–PF	90	2.47	2.47	36.74	0.035
C–W–SP–S–XG–TPPPh–PF	135	3.50	3.50	33.15	0.035
C–W–SP–S–CNA–PF	120	3.66	5.44	26.75	0.030
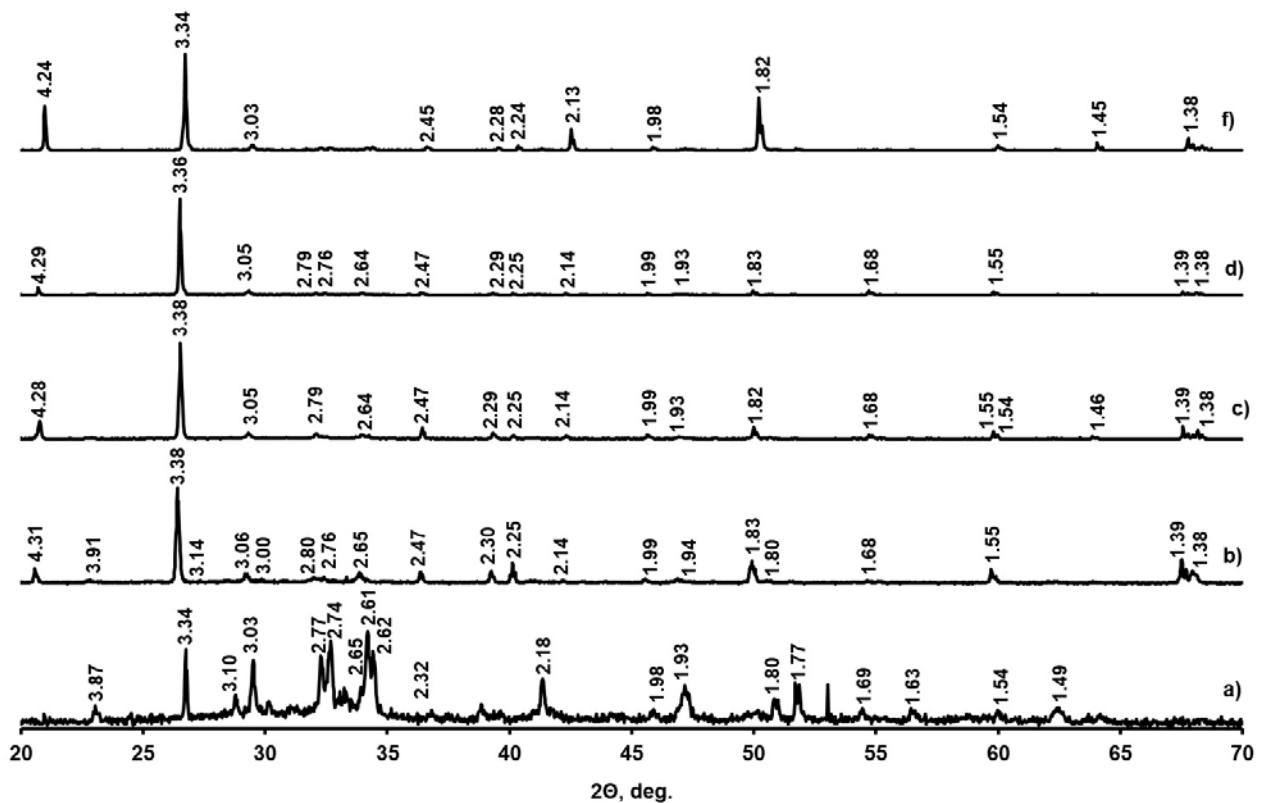
Fig. 3. X-Ray diffraction patterns of the studied cement composites. Designated: a) C–W–SP; b) C–W–SP–S–PF; c) C–W–SP–S–MKL–PF; d) C–W–SP–S–XG–TPPPh–PF; e) C–W–SP–S–CNA–PF

($3CaO\cdot Al_2O_3\cdot 3CaSO_4\cdot 26H_2O$) and the initial non-hydrated phases of alite $3CaO\cdot SiO_2$ and belite $2CaO\cdot SiO_2$.

The analysis of the X-ray diffraction data regarding the phase composition of the composites for 3D printing which underwent hardening for 28 days (Fig. 3, Table 3), demonstrated that the prevailing phase is the quartz phase, because quartz sand is used as an aggregate in the system. However, the sand, as well as the fibre, has hardly any impact on the chemical composition of the newly formed cement composite. This can be

demonstrated by the C – W – SP – S – PF system, where, similar to the reference system 1 (without the aggregate), the dominant phases of the new composites are highly basic calcium silicate hydrates ($2CaO\cdot SiO_2\cdot H_2O$) and tobermorite $(CaO)_x\cdot SiO_2\cdot zH_2O$.

Each additive, on the contrary, results in the formation of additional phases in the system. Thus, the system with metakaolin (C – W – SP –S – MKL – PF) demonstrated the presence of aluminate phases (Fig. 3c) characterised by prismatic, acicular, and fibrous morphology

Condensed Matter and Interphases / Конденсированные среды и межфазные границы 2023;25(1): 112–124

G. S. Slavcheva et al. Studying the effect of modifying additives on the hydration and hardening of cement...

Table 3. Phase composition and degree of hydration of the studied cement systems (duration of hardening 28 days)

System	W/C	D_h, %	Phase composition
C – W – SP	0.33	73	$2CaO \cdot SiO_2 \cdot H_2O$ $(CaO)_x \cdot SiO_2 \cdot zH_2O$ $Ca(OH)_2$ $3CaO \cdot SiO_2$
C – W – SP – S – PF	0.28	95	SiO_2 $2CaO \cdot SiO_2 \cdot H_2O$ $(CaO)_x \cdot SiO_2 \cdot zH_2O$ $Ca(OH)_2$ $3CaO \cdot SiO_2$
C – W – SP –S – MKL – PF	0.29	93	SiO_2 $(CaO)_x \cdot SiO_2 \cdot zH_2O$ $3CaO \cdot Al_2O_3 \cdot CaSO_4 \cdot 32H_2O$ $CaO \cdot SiO_2 \cdot H_2O$ $3CaO \cdot SiO_2$
C – W – SP –S – XG – TPPPh – PF	0.28	98	SiO_2 $xCaO \cdot SiO_2 \cdot zH_2O$ $2CaO \cdot SiO_2 \cdot H_2O$ $CaHPO_4 \cdot 2H_2O$
C – W – SP – S – CNA – PF	0.26	98	SiO_2 $(CaO)_x \cdot SiO_2 \cdot zH_2O$ $CaO \cdot SiO_2 \cdot H_2O$ $3CaO \cdot Al_2O_3 \cdot CaSO_4 \cdot 32 H_2O$ $3CaO \cdot SiO_2$

(Fig. 4c). The presence of such phases can enhance the shape retention and the strength of this system.

The C – W – SP – S – XG – TPPPh –PF system with xanthan gum and potassium pyrophosphate demonstrated, similar to the reference system, the presence of dyscrystalline highly basic calcium silicate hydrates and tobermorite forming pronounced cluster crystals (Fig. 3d, 4d). There was also a small amount of dicalcium phosphate ($CaHPO_4 \cdot 2H_2O$), which is explained by the partial interaction of the additive with the hydration products.

In the C – W – SP – S – CNA – PF system with SiO_2 based complex nanoadditives, a well-crystallized tobermorite phase and low base calcium silicate hydroxides ($CaO \cdot SiO_2 \cdot H_2O$) (Fig. 3e, 4e) were dominant. There was also a small amount of ettringite ($3CaO \cdot Al_2O_3 \cdot CaSO_4 \cdot 32H_2O$), which increased the form stability and strength of the system.

All the systems demonstrated high values of hydration degrees, 95–98 % (Table 3), with the maximum hydration degree of 98 % being characteristic for all the systems with the XG + TPPPh complex modifying additive and the CNA additive.

Therefore, we can say that quartz sand does not affect the phase composition of the new hardening system, while the modifying additives have a direct impact on the hydration products of the studied cement systems, since they participate in heterogeneous processes of phase formation. At the same time, the hydration degree of cement increased significantly. The kinetics of hydration and the composition of the new composites are affected the most by the metakaolin additive and the SiO_2 based complex nanosized additive. They increase the formation of low base calcium silicate hydroxides, which is explained by the fact that they have a similar crystal chemical structure with the new the cement composite. Polypropylene fibre is practically inert to the hydration and hardening process.

Condensed Matter and Interphases / Конденсированные среды и межфазные границы 2023;25(1): 112–124

G. S. Slavcheva et al. Studying the effect of modifying additives on the hydration and hardening of cement...
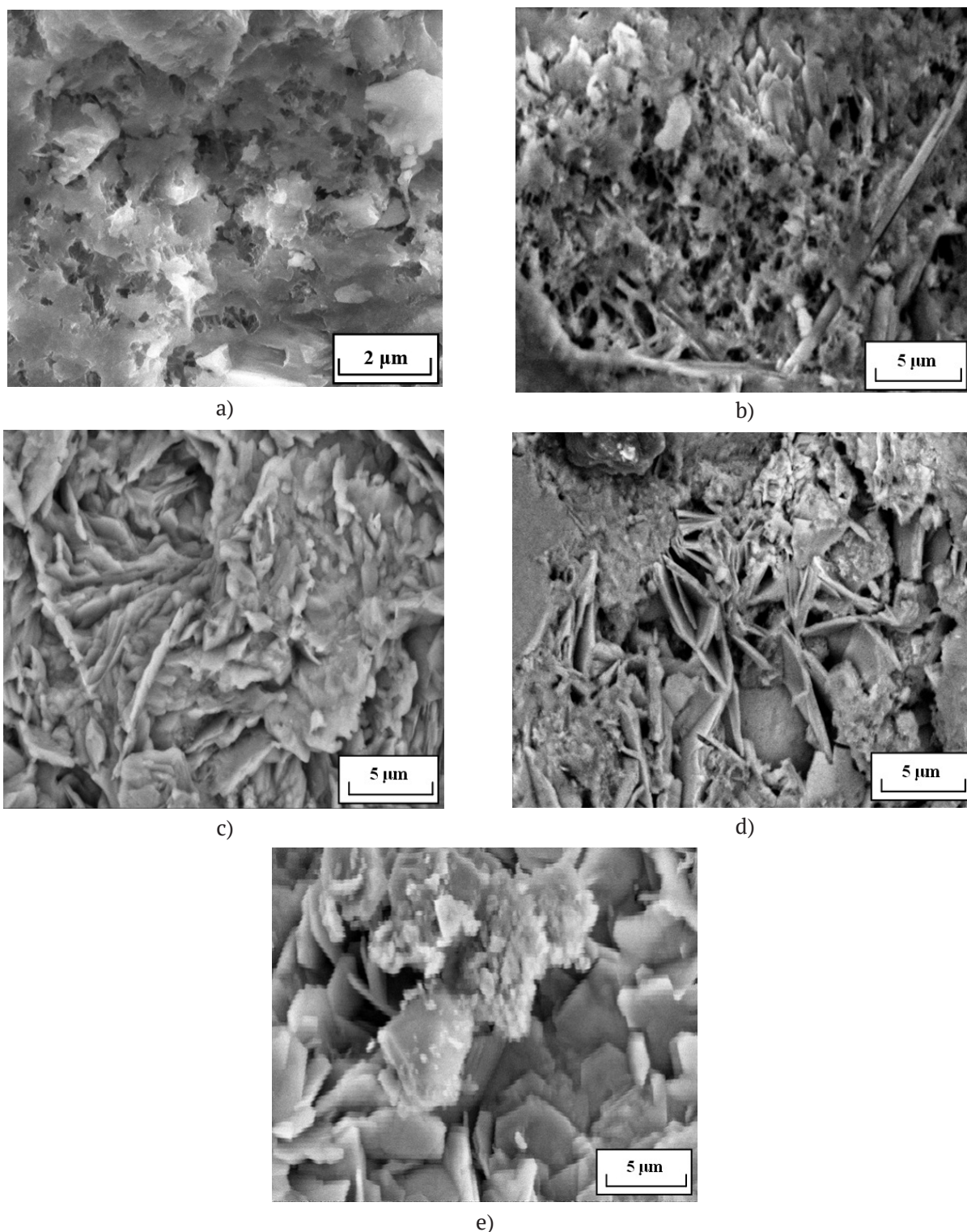
Fig. 4. Micrographs of the studied cement hardening systems. Designated: a) C–W–SP; b) C–W–SP–S–PF; c) C–W–SP–S–MKL–PF; d) C–W–SP–S–XG–TPPPh–PF; e) C–W–SP–S–CNA–PF

Condensed Matter and Interphases / Конденсированные среды и межфазные границы   2023;25(1): 112–124

G. S. Slavcheva et al.   Studying the effect of modifying additives on the hydration and hardening of cement...

3.3. Kinetics of the setting-up and hardening of cementitious sand-based materials

Table 4 presents experimental data for all the studied systems regarding the beginning of the setting process τ, plastic strength P_{pl} at the beginning of setting registered by a standard method, and the compressive strength for standard hardening time. According to the standard method for determination of the speed of setting, the beginning of the process and the value of P_{pl} at the moment of actual setting differ greatly. The beginning of setting is within the range of 45 – 165 minutes, the plastic strength is P_{pl} = 28 – 357 kPa.

The lowest plastic strength (28.35 kPa) and the longest setting time (165 minutes) are characteristic for systems without additives (C – W – SP – S – PF). Quartz sand is chemically inert to the materials of the cement clinker and under standard hardening conditions does not have any noticeable effect on the visco-plastic properties of the systems. Therefore, the plastic strength of the studied systems with sand is affected significantly by the modifying additives used.

Introduction of metakaolin increases the plastic strength significantly and slightly reduces the setting time. Thus, the setting time in this system is 107 minutes with the corresponding P_{pl} = 357 kPa (Table 4).

This can be accounted for by the fact that metakaolin particles, having similar crystal chemical structure with the cement clinker, can occupy space between cement grains in a particular way. This results in a denser spatial packing of solid phase particles leading to a denser structure of the whole system due to a smaller number of pores and voids.

For cement mixtures modified with xanthan gum and potassium pyrophosphate, the setting process started after 136 minutes with the corresponding P_{pl} = 179.19 kPa (Table 4). This can be explained by the fact that xanthan gum can modify the dispersion medium. It affects the density of the dispersion medium and can structure the liquid phase, which reduces the chemical activity of water molecules required for the hydration of cement clinker minerals. These processes result in greater structural strength of the system and faster setting of cement.

Although potassium pyrophosphate accelerates the hydration of cement, this electrolyte additive increases the flow rate of the system and, correspondingly, reduces its plastic strength. As a result, setting of systems with the XG + TPPPh modifier starts practically at the same time is setting of the reference system without any modifiers. At the same time, the plastic strength is 3-6 times higher than that of the reference systems.

Setting of mixtures with CNA starts after 45 minutes with P_{pl} = 293.96 kPa. The faster setting can be explained by the fact that nanosized SiO_2 particles in the CNA, thanks to large surface energy and similar crystal chemical structure with the cement clinker, can accelerate heterogeneous processes of formation of hydrated newgrowths. As a result, the hydration, setting, and strength gaining processes accelerate. At the same time, the superplasticiser which was part of the CNA, due to adsorption on the surface of the hydrated phases of the cement system reduces their interfacial energy, which results in their dispersion. In this case, some of the immobilised water is released, which provides for an increase in the plasticity of the mixture and, accordingly, a slight decrease in plastic strength.

Thus, modifying additives have great effect on the setting speed and the plastic strength of mixtures for 3D printing. Depending on the type of the additive, the difference in the plastic

Table 4. Experimental data regarding the setting and hardening of the cement mixtures for 3D printing

№	System composition	W/C	Setting processes		Compressive strength, MPa				
			P_{pl}, kPa	τ, min	1 day	3 days	7 days	14 days	28 days
1	C–W–SP	0.33	25.92	105	19.41	29.28	35.19	48.17	57.39
2	C–W–SP–S–PF	0.28	28.33	165	20.74	40.90	51.70	58.41	61.01
3	C–W–SP–S–MKL–PF	0.29	356.60	107	25.03	43.12	55.30	60.65	62.70
4	C–W–SP–S–XG–TPPPh–PF	0.28	179.19	136	7.33	39.95	49.92	49.73	58.30
5	C–W–SP–S–CNA–PF	0.26	293.96	45	26.52	45.07	57.36	61.07	65.80

Condensed Matter and Interphases / Конденсированные среды и межфазные границы   2023;25(1): 112–124

G. S. Slavcheva et al.   Studying the effect of modifying additives on the hydration and hardening of cement...

strength can reach 7–12 times, and the difference in the setting speed can reach 1.5–3 times.

An analysis of the study of the strength of cement composites demonstrated that modified cement systems gain strength more intensively, and the values R_{com} are higher than those for the reference system (Table 4).

We should note that the hardening process has the following peculiarities.

The highest values for compressive strength at the initial stages of hardening and after the hardening is complete are demonstrated by cement composites with CNA additives (R_{com} = 27 MPa at 1 day, R_{com} = 66 MPa at 28 days) and metakaolin (R_{com} = 25 MPa at 1 day, R_{com} = 63 MPa at 28 days). A marked increase in the strength of these systems is explained by the close resemblance of the crystal chemical structure of the additives to the cement clinker minerals and by the physicochemical activity.

Cement composites modified with xanthan gum and potassium pyrophosphate are characterised by low strength. For the C – W – SP –S – XG – TPPPh – PF system, 1 day after the beginning of hardening R_{com} is 7 MPa, which is three times lower than for the reference system after 28 days of hardening (R_{com} = 58 MPa).

Having analysed the effect of the modifying additives on the structure formation process and the properties of mixtures and composites for 3D printing, we can assume the following.

1) Metakaolin particles, due to similar crystal chemical structure with the cement clinker, can behave as nuclei during the structure formation of the cement composite. Located between the cement grains, they result in a denser spatial packing of solid phase particles which affects the porosity of the cement system and makes its structure denser. On the one hand, this increases the plastic strengths of the system in the visco-plastic state. On the other hand, it increases the strength of the cement composite during hardening.

2) Due to its chemical nature, potassium pyrophosphate can change the ion composition and the viscosity of the dispersion medium, accelerating the hydration of the cement clinker and increasing the density and stability of the cement system.

3) Xanthan gum particles are chemically inert to cement clinker minerals. Therefore, they mainly affect the properties of the dispersion medium. When introduced into the cement system, xanthan gum increases the viscosity and density of the liquid phase, as well as the structure formation. This enhances the structural strength of the cement system and slows down the setting and strength gaining processes.

4) A complex nanosized additive based on SiO_2 nanoparticles accelerates the heterogeneous processes of phase formation of hydrated compounds thanks to similar crystal chemical structure and increased surface energy. At the same time, the hydration, setting, and strength gaining processes accelerate.

4. Conclusions

The study determined that the introduction of modifying additives of various nature into cement composite mixtures for 3D printing significantly affects their rheological behaviour, as well as the hydration, and strength gaining processes. The study demonstrated that cementitious sand-based materials modified with CNA and metakaolin are optimal with regard to their plasticity, the shape retention, and the speed of the hydration, setting, and strength gaining processes. The highest values for compressive strength for the said systems were registered after 28 days of hardening. The hydration products of cement composites with CNA and metakaolin additives consists mainly of low base calcium silicate hydroxides. Metakaolin also results in the formation of ettringite.

Therefore, in our study, we determined the optimal compositions for cement composite materials. These compositions make it possible to obtain composites with set properties (faster setting, required degree of plasticity and plasticc yield strength value, physical, mechanical, climate-related indicators). Received patents [23–25] prove that the suggested compositions of cement composites are of great practical value for 3D-build printing .

Author contributions

G.S. Artamonova, O.V. Slavcheva: scientific leadership, research concept, methodology development, text writing and editing, final conclusions. D.S. Babenko, M.A. Shvedova: conducting experimental studies, systematisation and description of the results.

Condensed Matter and Interphases / Конденсированные среды и межфазные границы   2023;25(1): 112–124

G. S. Slavcheva et al.   Studying the effect of modifying additives on the hydration and hardening of cement...

Conflict of interests

The authors declare that they have no known competing financial interests or personal relationships that could have influenced the work reported in this paper.

References

1. Vatin N. I., Chumadova L. I., Goncharov I. S., … Finashenkov E. A. 3D printing in construction. *Construction of Unique Buildings and Structures*. 2017;1(52): 27–46. (In Russ.). https://doi.org/10.18720/CUBS.52.3

2. Pustovgar A. P., Adamcevich A. O., Volkov A. A. Technology and organization of additive construction. *Industrial and Civil Engineering*. 2018;9: 12–20. (In Russ., abstract in Eng.). Available at: https://www.elibrary.ru/item.asp?id=36296905

3. Puharenko Yu. V., Hrenov G. M. Calculation of the composition when designing concrete mixtures for continuous formless molding. *Zhilishchnoe stroitel'stvo = Housing construction*. 2022;4:40–45. (In Russ., abstract in Eng.). https://doi.org/10.31659/0044-4472-2022-4-40-45

4. Beznogova O. Yu., Potapova E. N. Materials for additive manufacturing construction. *Uspekhi v himii i himicheskoj tekhnologii*. 2022;3(252): 16–18. (In Russ., abstract in Eng.). Available at: https://www.elibrary.ru/item.asp?id=48730949

5. Tramontin Souza M., Maia Ferreira I., Guzi de Moraes E., … Novaes de Oliveira A. P. Role of chemical admixtures on 3D printed Portland cement: Assessing rheology and buildability. *Construction and Building Materials*. 2022;314: 125666. https://doi.org/10.1016/j.conbuildmat.2021.125666

6. Kalpana M., Vaidevi C., Vijayan D. S., Benin S. R. Benefits of metakaolin over microsilica in developing high performance concrete. *Materials Today: Proceedings*. 2020;33(1): 977–983. https://doi.org/10.1016/j.matpr.2020.06.566

7. Bondarev B. A., Korneeva A. O., Rogotovskij A. N., Meshcheryakov A. A. Development mixtures for additive technologies. *News of Higher Educational Institutions. Construction*. 2021;11(755): 55–63. (In Russ., abstract in Eng.). https://doi.org/10.32683/0536-1052-2021-755-11-55-63

8. Dem'yanenko O. V., Kopanica N. O., Sorokina E. A. Performance characteristics of 3D printing construction mixes depending on thermally-modified peat additive. *Vestnik Tomskogo gosudarstvennogo arkhitekturno-stroitel'nogo universiteta. Journal of Construction and Architecture*. 2018;20(4): 122–134. (In Russ., abstract in Eng.). https://doi.org/10.31675/1607-1859-2018-20-4-122-134

9. Zagorodnuk L. K., Elistratkin M. Yu., Podgornyi D. S., Al Mamuri S. Composite binders for 3d additive technologies. *The Russian Automobile and Highway Industry Journal*. 2021;18(4): 428–439. (In Russ., abstract in Eng.). https://doi.org/10.26518/2071-7296-2021-18-4-428-439

10. Dey D., Srinivas D., Panda B., Suraneni P., Sitharam T. G. Use of industrial waste materials for 3D printing of sustainable concrete: A review. *Journal of Cleaner Production*. 2022;340: 130749. https://doi.org/10.1016/j.jclepro.2022.130749

11. Chen M., Li L., Zheng Y., Zhao P., Lu, L., Cheng X. Rheological and mechanical properties of admixtures modified 3D printing sulphoaluminate cementitious materials. *Construction and Building Materials*. 2018;189: 601–611. https://doi.org/10.1016/j.conbuildmat.2018.09.037

12. Liu J., Yu C., Shu X., Ran Q., Yang Y. Recent advance of chemical admixtures in concrete. *Cement and Concrete Research*. 2019;124: 105834. https://doi.org/10.1016/j.cemconres.2019.105834

13. Kristombu Baduge S., Navaratnam S., Abu-Zidan Y., … Aye, L. Improving performance of additive manufactured (3D printed) concrete: A review on material mix design, processing, interlayer bonding, and reinforcing methods. *Structures*. 2021;29: 1597–1609. https://doi.org/10.1016/j.istruc.2020.12.061

14. Shaikh F. U. A., Luhar S., Arel H. S., Luhar I. Performance evaluation of Ultrahigh performance fibre reinforced concrete – A review. *Construction and Building Materials*. 2020;232: 117152. https://doi.org/10.1016/j.conbuildmat.2019.117152

15. Zeyad A. M. Effect of fibers types on fresh properties and flexural toughness of self-compacting concrete. *Journal of Materials Research and Technology*. 2020;9(3): 4147–4158. https://doi.org/10.1016/j.jmrt.2020.02.042

16. Slavcheva G. S., Artamonova O. V., Shvedova M. A., Britvina E. A. Effect of viscosity modifiers on structure formation in cement systems for construction 3D printing. *Inorganic Materials*. 2021;57: 94–100. https://doi.org/10.1134/S0020168521010143

17. Russel N., Lanos C. Plastic fluid flow parameters identification using a simple squeezing test. *Applied Rheology*. 2003;13(3): 3–5. https://doi.org/10.1515/arh-2003-0009

18. Perrot A., Rangeard D., Pierre A. Structural built-up of cement-based materials used for 3D-printing extrusion techniques. *Materials and Structures*. 2016;49(4): 1213–1220. https://doi.org/10.1617/s11527-015-0571-0

19. Slavcheva G. S., Babenko D S., Shvedova M. A. Analysis and criteria assessment of rheological behavior of mixes for construction 3-D printing. *Stroitel'nye Materialy*. 2018;12: 34–40. (In Russ., abstract in Eng.). https://doi.org/10.31659/0585-430X-2018-766-12-34-40

Condensed Matter and Interphases / Конденсированные среды и межфазные границы   2023;25(1): 112–124

G. S. Slavcheva et al.   Studying the effect of modifying additives on the hydration and hardening of cement...

20. Lootens D., Joussett O., Matinie L., Roussel N., Flatt R. J. Yield stress during setting of cement pastes from penetration test. *Cement and Concrete Research*. 2009;39: 401–408. https://doi.org/10.1016/j.cemconres.2009.01.012

21. *JCPDS – International Centre for Diffraction Data*. © 1987 – 1995. JCPDS – ICDD. Newtown Square, PA. 19073. USA. Available at: https://www.icdd.com/

22. Bullard J. W., Jennings H. M., Livingston R. A. Mechanisms of cement hydration. *Cement and Concrete Research*. 2011;41: 1208–1223. https://doi.org/10.1016/j.cemconres.2010.09.011

23. Slavcheva G. S., Artamonova O. V., Shvedova M. A., Britvina E. A. *Two-phase cement-based mixture for composites in 3D construction printing technology*. Patent RF No. 2729086, 2020. Publ. 04.08.2020, bull. No. 22. (In Russ).

24. Slavcheva G. S., Artamonova O. V., Shvedova M.A., Britvina E.A. *Two-phase cement-based mixture for composites in 3D construction printing technology*. Patent RF No. 2729220, 2020. Publ. 05.08.2020, bull. No. 22. (In Russ).

25. Artamonova O. V., Slavcheva G. S., Shvedova M. A., Britvina E. A., Babenko D. S. *Nanomodified cement composite for construction 3D printing*. Patent RF, No. 2767643, 2022. Publ. 18.03.2022, bull. No. 8. (In Russ).

Information about authors

Galina S. Slavcheva, Cand. Sci. (Tech.), Associate Professor, Professor at the Department of Technology of Building Materials, Products and Structures, Voronezh State Technical University (Voronezh, Russian Federation).

https://orcid.org/0000-0001-8800-2657

gslavcheva@yandex.ru

Olga V. Artamonova, Dr. Sci. (Tech.), Associate Professor, Professor at the Department of Chemistry and Chemical Technology of Materials, Voronezh State Technical University (Voronezh, Russian Federation).

https://orcid.org/0000-0001-9157-527X

ol_artam@rambler.ru

Dmitry S. Babenko, PhD applicant, Engineer, of Higher School of Building Materials Science, Voronezh State Technical University (Voronezh, Russian Federation).

babenko.dmitrii@bk.ru

Maria A. Shvedova, assistant of the Department of Chemistry and Chemical Technology of Materials, Voronezh State Technical University (Voronezh, Russian Federation).

https://orcid.org/0000-0002-6484-8719

marishwedowa@mail.ru

Original articles

Research article
https://doi.org/10.17308/kcmf.2023.25/10980

The equilibrium shape of rolled out meniscus

A. A. Sokurov[✉]

Institute of Applied Mathematics and Automation – the filial branch of Federal State Budgetary Scientific Establishment
«Federal Scientific Center «Kabardin-Balkar Scientific Center of Russian Academy of Sciences»,
89 A Shortanova str., Nalchik 360000, Russian Federation

Abstract

The paper considers the issue of the equilibrium shape of the rolled out capillary meniscus in a homogeneous gravitational field. The approach used in this work differs from the earlier ones, as it takes into account the size dependence of the surface tension. With the help of such models, it will be possible to understand better the behaviour of small capillary bodies and to reveal the effects caused by the size dependence of physical parameters. For the purpose of the study, we propose to use an analogue of the well-known Tolman formula expressing the size dependence of the surface tension for the case of an interface with an arbitrary geometry. Taking into account the size dependence of the surface tension gives us equations which are predictably more complicated than the classical ones. Because of their complex nonlinearity, they cannot be solved by elementary functions, hence numerical methods are applied. The mathematical model of the meniscus is presented in a form that is better suited for numerical modelling of the profiles. We carried out computational experiments to determine the degree and nature of the effect of the parameter responsible for the size dependence of the surface tension on the equilibrium shape of the meniscus. We analysed the special cases when the exact solution of the Laplace equation and the exact relations between the meniscus profile coordinates can be obtained.

Keywords: Capillary meniscus, Surface tension, Size dependence, Capillary surface, Laplace equation, Capillary phenomena, Interfaces

✉ Aslan A. Sokurov, e-mail: asokuroff@gmail.com

1. Introduction

Rolled out menisci, along with sessile/pendant drops and liquid bridges, are among the main types of axisymmetric capillary menisci. They can usually be observed when a cylindrical rod or spherical body is partially submerged in a liquid. Due to wetting, the surface of the liquid curves and takes a certain shape. The small volume of liquid that is now above the zero level is the rolled out meniscus. In English-language studies, these capillary systems are referred to by various names such as holms, rod menisci, etc. In Russian-language sources, the term "neck" can be used. We use the terminology adopted in the monograph [1]. A distinctive feature of this type of meniscus is its surface that asymptotically transitions to a horizontal plane as it moves away from the wetting line.

The study of the physical problems associated with rolled out menisci is of great theoretical and practical importance [2–6]. These configurations are observed, for example, in experiments to determine surface and linear tension, in studies of wetting and spreading phenomena, in technologies for growing single crystals from melts (Czochralski and Stepanov techniques), in studies of heat and mass transfer and electrical conductivity in nanosystems, flotation, probe microscopy and lithography, and in nanofluidics.

In the vast majority of cases where the rolled out meniscus is used as a model object, the problem of its equilibrium shape has to be considered. The main point of the problem is to determine the shape the meniscus takes in an external force field. Based on its solution, it is possible to draw qualitative and quantitative conclusions about the patterns of some processes occurring at the interface between immiscible media. The equilibrium shape problem in its general formulation does not have an exact solution. Therefore, it is crucially important to develop numerical methods which, in certain situations, make it possible to calculate the profiles of rolled out menisci with a good accuracy. Among the publications devoted to this issue, we should mention [7–13]. In general, the studies pay much less attention to rolled out menisci than to drops and bridges.

In this study, we considered the equilibrium shape problem of the rolled out meniscus in a homogeneous gravitational field. The novelty of the approach is that the model takes into account the size dependence of the surface tension, which is described by the generalised Tolman formula.

2. Size dependence of surface tension

The surface tension σ is the most important thermodynamic characteristic of the interface; it is the cause of almost all capillary phenomena [1]. It is well known that the value of surface tension, provided that all other conditions are equal, depends on the curvature of the interface [14–18]. This relationship is commonly referred to as the size dependence. Physically, the dependence is due to a change in the interatomic or intermolecular interactions near the interface. For example, the energies required to evaporate atoms or molecules from flat and curved surfaces can be ten times different from each other. If the surface is concave, the evaporation energy is higher than in the case of a flat interface. For a convex surface, the evaporation energy is lower (see Fig. 1).

The effect of the size dependence of the surface tension is most pronounced in low-dimensional thermodynamic systems, so studying it is especially relevant for the development of modern nanotechnology. At this point, the theory of size effects is certainly an independent (not exhaustively developed) direction in the physics of interfacial phenomena, which is considered to be an underlying principle of the type II capillary phenomena (according to L. M. Scherbakov's terminology).
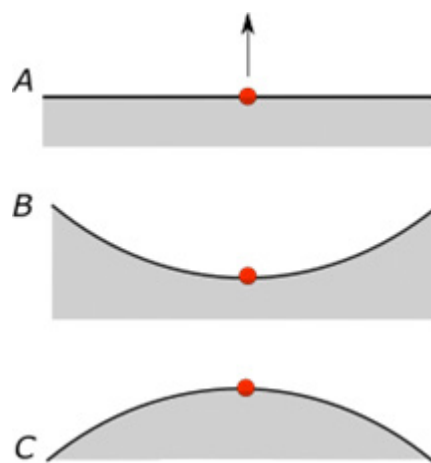

Fig. 1. Particle at the interface

The dependence of the surface tension for a small spherical drop is determined by the well-known Tolman formula [14, 15]:

$$\sigma = \frac{\sigma^{(\infty)}}{1 + \dfrac{2\delta}{R}}, \tag{1}$$

Where $\sigma^{(\infty)}$ is the surface tension of a flat interface, R is the drop radius, and δ is a non-negative parameter that describes the thickness of the interface (the Tolman length). For interfaces with arbitrary geometry, we generalised formula (1) [19]:

$$\sigma = \frac{\sigma^{(\infty)}}{1 + \delta\left(\dfrac{1}{R_1} + \dfrac{1}{R_2}\right)}, \tag{2}$$

where R_1 and R_2 are the radii of curvature of the interface in main directions. As can be seen from (2), $\sigma \to \sigma^{(\infty)}$ at $\delta \to 0$.

3. Theoretical model

Before proceeding to the equations, let us note the following. It is common to consider the size dependence of the surface tension when the volume of the condensed phase is rather small. On the contrary, the influence of gravity on the meniscus shape is significant at larger sizes. So, where the size dependence of the surface tension is taken into account, the effect of gravity can be ignored, and vice versa. However, the thickness of the interface layer δ increases with increasing temperature. Therefore, the dependence of the surface tension on the surface curvature, apparently, should also appear in macroscopic systems, for example, near a critical point. Second, in the considerations below, the gravitational field can be easily replaced by an artificial homogeneous gravitational field of higher strength. In this case, it only affects the numerical value of just one parameter. Anyway, it is important to derive the most general equations which take into account both the size dependence of surface tension and the gravitational field.

Let us consider a rolled out meniscus formed by the contact of a vertically placed cylinder with free surface of liquid. There are no restrictions on the radius of the cylinder in this problem. However, it should not be so small that a macroscopic description of the meniscus is no longer applicable.

The coordinate system associated with the meniscus profile and the designations are shown in Fig. 2: s is the arc length of the profile measured from the tangential point, φ is the slope angle of the tangent to the meniscus profile with the horizontal axis x, and (x, z) are the coordinates of an arbitrary point of the profile. In the gravitational field, the condition of mechanical equilibrium of the meniscus is defined by Laplace formula for excess pressure [1]:

$$\sigma\left(\frac{1}{R_1} + \frac{1}{R_2}\right) = -|\rho_l - \rho_v| gz, \tag{3}$$

where ρ_l, ρ_v are the densities of the liquid and gas phases respectively, g is the gravitational acceleration. We should further keep in mind that the value of the surface tension σ is not constant as previously thought. It depends on the mean curvature of the surface by formula (2). After inserting formula (2) in (3), we get:

$$\frac{1}{R_1} + \frac{1}{R_2} = -\frac{\beta z}{1 + \delta\beta z}, \tag{4}$$

where $\beta = |\rho_l - \rho_v| g / \sigma^{(\infty)}$ is the capillary constant. If the surface has rotational symmetry, its principal curvatures are defined by the meridian section $z(x)$:

$$\frac{1}{R_1} = \pm\frac{d^2z / dx^2}{\left[1 + \left(dz / dx\right)^2\right]^{3/2}},$$

$$\frac{1}{R_2} = \pm\frac{dz / dx}{x\left[1 + \left(dz / dx\right)^2\right]^{1/2}}.$$

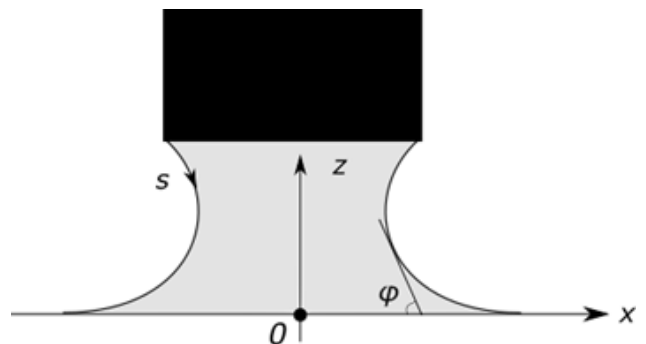Then, after determining the sign, (4) transforms to the equation:

Fig. 2. Meniscus profile

$$\frac{d^2z/dx^2}{\left[1+\left(dz/dx\right)^2\right]^{3/2}}+\frac{dz/dx}{x\left[1+\left(dz/dx\right)^2\right]^{1/2}}=$$

$$=\frac{\beta z}{1+\delta\beta z}. \tag{5}$$

Usually, the equation for the rolled out meniscus profile is extended with the boundary conditions of the form:

$$\left.\frac{dz}{dx}\right|_{x=x_0}=\tan\left(\pi-\varphi_0\right),\left.\frac{dz}{dx}\right|_{x\to+\infty}=0, \tag{6}$$

where x_0 is the radius of the contact area, i.e., the cylinder, and φ_0 is the slope angle of the tangent at the point $x=x_0$. The first condition (6) is due to wetting of the cylinder by liquid, the second condition is caused by asymptotic degeneration of the meniscus surface into a plane as it extends away from the contact line.

The principal curvatures of the rotation surface can be expressed in another way:

$$\frac{1}{R_1}=\frac{d\varphi}{ds},\frac{1}{R_2}=\frac{\sin\varphi}{x}. \tag{7}$$

Based on (7), the basic equation (4) was rewritten as follows:

$$\frac{d\varphi}{ds}=-\frac{\beta z}{1+\delta\beta z}-\frac{\sin\varphi}{x}. \tag{8}$$

On the other hand, the expressions for a smooth flat curve are:

$$\frac{dx}{ds}=\cos\varphi,\frac{dz}{ds}=-\sin\varphi. \tag{9}$$

Combining (8) and (9), we finally obtained a system of equations:

$$\frac{dx}{d\varphi}=-\frac{\left(1+\delta\beta z\right)x\cos\varphi}{\beta xz+\left(1+\delta\beta z\right)\sin\varphi}, \tag{10a}$$

$$\frac{dz}{d\varphi}=\frac{\left(1+\delta\beta z\right)x\sin\varphi}{\beta xz+\left(1+\delta\beta z\right)\sin\varphi}. \tag{10b}$$

Thus, equilibrium profiles of the rolled out meniscus in the gravitational field, taking into account the size dependence of the surface tension, are described by solutions of equations (5) or (10). It is easy to check that in the absence of size effects, when the value of δ is zero, these equations transfer to the equations known from

publications [1, 10]. Note that only axisymmetric configurations are involved. In the absence of symmetry, the mathematical side of the issue gets very complicated. Instead of ordinary differential equations we obtain partial derivative equations.

It is impossible to analytically derive a general solution of equations (5) or (10), so we have to use numerical methods. The most convenient technique for the numerical simulation of rolled out meniscus profiles [10] is based on the linearisation of equation (5). For now, we assume that δ = 0. For large values of the variable x, the inequality $dz/dx\ll 1$ is satisfied. Therefore, if we neglect the infinitesimal quantities of higher order in the denominator, (5) transforms into the equation:

$$\frac{d^2z}{dx^2}+\frac{1}{x}\frac{dz}{dx}-\beta z=0. \tag{11}$$

The solution of equation (11), having a horizontal asymptote, is defined by the expression:

$$z\left(x\right)=C\,K_0\left(\sqrt{\beta}x\right), \tag{12}$$

where C is the constant of integration, $K_0\left(y\right)$ is the modified zero-order Bessel function of the second kind. Function (12) describes only the "tail" of the meniscus profile, and it is not particularly interesting: z ≈ 0. In order to determine the part of the profile belonging to the region of small values of x, it is first necessary to match an arbitrary, but sufficiently large value of $x=x^*$ with the corresponding $z=z^*$ and the angle $\varphi=\varphi^*$ at a fixed C, using representation (12).

$$\varphi^*=\tan^{-1}\left[\sqrt{\beta}\,C\,K_1\left(\sqrt{\beta}x\right)\right],$$

where $K_1\left(y\right)$ is the modified zero-order Bessel function of the second kind. Then the set of numbers φ^*, x^*, and z^* is used as the initial data of the Cauchy problem for system (10). The latter can be effectively solved, for instance, by the Runge-Kutta or Adams methods.

However, the above procedure is not suitable at $\delta>0$, since equation (5) cannot be linearised in the same way. In this case, we take system (10) as the basis and inserted $\psi=\pi-\varphi$ in it.

$$\frac{dx}{d\psi}=-\frac{\left(1+\delta\beta z\right)x\cos\psi}{\beta xz+\left(1+\delta\beta z\right)\sin\psi}, \tag{13a}$$

$$\frac{dz}{d\psi}=-\frac{\left(1+\delta\beta z\right)x\sin\psi}{\beta xz+\left(1+\delta\beta z\right)\sin\psi}. \tag{13b}$$

Due to the characteristic of the rolled out meniscus, $z \to 0$ when $x \to +\infty$. So, the conditions to (13) must be as follows:

$$x(\psi = \psi_0) = x_0 < +\infty, z(\psi = \pi) = 0. \qquad (14)$$

Problem (13)–(14) is also a boundary value problem. But unlike (5)–(6), it is considered on the finite segment $\psi \in [\psi_0, \pi]$ and it is easy to solve numerically by the shooting method.

In order to transform system (13) to dimensionless coordinates, it is appropriate to choose capillary length as a characteristic value $1/\sqrt{\beta}$. Upon dividing both parts of each of equations (13) by $\sqrt{\beta}$, we obtained:

$$\frac{dX}{d\psi} = -\frac{(1+Z\Delta)X\cos\psi}{XZ + (1+Z\Delta)\sin\psi}, \qquad (15a)$$

$$\frac{dZ}{d\psi} = -\frac{(1+Z\Delta)X\sin\psi}{XZ + (1+Z\Delta)\sin\psi}, \qquad (15b)$$

$$X(\psi = \psi_0) = X_0, Z(\psi = \pi) = 0. \qquad (16)$$

where $X = \sqrt{\beta}x$, $Z = \sqrt{\beta}z$, and $\Delta = \sqrt{\beta}\delta$. Fig. 3 illustrates typical solutions to problems (15)–(16). The results of 3D modelling of the rolled out meniscus surface are shown in Fig. 4.

As noted above, the problem of equilibrium shape of capillary surface cannot be solved analytically. This is due to the complicated nonlinearity of the Laplace equation. Sometimes, however, it is possible to simplify the nonlinearity and to derive different kinds of exact formulas or analytical approximations to the theoretical profile. For example, in the absence of external force fields, the capillary surface transforms to a surface with a constant mean curvature. A sessile (pendant) drop takes a spherical shape, the bridge surface takes a catenoidal shape. Similarly, if we neglect the contribution of gravity in equilibrium equation (5) for the
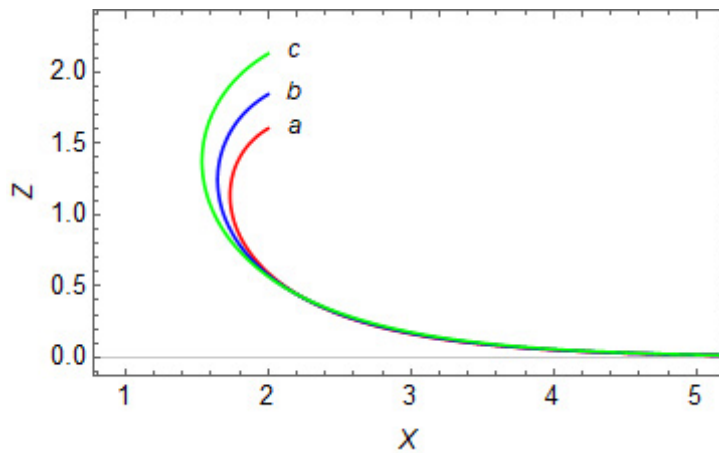

Fig. 3. Dimensionless profiles of the meniscus at $X_0 = 2$, $\psi_0 = 30°$ and different Δ: $a = 0$, $b = 0.4$, $c = 1$
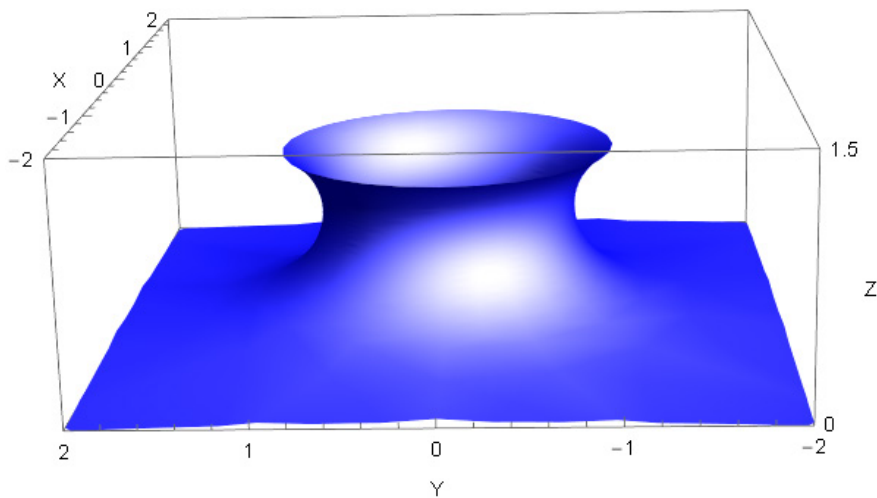

Fig. 4. 3D model of the meniscus

rolled out meniscus and assume $\beta = 0$, the exact solution is:

$$z(x) = C_1 \pm C_2 \ln\left(x + \sqrt{x^2 - C_2^2}\right), \qquad (17)$$

where $C_{1,2}$ are the constants. In (17), however, the value of the constant C_2 must be zero, otherwise the function $z(x)$ is unbounded. As a result, the meniscus surface turns into the plane $z \equiv 0$. This trivial solution is obviously of no physical interest. In contrast to other basic types of menisci, the formation of a rolled out meniscus under gravity-free conditions is impossible. Without the action of the force field, the liquid of limited volume gathers into a ball, and the second boundary condition (6) cannot be satisfied.

A more important special case is the two-dimensional (cylindrical) meniscus, where the azimuthal curvature $1/R_2$ at each point is zero: $\sin\varphi / x \approx 0$. For the rolled out meniscus, this leads to the relationship between the coordinate z and the angle φ:

$$\frac{z}{\delta} - \frac{\ln(1 + \delta\beta z)}{\beta\delta^2} = 1 - \cos\varphi. \qquad (18)$$

It is still not possible to derive z from it at positive values of δ using elementary functions. We have to solve the nonlinear equation, but it is already scalar, not differential. By tabulating the function $z(\varphi)$ with expression (18) over a certain range of the angle φ, the corresponding values of x can easily be deduced from the definition of the derivative.

If the parameter δ is decreased to zero, the left-hand side of (18) tends to $\beta z^2 / 2$. Then (10) and (18) provide the exact expressions for x and z known from earlier research [1]:

$$z = \frac{2}{\sqrt{\beta}}\sin\frac{\varphi}{2}, x = C - \frac{1}{\sqrt{\beta}}\left(\ln\tan\frac{\varphi}{4} + 2\cos\frac{\varphi}{2}\right), \quad (19)$$

where the constant C is defined by the condition $x(\varphi_0) = x_0$. As follows from (19), the maximum possible height z_0 of the rolled out meniscus is $2/\sqrt{\beta}$, irrespective of the value of x_0. For three-dimensional menisci, the maximum height generally increases as the radius of the contact line increases.

On the other hand, although z cannot be expressed analytically from expression (18), it allows one to analyse the nature of the

dependence of the maximum height z_0 of the meniscus on the parameters β and δ. Then we inserted $\varphi = \pi$ in (18):

$$\frac{z_0}{\delta} - \frac{\ln(1 + \delta\beta z_0)}{\beta\delta^2} = 2. \qquad (20)$$

Using the implicit function differentiability theorem, we obtained the following expression from implicit equation (20):

$$\frac{dz_0}{d\beta} < 0, \quad \frac{dz_0}{d\delta} > 0,$$

i.e. the increase in δ is accompanied by an increase in z_0, and an increase in β is accompanied by a decrease in z_0. Note that even upon taking into account the size dependence of the surface tension, the maximal meniscus height z_0 does not depend on x_0. Moreover, the behaviour of δ upon changing of the capillary constant β does not depend on the Tolman length δ.

4. Conclusions

Equilibrium surface of the rolled out capillary meniscus in homogeneous gravitational field is described by solutions of nonlinear differential equations and their systems. The size dependence of the surface tension gives additional terms in the equations, further complicating the nature of nonlinearity. It is not possible to formulate their exact solutions in general terms. Therefore, numerical methods must be used to calculate the meniscus profiles. Due to the specific boundary conditions, the use of numerical techniques is also limited. The most practical method for numerical simulation of rolled out meniscus profiles, based on the linearisation of the Laplace equation, is not applicable in the presence of the parameter responsible for the size dependence. Thus, boundary value problems are the only option. However, with the proper choice of the variable parameters of the meniscus profile arc, the area where the solution is sought can be reduced to a finite segment instead of an infinite semi-axis. Then, well-known numerical methods, e.g. the shooting method can be applied.

In this study, we carried out computational experiments to determine the degree and nature of the effect of the parameters of the meniscus mathematical model on its equilibrium shape. From the analysis of the results, it follows, in

particular, that the size dependence of the surface tension can cause a significant distortion of the meniscus shape.

Conflict of interests

The author declares that they have no known competing financial interests or personal relationships that could have appeared to influence the work reported in this paper.

References

1. Rusanov A. I., Prokhorov V. A. *Interfacial tensiometry**. Saint Petersburg: Khimija Publ.; 1994. 400 p. (In Russ.)

2. Rapacchietta A. V., Neumann A. W., Omenyi S. N. Force and free-energy analyses of small particles at fluid interfaces: I. Cylinders. *Journal of Colloid and Interface Science*. 1977;59(3): 541–554. https://doi.org/10.1016/0021-9797(77)90050-9

3. Ivanov I. B., Kralchevsky P. A., Nikolov A. D. Film and line tension effects on the attachment of particles to an interface: I. Conditions for mechanical equilibrium of fluid and solid particles at a fluid interface. *Journal of Colloid and Interface Science*. 1986;112(1): 97–107. https://doi.org/10.1016/0021-9797(86)90072-X

4. Bozon A., Fries L., Kammerhofer J., Forny L., Niederreiter G., Palzer S., Salman A. Effect of heterogeneous hydrophobic coating on floating of insoluble particles. *Powder Technology*. 2022;395: 592–603. https://doi.org/10.1016/j.powtec.2021.10.015

5. Feng D., Nguyen A. Contact angle variation on single floating spheres and its impact on the stability analysis of floating particles. *Colloids and Surfaces A: Physicochemical and Engineering Aspects*. 2017;520: 442–447. https://doi.org/10.1016/j.colsurfa.2017.01.057

6. Klochko L., Mandrolko V., Castanet G., Pernot G., Lemoine F., Termentzidis K., Lacroix D., Isaiev M. Molecular dynamics simulation of thermal transport across solid/liquid interface created by meniscus. *arXiv*. 2021; https://doi.org/10.48550/arXiv.2110.11609

7. Ward T. Evaporation driven detachment of a liquid bridge from a syringe needle in repose. *Physics of Fluids*. 2020;32: 084105. https://doi.org/10.1063/5.0016257

8. Lee J. The static profile for a floating particle. *Colloids and Interfaces*. 2018;2(2): https://doi.org/10.3390/colloids2020018

9. Huh C., Mason S. G. The flotation of axisymmetric particles at horizontal liquid interfaces. *Journal of Colloid and Interface Science*. 1974;47(2): 271–289. https://doi.org/10.1016/0021-9797(74)90259-8

10. Huh C., Scriven L. E. Shapes of axisymmetric fluid interfaces of unbounded extent. *Journal of Colloid and Interface Science*. 1969;30(3): 323–337. https://doi.org/10.1016/0021-9797(69)90399-3

11. O'brien S. B. G. The meniscus near a small sphere and its relationship to line pinning of contact lines. *Journal of Colloid and Interface Science*. 1996;183(1): 51–56. https://doi.org/10.1006/jcis.1996.0517

12. Lo L. The meniscus on a needle – a lesson in matching. *Journal of Fluid Mechanics*. 1983;132: 65–78. https://doi.org/10.1017/S0022112083001470

13. Hyde A., Phan C., Ingram G. Determining liquid-liquid interfacial tension from a submerged meniscus. *Colloids and Surfaces A: Physicochemical and Engineering Aspects*. 2014;459: 267–273. https://doi.org/10.1016/j.colsurfa.2014.07.016

14. Rusanov A. I. *Phase equilibria and surface phenomena**. Leningrad: Khimija Publ.; 1967. 388 p. (In Russ.)

15. Tolman R. C. The effect of droplet size on surface tension. *The Journal of Chemical Physics*. 1949;17: 333–337. https://doi.org/10.1063/1.1747247

16. Rekhviashvili S. Sh, Kishtikova E. V. On the size dependence of the surface tension. *Technical Physics*. 2011; 56(1): 143–146. https://doi.org/10.1134/s106378421101021x

17. Rekhviashvili S. Sh. Size dependence of the surface tension of a small droplet under the assumption of a constant tolman length: critical analysis. *Colloid Journal*. 2020;82: 342–345. https://doi.org/10.1134/S1061933X20030084

18. Burian S., Isaiev M., Termentzidis K., Sysoev V., Bulavin L. Size dependence of the surface tension of a free surface of an isotropic fluid. *Physical Review E*. 2017;95(6): 062801. https://doi.org/10.1103/physreve.95.062801

19. Sokurov A. A., Rekhviashvili S. Sh. Modeling of equilibrium capillary surfaces with the size dependence of surface tension. *Condensed Matter and Interphases*. 2013;15(2):173–178. (In Russ.). Available at: http://www.kcmf.vsu.ru/resources/t_15_2_2013_014.pdf

* Translated by author of the article.

Information about author

Aslan A. Sokurov, Cand. Sci. (Phys.–Math.), Junior Researcher at the theoretical and mathematical physics department, Institute of Applied Mathematics and Automation – the filial branch of Federal State Budgetary Scientific Establishment «Federal Scientific Center «Kabardin-Balkar Scientific Center of Russian Academy of Sciences» (Nalchik, Russian Federation).

https://orcid.org/0000-0001-9886-3602
asokuroff@gmail.com

Original articles

X-ray photoelectron spectroscopy of hybrid 3T3 NIH cell structures with internalized porous silicon nanoparticles on substrates of various materials

S. S. Titova[1✉], L. A. Osminkina[2,3], I. S. Kakuliia[1], O. A. Chuvenkova[1], E. V. Parinova[1], S. V. Ryabtsev[1], R. G. Chumakov[4], A. M. Lebedev[4], A. A. Kudryavtsev[5], S. Yu. Turishchev[1]

[1]Voronezh State University,
1 Universitetskaya pl., Voronezh 394018, Russian Federation

[2]Lomonosov Moscow State University,
1, 2 Leninskie Gory, Moscow 119991, Russian Federation

[3]Institute for Biological Instrumentation of Russian Academy of Sciences
7 Institutskaya ul., Pushchino 142290, Russian Federation

[4]National Research Center "Kurchatov Institute",
1 Akademika Kurchatova pl., Moscow 123182, Russian Federation

[5]Institute of Theoretical and Experimental Biophysics of Russian Academy of Sciences,
3 Institutskaya ul., Pushchino 142290, Russian Federation

Abstract

The work is related to the study of a biohybrid material based on mammalian 3T3 NIH mouse fibroblast cells with immobilized porous silicon particles including nanocrystals about 10 nm in size by photoelectron spectroscopy. The influence of the surface material of the substrate on which the biohybrid material is grown on the possibility of conducting studies of the physico-chemical state of the developed surface is studied. Nickel as well as gold and titanium, known for their biocompatibility, were used as surface materials for cell growth and subsequent internalization of silicon particles. The method of optical microscopy in the reflected light mode was used to assess the distribution of cells on surfaces. It is shown that the nickel surface is not suitable for the synthesis and subsequent studies of biohybrid structures. At the same time, on the surface of gold and titanium, cellular material and structures based on it are available for measurements, including by photoelectron spectroscopy, a high-precision method for studying the atoms charge state and the physico-chemical state of the surface as a whole. The X-ray photoelectronic spectra show all the main components expected to be detected after drying and subsequent vacuuming of the studied objects: the surface material of the substrates and arrays of cell cultures grown on the substrates. No signal from silicon atoms was detected on the nickel surface. In the case of a gold surface, the proximity of the binding energies of the gold core levels (substrate) and silicon (internalized particles) leads to the fact that the signal of gold atoms, which is significant in its intensity, does not allow detecting a signal from silicon atoms, which is weaker in intensity. The signal of silicon atoms in biohybrid structures is reliably detected only when using titanium substrates, including for a control sample containing porous silicon nanoparticles without incubation in cells. Thus, it is shown that the surface of the titanium foil can be used for studies by photoelectron spectroscopy of a biohybrid material based on mammalian 3T3 NIH mouse fibroblast cells with immobilized porous silicon particles.The obtained result is important for high-precision diagnostics of the physico-chemical state of biohybrid materials and structures based on them with a low content of silicon atoms when solving problems of studying the compatibility and possibilities of using silicon nanomaterials for medical, including therapeutic and other applications.

✉ Sofiia S. Titova, e-mail: titova@phys.vsu.ru

Condensed Matter and Interphases / Конденсированные среды и межфазные границы   2023;25(1): 132–138

S. S. Titova et al.   X-ray photoelectron spectroscopy of hybrid 3T3 NIH cell structures with internalized porous...

1. Introduction

Biohybrid structures, which are essentially a combination of biological objects and inorganic materials [1–4], are positioning at the subject of interest intersection of physics, chemistry and biology and stimulates special attention to the properties of such objects and is the subject of research by high-precision diagnostic methods. The physico-chemical processes under the internalization of inorganic particles into living cells, the associated changes in their physico-chemical state, composition, structure and other properties are insufficiently and sometimes fragmentary studied. On the other hand, information about the result of these processes is certainly important when studying the application of biohybrid structures. Structures in which silicon nanoparticles act as an embedded object are no exception [4–6]. Silicon nanoparticles, due to their special biological properties, such as biocompatibility [6–7], biodegradability [8-9], sensibilization of impacts [10–11] and low toxicity [6, 12], represent a promising material in the fields of therapy and diagnostics (theranostics) [4, 10, 13]. It is worth noting that nanoparticles created from crystalline silicon are inferior in efficiency to nanoparticles formed from porous silicon, primarily due to the extremely developed surface [14]. Therefore, the study of biohybrid structures, for which the embedded element is porous silicon nanoparticles, is relevant and in demand.

The method of X-ray photoelectron spectroscopy (XPS) has an extremely high sensitivity to the physico-chemical state of the developed surface [15–17]. An urgent issue is to establish the applicability of the XPS to the study of biohybrid structures, where one of the main tasks is to select the material on which a complex composition and structure of the sample will be applied. The need for an adequate choice of substrate is given by the issues of storage and transportation of the prepared sample, its stability and the effectiveness of choosing a research strategy generally. The substrate material should be inert to the biological processes taking place during the formation of the sample on given surface, on the other hand, the substrate should not make a significant contribution to the results of spectroscopic, microscopic or other studies. The question of the suitability of various substrate materials, on the surface of which a biohybrid material can be layered for investigation by the XPS is investigated in this paper.

2. Experimental

The following materials were selected to study the suitability of the substrate when registering the XPS data: nickel foil (AlfaAesar, 99.7%), a gold film with a thickness of about 100 nm on a nickel foil formed by magnetron sputtering of a gold target (99.99%) and titanium foil (AlfaAesar, 99.5%). The biohybrid material was a cell culture of 3T3 NIH mouse fibroblasts with immobilized porous silicon particles including nanocrystals ~10 nm in size according to [18]. The cells were grown in Petri dishes on selected substrates, after which they were incubated with porous silicon nanoparticles (p-SiNPs) for 24–72 hours. p-SiNPs were obtained by mechanical grinding of porous silicon films in suspension mode in a planetary mill Fritsch Pulverisette 7 [14, 19]. Porous silicon films were produced by electrochemical etching of c-Si(100) crystalline

Condensed Matter and Interphases / Конденсированные среды и межфазные границы   2023;25(1): 132–138

S. S. Titova et al.   X-ray photoelectron spectroscopy of hybrid 3T3 NIH cell structures with internalized porous...

silicon wafers for an hour in HF:C_2H_5OH = 1:1 (current density 50 mA/cm²) [14, 19]. Suspensions of nanoparticles with a concentration of 0.5 mg/ml were used. After the time elapsed, the cells were fixed with formaldehyde, then washed and dried. The samples obtained by this method were named, in accordance with the substrate material, as BioHyb on Ni, BioHyb on Au, BioHyb on Ti. As a control sample a suspension of porous silicon nanoparticles were used applied to titanium foil and dried in natural conditions before vacuuming in a spectrometer chamber (p-SiNPs on Ti). The samples obtained were studied on a Bresser science MTL-201 optical microscope in the reflected light mode to observe the specifics in the cells distribution and collect statistics on the substrates coverage by cellular material.

XPS studies was carried out on the ESCA module of the ultrahigh vacuum "KISI-Kurchatov" synchrotron NANOPES experimental end-station of the National Research Center "Kurchatov Institute" (Moscow) equipped with the SPECS Phoibos 150 energy analyzer [20]. Monochromatized Al Ka radiation of an X-ray tube (1486.61 eV) was used with the analysis depth that was estimated as ~ 2–3 nm [21]. Survey spectra were recorded in the binding energy range 0–1200 eV. A standard approach to data calibration based on independent recording of the pure gold foil (Au 4f) signal was used since due to the presence of cellular material on the foils surface it was not possible to use standard C1s calibration of the hydrocarbon contamination line [21]. To compare and analyze the main features of the XPS spectra the well-known databases were used [21–23].

3. Results and discussion

The biohybrid structures formation modes, including the times and concentrations of components, were selected during incubation so that a one cell thickness layer was formed on the surface of the substrates, without significant agglomerations. The process was controlled microscopically. The results of optical microscopy (Fig. 1) showed noticeable differences in the surfaces coverage by cells containing p-SiNPs. In the case of BioHyb on Au and BioHyb on Ti samples (Fig. 1), in contrast to the BioHyb on Ni sample (Fig. 1, indicated by arrows) an integral

and compacted structure of cellular material distributed over the surface is visible. In the case of nickel substrates, the coating with cells is smeared and their number is smaller. For the surface of the gold, the edges of cellular structures are sharper, clearer, which confirms the known biocompatibility of gold [24, 25]. However, significant areas of the gold surface are noticeable that are not covered with cellular material and can give a significant intensity of the XPS signal from the substrate that are not from hybrid structures. For titanium foil that is also known for its biocompatibility the number of cells on the surface is maximum, the coating is more uniform.

Statistical diagrams calculated with the use of ImageJ software package show that in the case of BioHyb on Ni and BioHyb on Au samples the total area of structural elements (in Fig. 1) is less for biohybrid material on the surface if compared to the BioHyb on Ti sample.

The percentage ratio of the biohybrid structures total areas to the ones of the substrate, for BioHyb on Ni sample was 17%. This value is less than for BioHyb on Au and BioHyb on Ti (23 and 24%, respectively). Thus, from the surface coating point of view nickel can be considered the least suitable. During incubation, nickel and its oxides can be toxic to cells (with silicon nanoparticles) [24]. Additionally, as the result of the cellular material weak adhesion to the nickel surface a significant part of the cells can be found destroyed and left the substrate after drying and vacuuming.

The X-ray photoelectron spectroscopy results are presented by the survey spectra in Fig. 2. It can be seen that in the spectrum of the biohybrid structure on a nickel substrate (Fig. 2, BioHyb on Ni) there are lines of core levels and Auger series of sodium, nickel, carbon, nitrogen and oxygen. The silicon lines absence may indicate an insufficient number of p-SiNPs combined with the cell culture for detection, or their complete absence in the sample. The presence of sodium and nitrogen lines may be due to the nutrient medium components used in cell growth or directly by elements of cell culture.

In the survey spectrum for the BioHyb on Au sample (Fig. 2) there are lines of carbon, nitrogen, oxygen, sodium, chlorine, nickel and

Condensed Matter and Interphases / Конденсированные среды и межфазные границы   2023;25(1): 132–138

S. S. Titova et al.   X-ray photoelectron spectroscopy of hybrid 3T3 NIH cell structures with internalized porous…
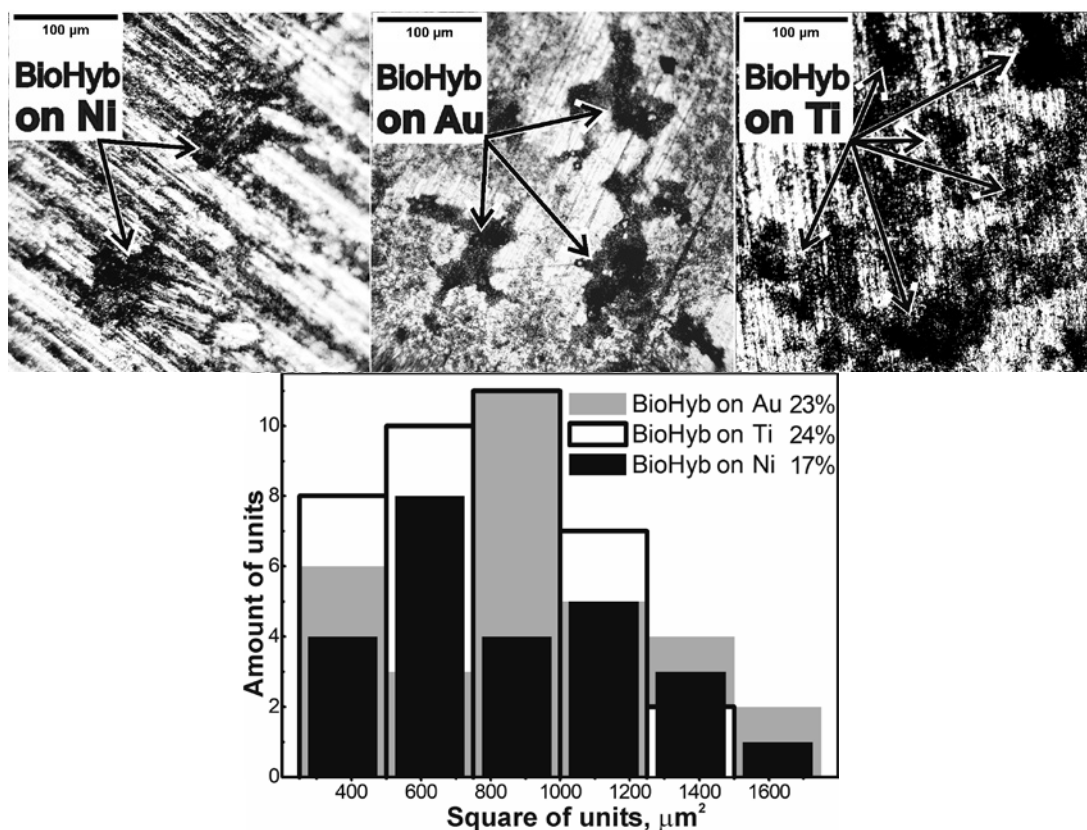

Fig. 1. Optical microscopy and statistical diagrams for biohybrid structures grown on nickel (BioHyb on Ni), gold (BioHyb on Au) and titanium (BioHyb on Ti)
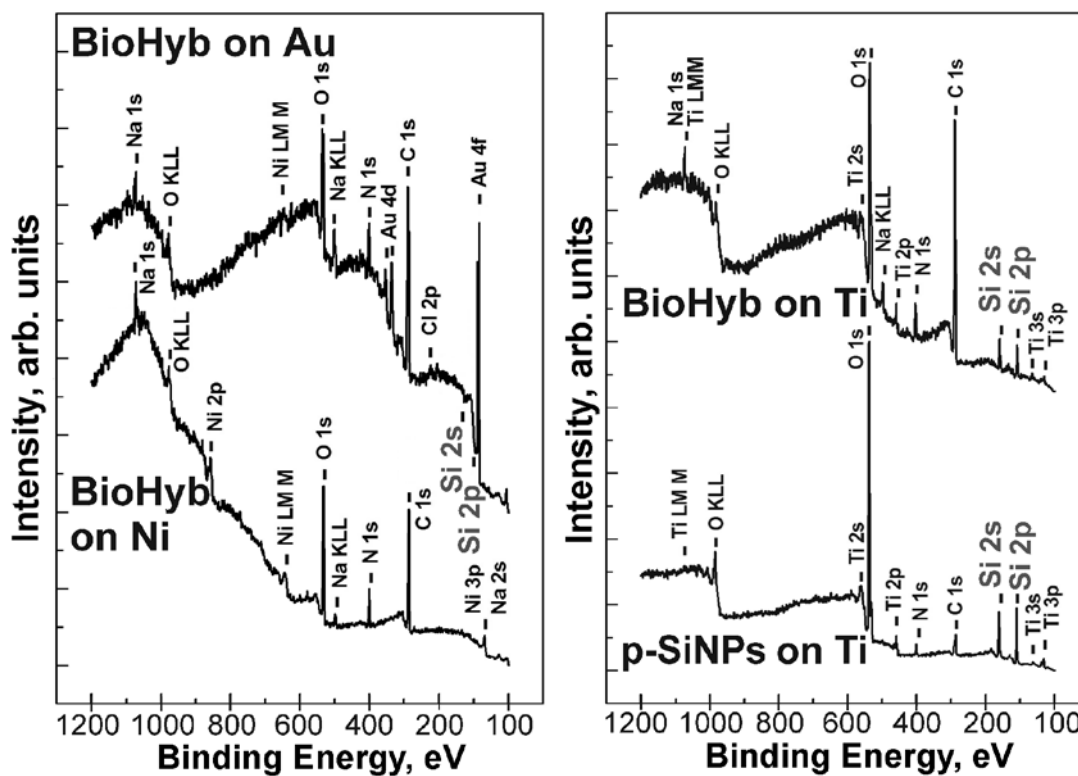

Fig. 2. XPS surveys for biohybrid material grown on gold (BioHyb on Au), nickel (BioHyb on Ni), titanium (BioHyb on Ti), and reference p-SiNPs suspension sample on titanium substrate dried in normal conditions

Condensed Matter and Interphases / Конденсированные среды и межфазные границы   2023;25(1): 132–138

S. S. Titova et al.   X-ray photoelectron spectroscopy of hybrid 3T3 NIH cell structures with internalized porous…

possibly silicon. Although the Au 4*f* gold line is particularly intense. The presence of a nickel atoms signal in the survey spectrum is most likely due to a part of the nickel substrate that is not covered with gold ingress under the X-ray beam when recording spectra. The sodium and nitrogen lines are associated with the nutrient medium components used in cell cultivation or directly with the elements of cell culture. It is worth noting that the extremely high intensity of the gold $4f_{5/2,7/2}$ spin-doublet line at energies of 84 eV and 87 eV practically leveled the observing and registering possibility of the Si 2*p* silicon line at binding energies of ~ 100 eV (as well as for Si 2*s*, ~ 150 eV). In these areas of observation, the silicon core levels lines signal is probably present, but due to the insignificant amount of the p-SiNPs substance (possibly screened by the cells bio-shells) its intensity is significantly small. Including at the level of XPS survey spectrum background intensity formed by inelastic scattered electrons of substrate gold atoms which are much more quantitatively than silicon atoms. This makes gold unsuitable material for the study of biohybrid structures with silicon nanoparticles, despite good biocompatibility. Thus, the intense gold $4f_{7/2,5/2}$ lines presence hinders the identification and further study of the studied biohybrid materials.

In turn, in the spectrum of the BioHyb on Ti sample (Fig. 2), lines of titanium, carbon, nitrogen, oxygen, sodium and silicon can be observed. The sodium and nitrogen lines, as before, are due to the presence of these elements in the composition of the cellular material. Here, the silicon lines are significantly intense and clearly visible. As a result, it can be emphasized that the sample contains a sufficient number of porous silicon nanoparticles for their clear detection by the XPS method. The lines from the titanium substrate are far from the silicon lines and do not interfere with their identification.

A survey spectrum of the initial porous silicon nanoparticles dried from their suspension on a titanium substrate under natural conditions before vacuuming is given as a comparison (Fig. 2, p-SiNPs on Ti). All the lines characteristic of a biohybrid sample grown on the titanium surface are observed in the spectrum (Fig. 2 BioHyb on Ti), with the exception of the sodium line which is apparently a component of organic compounds or a nutrient medium used in cell growth. The low-intensity nitrogen line observation can be related to the specifics of titanium foil face cleaning.

4. Conclusions

The paper shows that according to optical microscopy data, gold and titanium are the best substrate materials for growing biohybrid structures with subsequent internalization of silicon nanomaterial and studying such objects. The biohybrid structure has good adhesion to the materials of such substrates and is stable in its distribution on the surface. The use of X-ray photoelectron spectroscopy to study the charge state of surface atoms, their physico-chemical state, including the substrate, cells and silicon particles, excludes the use of gold surfaces. It is shown that the surface of titanium foil can be used for XPS studies of biohybrid material based on mammalian 3T3 NIH mouse fibroblast cells with immobilized porous silicon particles. The obtained result can be used for high-precision diagnostics of the biohybrid materials physico-chemical state and structures based on them with a low content of silicon atoms, which is necessary to study the compatibility and possibilities of using silicon nanomaterials for medical, including therapeutic and other applications.

Author contributions

All authors made an equivalent contribution to the preparation of the publication.

Conflict of interests

The authors declare that they have no known competing financial interests or personal relationships that could have appeared to influence the work reported in this paper.

References

1. Sun L., Yu Y., Chen Z., Bian F., Ye F., Sun L., Zhao Y. Biohybrid robotics with living cell actuation. *Chemical Society Reviews*. 2020;49: 4043–4069. https://doi.org/10.1039/d0cs00120a

2. Ragni R., Scotognella F., Vona D.,… Farinola G. M. Hybrid photonic nanostructures by in vivo incorporation of an organic fluorophore into diatom algae. *Advanced Functional Materials*. 2018;28: 1706214. https://doi.org/10.1002/adfm.201706214

3. Martins M., Toste C., Pereira A. C. Enhanced light-driven hydrogen production by self-

Condensed Matter and Interphases / Конденсированные среды и межфазные границы   2023;25(1): 132–138

S. S. Titova et al.   X-ray photoelectron spectroscopy of hybrid 3T3 NIH cell structures with internalized porous…

photosensitized biohybrid systems. *Angewandte Chemie International Edition*. 2021;133: 9137–9144. https://doi.org/10.1002/anie.202016960

4. Mishra A., Melo J. S., Agrawal A., Kashyap Y., Sen D. Preparation and application of silica nanoparticles-*Ocimum Basilicum Seeds* Bio-Hybrid for the efficient immobilization of Iinvertase enzyme. *Colloids and Surfaces B: Biointerfaces*. 2020;188: 110796. https://doi.org/10.1016/j.colsurfb.2020.110796

5. Mishra A., Pandey V. K., Shankar B. S., Melo J. S. Spray drying as an efficient route for synthesis of silica nanoparticles-sodium alginate biohybrid drug carrier of doxorubicin. *Colloids and Surfaces B: Biointerfaces*. 2021;197: 111445. https://doi.org/10.1016/j.colsurfb.2020.111445

6. Ciobanu M., Pirvu L., Paun G., … Parvulescu V. Development of a new (bio)hybrid matrix based on Althaea Officinalis and Betonica Officinalis extracts loaded into mesoporous silica nanoparticles for bioactive compounds with therapeutic applications. *Journal of Drug Delivery Science and Technology*. 2019;51: 605–613. https://doi.org/10.1016/j.jddst.2019.03.040

7. Guo D., Ji X., Peng F., Zhong Y., Chu B., Su Y., He Y. Photostable and biocompatible fluorescent silicon nanoparticles for imaging-guided co-delivery of sirna and doxorubicin to drug-resistant cancer cells. *Nano-Micro Letters*. 2019;11: 27. https://doi.org/10.1007/s40820-019-0257-1

8. Gongalsky M. B., Sviridov A. P., Bezsudnova Yu. I., Osminkina L. A. Biodegradation model of porous silicon nanoparticles. *Colloids and Surfaces B: Biointerfaces*. 2020;190: 110946. https://doi.org/10.1016/j.colsurfb.2020.110946

9. Xu W., Tamarov K., Fan L., … Lehto V.-P. Scalable synthesis of biodegradable black mesoporous silicon nanoparticles for highly efficient photothermal therapy. *ACS Applied Materials & Interfaces*. 2018;10: 23529–23538. https://doi.org/10.1021/acsami.8b04557

10. Oleshchenko V. A., Kharin A. Yu., Alykova A. F., … Timoshenko V. Yu. Localized infrared radiation-induced hyperthermia sensitized by laserablated silicon nanoparticles for phototherapy applications. *Applied Surface Science*. 2020;516: 14566. https://doi.org/10.1016/j.apsusc.2020.145661

11. O'Farrell N., Houlton A., Horrocks B. R. Silicon nanoparticles: applications in cell biology and medicine. *International Journal of Nanomedicine*. 2006;1(4): 451–472. https://doi.org/10.2147/nano.2006.1.4.451

12. Ahire J. H., Behray M., Webster C. A., … Chao Y. Synthesis of carbohydrate capped silicon nanoparticles and their reduced cytotoxicity, in vivo toxicity, and cellular uptake. *Advanced Healthcare Materials*. 2015;4: 1877–1886. https://doi.org/10.1002/adhm.201500298

13. Juère E., Kleitz F. On the nanopore confinement of therapeutic drugs into mesoporous silicamaterials and its implications. *Microporous and Mesoporous Materials*. 2018;270: 109–119. https://doi.org/10.1016/j.micromeso.2018.04.031

14. Osminkina L. A., Gongalsky M. B., Motuzuk A. V., Timoshenko V. Y., Kudryavtsev A. A. Silicon nanocrystals as photo- and sono-sensitizers for biomedical applications. *Applied Physics B*. 2011;105: 665–668. https://doi.org/10.1007/s00340-011-4562-8

15. Parinova E. V., Antipov S. S., Belikov E. A., … Turishchev S. Y. TEM and XPS studies of bio-nanohybrid material based on bacterial ferritin-like protein Dps. *Condensed Matter and Interphases*. 2022;24(2): 265–272. https://doi.org/10.17308/kcmf.2022.24/9267

16. Shchukarev A., Backman E., Watts S., Salentinig S., Urban C. F., Ramstedt M. Applying Cryo-X-ray photoelectron spectroscopy to study the surface chemical composition of fungi and viruses. *Frontiers in Chemistry*. 2021;9: 666853. https://doi.org/10.3389/fchem.2021.666853

17. Shaposhnik A. V., Shaposhnik D. A., Turishchev S. Yu., … Morante J. R. Gas sensing properties of individual SnO_2 nanowires and SnO_2 sol–gel nanocomposites. *Beilstein Journal of Nanotechnology*. 2019;10: 1380–1390. https://doi.org/10.3762/bjnano.10.136

18. Koyuda D. A., Titova S. S., Tsurikova U. A., … Turishchev S. Yu. Composition and electronic structure of porous silicon nanoparticles after oxidation under air- or freeze-drying conditions. *Materials Letters*. 2022,312: 131608. https://doi.org/10.1016/j.matlet.2021.131608

19. Osminkina L. A., Agafilushkina S. N., Kropotkina E. A., … Gambaryan A. S. Antiviral adsorption activity of porous silicon nanoparticles against different pathogenic human viruses. *Bioactive Materials*. 2022;7: 39–46. https://doi.org/10.1016/j.bioactmat.2021.06.001

20. Lebedev A. M., Menshikov K. A., Nazin V. G., Stankevich V. G., Tsetlin M. B., Chumakov R. G. NanoPES photoelectron beamline of the Kurchatov Synchrotron Radiation Source. *Journal of Surface Investigation: X-ray, Synchrotron and Neutron Techniques*. 2021;15(5): 1039–1044. https://doi.org/10.1134/S1027451021050335

21. John F. *Moulder handbook of X-ray photoelectron spectroscopy*. John F. Moulder [et.al]. Minnesota: Perkin-Elmer Corporation Physical Electronics Division; 1992. 261 p.

22. Crist B. V. *Handbook of the elements and native oxide*. XPS International, Inc., 1999.

23. NIST Standard Reference Database 71. *NIST Electron Inelastic-Mean-Free-Path Database: Version 4.1*. www. srdata.nist.gov/xps

Condensed Matter and Interphases / Конденсированные среды и межфазные границы   2023;25(1): 132–138

S. S. Titova et al.   X-ray photoelectron spectroscopy of hybrid 3T3 NIH cell structures with internalized porous...

24. Gonchar K. A., Zubairova A. A., Schleusener A., Osminkina L. A., Sivakov V. Optical properties of silicon nanowires fabricated by environment-friendly chemistry. *Nanoscale Research Letters*. 2016;11(1): 357. https://doi.org/10.1186/s11671-016-1568-5

25. Georgobiani V. A., Gonchar K. A., Zvereva E. A., Osminkina, L. A. Porous silicon nanowire arrays for reversible optical gas sensing. *Physica Status Solidi (A) Applications and Materials Science*. 2018;215(1): 1700565. https://doi.org/10.1002/pssa.201700565

Information about the authors

Sofiia S. Titova, Laboratory assistant of General Physics Department, Voronezh State University, (Voronezh, Russian Federation).

https://orcid.org/0000-0001-6860-401X
titova@phys.vsu.ru

Liubov A. Osminkina, Cand. Sci. (Phys.-Math.), Leading Researcher, physics faculty, Lomonosov Moscow State University (Moscow, Russian Federation).

https://orcid.org/0000-0001-7485-0495
osminkina@physics.msu.ru

Iuliia S. Kakuliia, Leading Engineer of General Physics Department, Voronezh State University (Voronezh, Russian Federation).

https://orcid.org/0000-0002-0953-9024
kakuliia@phys.vsu.ru

Olga A. Chuvenkova, Cand. Sci. (Phys.-Math.), Senior Researcher, Joint Scientific and Educational Laboratory "Atomic and Electronic Structure of Functional Materials" of Voronezh State University and the National Research Center "Kurchatov Institute", Voronezh State University (Voronezh, Russian Federation).

https://orcid.org/0000-0001-5701-6909
chuvenkova@phys.vsu.ru

Elena V. Parinova, Cand. Sci. (Phys.-Math.), Researcher, Joint Scientific and Educational Laboratory "Atomic and Electronic Structure of Functional Materials" of Voronezh State University and the National Research Center "Kurchatov Institute", Voronezh State University (Voronezh, Russian Federation)

https://orcid.org/0000-0003-2817-3547
parinova@phys.vsu.ru

Stanislav V. Ryabtsev, Dr. Sci. (Phys.-Math.), Leading Researcher Joint Scientific and Educational Laboratory "Atomic and Electronic Structure of Functional Materials" of Voronezh State University and the National Research Center "Kurchatov Institute", Voronezh State University (Voronezh, Russian Federation)

https://orcid.org/0000-0001-7635-8162
ryabtsev@phys.vsu.ru

Ratibor G. Chumakov, Cand. Sci. (Phys.-Math.), Senior Researcher of the National Research Center "Kurchatov Institute" (Moscow, Russian Federation).

https://orcid.org/0000-0002-3737-5012
ratibor.chumakov@gmail.com

Alexei M. Lebedev, Cand. Sci. (Phys.-Math.), Senior Researcher of the the National Research Center "Kurchatov Institute" (Moscow, Russian Federation).

https://orcid.org/ 0000-0002-4436-6077
lebedev.alex.m@gmail.com

Andrey A. Kudryavtsev, Cand. Sci. (Phys.-Math.), Leading Researcher, Institute of Theoretical and Experimental Biophysics Russian Academy of Sciences (Pushchino, Russian Federation).

centavr42@mail.ru

Sergey Yu. Turishchev, Dr. Sci. (Phys.-Math.), Associate Professor, Head of the General Physics Department, Voronezh State University (Voronezh, Russian Federation).

https://orcid.org/0000-0003-3320-1979
tsu@phys.vsu.ru

Translated by Sergey Turishchev

Original articles

The effect of current density on the structure of nickel electrolytic foams and their catalytic properties during hydrogen production

T. S. Trofimova✉, **T. N. Ostanina, V. M. Rusoi, E. A. Mazurina**

Ural Federal University,
19 Mira str., Ekaterinburg 620002, Russian Federation

Abstract

The effect of current density on the regularities of nickel foam deposition processes has been studied. Porous nickel foams were obtained by electrochemical deposition in the galvanostatic mode at current densities of 0.3, 0.6, 0.9, and 1.2 A cm^{-2}. The obtained deposits were characterized by high porosity and well adherence to the substrate material. The electrolytic foams had macro- and micropores.

The features of the formation of the macropore system have been studied. It has been established that at low hydrogen evolution rates, a gradual formation of a porous structure occurs. While at higher rates, the formation of the matrix structure ends in the first minutes of electrolysis. It was shown that the log-normal distribution can be used to describe the formation of a hydrogen template as a system of macropores in electrolytic nickel foams over a wide range of current densities. A technique for the estimation of nickel foam macroporosity based on the data on the fraction of the surface occupied by macropores is proposed. The total porosity of deposits was calculated based on the data on the mass and volume of electrolytic foams. The catalytic activity of the obtained porous electrodes towards the hydrogen evolution reaction was analysed in an alkali solution. The value of depolarization at a current density of 0.3 A·cm^{-2} was used as a criterion for the efficiency of nickel foams. The value of depolarization for the obtained deposits varies in a wide range from 170 to 400 mV and strongly depends on the conditions of foam synthesis and their thickness.

It has been established that nickel foams obtained at 1.2 A·cm^{-2} exhibit the best catalytic properties due to their uniform structure characterized by a large number of macropores evenly distributed throughout the foam volume. This ensures maximum access of the reacting particles to the electrode surface.

Keywords: Porosity, Nickel, Electrodeposition, Catalytic properties, Depolarization

✉ Tina-Tini S. Trofimova, e-mail: t.s.kuloshvili@urfu.ru

Condensed Matter and Interphases / Конденсированные среды и межфазные границы   2023;25(1): 139–148

T. S. Trofimova et al.   The effect of current density on the structure of nickel electrolytic foams...

1. Introduction

Water electrolysis is a promising method for producing hydrogen due to the sufficient simplicity of the technology and the possibility of introducing "green" technologies into this process [1]. However, electrolysis is a relatively energy-intensive process. A significant contribution to energy losses is made by hydrogen and oxygen evolution reaction overpotentials. One of the ways to increase the efficiency of electrode processes is to use electrodes with a developed surface. In this case, porous electrodes are used, which have a large surface area compared to smooth electrodes. Due to the large fraction of the active surface, a decrease in the real current density, and, accordingly, overvoltage, is achieved.

Metal foams are porous electrodes possessing all properties of electrocatalytic electrodes. They are characterized by their high porosity and large available surface area, high mechanical strength, and good conductivity. The synthesis of porous metal electrodes is carried out by using the dynamic hydrogen bubble template method [2–6]. The formation of a porous structure occurs due to the crystallization of the metal around the hydrogen bubbles under conditions of high current densities, when metal ion reduction is accompanied by hydrogen evolution. In this case, part of the electrode surface is covered with gas bubbles, and the metal crystallizes in the form of branched dendrites on free surface areas. It is known that this method is used to obtain nickel [7, 8], cobalt [9, 10], copper foams [11, 12], as well as foams of their alloys [13–16].

The main advantage of the electrochemical deposition is the possibility of controlling the foam structure by changing the electrolysis conditions. The structure of the foams, in turn, affects their catalytic properties.

The literature usually contains a description of the morphological features of porous deposits [3,4,7,8,10] and does not provide quantitative patterns describing the process of formation of a system of large pores and a dendrite metal deposit between them. In a previous article [17], the main provisions of a phenomenological model that describe the process of the formation of nickel foams and allow to calculate the change in foam porosity during electrodeposition were proposed. The model is based on empirical regularities that describe the time-dependent change in the deposit growth rate, metal current efficiency, and the fraction of the outer surface occupied by large pores. The applicability of the previously proposed empirical equations for the quantitative description of nickel foam electrodeposition in a wide range of current densities for subsequent forecasting of the conditions for the synthesis of foams with desired properties is of interest.

The purpose of this study was investigation of the effect of current density on the regularities of nickel foam deposition, the formation of a system of large pores, and the catalytic properties of deposits with respect to the hydrogen evolution reaction.

2. Experimental

Nickel foams were prepared from a chloride electrolyte [18] containing 0.2 M $NiCl_2$ and 2 M NH_4Cl (pH = 3.2) in galvanostatic mode at current densities of 0.3, 0.6, 0.9, and 1.2 A·cm^{-2} per geometric surface of the electrode. Foams were produced within 1, 2, 3, 4, 5, 10, and 15 minutes at each current density. Three parallel experiments were carried out at each point. The working electrode was a copper plate, on the surface of which a nickel layer with the thickness of 9 μm was preliminarily deposited from a Watts electrolyte containing 280 g·l^{-1} $NiSO_4·7H_2O$, 50 g·l^{-1} NaCl, 35 g·l^{-1} H_3BO_3 at a current density of 0.015 A cm^{-2}. The area of the working surface of the electrode with nickel coating before the deposition of foam was 1 cm^2. Nickel foil was used as an auxiliary electrode. Autolab PGSTAT 302N electrochemical station (Metrohm Autolab AG, the Netherlands) was used for the deposition of foams and investigation of their catalytic properties. After deposition, the samples were thoroughly washed in distilled water and dried in air. Samples obtained at current densities of 0.3, 0.6, 0.9, and 1.2 A cm^{-2} are denoted in the study as 0.3Ni, 0.6Ni, 0.9Ni, and 1.2Ni, respectively. The mass of foams was determined by weighing with an accuracy up to four decimal places using LA 310S analytical balance (Sartorius, Germany). The total porosity was calculated taking into account the volume of foams.

Condensed Matter and Interphases / Конденсированные среды и межфазные границы   2023;25(1): 139–148

T. S. Trofimova et al.   The effect of current density on the structure of nickel electrolytic foams...

Surface morphology was analysed using an Olympus BX51 optical microscope (Olympus, Japan) and a Tescan VEGA 4 scanning electron microscope (SEM) (TESCAN, Czech Republic). The thickness of nickel deposits (h) was evaluated based on photo images of a thin section of the electrode cross section with a deposit.

The catalytic efficiency of the electrodes in relation to the hydrogen evolution reaction was evaluated by the analysis of the cathodic polarization curves obtained in 1 M NaOH solution at a potential scan rate of 3 mV·s^{-1}. The resulting electrolytic foam was the working electrode, and a graphite rod was used as the counter electrode. The potential was measured relative to a saturated silver chloride reference electrode. At least 3 curves were taken for each electrode until reproducible results were obtained. All studies were carried out at a temperature of 25°C.

3. Results and discussion

3.1. Morphology of nickel foams

Nickel electrolytic foams are characterized by the presence of macro- and micropores (Fig. 1). Macropores were formed in places where electrode surface is shielded by hydrogen bubbles and mainly represented by through-channels (Fig. 1e), the exits of channels to the foam surface are clearly visible on microphotographs (Fig. 1a–d).

Under the studied conditions, the metal was deposited as branched dendrites. The space between the dendrite branches and individual dendrites is a branched system of voids, with size much smaller than the size of macropores, and it can be called microporosity.

During 15 minutes of electrolysis at all current densities, the nickel foam thickness (h) increased linearly with the deposition time

a   b

c   d
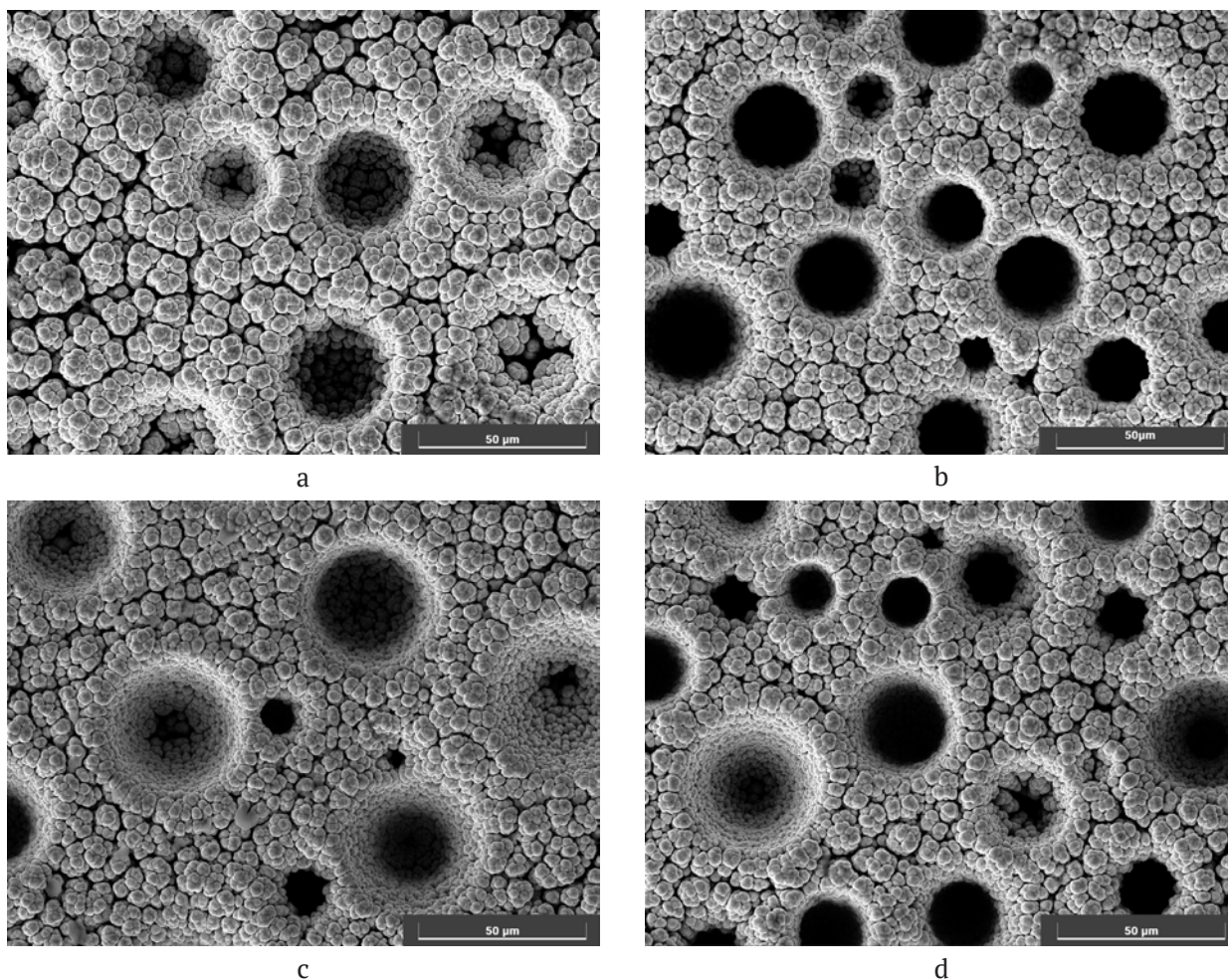
Fig. 1. SEM images of foams obtained at i = 0.3 (a), 0.6 (b), 0.9 (c), and 1.2 (d) A·cm^{-2}; t = 10 min. Image of the macropore on a foam cross section (d)

141

Condensed Matter and Interphases / Конденсированные среды и межфазные границы   2023;25(1): 139–148

T. S. Trofimova et al.   The effect of current density on the structure of nickel electrolytic foams...

(Fig. 2). At the same time, the deposition growth rate (dh/dt) increased with increase in current density (Table 1).
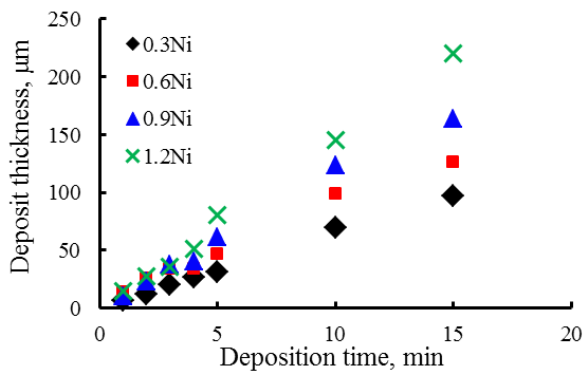
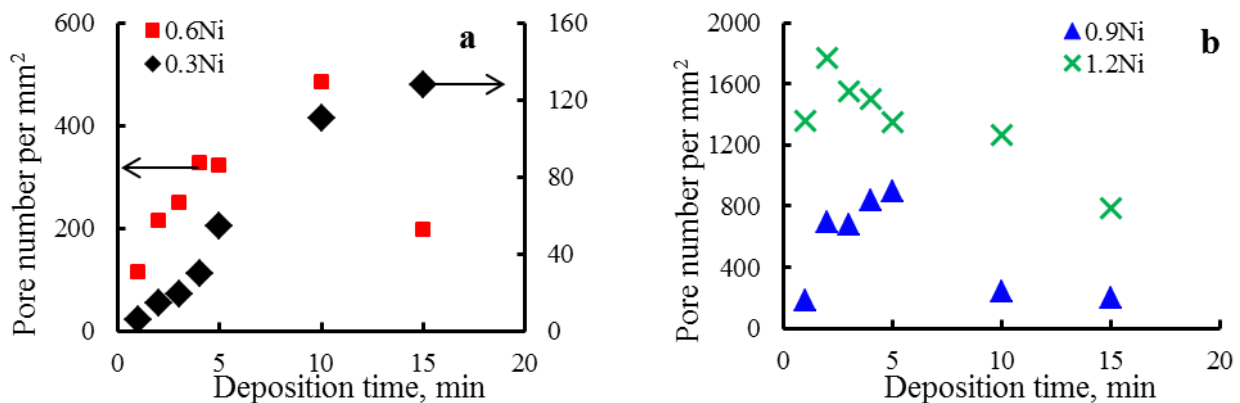**Table 1.** The effect of current density on the dendrite elongation rate and their radius

Deposition current density, A·cm^{-2}	dh/dt, cm/min	r_{tip}, μm
0.3	$0.64 \cdot 10^{-3}$	5.35
0.6	$0.97 \cdot 10^{-3}$	3.50
0.9	$1.07 \cdot 10^{-3}$	3.38
1.2	$1.25 \cdot 10^{-3}$	2.73

It is known [19] that, under conditions of diffusion limitations, metal deposition proceeds at the dendrite tips located at the deposit growth front, and the elongation rate (dh/dt) (Fig. 2) is determined by the limiting diffusion current density of spherical diffusion (i_{tip}) [19]:

$$\frac{dh}{dt} = \frac{\vartheta_{Ni}}{zF} i_{tip},\qquad(1)$$

$$i_{tip} = \frac{zFDC}{r_{tip}},\qquad(2)$$

where ϑ_{Ni} is molar volume of metal, m^3·mol^{-1}, D is the diffusion coefficient of nickel ions, m^2·s^{-1}, C is concentration of nickel ions in solution, mol·m^{-3}, dh/dt is the rate of dendrite elongation, m·s^{-1}.

The radius of dendrite branches was determined based on the deposit growth rate:

$$r_{tip} = \frac{DC \cdot \vartheta_{Me}}{dh/dt}.\qquad(3)$$

As follows from the literature data [19], the constancy of the growth rate during electrolysis indicates the formation of a dendrite deposit, characterised by uniform structure throughout the thickness. The calculated values of the tip radii decrease with increase in current density (Table 1) from 5.35 to 2.73 μm, which, as will be shown below, affects the microporosity of the foams.

Photographs of the outer surface of nickel foams obtained using an Olympus BX51 optical microscope (Olympus, Japan) were used to determine the diameter and number of macropores (Figs. 3 and 4). At least three samples obtained under the same conditions were analysed and at least 5 sites were selected on each of them. With an increase in the current density, an increase in the number of macropores per unit surface and a decrease in their average diameter were observed, which is consistent with the literature data [7, 11, 20]. Such dependences are explained by an increase in the rate of hydrogen evolution and, accordingly,

Fig. 2. Dependence of nickel foam thickness on deposition time at current density of 0.3, 0.6, 0.9, and 1.2 A of 0.3, 0.6, 0.9, and 1.2 A·cm^{-2}

Fig. 3. Change of macropore number at current densities of 0.3 and 0.6 A·cm^{-2} (a), 0.9 and 1.2 A·cm^{-2} (b)

Condensed Matter and Interphases / Конденсированные среды и межфазные границы   2023;25(1): 139–148

T. S. Trofimova et al.   The effect of current density on the structure of nickel electrolytic foams…

Fig. 4. Change of macropore diameters at current densities of 0.3, 0.6, 0.9, and 1.2 A·cm^{-2}

by a decrease in the residence time of a bubble on the deposit surface.

At current densities of 0.3 and 0.6 A·cm^{-2} within 10 minutes, an increase in the number of large pores up to 400 mm was observed^{-2} (Fig. 3a), which indicates the gradual formation of a porous structure. With an increase in current density up to 1.2 A·cm^{-2}, the formation of the template structure (formation of macropores more than 1600 mm^{-2}) finished within the first 2 minutes of electrolysis, then within 10 minutes the number of macropores decreased, but remained very high (Figs. 3b and 4). A similar pattern was observed for 0.9Ni samples, but for 5 minutes. With further electrolysis, there was a significant decrease in the number of pores and an increase in their size.

The difference in the dynamics of the formation of the macropore structure was associated with the intensity of hydrogen evolution. At low rates of hydrogen evolution, gas bubbles retained on the electrode surface for a time sufficient for their coalescence; therefore, for low current densities, the dependence of the number of pores and their sizes on the deposition time was observed. At high rates of hydrogen evolution, the bubbles quickly reached the critical diameter and immediately detached from the surface; therefore, the structure of the foams was more stable and changes less with time.

3.2. Determination of porosity

When metal foams are used as electrodes, the thickness of the porous layer and the fraction of the surface involved in the electrochemical process are important. Since the deposition rate

significantly depends on the current density, it is important to reveal how the structural properties change not with the deposition time, but with the thickness of the foams.

For deposits with different thickness obtained over different times, the fraction of the surface occupied by macropores θ_{macro} was calculated [17,21]. For calculations, several sites (K) on the electrode surface with deposits with the same area (s) were isolated. The total number of pores (N_k) and the diameter of each macropore (d_{jk}) were determined for each site. The fraction of the outer surface of the deposit occupied by macropores was estimated as follows:

$$\theta_{macro}(h) = \frac{\sum_{k=1}^{K} \sum_{j=1}^{N_k} \pi \frac{d_{jk}^2}{4}}{K \cdot s}. \tag{4}$$

According to the experimental data presented in Figs. 5, the dependence $\theta_{macro}(h)$ has a maximum, which is in good agreement with the data on changes in the number and diameter of macropores on time (Figs. 3 and 4). An increase in the fraction of the surface occupied by macropores was associated with an increase in the number of macropores and their diameter, and a decrease θ_{macro} occurred due to the merging of macropores.

The process of macropore formation is stochastic, therefore, for the approximation of the dependence of the fraction of large pores on the deposit thickness, a log-normal distribution was used [22]:

$$\theta_{macro}(H) = \frac{a}{\sigma\sqrt{2\pi}} \frac{1}{H} \exp\left[-\frac{1}{2\sigma^2}\left(\ln(H) - \mu\right)^2\right]. \tag{5}$$

Here σ and μ are distribution parameters, a is the scaling factor. Function argument $H = h/h_{st}$ is dimensionless, since the deposit thickness is divided by the unit of measurement $h_{st} = 1$ μm. Calculation of the σ, μ, a values was carried out by minimizing the sum of squared deviations of the experimental data θ_{macro} from data calculated by equation (5) [21]. The values of the determined coefficients are presented in Table 2.

As can be seen from the Table 2, the distribution parameters (σ and μ) for all porous deposits were close by the order of magnitude and regularly changed with increase in current density. The physical meaning of the parameters is still unclear, but it is important that the log-

Condensed Matter and Interphases / Конденсированные среды и межфазные границы   2023;25(1): 139–148

T. S. Trofimova et al.   The effect of current density on the structure of nickel electrolytic foams...

Table 2. The values of the empirical coefficients of Eq. 10 and the determination coefficient

Deposit	Coefficients and R^2			
	a	σ	μ	R^2
0.3 Ni	72.24	0.81	5.50	0.994
0.6 Ni	73.00	0.87	5.10	0.995
0.9 Ni	87.26	0.91	5.09	0.996
1.2 Ni	99.22	1.00	5.09	0.990

normal distribution describes well the change in the fraction of the surface occupied by macropores in a wide range of current densities. This indicates the similarity of the mechanisms of macropore formation, as well as the invariance of this mechanism with an increase in the current density of foam deposition. The good agreement of the experimental values of the fraction of macropores (Fig. 5) with the values calculated using the approximating equation 5 indicates the stochastic nature of the process of formation of the macropore system.

The total porosity was determined taking into account the mass (m_{Ni}) and volume of porous deposit (V_{dep}):

$$\beta_\Sigma = \frac{V_{pore}}{V_{dep}} = 1 - \frac{m_{Ni}}{\rho_{Ni} \cdot V_{dep}}, \qquad (6)$$

where V_{dep} – overall volume of deposit, ρ_{Ni} is the density of nickel. $V_{dep} = S_{geom} \cdot h$, S_{geom} is the geometric area of the deposit surface, cm²; V_{pore} is the volume of all pores in the deposit. The values of total porosity for deposits of different thicknesses are presented in Table 3.
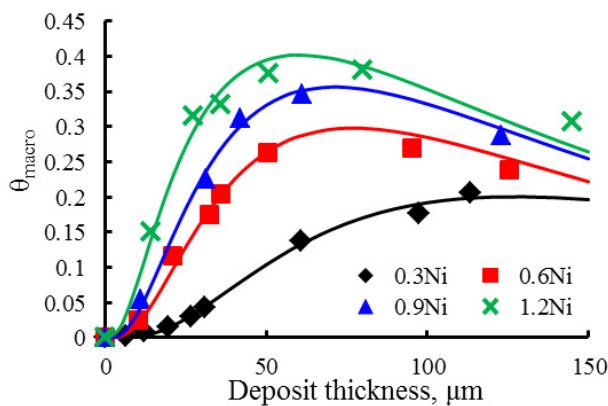
Fig. 5. Change of the θ_{macro} over the deposit thickness at i = 0.3, 0.6, 0.9, and 1.2 A·cm⁻². Markers – experimental data, lines – approximation by Eq. 5

Macroporosity is the ratio of the volume of large pores V_{macro} to deposit volume V_{dep}:

$$\beta_{macro} = V_{macro} \Big/ V_{dep}. \qquad (7)$$

The pore volume is the product of the cross-sectional area of the macropores at the deposit growth front (S_{macro}) and their depth. As can be seen from the micrograph (Fig. 1e), the macropores were through-pores; therefore, the average pore depth was taken as the thickness of the deposit layer (h):

$$V_{macro} = S_{macro} \cdot h. \qquad (8)$$

The macropore diameter varied with the deposit thickness. At the same time the porosity of the deposit changed. Therefore V_{macro} for deposits of different thickness was determined based on the experimental values $S_{macro,i} = \theta_{macro,i} \cdot S_{geom}$ using numerical integration of the dependence of the area of macropores on the thickness of the foam according to the equation:

$$V_{macro} = \sum_{i=1}^{M} \left[\frac{\left(S_{macro_i} + S_{macro_{i+1}}\right) \cdot \left(h_{i+1} - h_i\right)}{2} \right], \qquad (9)$$

here h_i is thickness of i-th deposit, μm; i = 0...M is foam sample number, M is quantity of deposit samples with different thicknesses obtained for different electrolysis times. At i = 0 electrolysis time was 0, respectively, h_i = 0 and S_{macro_i} = 0.

Macroporosity, as the proportion of macropores in the deposit volume, was determined:

$$\beta_{macro} = \frac{V_{macro}}{S_{geom} \cdot h}. \qquad (10)$$

The macroporosity for nickel foams of different thicknesses, calculated based on the experimental data, are represented by markers in Fig.6 and in Table 3. Macroporosity increased

Table 3 Values of total, macro- and microporosity of electrolytic foams obtained at current densities of 0.3, 0.6, 0.9, and 1.2 A·cm⁻² for 15 minutes

Deposit	β_Σ, %	β_{macro}, %	β_{micro}, %
0.3 Ni	62.9	9.1	53.8
0.6 Ni	49.2	19.4	29.9
0.9 Ni	47.3	26.6	20.7
1.2 Ni	41.6	31.1	10.5

Condensed Matter and Interphases / Конденсированные среды и межфазные границы   2023;25(1): 139–148

T. S. Trofimova et al.   The effect of current density on the structure of nickel electrolytic foams...

significantly with increase in foam deposition current density.

Taking into account the determined coefficients a, σ and μ (Table 2), the numerical integration of log-normal dependences was carried out $\theta_{macro}(H)$, and it allowed to calculate the volume of large pores for any deposit thickness:

$$V_{macro} = \int_0^h S_{macro}(h)dh = \int_0^h S_{geom} \cdot \theta_{macro}(h)dh. \quad (11)$$

Taking into account equation (10) macroporosity is:

$$\beta_{macro} = \frac{1}{h}\int_0^h \theta_{macro}(h)dh. \quad (12)$$

As can be seen in Fig. 6, the calculated curves are in good agreement with the values β_{macro} obtained based on experimental data, which indicates the applicability of equation 5 for describing the process of formation of the porous structure of nickel foams.

It should be noted that the total porosity of the foams was much higher than the macroporosity, which is due only to the presence of channels for the release of hydrogen bubbles. Total porosity also includes microporosity. It is not possible to determine the shape and size of microvoids, but it is possible to estimate their fraction, microporosity. Microporosity was calculated as the difference between the total porosity and macroporosity of deposits $\beta_{micro} = \beta_\Sigma - \beta_{macro}$.

The results of calculations of the total porosity, macroporosity, and microporosity for foams obtained at different current densities after 15 minutes of electrolysis are presented in Table 3. It can be seen that the total porosity of the foams gradually decreased with increasing deposition current density. In this case, the fraction of macropores and their contribution to the total porosity increased significantly, and microporosity decreased. The decrease in microporosity was associated with an increase in the number of dendrite branches on the foam surface between large pores, which led to their more compact arrangement. This conclusion is confirmed by the analysis of micrographs of samples using SEM (Fig. 1). The combination of macro- and microporosity provides the
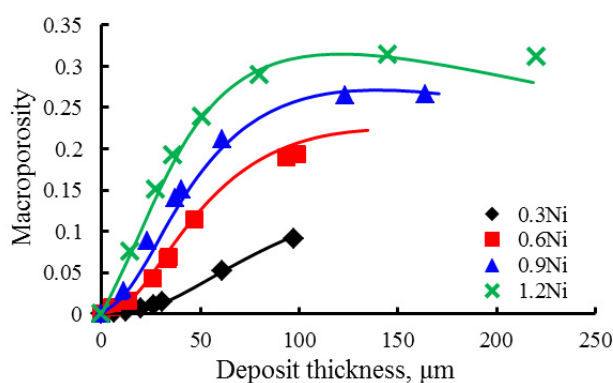

Fig. 6. Change of microporosity over the deposit thickness at i = 0.3, 0.6, 0.9, and 1.2 A·cm^{-2}. Markers – experimental data, lines – calculation by Eq. 12.
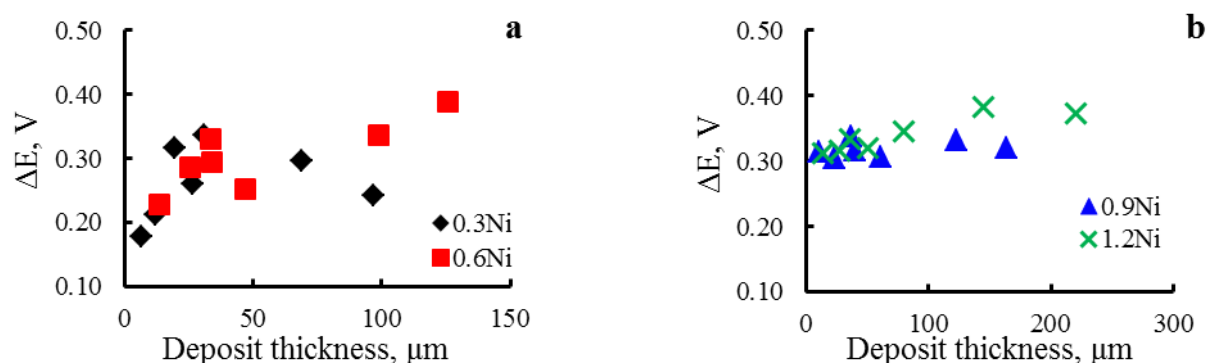
high efficiency of nickel foams as electrode materials.

3.3. Assessment of catalytic properties

For the evaluation of the catalytic properties of nickel foams with respect to the hydrogen evolution reaction, cathodic polarization curves were recorded in a 1 M NaOH solution. The polarization curves obtained on porous deposits were shifted to more positive potentials compared to the smooth nickel electrode.

The depolarization was chosen as a criterion of catalytic properties. The depolarization value is the difference in the potentials of the porous (E_{dep}) and a smooth nickel electrode (E_{sm}): $\Delta E = E_{dep} - E_{sm}$ at current density i = 0.3 A·cm^{-2}. This current density is used in the electrolysis of water in alkaline electrolytic cells [23].

As can be seen from Fig. 7, the depolarization of hydrogen evolution process varies in the range from 170 to 400 mV, depending on the mode of the production of foams and their thickness. The catalytic properties of the 0.3Ni and 0.6Ni samples strongly depend on the deposit thickness (Fig. 7a). This fact can be explained by the heterogeneity of the foam structure over the thickness: the number of pores and their sizes vary within a fairly wide range, which affects the surface area available for the hydrogen evolution reaction. As was shown above, 0.9Ni and 1.2Ni samples were characterized by the presence of a regular pore structure with a low variation of thickness. Due to this, their catalytic properties were quite stable and did not depend on the thickness of the deposit. In general, the good catalytic properties

Condensed Matter and Interphases / Конденсированные среды и межфазные границы   2023;25(1): 139–148

T. S. Trofimova et al.   The effect of current density on the structure of nickel electrolytic foams...

Fig. 7. Dependence of hydrogen evolution depolarization in 1 M NaOH at $i = 0.3$ A·cm^{-2} on the deposit thickness for 0.3Ni and 0.6Ni (a), 0.9Ni and 1.2Ni (b) samples

of the 0.9Ni and 1.2Ni samples can be explained by the high macroporosity, which makes a large part of the electrode surface accessible for the HER reaction.

4. Conclusion

It was shown that within 15 minutes of electrolysis, the growth rate of nickel foams remains constant and increased with increase in current density.

It has been established that at low current densities, a gradual formation of a porous structure occurred, which led to inhomogeneity in the size and number of pores throughout the thickness of the deposit. At the same time, at high current densities, the formation of the template structure ends in the first minutes of electrolysis and after the fraction of the surface occupied by macropores remained high.

It was shown that the log-normal distribution can be used to describe the formation of a hydrogen template as a system of macropores in electrolytic nickel foams in a wide range of current densities.

The macroporosity of deposits increased, while the total porosity and the fraction of micropores decreased with a change in the deposition current density from 0.3 to 1.2 A·cm^{-2}, which improves the catalytic properties of deposits.

Catalytic properties with respect to the hydrogen evolution reaction in an alkali solution for deposits obtained at current densities of 0.9 and 1.2 A·cm^{-2}, remained high at any foam thickness due to the formation of a more uniform porous structure of deposits with a high number of large pores of small diameter.

Contribution of the authors

The authors contributed equally to this article.

Conflict of interests

The authors declare that they have no known competing financial interests or personal relationships that could have influenced the work reported in this paper.

References

1. Li X., Zhao L., Yu J., Liu X., Zhang X., Liu H., Zhou W. Water splitting: from electrode to green energy system. *Nano-Micro Letters*. 2020;12: 131. https://doi.org/10.1007/s40820-020-00469-3

2. Herraiz-Cardona I., Ortega E., Vázquez-Gómez L., Pérez-Herranz V. Double-template fabrication of three-dimensional porous nickel electrodes for hydrogen evolution reaction. *International journal of hydrogen energy*. 2012;37(3): 2147–2156. https://doi.org/10.1016/j.ijhydene.2011.09.155

3. Siwek K. I., Eugenio S., Santos D. M. F., Silva M. T., Montemor M. F. 3D nickel foams with controlled morphologies for hydrogen evolution reaction in highly alkaline media. *International journal of hydrogen energy*. 2019;44(3): 1701–1709. https://doi.org/10.1016/j.ijhydene.2018.11.070

4. Swain N., Mitra A., Saravanakumar B., Balasingam S. K., Mohanty S., Nayak S. K., Ramadoss A., Construction of three-dimensional MnO$_2$/Ni network as an efficient electrode material for high performance supercapacitors. *Electrochimica Acta*. 2020;342: 136041. https://doi.org/10.1016/j.electacta.2020.136041

5. Shi Y., Zhang L., Zhang Y., Li J., Fu Q., Zhu X., Liao Q. Construction of a hierarchical porous surface composite electrode by dynamic hydrogen bubble template electrodeposition for ultrahigh-performance thermally regenerable ammonia-based batteries.

Condensed Matter and Interphases / Конденсированные среды и межфазные границы   2023;25(1): 139–148

T. S. Trofimova et al.   The effect of current density on the structure of nickel electrolytic foams…

Chemical Engineering Journal. 2021;423: 130339. https://doi.org/10.1016/j.cej.2021.130339

6. Qiu, H., Tang, T., Asif, M., Huang, X., Hou, Y. 3D porous Cu current collectors derived by hydrogen bubble dynamic template for enhanced Li metal anode performance. *Advanced Functional Materials.* 2019;29: 1808468. https://doi.org/10.1002/adfm.201808468

7. Yu X., Yuan Z. The structure evolution mechanism of Ni films depending on hydrogen evolution property during electrodeposition process. *Metallurgical and Materials Transactions B.* 2019;50: 587–594. https://doi.org/10.1007/s11663-019-01512-4

8. Sengupta S., Patra A., Jena S., Das K., Das S. A study on the effect of electrodeposition parameters on the morphology of porous nickel electrodeposits. *Metallurgical and Materials Transactions A.* 2018;49: 920–937. https://doi.org/10.1007/s11661-017-4452-8

9. González-Buch C., Herraiz-Cardona I., Ortega E., García-Antón J., Pérez-Herranz V. Synthesis and characterization of macroporous Ni, Co and Ni–Co electrocatalytic deposits for hydrogen evolution reaction in alkaline media. *International Journal of Hydrogen Energy.* 2013;38(25): 10157–10169. https://doi.org/10.1016/j.ijhydene.2013.06.016

10. Vainoris M., Tsyntsaru N., Cesiulis H. Modified electrodeposited cobalt foam coatings as sensors for detection of free chlorine in water. *Coatings.* 2019;9: 306. https://doi.org/10.3390/coatings9050306

11. Zhang H., Ye Y., Shen R., Ru Ch., Hu Y. Effect of bubble behavior on the morphology of foamed porous copper prepared via electrodeposition. *Journal of The Electrochemical Society.* 2013;160: D441. https://doi.org/10.1149/2.019310jes

12. Cui L., Hu L., Shen Q., Liu X., Jia H., Xue J. Three-dimensional porous Cu_2O with dendrite for efficient photocatalytic reduction of CO_2 under visible light. *Applied Surface Science.* 2022;581: 152343. https://doi.org/10.1016/j.apsusc.2021.152343

13. Teng X., Wang J., Ji L., Liu Y., Zhang C., Chen Z. Fabrication of three-dimensional multiscale porous alloy foams at a planar substrate for efficient water splitting. *ACS Sustainable Chemistry & Engineering.* 2019;7(5): 5412–5419. https://doi.org/10.1021/acssuschemeng.8b06452

14. Eugénio S., Demirci U. B., Silva T. M., Carmezim M. J., Montemor M. F. Copper-cobalt foams as active and stable catalysts for hydrogen release by hydrolysis of sodium borohydride. *International Journal of Hydrogen Energy.* 2016;41(20): 8438–8448. https://doi.org/10.1016/j.ijhydene.2016.03.122

15. Swain N., Saravanakumar B., Mohanty S., Ramadoss A., Engineering of thermally converted 3D-$NiOCo_3O_4$/Ni//3D-Υ-Fe_4NC@Ni/SS porous electrodes for high-performance supercapatteries. *Electrochimica Acta.* 2022;412: 140076. https://doi.org/10.1016/j.electacta.2022.140076

16. Mirzaee M., Dehghanian Ch. Nanostructured Ni-Cu foam electrodepositedon a copper substrate applied as supercapacitor electrode. *Acta Metallurgica Slovaca.* 2018;24: 325–336. https://doi.org/10.12776/ams.v24i4.1138

17. Trofimova T. S., Ostanina T. N., Nikitin V. S., Rudoi V. M., Ostanin N. I., Trofimov A. A. Modeling of the porous nickel deposits formation and assessing the effect of their thickness on the catalytic properties toward the hydrogen evolution reaction. *International Journal of Hydrogen Energy.* 2021;46: 16857–16867. https://doi.org/10.1016/j.ijhydene.2021.02.093

18. Marozzi C. A., Chialvo A. C. Development of electrode morphologies of interest in electrocatalysis. Part 1: Electrodeposited porous nickel electrodes. *Electrochimica Acta.* 2000;45: 2111–2120. https://doi.org/10.1016/S0013-4686(99)00422-3

19. Diggle J. W., Despic A. R., Bockris J. O. The mechanism of the dendritic electrocrystallization of zinc. *Journal of The Electrochemical Society.* 1969;116: 1503. https://doi.org/10.1149/1.2411588

20. Eugénio S., Silva T. M., Carmezim M. J., Duarte R. G., Montemor M. . Electrodeposition and characterization of nickel-copper metallic foams for application as electrodes for supercapacitors. *Journal of Applied Electrochemistry.* 2014;44: 455–65. https://doi.org/10.1007/s10800-013-0646-y

21. Trofimova T. S., Darintseva A. B., Ostanina T. N., Rudoi V. M., Il'ina I.E. Effect of the structure and morphology of Ni-based porous deposits on their electrocatalytic activity towards hydrogen evolution reaction. *Powder Metallurgy and Functional Coatings.* 2021;(4): 57–67. (In Russ., abstract in Eng.). https://doi.org/10.17073/1997-308X-2021-4-57-67

22. Eadie W. T., Dryard D., James F. E., Roos M., Sadoulet B. *Statistical methods in experimental physics.* North-Holland, Amsterdam; 1971. 296 p.

23. Bernäcker C. I., Rauscher T., Büttner T., Kieback B., Röntzsch L. A Powder metallurgy route to rroduce raney-nickel electrodes for alkaline water electrolysis. *Journal of The Electrochemical Society.* 2019;166(6): F357–F363. https://doi.org/10.1149/2.0851904jes

Information about the authors

Tina-Tini S. Trofimova, Junior Researcher Scientific of the Laboratory of Electrochemical Devices and Materials, Institute of Chemical Engineering, Ural Federal University (Ekaterinburg, Russia).

https://orcid.org/0000-0002-4135-8856
t.s.kuloshvili@urfu.ru

Condensed Matter and Interphases / Конденсированные среды и межфазные границы   2023;25(1): 139–148

T. S. Trofimova et al.   The effect of current density on the structure of nickel electrolytic foams...

Tatiana N. Ostanina, Dr. Sci. (Chem.), Professor of the Technology of Electrochemical Manufactures Department, Institute of Chemical Engineering, Ural Federal University (Ekaterinburg, Russia).

https://orcid.org/0000-0002-6149-7204
t.n.ostanina@urfu.ru

Valentin M. Rudoi, Dr. Sci. (Chem.), Professor of the Technology of Electrochemical Manufactures Department, Institute of Chemical Engineering, Ural Federal University (Ekaterinburg, Russia).

https://orcid.org/0000-0002-8055-8148
v.m.rudoi@urfu.ru

Elizaveta A. Mazurina, Master's Degree student of the Technology of Electrochemical Manufactures Department, Institute of chemical engineering, Ural Federal University (Ekaterinburg, Russia).

https://orcid.org/0000-0001-5507-0311
maz_liza@mail.ru

Department of General and Inorganic Chemistry of Voronezh State University celebrates its 90th anniversary

The Department of General and Inorganic Chemistry was founded in 1932. It was headed by Associate Professor A.P. Buntin, who later became the rector of Tomsk State University. From 1932 to 1964, Professor A. P. Palkin headed the department, he was a student of the outstanding Russian scientist academician N. S. Kurnakov, the creator of physical and chemical analysis and founder of the largest school of inorganic chemists in the USSR.

The peaceful activity of the department was interrupted by the war. Many employees and students joined the army. The scientific and educational work was reorganized. Within their capacities, the remaining team started assistance to the front. A great responsibility fell on the shoulders of the associate professor of the department N. I. Glistenko, who headed the university (Rector of VSU from 1941 to 1945), and the head of the department, Professor A. P. Palkin, who in 1939 became dean of the Faculty of Chemistry.

Since 1962, the department has been repeatedly reorganized. On its basis, the country's first Department of Semiconductor Chemistry was created, headed by Associate Professor Ya. A. Ugai (later – Professor, Doctor of Chemical Sciences, Honoured Scientist of the Russian Federation, USSR National Prize in Science laureate, Distinguished Citizen of Voronezh). In 1964, after the death of A. N. Palkin for a short period, the department was headed by the former rector of VSU N. I. Glistenko. In 1966, in accordance with the decision of the Faculty's Academic Council, the Departments of Inorganic Chemistry and Semiconductor Chemistry were merged into one – the Department of Inorganic Chemistry, headed by Professor Ya. A. Ugai. In 1970, this department was reorganized into the Department of General and Inorganic Chemistry. Its main scientific direction is semiconductor materials science, which is inextricably linked with microelectronics.

Recently, the training of specialists at the Department of General and Inorganic Chemistry was led by the Honoured Worker of Higher Education, Professor E. G. Goncharov (a fellow of the Faculty of Chemistry of the Voronezh State University. He will turn 90 on April 17, 2023), Honorary Workers of Higher Professional Education of the Russian Federation Professor I. Ya. Mittova and V. N. Semenov. It should be noted that Professor of the Department of General and Inorganic Chemistry, Honoured Worker of Higher School Yu. P. Afinogenov was the dean of the Faculty of Chemistry for 33 years.

The editorial board of "Condensed Matter and Interphases"

Translated by Valentina Mittova

Professor Evgeny Goncharov celebrates his 90th anniversary

E. G. Goncharov was born on April 17, 1933. After he finished school, he studied at the Voronezh State University at the Faculty of Chemistry and was sent to work at the Chemical Automatics Design Bureau (KBKHA) in 1955, where he worked his way up from engineer to the head of the central factory laboratory and deputy chief metallurgist in eight years. He participated in the creation of liquid-propellant rocket engines, allowing the launch of the first manned spacecraft.

During this period of time, Evgeny G. Goncharov successfully combined his industrial activity with scientific work in the field of semiconductor chemistry, he was enrolled into the extramural postgraduate programme at the Department of Inorganic Chemistry of Voronezh State University.

In the early sixties, E. G. Goncharov headed the laboratory of powerful transistors at the Central Design Bureau of the Voronezh Semiconductor Plant, dealing with the problem of the creation and introduction into production of a new generation of semiconductor materials.

From 1965 until his retirement (2019), he worked continuously at the Faculty of Chemistry of Voronezh State University. In 1967, Evgeny G. Goncharov defended his PhD thesis, in 1990 he defended his DSc thesis in the field of semiconductor materials, and in 1991 he was awarded the title of professor. From 1990 to 2011 he was the Head of the Department of General and Inorganic Chemistry of Voronezh State University.

All these years, the main scientific interests of E. G. Goncharov were concentrated in the field of solid state chemistry, the study of the mechanism of synthesis and defect formation in semiconductor chemical compounds and solid solutions based on them.

Scientific results are presented in three monographs "Phase equilibria between phosphorus, arsenic, antimony, and bismuth", "Semiconductor phosphides and arsenides of silicon and germanium", "Solid solutions in ternary systems with elements of the fifth group" and in more than 400 scientific articles. E. G. Goncharov was advisor for 20 PhD theses.

In recent years, based on extensive teaching experience, E. G. Goncharov and co-authors published a number of textbooks, many of which were awarded with the classified publication title of the Ministry of Higher Education or recommended by educational and methodological association for classical university education: "Phase diagrams of multicomponent systems" (certified by the Ministry of Higher Education, 2005), "Structure of matter and chemical bonding in the course of inorganic chemistry" (recommended by the educational and methodological association, 2008), "General chemistry.

Selected chapters" (recommended by the educational and methodological association, 2010), "Theoretical foundations of inorganic chemistry" (recommended by the educational and methodological association, 2014), "Short course of theoretical inorganic chemistry" (recommended by the educational and methodological association, 2017).

E. G. Goncharov was a member of two dissertation boards in chemical sciences, was a member of the editorial board of the journals "Condensed Matter and Interphases", "Proceedings of Voronezh State University" (series Chemistry. Biology. Pharmacy), was a member of the Russian National Committee for Thermal Analysis and Calorimetry of the Russian Academy of Sciences.

In 1999, for fruitful educational and scientific work, academic staff training programmes, Evgeny G. Goncharov was awarded with the title of Honoured Worker of Higher Education of the Russian Federation."

Evgeny G. Goncharov is not only an excellent scientist and teacher, he is well versed in literature, sports, music, perfectly plays the piano. His entire career and creative life were described in the books of memoirs "My Way to the University" (2014) and "Islands of Memory" (2021).

We wish dear Evgeny G. Goncharov, who is the same age as the Faculty, good health and never his lose the connection with the Faculty of Chemistry.

The team of the Department of General and Inorganic Chemistry and the editorial board of the journal

Translated by Valentina Mittova

We remember Professor Valentin Z. Anokhin (1937–1991)

Valentin Z. Anokhin was born on October 7, 1937 in the city of Livny. He studied at a secondary school in Grodno (Belorussian SSR), he graduated from school in 1954 and was awarded with a gold medal for academic excellence. In the same year he entered the chemical faculty of Voronezh State University; after graduation in 1959, V. Z. Anokhin was assigned to the design bureau of the Elektronika plant, which was then under construction, where he worked as an engineer at the Technical Information Bureau for three years.

In 1962, he was enrolled on a PhD programme at VSU, and then was accepted as a lecturer at the Department of General and Inorganic Chemistry. In 1968 V. Z. Anokhin defended his PhD thesis and continued to work at the department as an assistant professor. In 1988, Valentin Z. Anokhin defended his doctoral thesis "Kinetics and Mechanism of Thermal Oxidation of Silicon" in Moscow State University, and in 1990 he gained the title of full professor of the Department of General and Inorganic Chemistry. In this position, he worked until his death in August 1991.

During his work at VSU, V. Z. Anokhin published over 150 scientific papers, and the monograph "Thermal oxidation of silicon". He was a member of the creative team that took part in writing several chapters in Y. A. Ugai's "General Chemistry" and "Inorganic Chemistry" textbooks, approved by the Ministry of Higher and Secondary Specialized Education of the USSR as the first textbooks for university students studying in the speciality "Chemistry".

Valentin Z. Anokhin made a significant contribution to the development of scientific areas related to the kinetics of interaction processes on the surface of semiconductor materials, as well as the processes of synthesis and study of the properties of binary and ternary semiconductor compounds. His talent manifested as such a stormy creative manner that his colleagues quite deservedly called Valentin Z. Anokhin a "generator of ideas".

V. Z. Anokhin was an exceptionally creative person, not only in scientific activities, he also conducted active social work. When he was still a student, Valentin Z. Anokhin became one of the founders of the VSU cameo theatre of the Faculty of Chemistry, and until the last years of his life he was writing skits and performances for the team of the cameo theatre. For active participation in amateur performances and leadership of the artistic teams of the Faculty of Chemistry, he was repeatedly awarded with honorary certificates and the rector's letters of acknowledgement.

V. Z. Anokhin was highly respected among his colleagues, and the students considered him one of the best teachers of the Faculty of Chemistry. For his proactive approach to life, he was elected secretary of the party committee of the Faculty of Chemistry and was made a member of the local and trade union committees of the Voronezh State University. His colleagues and comrades, celebrating the 85th anniversary of Valentin Z. Anokhin, agree that he lived a short, but very bright and full life, and left indelible mark in the history of the Faculty of Chemistry and the University.

The team of the Department of General and Inorganic Chemistry

Translated by Valentina Mittova

Guide for Authors – 2023

Manuscripts should be submitted as single **Microsoft Word 2003** files.
Preferred font 12 pt Times New Roman (please, do not use any other fonts, except for Symbol), 1.5 spaced lines, 1.25 cm first-line indent. Decimal values (e.g. 0.1; 0.9; 2.3) should be written using a decimal point.

Modelling of interdiffusion and phase formation in thin-film two-layer systems of polycrystalline oxides of titanium and cobalt
(All proper nouns should be capitalized; titles and subtitles should be left-aligned)

N. N. Afonin*1, V.A. Logacheva2
*1Voronezh State Pedagogical University,
86 ul. Lenina, Voronezh 394043, Russian Federation*
(Official name and address of the organisation)
*2Voronezh State University,
1 Universitetskaya pl., Voronezh 394018, Russian Federation*

Abstract
The abstract should be 200–250 words and include the following sections.

Purpose: States the problem considered in the article, its importance, and the purpose of the research.

Experimental: Provides information about the objects being studied and the methods used.

Conclusions: Provides a brief description of the principal results, major conclusions, and their scientific and practical relevance.

Keywords: Please, provide 5–10 keywords for the principal concepts, results, and terms used in the article.

_____
*Nikolay N. Afonin, nafonin@vspu.ac

Article structure
The main text of the manuscript should have the following structure.

1. Introduction
The introduction (1–2 pages) states the problem under consideration, its relevance, and the most important tasks that need to be resolved. Describe the scientific problems which have not yet been solved and which you sought to solve in your research. The introduction should contain a short critical review of previously published works in this field and their comparative analysis. It is recommended that the analysis is based on 20–30 studies (no more than 20% of references to the author's own works, at least 50% of the references should be to articles published within the previous 5 years). **The purpose** of the article is indicated by the problem statement.

The Vancouver reference style is used in the journal: bibliographic references in the text of the article are indicated by numbers in square brackets; in the references section, the references are numbered in the order they are mentioned in the text.

Example of references in-text citations:
Single crystals of difluorides of alkaline earth elements are widely used as photonics materials [1–3] as well as matrices for doping with rare-earth ions [4, 10].

References should primarily be made to original articles published in scientific journals indexed by global citation databases. References should indicate the names of all authors, the title of the article, the name of the journal, year of publication, volume (issue), number, pages, and DOI (Digital Object Identifier https://search.crossref.org/). If a DOI is lacking, a link to the online source of the article must be indicated. References to dissertation abstracts are acceptable if the texts are available online. It is vital that our readers can find any of the articles or other sources listed in the reference section as fast as possible. Links to unpublished literature sources or sources not available online are unacceptable.

2. Experimental
The experimental section (2–3 pages) provides the details of the experiment, the methods, and the equipment used. The object of the study and the stages of the experiment are described in detail and the choice of research methods is explained.

3. Results and discussion
Results and discussion (6–8 pages) should be brief, but detailed enough for the readers to assess the conclusions made. It should also explain the choice of the data being analysed. Measurement units on graphs and diagrams should be separated with a coma. **Formulae should be typed using Microsoft Office Equation 3 or Math Type** and aligned on the left side. Latin letters should be in italics. Do not use italics for Greek letters, numbers, chemical symbols, and similarity criteria.

All subheadings should be in italics.

Example:
1.1. X-ray diffraction analysis

Example of figure captions in the text of the article: Fig. 1, curve *1*, Fig. 2b.

A complete list of figures should be provided at the end of the paper after the information about the authors.

Figures and tables should not be included in the text of the article. They should be placed on a separate page. Figures should also be **submitted as separate** *.tif, *.jpg, *.cdr, or *.ai. files. **All figures should have a minimum resolution of 300 dpi.** Name each figure file with the name of the first author and the number of the figure.

4. Conclusions

Conclusions (1 paragraph) should briefly state the main conclusions of the research. Do not repeat the text of the article. The obtained results are to be considered with respect to the purpose of the research. This section includes the conclusions, a summary of the results, and recommendations. It states the practical value of the research and outlines further research problems in the corresponding field.

Contribution of the authors

At the end of the Conclusions the authors should include notes that explain the actual contribution of each co-author to the work.

Example 1:

Nikolay N. Afonin – Scientific management, Research concept, Methodology development, Writing – original draft, Final conclusions.

Vera A. Logachova – Investigation, Writing – review & editing.

Example 2:

The authors contributed equally to this article.

Conflict of interests

The authors declare that they have no known competing financial interests or personal relationships that could have influenced the work reported in this paper.

References

(The references are to be formatted according to the Vancouver Style. The reference list should only include articles published in peer-reviewed journals)

*Examples***:**

Articles in scientific journals

1. Bahadur A., Hussain W., Iqbal S., Ullah F., Shoaib M., Liu G., Feng K. A morphology controlled surface sulfurized CoMn2O4 microspike electroncatalyst for water splitting with excellent OER rate for binder-free electrocatalytic oxygen evolution. *Journal of Materials Chemistry A*. 2021;20(9): 12255–12264. https://doi.org/10.1039/D0TA09430G

2. Alexandrov A. A., Mayakova M. N., Voronov V. V., Pominova D. V., Kuznetsov S. V., Baranchikov A. E., Ivanov V. K., Fedorov P. P. Synthesis upconversion luminophores based on calcium fluoride. *Condensed Matter and Interphases*. 2020;22(1): 3–10. https://doi.org/10.17308/kcmf.2020.22/2524

3. Kopeychenko E. I., Mittova I. Y., Perov N. S., Alekhina Y. A., Nguyen A. T., Mittova V. O., Pham V. Synthesis, composition and magnetic properties of cadmium-doped lanthanum ferrite nanopowders. *Inorganic Materials*. 2021;57(4): 367–371. https://doi.org/10.1134/S0020168521040075

Books: print

4. Nakamoto K. *Infrared and Raman spectra of inorganic and coordination compounds*. New York: John Wiley; 1986. 479 p.

5. Fedorov P. P., Osiko V. V. *Crystal growth of fluorides. In: Bulk Crystal Growth of Electronic. Optical and Optoelectronic Materials*. P. Capper (ed.). Wiley Series in Materials for Electronic and Optoelectronic Applications. John Wiley & Son. Ltd.; 2005. pp. 339-356. https://doi.org/10.1002/9780470012086.ch11

6. *Nanostructured oxide materials in modern micro-, nano- and optoelectronics*. V. A. Moshnikov, O. A. Aleksandrova (eds.). Saint Petersburg: Izd-vo SPbGETU "LETI" Publ., 2017. 266 p. (in Russ.)

Conference proceedings: individual papers

7. Afonin N. N., Logacheva V. A., Khoviv A. M. Synthesis and properties of functional nanocrystalline thin-film systems based on complex iron and titanium oxides. In: *Amorphous and microcrystalline semiconductors: Proc. 9th Int. Conf., 7–10 July 2014*. St. Petersburg: Polytechnic University Publ.; 2014. p. 356–357. (In Russ.)

Website

8. NIST Standard Reference Database 71. *NIST Electron Inelastic-Mean-Free-Path Database: Version 1.2.* Available at: www.nist.gov/srd/nist-standard-reference-database-71

Patent

9. Chekanov V. V., Kandaurova N. V., Rakhmanina Yu. A., Chekanov V. S. *Ultrasound indicator 2.* Patent RF, no. 2446384, 2012. Publ. 27.03.2012, bull. no. 9. (In Russ.)

Information about the authors

This section should include the full last and first name(s) of the author(s), their academic degree, academic title, affiliation, position, city, country, e-mail, and ORCID (register for an ORCID here https://orcid.org/register).

Example:

Nikolay N. Afonin, Dr. Sci. (Chem.), Research Fellow, Professor at the Department of Science and Technology Studies, Voronezh State Pedagogical University (Voronezh, Russian Federation).

https://orcid.org/0000-0002-9163-744X

nafonin@vspu.ac.ru

Vera A. Logachova, Cand. Sci. (Chem.), Research Fellow at the Department of General and Inorganic Chemistry, Voronezh State University (Voronezh, Russian Federation).

https://orcid.org/0000-0002-2296-8069

kcmf@main.vsu.ru

Tien Dai Nguyen, PhD in Advanced Materials Science and Engineering, Lecturer/ Research at Institute of Theoretical and Applied Research (ITAR), Duy Tan University (DTU), Hanoi, Vietnam.

https://orcid.org/0000-0002-9420-210X

nguyentiendai@duytan.edu.vn

Valery V. Voronov, Cand. Sci. (Phys.-Math.), Head of the Laboratory, Prokhorov General Physics Institute of the Russian Academy of Science (Moscow, Russian Federation).

https://orcid.org/0000-0001-5029-8560

voronov@lst.gpi.ru

A complete list of figures should be provided at the end of the paper after the information about the authors.

Example:

Fig. 1. Dependences of the parameters *a* and *c* of the tetragonal lattice of nanocrystalline PdO films on the oxidation temperature T_{ox}: *1* – single-phase PdO films, *2* – heterophase PdO + Pd films; *3* – data of the ASTM standard [22, 23]

Table 1. The values of relative electronegativity (ENE) of some chemical elements [30] and the proportion of the ionic component of the chemical bond in binary compounds of the AB composition formed by these elements
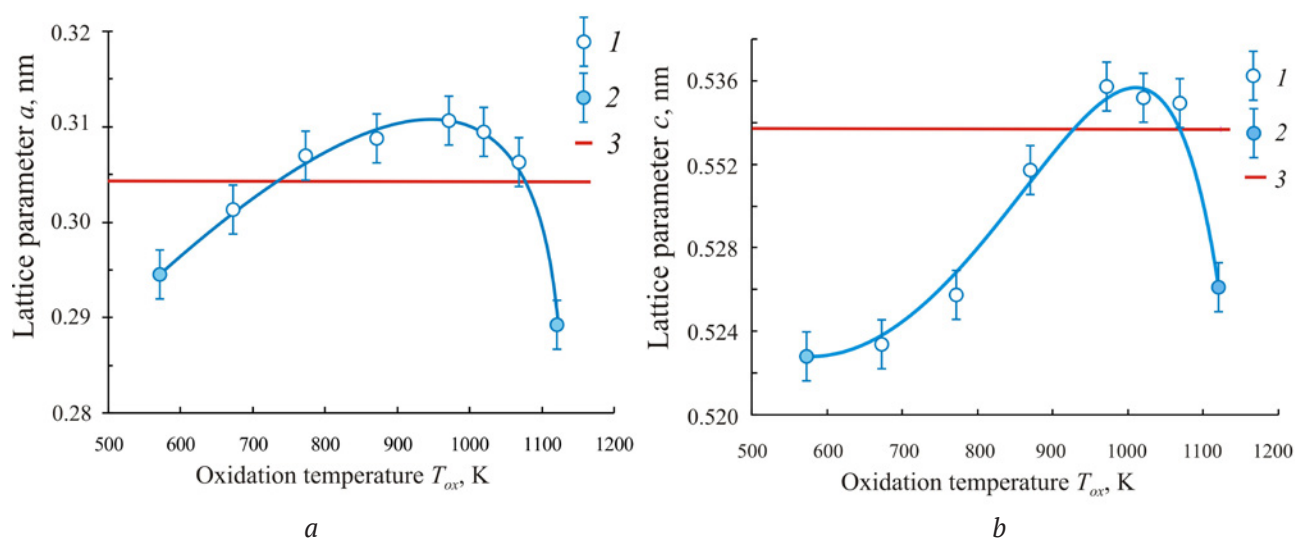
a   *b*

Fig. 1. Dependences of the parameters *a* and *c* of the tetragonal lattice of nanocrystalline PdO films on the oxidation temperature T_{ox}: *1* – single-phase PdO films; *2* – heterophase PdO + Pd films; *3* – data of the ASTM standard [22, 23]

Table 1. Values of the ionic radii of palladium Pd^{2+} and oxygen O^{2-} [30–32]

Ion	Coordination number CN	Coordination polyhedron	Values of ionic radii R_{ion}, nm
Pd^{2+}	4	Square (rectangular)	0.078 [30]; 0.086 [31]; 0.078 [32]
O^{2-}	4	Tetragonal tetrahedron	0.132 [30]; 0.140 [31]; 0.124* [31]; 0.132 [32]

*The values of ionic radius were obtained on the basis of quantum mechanical calculations.

ACCOMPANYING DOCUMENTS
(The following documents should be submitted as PDF files)
1. Covering letter (with authorisation for open access publication)
2. License agreement (signed by all authors) https://journals.vsu.ru/kcmf/Licensingcontract
3. Manuscript.

EDITING AND PROOFREADING
When the layout is ready it is sent back to the authors for proofreading. The article should be sent back to the publisher within a maximum of three days. The authors may only correct printing mistakes and introduce minor changes to the text or tables.